EXPERIMENTAL AND THEORETICAL STUDIES OF THE HYDROGEN EXCHANGE REACTION

Thesis by

Maria Rebecca Giorgi

In Partial Fulfillment of the Requirements

for the Degree of

Doctor of Philosophy

Division of Chemistry and Chemical Engineering

California Institute of Technology

Pasadena, California

1992

(Defended February 18, 1992)

In memory of my parents, Michele and Matilde Giorgi

ACKNOWLEDGEMENTS

The completion of this thesis has required the assistance of many people. I would like to thank my research advisor, Aron Kuppermann, for his help, patience and encouragement over the years, especially during the difficult times.

I also wish to thank the members of my committee, Prof. J. L. Beauchamp, Prof. H. B. Gray and Prof. B. V. McKoy for their interest in my work, and concern for my career. I also acknowledge the help and support that Prof. F. C. Anson has provided in the past two years.

I owe my interest in reaction dynamics to my undergraduate advisor, Richard Bernstein, who introduced me to the field, and guided me through my first attempts at experimental work.

Through the years, I have understood the importance of working in a friendly atmosphere (which I originally took for granted): the members of the Kuppermann group, past an present, have provided me with an infinite source of scientific as well as personal advice. I have always had the opportunity to discuss my problems within the group, and have formed long-lasting friendships, that have allowed me to get through several crises. Mary Rodgers and I started our work at the same time, and I cannot imagine what my life as a graduate student would have been like without her friendship. She has always been my first choice (lucky for her!) for advice, and I am grateful for the time she has spent listening to me. For the past year, I have greatly missed the advice and expertise of Steve Cuccaro, whom I consulted about almost any aspect of my work for the previous five years; I am glad that he has still accepted inquiries over the phone, and hope that we will keep in touch. I am very grateful to Garth Parker, who patiently taught me how to operate the equipment for the $H + H_2$ experiments: he always seemed to have time to answer my questions (even when it was apparent that he didn't), and had a unique desire to share his knowledge with others, and an instinct to want to make

life easier for his fellow group members. I would like to thank Isaac Xavier and Kerry Walzl for teaching me the secrets of the electron impact spectrometer, and helping me get through my first experimental efforts in graduate school. In the past half year, I have benefited from the invaluable help of Mark Wu who helped me get through the theoretical portion of this thesis. My understanding of the field of chemical dynamics has significantly been enhanced by the study of colinear reactions using the computer programs that he provided and explained to me. I also wish to thank Carrie Stroud for her friendship and support, especially during the last few months. From the scientific point of view, it has definitely helped me to discuss various aspects of colinear reactions with her; on the personal level, it has been fun to re-live some of the experiences of my younger years as a graduate student (good and bad).

Altough my interaction with them was more limited, I would also like to acknowledge the contributions that other Kuppermann group members have made to my scientific and personal development: Paul Hipes, Zhengwei Peng, Jin Qiu, Søren Padkjaer, N. Vaidehi, Amy Shaw and Sandor Kristyan have all contributed to my undestanding with their questions, and the sharing of their experiences.

I have also to thank many members of other research groups for their help and support: Shenda Baker has always been there for me whenever I have needed help or advice; I hope that despite the distance we will keep in touch.

I have always found the subbasement of Noyes to be a friendly environment and would like to thank all its inhabitants, past and present. In particular, for the past couple of years, I have found myself adopted by the members of the Weitekamp group; I have found them to always be receptive to my problems, and have thoroughly enjoyed having them as neighbors. My thesis and I have greatly benefited from the constant supply of superb coffee beans, and I thank them for that.

Many members of the Zewail group helped me get through tough times with the laser systems employed in this thesis: Larry Peng, Marcos Dantus, Ian Sims, and Martin Gruebele have all helped me overcome serious difficulties, and kept the experiments running. Martin has also been invaluable as a source of scientific advice, both theoretical and experimental, and I am very grateful for the interest that he has taken in my work, which has greatly increased my understanding and boosted my confidence.

During my experimental years, I have found the Chemistry Department shops indispensable for the timely progress of my project. Tom Dunn, Guy Duremberg, Tony Stark, Ray Garcia, Gabor Faludi, John Pirolo and Jess Miller have all contributed to keeping my projects running. I sincerely appreciate their prompt response, whenever an "emergency" arose, and there were many such occasions. I also would like to thank Dan Zirin and Dave Malerba for their help with the departmental VAX.

My years as a graduate student have also been made happier by the warmth of my friends outside of Caltech. I thank the Arnazzi family, especially Hector, Patricia and Lourdes for their love and support during these difficult years.

Finally I would like to acknowledge the people that are dearest to me, and whose love and faith in me has never waivered: my fiancé, David Shykind, has had to put up with me for what have been the most difficult years of my life, and I only hope that I can some day help him as much. His family, especially his parents Ed and Arlene, have welcomed me into their family and have not hesitated to make me feel part of it. I am grateful for that, and look forward to spending time with them in the future.

Back home in Italy, I have a wonderful family that has shared all of my joy, pride and pain. My brother Vittorio has been an inspiration for me through my

life, an example of integrity, discipline and persistence; I only wish that we had not chosen to live a continent apart!

My grandmother Maria Rebecca and my uncles Giulio and Nello have always had complete faith in my abilities, and I will always thank them for that.

It is not my intention to end with a sad note, but I will always regret not having the two people who are most responsible for my success with me, as I complete this Ph.D. thesis, my father Michele and my mother Matilde. Their premature departures have been the hardest of life's lessons to accept, and I have missed them greatly during the past few years. I am however happy that I have completed what we originally set out to do, over a decade ago, with immense sacrifice on their part.

Many, many thanks!!

ABSTRACT

This thesis consists of experimental and theoretical efforts to better understand the hydrogen exchange reaction. Colinear quantum mechanical calculations were conducted on the isotopic H + H_2 reaction, using the method of hyperspherical coordinates. Reaction probabilities and rate constants have been obtained for thirteen isotopic hydrogenic systems, and the results compared to those of conventional transition state theory and transition state theory with quantum corrections. The validity of the conservation of vibrational energy (CVE) and the vibrationally adiabatic (VA) approximations were tested. It was found that the VA approximation gives fairly accurate rate constants, although it is inadequate at predicting low temperature isotope effects. On the other hand, conventional transition state theory predicts isotope effects accurately, except in the cases where tunnelling is a major effect, such as the H_3 system.

The second part of the thesis illustrates the technique of vacuum ultraviolet laser induced fluorescence for the state-specific detection of molecular hydrogen. Preliminary investigations of the potential application of the LIF technique to the detection of products of the hydrogen exchange reaction are described.

TABLE OF CONTENTS

CHAPTER I

INTRODUCTION

I. INTRODUCTION

The reaction of hydrogen atoms with hydrogen molecules has been of fundamental interest since London[1] obtained the first potential energy surface calculated from quantum theory. It was the first reaction to show curvature in the Arrhenius plot, and therefore the model for theories of quantum mechanical tunnelling. Because each atom can be replaced with a D or a T atom, it has been the preferred prototype for the study of isotope effects.

The colinear model of the hydrogen exchange reaction has been very successful in explaining the dominant features of the dynamics,[2-6] and has been used extensively to calculate reaction probabilities and rate constants for various isotopic combinations.

The potential energy surface of H_3 has now been calculated accurately for many geometries,[7,8] and fully converged three-dimensional quantum mechanical calculations[9-13] have become available for comparison with molecular beam[14,15] and bulb experiments.[16-24]

This dissertation can be divided into two sections: in the first part, quantum mechanical calculations illustrating isotope effects in the colinear $H + H_2$ reaction are presented; the second section describes preliminary attempts to detect nascent rovibrational populations from the hot atom reaction using vacuum-ultraviolet laser induced fluorescence.

The organization of this thesis is as follows: Chapter II is an attempt to review the vast literature available on this reaction: both the colinear and the three dimensional quantum reactive scattering results are summarized, and compared to semiclassical results. The experimental work is also reviewed. Chapter III discusses the colinear quantum mechanical calculation of isotope effects using the method of hyperspherical coordinates. Accurate reaction probabilities are presented, and rate constants compared to the results of conventional transition state theory, and

transition state theory with one-dimensional quantum corrections. Approximate transmission coefficients are obtained for both the conservation of vibrational energy model (CVE) and the vibrationally adiabatic (VA) model. It is found that conventional transition state theory predicts isotope effects to a greater accuracy than its corrected counterparts, except for the cases when tunnelling is a major effect. Both the CVE and VA approximations fail to predict iosotope effects, even though the VA rate constants are in fair agreement with the quantum mechanical ones.

Chapters IV through VI are an account of the experimental work: Chapter IV describes the generation of tunable VUV laser radiation for the state-specific detection of molecular hydrogen; Chapter V describes the application of this technique to H_2 . A comparison is made with the results of Coherent Anti-Stokes Raman Spectroscopy (CARS) and Resonance-Enhanced Multiphoton Ionization (REMPI). Chapter VI describes the experimental set-up for study of the H + H_2 reaction and the preliminary results obtained.

Several appendices follow: Appendix 1 describes in detail the electronics used in the VUV experiments, with particular emphasis on the newly built equipment.

Appendices 2 and 3 describe the technique of electron-impact spectroscopy and the study of two polyatomic systems, the diketene molecule and the radical CF_2.

REFERENCES

1. F. London, *Z. Electrochem.* **35**, 552 (1929).
2. D. G. Truhlar and A. Kuppermann, *J. Chem. Phys.* **52**, 3841 (1970).
3. D. G. Truhlar and A. Kuppermann, *J. Chem. Phys.* **54**, 4881 (1971).
4. D. G. Truhlar and A. Kuppermann, *J. Chem. Phys.* **56**, 2232 (1972).
5. D. G. Truhlar and A. Kuppermann, *Chem. Phys. Lett.* **9**, 269 (1971).
6. D. G. Truhlar, A. Kuppermann and J. T. Adams, *J. Chem. Phys.* **52**, 3841 (1970).
7. D. G. Truhlar and R. E. Wyatt, *Ann. Rev. Phys. Chem.* **27**, 1 (1976).
8. D. G. Truhlar and R. E. Wyatt, *Adv. Chem. Phys.* **36**, 141 (1977).
9. D. E. Manolopoulos and R. E. Wyatt, *Chem. Phys. Lett.* **159**, 123 (1989).
10. J. H. Zhang and W. H. Miller, *Chem. Phys. Lett.* **153**, 465 (1988); *J. Chem. Phys.* **90**, 7610 (1989); *Chem. Phys. Lett.* **159**, 130 (1989.).
11. J. H. Zhang and W. H. Miller, *J. Chem. Phys.* **91**, 1528 (1989); *J. Chem. Phys.* **92**, 1811 (1990.).
12. M. Mladenovic, M. Zhao, D. G. Truhlar, D. W. Schwenke, Y. Sun and D. J. Kouri, *J. Phys. Chem.* **92**, 7035 (1988).
13. M. Zhao, D. G. Truhlar, D. W. Schwenke and D. J. Kouri, *J. Phys. Chem.* **94**, 7074 (1990).
14. S. A. Buntin, C. F. Giese and W. R. Gentry, *J. Chem. Phys.* **87**, 1443 (1987).
15. R. E. Continetti, B. A. Balko and Y. T. Lee, *J. Chem. Phys.* **93**, 5719 (1990).
16. J. C. Nieh and J. J. Valentini, *Phys. Rev. Lett.* **60**, 519 (1988); *J. Chem. Phys.* **92**, 1083 (1990).
17. D. L. Phillips, H. B. Levene and J. J. Valentini, *J. Chem. Phys.* **90**, 1600 (1989).
18. R. S. Blake, K. D. Rinnen, D. A. V. Kliner and R. N. Zare, *Chem. Phys. Lett.* **153**, 365 (1988).

19. K. D. Rinnen, D. A. V. Kliner, R. S. Blake and R. N. Zare, *Chem. Phys. Lett.* **153**, 371 (1988).

20. K. D. Rinnen, D. A. V. Kliner and R. N. Zare, *J. Chem. Phys.* **91**, 6514 (1989).

21. D. A. V. Kliner and R. N. Zare, *J. Chem. Phys.* **92**, 2107 (1990).

22. D. A. V. Kliner, K. D. Rinnen and R. N. Zare, *Chem. Phys. Lett.* **166**, 107 (1990).

23. D. A. V. Kliner D. A. Adelman and R. N. Zare, *J. Chem. Phys.* **94**, 1069 (1991).

24. D. A. V. Kliner D. A. Adelman and R. N. Zare, *J. Chem. Phys.* **95**, 1648 (1991).

CHAPTER II

BACKGROUND

I. INTRODUCTION

The hydrogen exchange reaction has played a fundamental role in both theoretical and experimental reaction dynamics. It is the simplest chemical reaction involving neutral species, and the preferred prototype for several reasons: (1) the potential energy surface can be calculated accurately; (2) the first excited electronic state is higher in energy than for most other systems, and thus, the assumption that the reaction takes place on a single potential energy surface is justified; (3) the small masses of the reacting atoms allows interesting quantum mechanical effects to influence reactive scattering to a greater extent than for most other reactions.

There are 15 possible isotopic combinations of H, D and T, and 21 distinct reactions, which make it an ideal system to study isotope effects on the dynamics.

The hydrogen exchange reaction has been extensively reviewed in the past fifteen years.[1-3] This chapter will attempt to summarize the major theoretical and experimental findings in this field.

II. POTENTIAL ENERGY SURFACES

The $H + H_2$ reaction takes place on a single electronic surface, with the nuclear motion determined by an effective interaction potential, estimated by invoking the Born-Oppenheimer approximation and separating the electronic and nuclear coordinates.

The earliest attempt to describe the hydrogen exchange reaction was by London[4] in 1929: he obtained a formula for the lowest adiabatic electronic state of H_3 in terms of Coulomb and exchange integrals between each pair of atoms. Eyring and Polanyi[5] later used the London formula and evaluated the integrals using a semiempirical method: this surface later became known as the LEP potential. The basis of the LEP method is to express the ground-state energy of H_2 as the sum of Q_{ij}, the Coulomb integral and J_{ij}, the exchange term. A Morse potential for H_2 gives a semiempirical value for the sum of these two terms at each bond distances. At times it was assumed that Q_{ij} was always a constant fraction ρ of the sum at large R; in practice, ρ was used as an adjustable parameter, with values form 0.0 to 0.2. For any value of the parameter ρ, the lowest energy configuration is predicted to be linear. At low values of ρ the barrier is symmetric, but too high; as ρ is increased, the barrier is lowered, but the lowest energy configuration starts to display a local minimum with two nonsymmetric saddle points at the sides.

No new semiempirical valence-bond calculation was attempted until 1955, when Sato[6-8] developed a method which involved one more parameter and an approximate form of the H_2 triplet state; the new parameter k was treated as the square of the orbital overlap integral, previously neglected by the LEP method. Sato's surface, known as the LEPS surface leads to a symmetric saddle point for all values of k, with 0.35 eV as the best value for the barrier height.

A symmetric saddle point is also predicted by a different semiempirical method used by Porter and Karplus,[9] who tried to include not only overlap integrals, but

also multiple exchange integrals. A barrier of 0.398 eV was predicted by the second of their surfaces, known as the PK2, and used extensively in dynamical calculations.

The *ab initio* variational method has also been used to calculate the H_3 surface: the first attempt was by Coolidge and James[10] in 1934. Theirs and a subsequent calculation by Hirschfelder *et al.*[11] confirmed a linear, symmetric saddle point, and placed the H_3 binding energy at -2.94 eV.

The historical development of *ab initio* calculations can be divided in three stages: the first stage involved a minimum basis set of three $1s$ orbitals; the second used an extended basis set of more than three spherical basis functions centered at the nuclei, and finally the third used more general bases including p and d orbitals, pseudo-natural orbitals and configuration interactions.[2]

Shavitt, Stevens, Minn and Karplus[12] used a double-zeta-plus-polarization basis set to perform a CI calculation involving 200 symmetry adapted configurations for linear symmetric geometries. This surface predicts the minimum energy path to occur for the colinear configuration and the highest potential energy along this path to be at the symmetric configuration where the two bond lengths are equal: the barrier is predicted to be at 0.477 eV. The potential energy surface of Shavitt *et al.* was fit to an analytical expression as function of the two bond distances, containing 28 linear parameters and 1 nonlinear. By comparison with the experiments of Westenberg and de Haas,[13] Shavitt estimated the true barrier at 0.424 eV, and suggested that the SSMK surface be scaled by $0.424/0.477 = 0.89$. The method of Wall and Porter[14] of constructing parametrized potential energy surfaces was applied by Truhlar and Kuppermann[15] to obtain a surface with the scaled barrier height and the transition state parameters of the SSMK surface; this surface is referred to as the scaled SSMK surface, or the Truhlar-Kuppermann surface.

An absolute upper bound on the barrier height was obtained by Liu[16] who calculated the energy of the H_3 molecule at -4.302 eV; this yields a value of 0.446

eV for the barrier height, when compared to the exact H_2 binding energy. Siegbahn and Liu[17] later treated nonlinear geometries, using a basis set consisting of 4 *s*-type, 3 *p*-type and 1-*d* type Gaussian orbitals. They calculated the barrier to be 0.429 eV, and found the new colinear surface to be parallel to the previous one. Truhlar and Horowitz[18] made an accurate least-squares fit to the Liu and Siegbahn surface, which provided essentially exact agreement with all saddle point properties. This surface, known as the LSTH surface, achieves a barrier of 0.425 eV. The LSTH surface includes a small van der Waals' well about 1.6 meV deep at $R_{H-H_2} = 6.59a_0$. More recent *ab initio* results by Liu[19] indicate a slightly lower barrier height of 0.418 eV.

A recent effort by Truhlar and co-workers[20,21] resulted in a new parametrization of the H_3 surface known as the double-many-body expansion (DMBE) surface; this surface was designed to be valid at higher energies than the LSTH, and treat long-range interactions more accurately. This surface has a barrier of 0.418 eV. This surface, like the LSTH, makes use of the 267 *ab initio* points of Siegbahn and Liu,[17] with the addition of 31 points from Blomberg and Liu.[22] Varandas *et al.*[21] calculated 18 new geometries, giving a total of 316 points.

III. THEORY OF THE HYDROGEN EXCHANGE REACTION: COLINEAR MODEL

A. Semiclassical Results

Classical transition probabilities for the H + H_2 reaction were calculated by Diestler and Karplus,[23] who carried out a Monte Carlo average over a large number of trajectories, with H_2 in its ground vibrational state. Comparison with quantum mechanical calculations showed that, although the general behavior of the two curves was very similar, the QM reaction probabilities were consistently larger than the CM results up to 0.3 eV, due to quantum mechanical tunnelling through the barrier.

Semiclassical transition state theory was applied to the colinear H + H_2 reaction by Miller[24,25] and Chesnavich.[26] They pointed out that for low energies, the fundamental assumption of transition state theory- namely that flux through a particular surface in configuration space dividing reactants and products can be identified as reactive flux- is essentially valid. However, the additional approximations of separability of motion along the reaction coordinate or vibrationally adiabatic motion often invoked in TST calculations poorly represent the threshold region. Therefore they carried out classical trajectory calculations on the Porter-Karplus and the Truhlar and Kuppermann surfaces, with a classical microcanonical average[27] over initial states of the H_2 molecule

This method leads to an intuitive picture of the tunnelling dynamics as taking place along a periodic classical trajectory along the upside-down potential energy surface. Without the additional assumptions, this semiclassical approximation leads to rate constants that are a factor of 2 or 3 smaller than QM ones, versus factors of 30-70 for conventional TST.

Garrett and Truhlar[28] considered variational transition state theories to minimize the TST rate constant by changing the location of the dividing surface;

their results confirm the validity of the fundamental assumption of transition state theory at low energy and show a marked improvement over conventional TST at higher energies. Traditionally quantum effects are introduced into TST as follows:[29,30] first, the reaction coordinate is separated out and treated classically; then, the remaining degrees of freedom of the transition state are quantized, together with the reactant bound states. The rate constant is then evaluated using quantal partition functions. A more accurate method involves incorporating quantum effects in the reaction coordinate motion. Approximate transmission coefficients were obtained using several one-dimensional models to estimate the tunnelling contributions. The most realistic model uses the Marcus-Coltrin tunnelling path.[28-30] This approach leads to rate constants that are within 10% of the quantal results at high temperatures, and within 60 % at low temperatures (see Table 1).

B. Quantum Mechanical Results

Exact quantum mechanical probabilities for colinear reactions were first obtained by Mortensen and Pitzer.[31] More extensive calculations on the H_3 system were carried out by Truhlar and Kuppermann[32-35] on the SSMK surface, using the finite-difference-boundary-value method (FDBVM) of Diestler and McKoy:[36] this method consists of selecting a set of grid points over the interaction region as well as the asymptotic region, then using the finite difference method to obtain a set of linearly independent solutions of the Schroedinger equation at the grid points. The solutions are then analyzed numerically in the asymptotic region in terms of a product of an internal eigenfunction of the separated molecule and a travelling wave in the relative motion. Scattering solutions for each of the open channels are then formed from linear combinations of the wavefunctions, and probabilities are computed from analysis of the outgoing flux. These steps are repeated for several values of the step size. Truhlar and Kuppermann chose to analyze their solutions in

terms of standing waves, which directly yields the elements of the reactance matrix **R**. The scattering matrix **S** is obtained from **R** by the well known formula:

$$\mathbf{S} = (1 - i\mathbf{R})^{-1}(1 + i\mathbf{R}). \tag{1}$$

Exact rate constants were computed for several hydrogenic systems. In one dimension the rate constant for a bimolecular reaction A + BC → AB + C is defined by:

$$d[A]/dt = d[BC]/dt = -k_r[A][BC], \tag{2}$$

where [A] and [BC] are concentrations in molecules/cm and k_r is the rate constant in cm molecule^{-1} sec^{-1}. For BC in the nth vibrational state and a thermal distribution of relative translational energies, the rate constant is given by:

$$k_r(n,T) = (2\pi\mu kT)^{-1/2}\int_0^\infty P_n(E_n)exp(-E_n/kT)dE_n, \tag{3}$$

where k is Boltzmann's constant, T the absolute temperature and $P_n(E_n)$ is the reaction probability with initial relative translational energy E_n.

For a thermal distribution of initial vibrational states the rate constant is:

$$k_r(T) = \sum_n k_r(n,T)p_n(T), \tag{4}$$

where

$$p_n(T) = (Q^v)^{-1}exp[-({E_n}^v - {E_0}^v)/kT] \tag{5}$$

is the fraction of reagent molecules in vibrational state n, with energy ${E_n}^v$, and Q^v is the vibrational partition function.

Reactive and nonreactive probabilities were calculated for the H_3 system and the rate constant evaluated by Eq.(3): considerable nonlinearity was observed in the Arrhenius plot, indicating a significant tunnelling contribution. Also, in the region above the vibrational excitation threshold there are rapid oscillations in

every reactive and nonreactive probability vs. energy curve. These were explained by means of Miller's and Marcus's semiclassical theories,[37,38] according to which the oscillations are due to interfering amplitudes for different semiclassical paths between reagents and products with the correct quantized energy levels.

The exact results were also compared to the results of transition state theory, the one-dimensional rate constant being:

$$k_0{}^{TST} = (kT/h)(Q^{vs}/Q^{rel}Q^{v})exp(-E_a/kT). \tag{6}$$

If tunnelling corrections are included the actual rate constant is given by:

$$k^{TST} = \kappa_1(T)k_0{}^{TST}(T), \tag{7}$$

where $\kappa_1(T)$ is the tunnelling correction, sometimes referred to as the transmission coefficient, defined as:

$$\kappa_1(T) = \frac{\int_0{}^{\infty} T_1(E0)exp(-E_0/kT)dE_0}{\int_0{}^{\infty} T_1{}^{cl}(E_0)exp(-E_0/kT)dE_0}, \tag{8}$$

where $T_1(E_0)$ is the quantum mechanical transmission probability at translational energy E_0 and $T_1{}^{cl}$ is the classical transmission probability, which is zero for $E_0 < E_a$ and 1 otherwise.

The transition state results for the H_3 system were found to be inaccurate by 11 % at 1000 K. Above this temperature the agreement improves, however, errors of 40-70 % occur in the range between 450 K and 300 K. Inclusion of the tunnelling correction improves the temperature dependence of the TST rate constant below 500 K.

The isotopic H + H_2 reaction was studied by Russell and Light[39] who performed quantum calculations on the following reactions: $H + H_2 \rightarrow H_2 + H$, $H + DH \rightarrow HD + H$, $D + HD \rightarrow DH + D$, $H + HD \rightarrow H_2 + D$, $H + D_2 \rightarrow HD + D$.

Truhlar, Kuppermann and Adams[40] performed calculations on the following colinear isotopic H_3 systems for translational energies up to 0.5 eV: $H + H_2 \rightarrow H_2 + H$, $D + D_2 \rightarrow D_2 + D$, $D + H_2 \rightarrow DH + H$, $H + D_2 \rightarrow HD + D$.

In general, the probability versus energy curves have the same shape, but differ in the steepness of the rise and position of the rise. The steepness is believed to be correlated with the likelihood of tunnelling, and the position of the rise with release of energy into the reaction coordinate due to vibrational adiabaticity of the motion perpendicular to the reaction coordinate. It was noticed that a larger imaginary frequency for the asymmetric stretching mode of the transition state meant a less steep rise of the probability curve, leading to H_3 being less steep than D_3 and $D + H_2$ less than $H + D_2$. This is in agreement with expectations of tunnelling along the reaction coordinate. Another factor is the curvature of the reaction path[39] which leads to an effective raising of the barrier (sometimes referred to as "centrifugal effects"), and a lowering of the reaction probability for low energies. Although the curvature is expected to be the same for all the isotopes, the "effective" curvature is found to be dependent on the masses: the effect of curvature was found to be more pronounced in the H transfer reactions than in the D transfer reactions.[39]

More recently, Park and Light[41] used the exact direct quantum formulation of the rate constant of Miller[27] to calculate $k_r(T)$; their results compare well with the quantum results.

The results of variational transition state theory, quantum calculations and conventional transition state theory without quantum corrections are summarized in Table 1.

IV. THREE DIMENSIONAL THEORETICAL STUDIES

A. Quasiclassical Trajectories

The first classical trajectory calculation was carried out by Hirschfelder *et al.*[42] in 1936. Detailed quasiclassical trajectory calculations on the H + H_2 system were performed by Karplus, Porter and Sharma[43–45] on the PK2 surface. The cross section versus energy curves show similar smoothly rising behavior for all the J values studied: the threshold for J=0 is at E_{rel} = 0.247 eV (total energy E = 0.52 eV, compared to the 0.4 eV barrier), and the cross section levels off around 1.1 eV at a value of 4.5 $a_0{}^2$. The curves become steeper and the plateau increases for higher values of J. The calculations were later extended to higher energies and to other isotopic combinations.[1]

Mayne and co-workers[46–49] used the LSTH surface to calculate cross sections up to 2 eV total energy: they found a threshold of E_{rel} = 0.31 eV. The effects of isotopic substitution, and vibrational and rotational excitation on reactivity, were also studied, and rate constants and angular distributions were included.

The following isotope effects were observed: in the series H,D,T + H_2 , T is more reactive than D, which is more reactive than H, while in the series H + H_2 , D_2 , T_2 , H_2 is more reactive than D_2 , which is more reactive than T_2 .

More recently Blais and Truhlar[50–54] have performed QCT calculations at the same energies as those sampled by experimenters for the H + D_2 system. The results for the inelastic and reactive cross sections at E_{rel} = 1.3 eV, 1.1 eV and 0.98 eV agreed well with those of Gerrity and Valentini[55–57] and Marinero, Rettner and Zare.[58,59] Later they extended their work to higher energies to compare with the recent experiments of Rinnen, Kliner, Blake and Zare[60] at 1.5, 1.6, 2.25 and 2.4 eV translational energy. The DMBE surface was employed in these studies, and the calculated HD rotational distributions were found to agree remarkably with experiment.

The same group also studied the D + H_2 reaction both quasiclassically and by a full quantum study. The state-to-state cross sections from the QCT calculation were found to be systematically larger than the quantum ones at all the energies studied.

Differential and state-to-state integral cross sections for the D + H_2 system have recently been obtained in the energy range 0.35-1.1 eV by Aoiz *et al.*;[61-63] good agreement was found between these results and those of Blais and Truhlar, and qualitative agreement was also found with the exact quantum results of Zhang and Miller,[64] although QCT cross sections were found to be larger than the quantum ones for v'=1 and smaller for v'=0. Comparison with the experiments of Buntin *et al.*,[65] Phillips *et al.*,[66] and Kliner *et al.*[67] revealed good agreement as far as the rotational distributions were concerned, but the indication of resonant behavior found in the experiments of Phillips *et al.* was not confirmed by the QCT study.

B. Quantum Mechanical Scattering

The most accurate of quantum dynamical methods is the coupled channel (CC) method, which involves solving the Schroedinger equation exactly: a reaction coordinate is chosen, and the wavefunction is expanded in a suitable basis set in the remaining degrees of freedom. The resulting set of coupled differential equations is obtained, and the expansion coefficients are found by standard methods. Analysis of the resulting solutions yields a scattering matrix, from which probabilities and cross sections can be derived. Because of the complexity of the calculation for systems other than H_3, approximations to the CC method have been sought: the coupled states (CS) approach neglects the couplings between different projection quantum states in the rotational basis.[3] Further simplifications involve even more drastic approximations to the rotational motion: the "infinite-order sudden approximation" (IOSA) argues that since the rotational periods are usually slow compared to vibrational ones, it is justified to assume a fixed angle

between the atom and the diatomic molecule in both the reagent and the product channel. The "reduced-dimensionality exact quantum" method (RDEQ), on the other hand, treats the coupled rotational and bending motions adiabatically.[3]

The earliest three-dimensional coupled channel calculation was conducted by Schatz and Kuppermann[68,69] in 1975 on the H_3 system using the PK2 surface: the energy range was from 0.03 eV to 0.43 eV translational energy. Their findings can be summarized as follows: reactive differential cross sections are backwards peaked, while inelastic nonreactive differential cross sections show backwards as well as sideways peaking; elastic nonreactive ones are forward peaked, and decreasing monotonically as the scattering angle is increased. Integral cross sections show significant product rotational angular momentum polarization, with the m_j =0 to m'_j=0 nonreactive transition dominating for low reagent rotational quantum number j. The effective threshold occurs at a total energy of 0.55 eV, and the behavior of the reaction probability for the colinear (1D), coplanar (2D) and 3D case is remarkably similar. Two important differences, however, provide insight into the dynamics of the collision: an energy shift of about 0.05 eV occurs in going from 1D to 2D, and form 2D to 3D; In the 2D case, the shift arises from an additional bending energy required in the coplanar transition state over the colinear one; this bending energy is added to the symmetric stretch energy of the colinear transition state which causes the colinear threshold energy to be above the barrier height. In the 3D case, the bending mode is doubly degenerate so that a second quantum of bending energy is required. The second difference lies in the maximum value that the probability achieves: the colinear probability peaks near unity, while the planar only reaches 0.6, and the 3D only 0.45 . This effect is mainly attributed to the orientation dependence of the barrier, which varies from 0.396 eV in the colinear configuration to 2.8 eV at 90°. Comparison of the exact quantum calculations with the semicalssical results of Karplus, Porter and Sharma[44,45] showed good agreement

except in the low energy region, where tunnelling effects cause the quantum rate constant to exceed the quasiclassical one by a factor of 18 at 200 K.

Quantum mechanical scattering calculations on the H_3 system were performed also by Elkowitz and Wyatt[70] on the PK2 surface and by Walker *et al.*[71] on the LSTH: the effect of the LSTH surface amounts to a shift of 0.05 eV in the threshold, and of 0.15 eV in the location of the first resonance. For the range E_{rel} = 0.33-0.73 eV, the LSTH cross sections are 20-30% lower than the corresponding ones on the PK2.

Coupled states calculations on the H + H_2 reaction have been conducted by Colton and Schatz,[72,73] and by Schatz[74] for the H + D_2 reaction, both on the LSTH surface.

Another approach to developing approximations to CC and CS reactive scattering is to use distorted wave theory.[75,82] This method considers the reaction as a minor perturbation on the nonreactive collision: the reactive scattering matrix can be approximated by the matrix element of a perturbative Hamiltonian. Tang and co-workers[76–81] have extensively applied the method to the D + H_2 reaction: in general, the method is expected to be accurate for reaction probabilities less than 0.1, which for the H + H_2 system occurrs at about 0.6 eV total energy.

In the past few years new coupled channel results have been obtained: Webster and Light[83,84] studied seven reactions containing H and D atoms: H + H_2, D + H_2, H + DH, H + HD, H + D_2, D + HD, D + DH.

R-matrix propagation was used to solve the coupled equations for reactive scattering, using three sets of Jacobi coordinates: reaction probabilities were obtained for the J=0 partial wave, and resonances were observed for all seven systems.

Another class of methods which has been used in studies of the H_3 system is based on the use of hyperspherical coordinates, which are described in several

articles.[85-88] Hipes and Kuppermann[89,90] have presented reaction probabilities and lifetimes for J=0 for the H_3 system in the range E_{tot} = 0.40-1.60 eV on the PK2 surface. They observed six resonances at the following energies: 0.61, 0.847, 0.971, 1.170, 1.382 and 1.56 eV. The calculation was repeated for the LSTH surface[91] and resonances were found at 0.65, 0.880, 0.981, 1.193, 1.363 and 1.55 eV. These resonances have been identified with progressions in the symmetric stretching and bending motions of the H_3 transition state.

In the past two or three years, several converged calculations have appeared for the systems H + H_2 and D + H_2 .[92-95] The methods used can be organized in three basic types: the propagation methods of Kuppermann and co-workers,[89-91,96-98] Pack *et al.*,[98-100] Schatz,[101] Linderberg and co-workers[102] and Launay and Le Dourneuf,[103] all employing some form of hyperspherical coordinates; the variational methods of Manolopoulos and Wyatt,[92,104-109] Miller,[93-94] and the Truhlar and Kouri groups[95,110-117] using Jacobi coordinates; and the method of Webster and Light,[83,84] using a "natural collision coordinate" system similar to the earlier work.[68-71] The converged theoretical cross sections agree very well with one another, but bear little resemblance to the experimental observations of Nieh and Valentini,[118] except for a general agreement on the energy-averaged magnitudes of the two cross sections. In particular, the theoretical cross sections show none of the resonant structures observed in the experiment. A possible explanation of the discrepancies will be pursued in the next section.

V. EXPERIMENTAL STUDIES

A. Rate Constant Measurements

The first measurements of the rate constant for the hydrogen exchange reaction were by Farkas;[119,120] later Le Roy and co-workers[121-125] and Westenberg and de Haas[13,126] studied the H + H_2 , H + D_2 , D + D_2 and D + H_2 reactions at temperatures ranging from room temperature to 750 K. The first group used a hot tungsten filament to produce the atomic species and an isothermal calorimeter to determine the atom concentrations. The second group used a microwave discharge and ESR detection of the atoms. In both cases, significant curvature of the Arrhenius plot was observed at low temperatures, an effect which is usually attributed to tunnelling. More recently, Michael and co-workers[127,128] measured the rate constant for the H + D_2 and D + H_2 reactions over the range 724-2061 K by a flash-photolysis shock tube technique. This work agrees well with the previous determinations, and extends the temperature range significantly. Table 2 and 3 summarize the results of theory and experiments and compares the various determinations of the rate constant.

B. Crossed Molecular Beam Experiments

The main result of crossed molecular beam experiments[129,130] is the differential cross section (DCS) for the reaction, which gives detailed information about the time scale (faster or slower than rotation) and the mechanism (direct or complex formation) of the reaction.

Almost all the experiments were conducted on the D + H_2 system: the H_2 molecules were introduced in the apparatus via an effusive jet and crossed at right angles with a beam of D atoms produced in a high temperature oven or a gas discharge. The product HD molecules were detected by a rotatable mass spectrometer tuned to mass 3.

The early experiments of Geddes *et al.*[131] suffered from a significant uncertainty in the relative energy of the reactants. Product HD was predominantly scattered backwards and little internal excitation of the molecular product was observed from the velocity distributions of the scattered products.

Toennies and co-workers[132–134] used a time-of-flight mass spectrometer and a chopper to determine HD product velocities. The differential cross section they obtained was peaked at 125° rather than 180°, and it was determined that, although little vibrational excitation was observed (< 10 %), about 48 % of the energy went into HD rotation.

Kwei and Lo[135] conducted crossed beam experiments on the H + T_2 system, using a getter surface of MoO_3 buttons located at 10° intervals to detect H or T atoms: T atoms were predominantly scattered forward, indicating that the molecular product was scattered backwards.

Recently Gentry and co-workers[136] developed a novel D atom source to try and minimize the relative energy spread of the reactants: they used laser photolysis of D_2S at 193 nm, and achieved a velocity resolution of $\Delta v/v = 11$ %, a factor of four better than the previous experiments. Slightly more vibrational excitation of the molecular product was observed in these experiments than in the previous ones.[133]

The recent experiment of Continetti, Balko and Lee[137] used DI photodissociation at 248 nm as a source of D atoms to measure product velocity and angular distributions at a collision energy of 0.53 eV. This experiment constitutes the most complete set of DCS measurements for the D + H_2 reaction: at the level of DH integral cross sections, the results show an overall agreement with theory,[93,94] however a comparison of the differential cross sections shows significant differences between the theoretical and experimental curves for rotationally excited DH. This discrepancy was attributed to possible inadequacy of the LSTH surface, in particular

the bending potential at high energies. It appears that the differential cross sections are considerably more sensitive to the details of the potential energy surface than the integral cross sections, as demonstrated by the good agreement between the theory[93,94] and the hot atom experiments,[154] as discussed in the next section. In particular, the effects of dynamical resonances, which have been observed to disappear in the integral cross sections when averaged over the orbital angular momentum states of the reactants,[93,94] are expected to persist to a much greater extent in the product angular distributions.[138,139]

C. Hot Atom Experiments

This category of experiments makes use of a photolysis source to generate the reagent atomic species with excess translational energy and a very narrow energy spread: the use of pulsed lasers makes it particularly well suited to observe nascent product internal state distributions.

The hydrogen halides and H_2S are the most commonly used precursor molecules for hot H atom production. Before the advent of lasers, hydrogen halides were continuously photodissociated by spectral lamps. In this type of experiment, the velocity distribution would show two peaks, one corresponding to the recoiling H atom, and the other to thermalized atoms: the integrated reaction yield as a function of energy would be measured by determining the fraction of hot H atoms that undergo reactive collisions, and by scanning the energy by changing the photolysis wavelength.

This technique was first applied to mixtures of DI/H_2 by Carter *et al.*[140] and to HBr/D_2 mixtures by Martin and Willard.[141] White and Kuppermann[142,144] photolyzed DI/H_2 and DBr/H_2 mixtures at energies in the range 0.15 to 0.90 eV, and observed a threshold of 0.33 eV. Betts[143] extended the range to $E_{rel} = 1.43$ eV , and provided a revised threshold of 0.25 eV.

The first set of laser experiments involve a determination of the total reactive cross section:[145,146] HBr, HCl and H_2S were used as precursors, and the cross section for the H + D_2 reaction was obtained by measuring the reagent H and product D number densities by VUV laser induced fluorescence at the Lyman-α wavelength.

Recently attention has been focused on obtaining the internal quantum state distribution of the product molecules. The reaction mixture is probed after a time delay short enough for the H atom to have undergone only one collision. Three techniques have been used to detect hydrogen molecules in a state specific manner: Coherent-Anti-Stokes Raman Spectroscopy (CARS), Resonance-Enhanced Multiphoton Ionization (REMPI) and Laser Induced Fluorescence (LIF). Gerrity and Valentini[55-57] photolyzed HI at 266 nm, 280 nm and 291 nm; the fixed frequency in the CARS process was provided by the doubled Nd:YAG at 532 nm, while the variable frequency was generated by a tunable dye laser. The anti-Stokes beam was separated from the three incident beams and detected by a photomultiplier tube. Time delays of 5 ns to 28 ns were used. Their results for H + D_2 were as follows: at 1.3 eV relative energy, HD was detected in J = 1-10, 12 for $v = 0$, J = 1-9 for $v = 1$ and J = 2-5 for $v = 2$. Zare and co-workers[58,59] used Raman shifted radiation from the second harmonic of a dye laser (195 nm) to detect HD by REMPI, and observed, for the same relative energy, HD in the following states: $v = 1$, J = 0-6; $v = 2$ J = 0-6. The $v = 0$ states were obscured by the large HD background.

The CARS distribution peaks at $J = 3$, 3 and 3, for $v = 0$, 1 and 2 respectively, while the REMPI peak at $J = 4$ and 2 for $v = 1$ and 2. This can be compared with the results of Blais and Truhlar,[50,51] who predicted peaks at J=8, 4 and 5 for $v = 0$, 1 and 2 respectively.

The experiments that followed generated significant controversy: in 1988, Nieh and Valentini[118,147] reported the experimental observation of dynamical Feshbach resonances in the H + p-H_2 $\rightarrow$ $o,p-H_2$ + H reaction. The resonances, first revealed in colinear quantum calculations[32-35] had also been found in three-dimensional calculations.[89,90] The resonances appeared as a sharp variation of the partial cross sections, namely the cross section into particular final vibrational and rotational states, as a function of collision energy. The oscillations in the cross section reflect the interference between two scattering amplitudes, a direct and a resonance one: the latter arises because of nonadiabatic coupling between the relative motion and the internal degreese of freedom, leading to the formation of quasibound excited states. The internal degrees of freedom that provide the resonant states are those the vibrational modes of the H_3 transition state, the vibrational motions that are perpendicular to the relative motion in the vicinity of the transition between reactants and products. The labelling of the resonances is by vibrational quantum numbers and follows the convention: (v_1, v_2^{Ω}, v_3), where v_1 is the symmetric stretch and v_2 the bending motion; the superscript Ω gives the component of vibrational angular momentum along the molecular axis. The asymmetric stretch v_3 is unbound at the transition state, so v_3 is undefined, and it is usually indicated by 0. For total energies in the range 0.95 eV to 1.3 eV, the resonances are (1,0,0), ($1,1^1$,0), ($1,2^0$,0) and ($1,2^2$,0) at E_{tot} = 0.98, 1.1 , 1.2 and 1.23 eV respectively.

Nieh and Valentini reported observing the (1,0,0), ($1,2^0$,0), ($1,2^2$,0) and the ($1,1^1$,0) at 0.97, 1.1, 1.2, and 1.26 eV. They used HI photolysis at wavelengths between 266 nm and 308 nm followed by CARS detection of product H_2 molecules: the time delay between the pump and the probe was 5 ns and the experiment was conducted in a flowing gas cell at a few Torr total pressure. The partial cross sections $\sigma(v' = 1, j)$ revealed clear maxima at the predicted resonance energies. The ratio of $\sigma(v' = 1)/\sigma(v' = 0)$ showed the effect even more clearly, because of

the predicted depletion of the v' = 0 level that accompanies the enhancement of the v' = 1 states.

However, with the completion of the fully converged quantum calculations[93,94] it appears that angular momentum averaging leads to the "washing-out" of the partial wave resonant structures from the integral cross sections. These calculations include 19 partial waves (J = 0-18), and show none of the maxima observed in the experiment.

As noted in the previous section, it has been suggested that what the experiment was actually measuring were *differential* cross sections in the backwards direction, but no clear explanation as to how that might be happening has been proposed so far.[137] It has also been proposed that the LSTH surface, although highly accurate, still does not account properly for the conical intersection with the second doublet surface at D_{3h} geometries, has a classical barrier which is now believed to be 0.15 kcal/mole too high, and does not treat the van der Waals region appropriately.[21] It seems, however, that recent calculations by Manolopoulos and Wyatt[92] on the DMBE surface are in accord with the LSTH results.

Recently, the experiment was repeated by Zare and co-workers,[148] using REMPI detection: no resonance structure was observed in the integral cross sections, and very good agreement was obtained with the calculations of Zhang and Miller.[64] The discrepancy between this experiment and the CARS one is currently the subject of ongoing discussion: the possibility of laser catalysis of the hydrogen exchange reaction is being investigated. This effect amounts to the interaction of the radiation with the system causing an "artifact" in the results.

Recent work has also appeared on the H + D_2 and the D + H_2 systems. Zare and co-workers[149–151] used (2 + 1) REMPI to detect nascent HD molecules form the H + D_2 reaction; this work completes the previous study of Marinero, Rettner and Zare[58,59] and agrees fairly well with the results of Gerrity and Valentini[55–57]

and the QCT calculations of Blais and Truhlar, though the calculated rotational distributions are slightly hotter. Very recently, Wyatt and co-workers[109] used the Kohn variational principle for the log-derivative matrix to calculate integral cross section and product distributions for the energies sampled by Zare and co-workers: the agreement between theory and experiment is outstanding. The main results are summarized in Tables 4 and 5.

Valentini and co-workers[152] also observed the presence of a dynamical resonance at 0.67 eV for the D + H_2 system, in contrast with the results of QCT calculations.[52] More recently, quantum mechanical scattering calculations and REMPI experiments have again questioned the validity of the CARS results, and show near perfect agreement between each other[154] as far as $v = 0$ distributions are concerned. However, serious discrepancies exist between theory[155] and experiment[156] for the $v = 1$ case, for which the calculated distributions are "hotter" by two or three rotational quanta. The origin of the discrepancy is unknown: one of the causes could be that few *ab initio* points exist on the potential energy surface for the high energies involved in this experiment. In addition, nonadiabatic effects arising from the conical intersection between the H_3 ground and first excited states could be involved.[157]

The main results of this section are reproduced in Tables 4 and 5.

In this thesis, an attempt has been made to use a third detection technique, that of laser induce fluorescence to detect the nascent products of the hydrogen exchange reaction. Despite the excellent sensitivity, these efforts have met with little success. The advantages and disadvantages of this technique will be discussed in a later chapter.

TABLE 1. Colinear Thermal Rate Constants[a]

REACTION	T(K)	k QTST[b] TK	PK2	QM[c] TK	TST[d] $\kappa = 1$
$H+H_2$	200	2.36×10^{-1}	7.45×10^{-1}	2.07×10^{-1}	6.99×10^{-3}
	300	5.18	2.38×10^{1}	5.87	1.78
	400	4.93×10^{1}	1.68×10^{2}	5.93×10^{1}	2.96×10^{1}
	500			2.65×10^{2}	1.65×10^{2}
	600	6.37×10^{2}	1.44×10^{3}	7.53×10^{2}	5.28×10^{2}
	1000	6.10×10^{3}	9.81×10^{3}	6.84×10^{3}	6.05×10^{3}
$H+D_2$	200	2.26×10^{-3}		1.27×10^{-3}	1.77×10^{-4}
	300	3.64×10^{-1}		3.17×10^{-1}	1.49×10^{-1}
	400	7.21		6.93	4.51
	500			4.75×10^{1}	
	600	1.77×10^{2}		1.74×10^{2}	
	1000	2.76×10^{3}		2.73×10^{3}	2.75×10^{3}
$D+H_2$	200	1.53×10^{-1}		2.14×10^{-1}	1.54×10^{-2}
	300	5.11		7.25	2.81
	400	6.96×10^{1}		6.82×10^{1}	3.98×10^{1}
	500			2.87×10^{2}	
	600	6.15×10^{2}		7.61×10^{2}	6.05×10^{2}
	1000	5.55×10^{3}		6.31×10^{3}	6.21×10^{3}
$D+D_2$	200	1.35×10^{-3}		2.68×10^{-3}	4.11×10^{-4}
	300	4.86×10^{-1}		5.54×10^{-1}	2.4×10^{-1}
	400	9.58		1.02×10^{1}	6.08
	500			6.20×10^{1}	
	600	2.10×10^{2}		2.14×10^{2}	1.67×10^{2}
	1000	3.06×10^{3}		2.78×10^{3}	2.8×10^{3}

a) Rate constants in cm molecule^{-1} sec^{-1}.

b) Transition State Theory of Ref. (28), with quantum corrections.

c) Ref. (40).

d) Conventional Transition State Theory with the transmission coefficient equal to 1.

TABLE 2. Comparison of Quasiclassical and Experimental Thermal Rate Constants[a]

REACTION	T(K)	$k(T)$		
		PK2	QCT[b] LSTH	EXPT[c]
$H+H_2$ [d]	200	8.32×10^{-19}	2.40×10^{-19}	
	300	3.09×10^{-16}	1.20×10^{16}	2.69×10^{-16}
	400	5.89×10^{-15}	3.09×10^{-15}	2.95×10^{-15}
	500	3.72×10^{-14}	2.19×10^{-14}	2.19×10^{-14}
	600	1.29×10^{-13}	8.32×10^{-14}	
$H+D_2$	200		1.20×10^{-20}	
	300	7.24×10^{-17}	1.20×10^{-17}	2.63×10^{-17}
	400	1.82×10^{-15}	4.27×10^{-16}	6.31×10^{-16}
	500	1.20×10^{-14}	4.57×10^{-15}	6.31×10^{-15}
	600	4.90×10^{-14}		3.09×10^{-14}
	1000			1.38×10^{-12}
$D+H_2$	200		1.41×10^{-18}	1.95×10^{-18}
	300	5.25×10^{-16}	3.63×10^{-16}	3.02×10^{-16}
	400	7.94×10^{-15}	6.17×10^{-15}	5.13×10^{-15}
	500	4.79×10^{-14}	3.72×10^{-14}	3.23×10^{-14}
	600	1.58×10^{-13}	1.29×10^{-13}	1.20×10^{-13}
	1000			2.27×10^{-12}

a) Rate constants in cm^3 $molecule^{-1}$ sec^{-1}.

b) Ref. (48).

c) Ref. (13), (121-128).

d) Distinguishable atom rate constants for $H + H_2$.

TABLE 3. Quantum Mechanical Thermal Rate Constants[a]

REACTION	T(K)	$k(T)$			
			CS[b]		CC[c]
		PK2	LSTH	PK2	LSTH
$H+H_2$ [d]	200	1.10×10^{-17}	1.00×10^{-18}	1.58×10^{-17}	
	300	9.55×10^{-16}	1.70×10^{-16}	1.00×10^{-15}	2.76×10^{-16}
	400	1.20×10^{-14}	3.39×10^{-15}	1.10×10^{-14}	
	500	5.89×10^{-14}	2.29×10^{-14}	5.01×10^{-14}	3.70×10^{-14}
	600	1.82×10^{-13}	8.71×10^{-14}	1.41×10^{-13}	1.27×10^{-13}
	1000				2.03×10^{-12}
$D+H_2$	200				1.09×10^{-18}
	300				3.20×10^{-16}
	400				4.54×10^{-15}
	500				3.30×10^{-14}
	600				1.21×10^{-13}
	1000				1.99×10^{-12}

a) Rate constants in $cm^3\,molecule^{-1}\,sec^{-1}$.

b) Ref. (73).

c) Ref. (68), (69), (94) and (158).

d) Distinguishable atom rate constants for $H + H_2$.

TABLE 4. Calculated and Experimental Total Reactive Cross Sections

REACTION	E_{tot} (eV)	QCT[a] Cross section ($bohr^2$)	QM[b] Cross Section ($bohr^2$)	Experimental[c] Cross section ($bohr^2$)
$H+D_2$	0.55	0.024		
	0.60	0.13		
	0.67	0.49		
	0.84	1.44		
	1.03	2.54		3.53
	1.17	3.07		
	1.30	3.43		
	1.50	4.04	3.78	
	1.73			3.92
	1.79	4.61		
	2.14			6.00
	2.30			6.96
	2.44	4.45		
	2.59	4.64		
$D+H_2$	0.55	0.002	0.012	
	0.60	0.14	0.14	
	0.70		0.75	
	0.78		1.57	
	0.85		2.46	
	0.94	3.31	4.02	2.53
	0.98		4.28	
	1.03		4.60	
	1.06	4.45	4.80	2.82
	1.086		5.01	
	1.25		5.79	
	1.35		6.19	
$H+H_2$	0.58	0.008		
	0.63	0.21		
	0.70	0.71		
	0.75	1.29		
	0.92	2.44		
	0.97			1.17
	1.068		2.12	
	1.10		3.06	1.43
	1.16			1.65
	1.27			2.39
	1.30		3.69	2.05

a) Refs. (48), (51), (53) and (61). Ref. (53) uses the DMBE surface, all others the LSTH.

b) Refs. (93), (103) and (113).

c) Refs. (145), (147) and (152).

TABLE 5. Hydrogen Exchange Reaction Product Energy Distributions

REACTION	METHOD	E_{rel}	$\frac{E_t}{E_{avail}}$	$\frac{E_v}{E_{avail}}$	$\frac{E_r}{E_{avail}}$
$H+D_2$	QCT[a]	0.55	0.89	0.02	0.10
		0.98	0.73	0.07	0.21
		1.10	0.70	0.08	0.23
		1.30	0.67	0.09	0.24
$H+D_2$	Hot-atom[b]	0.98	0.73	0.06	0.21
		1.10	0.74	0.04	0.22
		1.30	0.73	0.09	0.18
$H+D_2$	QM[c]	1.30	0.71	0.10	0.19
$D+H_2$	Crossed-beam[d]	0.95	0.67	0.07	0.25
		1.50	0.52	< 0.1	≈ 0.4
$D+H_2$	Hot-atom[e]	0.67	0.71	0.10	0.19
		0.79	0.70	0.05	0.25
$H+p-H_2$	Hot-atom[f]	0.70	0.83	0.09	0.08
		0.79	0.84	0.04	0.12
		1.00	0.78	0.06	0.16
		1.10	0.82	0.02	0.16

a) Refs. (50), (51).

b) Refs. (55)-(57), (151).

c) Ref. (109).

d) Refs. (65), (133).

e) Ref. (152).

f) Ref. (147).

REFERENCES

1. D. G. Truhlar and R. E. Wyatt, *Ann. Rev. Phys. Chem.* **27** 1 (1976).
2. D. G. Truhlar and R. E. Wyatt, *Adv. Chem. Phys.* **36** 141 (1977).
3. G. C. Schatz, in *The Theory of Chemical Reaction Dynamics*, edited by D. C. Clary, (D. Reidel Publishing, Boston, 1986) p.1-26.
4. F. London, *Z. Electrochem.* **35**, 552 (1929).
5. H. Eyring and M. Polanyi, *Naturwiss.* **18**, 914 (1930).
6. S. Sato, *Bull. Chem. Soc. Jpn.* **28**, 450 (1955).
7. S. Sato, *J. Chem. Phys.* **23**, 592 (1955).
8. S. Sato, *J. Chem. Phys.* **23**, 2465 (1955).
9. R. N. Porter and M. Karplus, *J. Chem. Phys.* **40**, 1105 (1964).
10. A. S. Coolidge and H. M. James, *J. Chem. Phys.* **2**, 811 (1934).
11. J. O. Hirschfelder, H. Diamond and H. Eyring, *J. Chem. Phys.* **5**, 695 (1937).
12. I. Shavitt, R. M. Stevens, F. L. Minn and M. Karplus *J. Chem. Phys.* **48**, 2700 (1968); erratum, **49**, 4048 (1968).
13. A. A. Westenberg and N. de Haas, *J. Chem. Phys.* **47**, 1393 (1967).
14. F. T. Wall and R. N. Porter, *J. Chem. Phys.* **36**, 3256 (1962).
15. D. G. Truhlar and A. Kuppermann, *J. Chem. Phys.* **56**, 2232 (1972).
16. B. Liu, *J. Chem. Phys.* **58**, 1925 (1973).
17. P. Siegbahn and B. Liu, *J. Chem. Phys.* **68**, 2457 (1978).
18. D. G. Truhlar and C. J. Horowitz, *J. Chem. Phys.* **68**, 2466 (1978).
19. B. Liu, *J. Chem. Phys.* **80**, 581 (1984).
20. B. C. Garrett, D. G. Truhlar, A. J. C. Varandas and N. C. Blais, *Int. J. Chem. Kinet.* **18**, 1065 (1986).
21. A. J. C. Varandas, F. B. Brown, C. A. Mead, D. G. Truhlar and N. C. Blais, *J. Chem. Phys.* **86**, 6258 (1987).

22. M. R. A. Blomberg and B. Liu, *J. Chem. Phys.* **82**, 1050 (1985).

23. D. J. Diestler and M. Karplus, *J. Chem. Phys.* **55**, 5832 (1971).

24. S. Chapman, B. C. Garrett and W. H. Miller, *J. Chem. Phys.* **63**, 2710 (1975).

25. S. Chapman, S. M. Hornstein and W. H. Miller, *J. Am. Chem. Soc.* **97**, 892 (1975).

26. W. J. Chesnavich, *Chem. Phys. Lett.* **53**, 300 (1978).

27. W. H. Miller, *J. Chem. Phys.* **61**, 1823 (1974).

28. B. C. Garrett and D. G. Truhlar, *J. Phys. Chem.* **83**, 1052 (1979); **83**, 1079 (1979); erratum *J. Phys. Chem.* **84**, 682 (1980).

29. B. C. Garrett and D. G. Truhlar, *J. Phys. Chem.* **84**, 805 (1984).

30. G. D. Billing, *Chem. Phys.* **89**, 199 (1984).

31. E. M. Mortensen and K. S. Pitzer, *Chem. Soc. (London) Spec. Publ.* **16**, 57 (1962).

32. D. G. Truhlar and A. Kuppermann, *J. Chem. Phys.* **52**, 3841 (1970).

33. D. G. Truhlar and A. Kuppermann, *J. Chem. Phys.* **54**, 4881 (1971).

34. D. G. Truhlar and A. Kuppermann, *J. Chem. Phys.* **56**, 2232 (1972).

35. D. G. Truhlar and A. Kuppermann, *Chem. Phys. Lett.* **9**, 269 (1971).

36. D. J. Diestler and B. V. McKoy, *J. Chem. Phys.* **48**, 2951 (1968).

37. W. H. Miller, *J. Chem. Phys.* **53**, 1949 (1970).

38. R. A. Marcus, *Chem. Phys. Lett.* **7**, 525 (1970).

39. J. D. Russell and J. C. Light, *J. Chem. Phys.* **54**, 4881 (1971).

40. D. G. Truhlar, A. Kuppermann and J. T. Adams, *J. Chem. Phys.* **59**, 395 (1973).

41. T. J. Park and J. C. Light, *J. Chem. Phys.* **88**, 4897 (1988).

42. J. O. Hirschfelder, H. Eyring and B. Topley, *J. Chem. Phys.* **4**, 170 (1936).

43. M. Karplus, R. N. Porter and R. D. Sharma, *J. Chem. Phys.* **40**, 2033 (1964).

44. M. Karplus, R. N. Porter and R. D. Sharma, *J. Chem. Phys.* **43**, 3259 (1965).

45. M. Karplus, R. N. Porter and R. D. Sharma, *J. Chem. Phys.* **45**, 3871 (1966).

46. H. R. Mayne, *J. Chem. Phys.* **73**, 217 (1980).

47. G. D. Barg, H. R. Mayne nad J. P. Toennies, *J. Chem. Phys.* **74**, 1017 (1981).

48. H. R. Mayne and J. P. Toennies, *J. Chem. Phys.* **75**, 1794 (1981).

49. C. A. Boonenberg and H. R. Mayne, *Chem. Phys. Lett.* **108**, 67 (1984).

50. N. C. Blais and D. G. Truhlar, *Chem. Phys. Lett.* **102**, 120 (1983).

51. N. C. Blais and D. G. Truhlar, *J. Chem. Phys.* **83**, 2201 (1985).

52. N. C. Blais and D. G. Truhlar, *J. Chem. Phys.* **88**, 5457 (1988).

53. N. C. Blais and D. G. Truhlar, *Chem. Phys. Lett.* **162**, 503 (1989).

54. N. C. Blais, M. Zao, M. Mladenovic, D. G. Truhlar, D. W. Schwenke, Y. Sun and D. J. Kouri, *J. Chem. Phys.* **91**, 1038 (1989).

55. D. P. Gerrity and J. J. Valentini, *J. Chem. Phys.* **79**, 5202 (1983).

56. D. P. Gerrity and J. J. Valentini, *J. Chem. Phys.* **81**, 1298 (1984).

57. D. P. Gerrity and J. J. Valentini, *J. Chem. Phys.* **82**, 1323 (1985).

58. C. T. Rettner, E. E. Marinero and R. N. Zare, in *Physics of Electronic and Molecular Collisions*, edited by J. Eichler, I. V. Hertel and N. Stolterfoht (North Holland, Amsterdam, 1984), p.51

59. E. E. Marinero, C. T. Rettner and R. N. Zare, *J. Chem. Phys.* **80**, 4142 (1984).

60. K. D. Rinnen, D. A. V. Kliner, R. S. Blake and R. N. Zare, *Chem. Phys. Lett.* **153**, 371 (1988).

61. F. J. Aoiz, V. Candela, V. J. Herrero and V. Saez Rabanos, *Chem. Phys. Lett.* **169**, 243 (1990).

62. F. J. Aoiz, V. J. Herrero and V. Saez Rabanos, *J. Chem. Phys.* **94**, 7991 (1991).

63. F. J. Aoiz, V. J. Herrero and V. Saez, *Chem. Phys. Lett.* **161**, 270 (1989).

64. J. Z. H. Zhang and W. H. Miller, *Chem. Phys. Lett.* **140**, 329 (1987); *J. Chem. Phys.* **88**, 3202 (1988).

65. S. A. Buntin, C. F. Giese and W. R. Gentry, *J. Chem. Phys.* **87**, 1443 (1987).

66. D. L. Phillips, H. B. Levene and J. J. Valentini, *J. Chem. Phys.* **90**, 1600 (1989).

67. D. A. V. Kliner, K. D. Rinnen and R. N. Zare, *Chem. Phys. Lett.* **166**, 107 (1990).

68. G. C. Schatz and A. Kuppermann, *J. Chem. Phys.* **65**, 4668 (1976).

69. A. Kuppermann and G. C. Schatz, *J. Chem. Phys.* **62**, 2502 (1975).

70. A. B. Elkowitz and R. E. Wyatt, *J. Chem. Phys.* **63**, 702 (1975).

71. R. B. Walker, E. B. Stechel and J. C. Light, *J. Chem. Phys.* **69**, 2922 (1978).

72. M. C. Colton and G. C. Schatz, *Chem. Phys. Lett.* **124**, 256 (1986).

73. M. C. Colton and G. C. Schatz, *Int. J. Chem. Kin.* **18**, 961 (1986).

74. G. C. Schatz, *Chem. Phys. Lett.* **108**, 532 (1984).

75. L. M. Hubbard, S. Shi and W. H. Miller, *J. Chem. Phys.* **78**, 2381 (1983).

76. K. T. Tang and B. H. Choi, *J. Chem. Phys.* **62**, 3642 (1975).

77. B. H. Choi and K. T. Tang, *J. Chem. Phys.* **63**, 2854 (1975).

78. Y. Y. Yung, B. H. Choi and K. T. Tang, *J. Chem. Phys.* **72**, 621 (1980).

79. J. C. Sun, B. H. Choi, R. T. Poe and K. T. Tang, *J. Chem. Phys.* **73**, 6095 (1980).

80. B. H. Choi, R. T. Poe and K. T. Tang, *J. Chem. Phys.* **81**, 4979 (1984).

81. M. S. Bowers, B. H. Choi, R. T. Poe and K. T. Tang, *Chem. Phys. Lett.* **116**, 239 (1985).

82. G. C. Schatz, L. M. Hubbard, P. S. Dardi and W. H. Miller, *J. Chem. Phys.* **81**, 231 (1984).

83. F. Webster and J. C. Light, *J. Chem. Phys.* **85**, 4744 (1986).

84. F. Webster and J. C. Light, *J. Chem. Phys.* **90**, 265 (1989;).*J. Chem. Phys.* **90**, 300 (1989).

85. A. Kuppermann, J. A. Kaye and J. P. Dwyer, *Chem. Phys. Lett.* **74**, 257 (1980); J. A. Kaye and A. Kuppermann, *Chem. Phys. Lett.* **77**, 573 (1981).

86. A. Kuppermann, *Theor. Chem.: Advances and Perpectives*, **6A**, 79 (1981).

87. G. Hauke, J. Manz and J. Römelt, *J. Chem. Phys.* **73**, 5040 (1980;).

88. J. Römelt, *Chem. Phys. Lett.* **74**, 263 (1980); *Chem. Phys. Lett.* **87**, 259 (1982).

89. A. Kuppermann and P. G. Hipes, *J. Chem. Phys.* **84**, 5962 (1986).

90. P. G. Hipes and A. Kuppermann, *Chem. Phys. Lett.* **133**, 1 (1987).

91. S. A. Cuccaro, P. G. Hipes and A. Kuppermann, *Chem. Phys. Lett.* **157**, 440 (1989).

92. D. E. Manolopoulos and R. E. Wyatt, *Chem. Phys. Lett.* **159**, 123 (1989).

93. J. H. Z. Zhang and W. H. Miller, *J. Chem. Phys.* **91**, 1528 (1989); W. H. Miller, *Ann. Rev. Phys. Chem.* **41**, 245 (1990); *J. Chem. Phys.* **92**, 1811 (1990).

94. J. H. Z. Zhang and W. H. Miller, *J. Chem. Phys.* **88**, 4549 (1988); *J. Chem. Phys.* **90**, 7610 (1989;).*Chem. Phys. Lett.* **159**, 130 (1989); *Chem. Phys. Lett.* **153**, 465 (1988).

95. M. Zhao, D. G. Truhlar, D. W. Schwenke and D. J. Kouri, *J. Phys. Chem.* **94**, 7074 (1990).

96. S. A. Cuccaro, P. G. Hipes and A. Kuppermann, *Chem. Phys. Lett.* **154**, 155 (1989).

97. Y. M. Wu, S. A. Cuccaro, P. G. Hipes and A. Kuppermann, *Chem. Phys. Lett.* **168**, 429 (1990).

98. G. A. Parker, R. T. Pack, B. J. Archer and R. B. Walker, *Chem. Phys. Lett.* **137**, 564 (1987).

99. R. T. Pack and G. A. Parker, *J. Chem. Phys.* **90**, 3511 (1989).

100. J. D. Kress, Z. Bačić, G. A. Parker and R. T. Pack, *Chem. Phys. Lett.* **157**, 585 (1989); *Chem. Phys. Lett.* **170**, 306 (1990).

101. G. C. Schatz, *Chem. Phys. Lett.* **151**, 409 (1988); *J. Chem. Phys.* **90**, 3582 (1989); *Chem. Phys. Lett.* **150**, 92 (1988).

102. J. Linderberg, S. B. Padkjaer, Y. Öhrn and B. Vessal, *J. Chem. Phys.* **90**, 6254 (1989).

103. J. M. Launay and M. Le Dourneuf, *Chem. Phys. Lett.* **163**, 178 (1989).

104. D. E. Manolopoulos, R. E. Wyatt, *Chem. Phys. Lett.* **152**, 23 (1988).

105. D. E. Manolopolous and R. E. Wyatt, *J. Chem. Phys.* **92**, 810 (1990).

106. D. E. Manolopoulos M. D'Mello and R. E. Wyatt, *J. Chem. Phys.* **93**, 403 (1990).

107. M. D'Mello, D. E. Manolopoulos and R. E. Wyatt, *Chem. Phys. Lett.* **168**, 113 (1990).

108. D. E. Manolopoulos, M. D'Mello, R. E. Wyatt and R. B. Walker, *Chem. Phys. Lett.* **169**, 482 (1990).

109. M. D'Mello, D. E. Manolopoulos and R. E. Wyatt, *J. Chem. Phys.* **94**, 5985 (1991).

110. J. Z. H. Zhang, D. J. Kouri, K. Haug, D. W. Schwenke, Y. Shima and D. G. Truhlar, *J. Chem. Phys.* **88**, 2492 (1988).

111. M. Mladenovic, M. Zhao, D. G. Truhlar, D. W. Schwenke, Y. Sun, D. J. Kouri, *Chem. Phys. Lett.* **146**, 358 (1988).

112. M. Zhao, M. Mladenovic, D. G. Truhlar, D. W. Schwenke, Y. Sun, D. J. Kouri, and N. C. Blais, *J. Am. Chem. Soc.* **111**, 852 (1989).

113. M. Mladenovic, M. Zhao, D. G. Truhlar, D. W. Schwenke, Y. Sun and D. J. Kouri, *J. Phys. Chem.* **92**, 7035 (1988).

114. M. Zhao, M. Mladenovich, D. G. Truhlar, D. W. Schwenke, O. Sharafeddin, Y. Sun and D. J. Kouri, *J. Chem. Phys.* **91**, 5302 (1989).

115. K. Haug, D. W. Schwenke, Y. Shima, D. G. Truhlar, J. Z. H. Zhang and D. J. Kouri, *J. Phys. Chem.* **90**, 6757 (1986).

116. M. Zhao, D. G. Truhlar, Y. Sun, D. J. Kouri and D. W. Schwenke, *Chem. Phys. Lett.* **156**, 281 (1989).

117. N. C. Blais, M. Zhao, M. Mladenovich, D. G. Truhlar, D. W. Schwenke, Y. Sun and D. J. Kouri, *J. Chem. Phys.* **91**, 1038 (1989).

118. J. C. Nieh and J. J. Valentini, *Phys. Rev. Lett.* **60**, 519 (1988).

119. A. Farkas, *Z. Electrochem.* **36**, 782 (1930).

120. A. Farkas, *Z. Physik Chem.* **B10**, 419 (1930).

121. W. R. Schulz and D. J. Le Roy, *Can. J. Chem.* **42**, 2480 (1964).

122. W. R. Schulz and D. J. Le Roy, *J. Chem. Phys.* **42**, 3869 (1965).

123. B. A. Ridley, W. R. Schulz and D. J. Le Roy, *J. Chem. Phys.* **44**, 3344 (1966).

124. D. J. Le Roy, B. A. Ridley and K. A. Quickert, *Disc. Far. Soc.* **44**, 92 (1967).

125. D. N. Mitchell and D. J. Le Roy, *J. Chem. Phys.* **58**, 3449 (1973).

126. A. A. Westenberg, *Disc. Far. Soc.* **44**, 169 (1967).

127. J. V. Michael, *J. Chem. Phys.* **92**, 3394 (1990).

128. J. V. Michael and J. R. Fisher, *J. Phys. Chem.* **94**, 3318 (1990).

129. R. B. Bernstein, *Chemical Dynamics via Molecular Beams and Laser Techniques*, (Oxford University Press, NY, 1982) Chapter 3.

130. R. D. Levine and R. B. Bernstein, *Molecular Reaction Dynamics and Chemical Reactivity*, (Oxford University Press, NY, 1987) Chapter 5.

131. J. Geddes, H. F. Krause and W. L. Fite, *J. Chem. Phys* **52**, 3297 (1970); *J. Chem. Phys.* **56**, 3298 (1972).

132. R. Gegenbach, Ch. Hahn and J. P. Toennies, *J. Chem. Phys.* **62**, 3620 (1975).

133. R. Götting, H. R. Mayne and J. P. Toennies, *J. Chem. Phys.* **80**, 2230 (1984); *J. Chem. Phys.* **85**, 6396 (1986).

134. R. Götting, J. P. Toennies and M. Vodegel, *Int. J. Chem. Kin.* **18**, 949 (1986).

135. G. H. Kwei and V. W. S. Lo, *J. Chem. Phys.* **72**, 6265 (1980).

136. S. A. Buntin, C. F. Giese and W. R. Gentry, *J. Chem. Phys.* **87**, 1443 (1987).

137. R. E. Continetti, B. A. Balko and Y. T. Lee, *J. Chem. Phys.* **93**, 5719 (1990).

138. R. E. Continetti, J. Z. H. Zhang and W. H. Miller, *J. Chem. Phys.* **93**, 5356 (1990).

139. S. A. Buntin, C. F. Giese and W. R. Gentry, *Chem. Phys. Lett.* **168**, 513 (1990).

140. R. J. Carter, W. H. Hamill and R. R. Williams, *J. Am. Chem. Soc.* **77**, 6457 (1955).

141. R. M. Martin and J. E. Willard, *J. Chem. Phys.* **40**, 3007 (1964).

142. J. M. White, Ph.D. Thesis, University of Illinois, Urbana, 1966.

143. J. A. Betts, Ph.D. Thesis, California Institute of Technology, 1971.

144. A. Kuppermann and J. M. White, *J. Chem. Phys.* **44**, 4352 (1966).

145. K. Tsukiyama, B. Katz and R. Bersohn, *J. Chem. Phys.* **84**, 1934 (1986).

146. U. Gerlach-Meyer, K. Kleinermanns and J. Wolfrum, *J. Chem. Phys.* **86**, 3047 (1987).

147. J. C. Nieh, and J. J. Valentini, *J. Chem. Phys.* **92**, 1083 (1990).

148. D. A. V. Kliner, D. A. Adelman and R. N. Zare, *J. Chem. Phys.* **94**, 1069 (1991).

149. R. S. Blake, K. D. Rinnen, D. A. V. Kliner and R. N. Zare, *Chem. Phys. Lett.* **153**, 365 (1988).

150. K. D. Rinnen, D. A. V. Kliner, R. N. Blake and R. N. Zare, *Chem. Phys. Lett.* **153**, 371 (1988).

151. K. D. Rinnen, D. A. V. Kliner and R. N. Zare, *J. Chem. Phys.* **91**, 7514 (1989).

152. D. L. Phillips, H. B. Levene and J. J. Valentini, *J. Chem. Phys.* **90**, 1600 (1989).

153. D. A. V. Kliner and R. N. Zare, *J. Chem. Phys.* **92**, 2107 (1990).

154. D. A. V. Kliner, K. D. Rinnen and R. N. Zare, *Chem. Phys. Lett.* **166**, 107 (1990).

155. N. C. Blais, M. Zhao, D. G. Truhlar, D. W. Schwenke and D. J. Kouri, *Chem. Phys. Lett.* **166**, 11 (1990).

156. D. A. V. Kliner, D. E. Adelman and R. N. Zare, *J. Chem. Phys.* **95**, 1648 (1991).

157. B. Lepetit and A. Kuppermann, *Chem. Phys. Lett.* **166**, 581 (1990).

158. T. J. Park and J. C. Light, *J. Chem. Phys.* **91**, 974 (1989); *J. Chem. Phys.* **94**, 2946 (1991).

CHAPTER III.

ISOTOPE EFFECTS
IN THE COLINEAR HYDROGEN EXCHANGE REACTION

I. INTRODUCTION

Triatomic exchange reactions of the type A + BC → AB + C, where the atoms are constrained to move in a straight line, are the simplest model for a reactive system. The low mathematical dimensionality of the problem allows a thorough study of the effects of translation and vibration on the reactivity without the complexities associated with molecular rotations. This model is useful for developing insight into the dynamics of the reaction, especially for systems that are colinearly dominated, i.e., for which colinear configurations have a lower energy than bent ones.

This chapter presents the results of colinear scattering calculations for several isotopic variants of the hydrogen exchange reaction at energies below 2 eV . Total reaction probabilities for initial reagent vibrational state $v = 0$ and 1 are presented, and thermal rate constants obtained. The results of transition state theory are compared with the quantum results, and exact transmission coefficients are obtained. Approximate transmission coefficients are calculated for three one-dimensional models for the two-dimensional barrier: the first model consists of a parabolic approximation to the motion along the minimum energy path; the second is a parabolic approximation along the vibrationally adiabatic path, and the third is an exact one-dimensional calculation using the vibrationally adiabatic barrier. Exact and approximate isotope effects are obtained and the results compared. The following isotopic reactions and their reverses were studied:

$$H + H_2 \rightarrow H_2 + H \tag{1}$$

$$H + HD \rightarrow H_2 + D \tag{2}$$

$$H + HT \rightarrow H_2 + T \tag{3}$$

$$D + HD \rightarrow DH + D \tag{4}$$

$$D + HT \rightarrow DH + T \quad (5)$$

$$T + HT \rightarrow TH + T \quad (6)$$

$$H + DH \rightarrow HD + H \quad (7)$$

$$H + TH \rightarrow HT + H \quad (8)$$

$$D + DH \rightarrow D_2 + H \quad (9)$$

II. THEORY

Throughout the chapter a single electronic potential energy surface will be assumed; furthermore, it will be assumed that the total energy of the system lies significantly below the bond dissociation energy of the molecule for dissociative processes and reverse recombinations to be ignored.

The coordinate system for the generic A + BC reaction is depicted in Figure 1. While bond distances are the natural variables of the potential energy surface, distances relating the position of atoms with respect to the center of mass of the diatom are preferred in collision theory, since the kinetic energy operator is found not to involve mixed partial derivatives. These coordinates, for which the kinetic energy term in the Hamiltonian is diagonalized,[1] are referred to as Jacobi coordinates.

The potential energy contours for a generic A + BC reaction in terms of the α coordinates are shown in Figure 2. This function is obtained by solving for the electronic motion in three dimensions for all colinear ABC configurations. The line of steepest ascents and descents is the minimum energy path. The potential energy function increases along all lines normal to this path, and its behavior resembles the well of a diatomic molecule. The system progresses from reagents to products, namely from region α of configuration space, denoted by A + BC, to region γ, corresponding to AB + C.

The line through the origin making an angle θ' with the R'_α axis is the one for which $R_{AB} = 0$, therefore the potential along it can be taken to be infinite: this implies that the relative ordering of the three atoms along the fixed straight line is maintained throughout the reaction. The angle θ' is given by:

$$\theta' = tan^{-1}[1 + m_B/m_C]. \tag{10}$$

The nuclear motion Hamiltonian neglecting spin interactions, can be written in terms of either the α or the γ coordinates as:

$$H = -\frac{\hbar^2}{2\mu_{A,BC}}\frac{\partial^2}{\partial {R'_\alpha}^2} - \frac{\hbar^2}{2\mu_{BC}}\frac{\partial^2}{\partial {r'_\alpha}^2} + V_\alpha(R'_\alpha, r'_\alpha),$$

$$H = -\frac{\hbar^2}{2\mu_{C,AB}}\frac{\partial^2}{\partial {R'_\gamma}^2} - \frac{\hbar^2}{2\mu_{AB}}\frac{\partial^2}{\partial {r'_\gamma}^2} + V_\gamma(R'_\gamma, r'_\gamma), \tag{11}$$

where

$$\mu_{A,BC} = \frac{m_A(m_B + m_C)}{m_A + m_B + m_C} \qquad \mu_{BC} = \frac{m_B m_C}{m_B + m_C} \tag{12}$$

are the reduced masses of the A + BC and the BC system respectively. The first term in the Hamiltonian represents the kinetic energy of relative motion of the atom with respect to the center of mass of the diatom, and the second the vibrational motion of the diatomic molecule.

The problem to be solved is that of finding solutions to the Schroedinger equation for the nuclear motion:

$$H\Psi = E\Psi, \tag{13}$$

subject to suitable aymptotic conditions:[2,5]

$$\Psi^{\alpha n'_\alpha} = \begin{cases} \widetilde{R'_\alpha \to \infty}\ exp(-ik'_{\alpha n'_\alpha} R'_\alpha)\phi_{\alpha n'_\alpha}(r'_\alpha) + \sum_{n_\alpha} f'^{\alpha n'_\alpha}_{\alpha n_\alpha} exp(ik'_{\alpha n_\alpha} R'_\alpha)\phi_{\alpha n_\alpha}(r'_\alpha) \\ \widetilde{R'_\gamma \to \infty}\ \sum_{n_\gamma} f'^{\alpha n'_\alpha}_{\gamma n_\gamma} exp(ik'_{\gamma n_\gamma} R'_\gamma)\phi_{\gamma n_\gamma}(r'_\gamma) \end{cases} . \tag{14}$$

The behavior at $R'_\alpha \to \infty$ indicates a BC molecule in vibrational state n'_α, moving towards atom A with relative wave vector $k'_{\alpha n'_\alpha}$; this term represents the incident wave. Superimposed to that is a sum over waves representing BC molecules moving away from A in vibrational state n_α, with wave vector $k'_{\alpha n_\alpha}$. Region γ lacks the incident term, and only has the reactive scattering term, representing AB molecules in internal state $\phi_{\gamma n_\gamma}$ with relative vave vector $k'_{\gamma n_\gamma}$.

Conservation of energy establishes that:

$$\frac{\hbar^2 {k'_{\alpha n'_\alpha}}^2}{2\mu_{A,BC}} + E_{\alpha n'_\alpha} = \frac{\hbar^2 {k'_{\alpha n_\alpha}}^2}{2\mu_{A,BC}} + E_{\alpha n_\alpha} = \frac{\hbar^2 {k'_{\gamma n_\gamma}}^2}{2\mu_{C,AB}} + E_{\gamma n_\gamma} = E, \tag{15}$$

where the $E_{\lambda n_\lambda}$ are the internal energies of states $\phi_{\lambda n_\lambda}$. Although the vibrational motion of the diatomic is quantized, the wave vectors $k'_{\lambda n_\lambda}$ and the total energy of the system E are not. Furthermore, E is usually a known quantity in state-resolved experiments. Energies $E_{\lambda n_\lambda} > E$, yield an imaginary wave vector $k'_{\lambda n_\lambda}$: this gives terms associated with "closed channels." The complex coefficient ${f'}^{\alpha n'_\alpha}_{\lambda n_\lambda}$ is the scattering amplitude from initial state $\alpha n'_\alpha$ to final state λn_λ. For open channels, the flux associated with the corresponding term is given by $v'_{\lambda n_\lambda}|{f'}^{\alpha n'_\alpha}_{\lambda n_\lambda}|^2$. The flux associated with the incoming wave packet is $v'_{\alpha n'_\alpha}$. The collision cross section for the $\alpha n'_\alpha \rightarrow \lambda n_\lambda$ process in the colinear world is a dimensionless probability given by the ratio of the two fluxes:

$$P^{\alpha n'_\alpha}_{\lambda n_\lambda} = (v'_{\lambda n_\lambda}/v'_{\alpha n'_\alpha})|{f'}^{\alpha n'_\alpha}_{\lambda n_\lambda}|^2. \tag{16}$$

The problem is significantly simplified if a coordinate system is introduced that results in the four reduced masses being replaced by a single reduced mass. Such a system of coordinates was introduced by Delves:[3,4]

$$\begin{aligned} R_\alpha &= a_\alpha R'_\alpha \qquad r_\alpha = (a_\alpha)^{-1} r'_\alpha \qquad a_\alpha = (\mu_{A,BC}/\mu_{BC})^{1/4} \\ R_\gamma &= a_\gamma R'_\gamma \qquad r_\gamma = (a_\gamma)^{-1} r'_\gamma \qquad a_\gamma = (\mu_{C,AB}/\mu_{AB})^{1/4} \end{aligned} \tag{17}$$

The Hamiltonian then becomes:

$$H = -\frac{\hbar^2}{2\mu}\left(\frac{\partial^2}{\partial {R_\alpha}^2} + \frac{\partial^2}{\partial {r_\alpha}^2}\right) + V_\alpha(R_\alpha, r_\alpha)$$

$$H = -\frac{\hbar^2}{2\mu}\left(\frac{\partial^2}{\partial {R_\gamma}^2} + \frac{\partial^2}{\partial {r_\gamma}^2}\right) + V_\gamma(R_\gamma, r_\gamma). \tag{18}$$

where the single reduced mass is independent of the choice of α or γ coordinates and is defined by:

$$\mu = [(m_A m_B m_C)/M]^{1/2}, \qquad M = m_A + m_B + m_C. \tag{19}$$

It can be shown[5] that the $(R_\alpha, r_\alpha) \rightarrow (R_\gamma, r_\gamma)$ transformation corresponds to a rotation in the Delves mass-scaled configuration space, and that the clockwise rotation angle is given by:

$$\omega = tan^{-1}[(m_A m_C)/(m_B M)]^{1/2}. \tag{20}$$

The two axes systems are orthogonal, and, unlike the unscaled (R'_α, r'_α), the equipotential surface does not change shape under the transformation. The motion of the ABC system in one physical dimension is identical to that of a single particle of mass μ moving in a two mathematical dimensional space, subject to the same potential V. The skew angle θ between the R_α and R_γ axes is given by:

$$\theta = tan^{-1}[(m_B M)/(m_A m_C)]^{1/2}, \tag{21}$$

and it is more acute than the θ' angle. This has pronounced effects on the dynamics of heavy-light-heavy systems where the scaled distances are compressed in the saddle point region, and the gradient of the potential energy increases sharply. These are the systems where quantum effects can be expected to be significant. The potential energy contours for the H_3 system, using the LSTH surface, are shown in Figure 3.

The direct result of colinear quantum scattering calculations is the scattering matrix that relates the incoming and outgoing waves associated with the reagents and products.

In the λ arrangement channel the wavefunction $\Psi^{\lambda' n'_\lambda}$ can be expanded in the basis set $\phi_{\lambda n_\lambda}$, which is forced to be complete and discrete by constraining the

diatomic potential $v_\lambda(r_\lambda) = V(R_\lambda \to \infty, r_\lambda)$ to a finite range, and therefore equal to zero beyond a certain value $r_{\lambda_{max}}$:

$$\Psi^{\lambda' n'_\lambda} \sim \sum_{\lambda n_\lambda} g^{\lambda' n'_\lambda}_{\lambda n_\lambda}(R_\lambda)\phi_{\lambda n_\lambda}(r_\lambda), \tag{22}$$

where the diatomic molecule eigenfunctions are defined as:

$$-\frac{\hbar^2}{2\mu}\frac{d^2\phi_{\lambda n_\lambda}}{dr_\lambda^2} + v_\lambda(r_\lambda)\phi_{\lambda n_\lambda} = E_{\lambda n_\lambda}\phi_{\lambda n_\lambda}, \tag{23}$$

subject to the condition:

$$\phi_{\lambda n_\lambda}(0) = \phi_{\lambda n_\lambda}(r_{\lambda_{max}}) = 0. \tag{24}$$

Substituting Eq. (22) and (18) into Eq. (13), multiplying both sides by $\phi^*_{\bar{\lambda}\bar{n}_{\bar{\lambda}}}$ and integrating over $r_{\bar{\lambda}}$ leads to the following set of differential equations:

$$-\frac{\hbar^2}{2\mu}\frac{d^2 g^{\lambda' n'_\lambda}_{\lambda n_\lambda}}{dR_\lambda^2} \sim (E - E_{\lambda n_\lambda}) g^{\lambda' n'_\lambda}_{\lambda n_\lambda}, \tag{25}$$

where $\bar{\lambda}$ has been replaced by λ. The solutions can be expressed as:

$$g^{\lambda' n'_\lambda}_{\lambda n_\lambda} \underset{R_\lambda \to \infty}{\sim} v^{-1/2}_{\lambda n_\lambda}[\mathcal{I}_{\lambda n_\lambda}(R_\lambda)A^{\lambda' n'_\lambda}_{\lambda n_\lambda} - \mathcal{O}_{\lambda n_\lambda}(R_\lambda)B^{\lambda' n'_\lambda}_{\lambda n_\lambda}]. \tag{26}$$

The $A^{\lambda' n'_\lambda}_{\lambda n_\lambda}$ and $B^{\lambda' n'_\lambda}_{\lambda n_\lambda}$ coefficients result from the integration, and $v_{\lambda n_\lambda}$ is the channel velocity:

$$v_{\lambda n_\lambda} = \hbar|k_{\lambda n_\lambda}|/\mu, \tag{27}$$

where:

$$k_{\lambda n_\lambda} = \hbar^{-1}[2\mu(E - E_{\lambda n_\lambda})]^{1/2}. \tag{28}$$

$\mathcal{I}_{\lambda n_\lambda}$ and $\mathcal{O}_{\lambda n_\lambda}$ are the incoming and outgoing waves:

$$\mathcal{I}_{\lambda n_\lambda}(R_\lambda) = \begin{cases} exp(-ik_{\lambda n_\lambda}R_\lambda) & \text{open channels} \\ exp(|k_{\lambda n_\lambda}|R_\lambda & \text{closed channels} \end{cases} \tag{29}$$

$$\mathcal{O}_{\lambda n_\lambda}(R_\lambda) = \begin{cases} exp(ik_{\lambda n_\lambda} R_\lambda) & \text{open channels} \\ exp(-|k_{\lambda n_\lambda}| R_\lambda & \text{closed channels} \end{cases} \tag{30}$$

In matrix form the equation for $g_{\lambda n_\lambda}^{\lambda' n'_\lambda}$ becomes:

$$\mathbf{g} \sim \mathbf{v}^{-1/2}[\mathcal{I}\mathbf{A} - \mathcal{O}\mathbf{B}]. \tag{31}$$

$\mathbf{g}$, $\mathbf{A}$ and $\mathbf{B}$ are matrices whose λn_λ row and $\lambda' n'_\lambda$ column elements are $g_{\lambda n_\lambda}^{\lambda' n'_\lambda}$, $A_{\lambda n_\lambda}^{\lambda' n'_\lambda}$ and $B_{\lambda n_\lambda}^{\lambda' n'_\lambda}$, while $\mathbf{v}$, $\mathcal{I}$ and $\mathcal{O}$ are diagonal matrices with elements $v_{\lambda n_\lambda}$, $\mathcal{I}_{\lambda n_\lambda}$ and $\mathcal{O}_{\lambda n_\lambda}$ respectively. The scattering matrix $\mathbf{S}$ is defined by:

$$\mathbf{B} = \mathbf{S}\mathbf{A}. \tag{32}$$

Therefore, the ratio $\frac{B_{\lambda n_\lambda}^{\lambda' n'_\lambda}}{A_{\lambda n_\lambda}^{\lambda' n'_\lambda}}$ is fixed: this indicates that, given the initial conditions, the outcome of the collision is entirely determined by the mathematical structure of the Schroedinger equation: knowledgde of the states and fluxes of the reagents allows calculation of the states and fluxes of the products.

The properties of $\mathbf{S}$ are discussed in the review by Lane and Thomas:[6] the most important result is that $\mathbf{S}$ is unique, unitary and symmetric, and that deviations from these properties reflect inaccuracies in the calculation. The uniqueness of $\mathbf{S}$ reflects its independence from the choice of $\mathbf{A}$, namely the initial conditions; as stated above, for two coefficient matrices A_1 and A_2 the Schroedinger equation forces the corresponding coefficients B_1 and B_2 to satisfy the property $\mathbf{B_1 A_1^{-1}} = \mathbf{B_2 A_2^{-1}}$ The symmetry of $\mathbf{S}$ reflects the principle of microscopic reversibility or detailed balancing. The unitarity of the open part of $\mathbf{S}$ is the result of conservation of particle flux.

Equation (31) can also be expressed in terms of standing waves:

$$\mathbf{g} \sim \mathbf{v}^{-1/2}[\mathcal{S}\mathbf{C} - \mathcal{C}\mathbf{D}], \tag{33}$$

where $\mathbf{C}$ and $\mathbf{D}$ are new matrices of integration constants and $\mathcal{S}$ and $\mathcal{C}$ are diagonal sine and cosine wave matrices whose elements are:

$$\mathcal{S}_{\lambda n_\lambda}(R_\lambda) = \begin{cases} sin(k_{\lambda n_\lambda} R_\lambda) & \text{open channels} \\ exp(|k_{\lambda n_\lambda}| R_\lambda & \text{closed channels} \end{cases} \tag{34}$$

$$\mathcal{C}_{\lambda n_\lambda}(R_\lambda) = \begin{cases} cos(k_{\lambda n_\lambda} R_\lambda) & \text{open channels} \\ exp(-|k_{\lambda n_\lambda}| R_\lambda & \text{closed channels} \end{cases} \tag{35}$$

The reactance matrix $\mathbf{R}$ is defined as:

$$\mathbf{D} = \mathbf{RC}. \tag{36}$$

It can be shown[6] that $\mathbf{R}$ is unique, real and that the open part is symmetric. The reactance matrix is related to the scattering matrix by the relationship:

$$\mathbf{S^o} = (\mathbf{I} + i\mathbf{R^o})(\mathbf{I} - i\mathbf{R^o})^{-1}. \tag{37}$$

The scattering amplitude $f_{\lambda n_\lambda}^{\lambda' n'_\lambda}$ is related to $\mathbf{S}^o$ by:

$$f_{\lambda n_\lambda}^{\lambda' n'_\lambda} = (v_{\lambda' n'_\lambda} / v_{\lambda n_\lambda})^{1/2} S^{o\,\lambda' n'_\lambda}_{\lambda n_\lambda}, \tag{38}$$

where the $v_{\lambda n_\lambda}$ are the channel velocities defined in Eq. (27). The reaction probability $P_{\lambda n_\lambda}^{\lambda' n'_\lambda}$ is then:

$$P_{\lambda n_\lambda}^{\lambda' n'_\lambda} = (v_{\lambda n_\lambda} / v_\lambda) |f_{\lambda n_\lambda}^{\lambda' n'_\lambda}|^2, \tag{39}$$

or, in terms of $\mathbf{S}$:

$$P_{\lambda n_\lambda}^{\lambda' n'_\lambda} = |S^{o\,\lambda' n'_\lambda}_{\lambda n_\lambda}|^2. \tag{40}$$

From microscopic reversibility it follows that:

$$P_{\lambda' n'_\lambda}^{\lambda n_\lambda} = P_{\lambda n_\lambda}^{\lambda' n'_\lambda} \tag{41},$$

and from the unitarity of $\mathbf{S}^o$ we derive the property of flux conservation:

$$\sum_{\lambda n_\lambda} P_{\lambda n_\lambda}^{\lambda' n'_\lambda} = 1. \tag{42}$$

III. METHODOLOGY

From the previous section, it is apparent that, in order to obtain reaction probabilities, it suffices to calculate the reactance matrix **R**. This can be obtained by calculating a sufficiently large number of linearly independent solutions of the Schroedinger equation and by expressing the **g** matrix in the form of Eq. (33); with knowledge of the **C** and **D** matrices of coefficients, **R** can be calculated by Eq. (36).

Several methods have been applied to obtain linearly independent solutions of the Schroedinger equation. Mortensen and Pitzer,[7] Diestler and McKoy[8] and Truhlar and Kuppermann[9-11] used Cartesian coordinates and finite difference method. McCullough and Wyatt[12,13] used a similar approach, but with the time-dependent Schroedinger equation. An integral equation approach was developed by Sams and Kouri[14] and applied by Adams *et al.*.[15] Mortensen and Gucwa[16] have used a variational approach, while Rabitz and co-workers[17] have used a finite element method.

As mentioned in the previous chapter, the most widely employed method of solving the Schroedinger equation for colinear atom-diatom systems has been the coupled channel (also known as close-coupling) method. This method is characterized by the use of a set of two variables, x and y, such that for a constant value of x, for example $\bar{x}$, the potential assumes very large values for very small and very large values of y. The wavefunction is expanded in the eigenfunctions of the one-mathematical-dimensional Hamiltonian in y with the potential $V(\bar{x}, y)$, and the set of coupled ordinary differential equations is solved. Several systems have been studied using this method.[18-29]

This work makes use of the circular polar coordinates (ρ, α) illustrated in Figure 3. This set of coordinates belongs to the set of hyperspherical coordinates,[30-38] which are distinguished by the use of a coordinate which measures

the size of the system, and is not specialized to one arrangement channel. This is called the hyperradius and it is the generalized collision (propagation) coordinate.

The nuclear motion Hamiltonian in these coordinates is:

$$H(\rho,\alpha) = -\frac{\hbar^2}{2\mu}\left[\frac{\partial^2}{\partial\rho^2} + \frac{1}{\rho}\frac{\partial}{\partial\rho} + \frac{1}{\rho^2}\frac{\partial^2}{\partial\alpha^2}\right] + V(\alpha,\rho). \tag{43}$$

Because of the divergence of V at $\alpha = 0$ and $\alpha = 60°$ for the H + H_2 reaction, the eigenfunctions of

$$h(\alpha;\bar{\rho}) = -\frac{\hbar^2}{2\mu\bar{\rho}^2}\frac{\partial^2}{\partial\alpha^2} + V(\alpha,\bar{\rho}) \tag{44}$$

form a discrete set of $\{\phi_n(\alpha;\bar{\rho})\}$ which covers the entire range of α. Expanding the eigenfunctions of $H(\rho,\alpha)$ according to:

$$\Psi^{\lambda' n'_\lambda} = \rho^{-1/2}\sum_n g_n^{\lambda' n'_\lambda}(\rho;\bar{\rho})\phi_n(\alpha;\bar{\rho}) \tag{45}$$

leads to the following matrix differential equation in $\mathbf{g}\ (\rho;\bar{\rho})$:

$$-\frac{\hbar^2}{2\mu}\frac{d^2\mathbf{g}(\rho;\bar{\rho})}{d\rho^2} + \mathbf{V}(\rho;\bar{\rho})\mathbf{g}(\rho;\bar{\rho}) = \mathbf{E}(\rho;\bar{\rho})\mathbf{g}(\rho;\bar{\rho}), \tag{46}$$

where $\mathbf{V}$ and $\mathbf{E}$ are the interaction and energy matrices whose n row and n' column are given by:

$$\mathrm{V}_n^{n'}(\rho;\bar{\rho}) = \langle n|\mathrm{V}(\alpha,\rho) - \frac{\bar{\rho}^2}{\rho^2}\mathrm{V}(\alpha,\bar{\rho})|n'\rangle \tag{47}$$

$$\mathrm{E}_n^{n'}(\rho;\bar{\rho}) = \left[\mathrm{E} + \frac{\hbar^2}{8\mu\rho^2} - E_n(\bar{\rho})\right]\delta_n^{n'}, \tag{48}$$

where $|n'\rangle = \phi_{n'}(\alpha;\bar{\rho})$, the integration variable is α and E is the total energy of the system. The scattering problem is solved as follows: a set of ρ_i is chosen $(i = 0, 1, ..., i_{max})$, and the wavefunctions $\phi_n(\alpha;\bar{\rho}_i)$ are calculated by a numerical method (such as finite difference) for a $\bar{\rho}_i$ in the range ρ_{i-1} and ρ_i. The coupled equations (46) are then integrated numerically from ρ_{i-1} to ρ_i, setting $\mathbf{g}(0;\bar{\rho}_0)$ = 0 and $\mathbf{g}'(0;\bar{\rho}_0) = \mathbf{I}$ and requiring continuity of $\Psi^{\lambda' n'_\lambda}(\alpha,\rho)$ and its derivative

with respect to ρ at the boundaries between the two ρ regions. The $\Psi^{\lambda' n' \lambda}(\alpha, \rho)$ are obtained for $0 \leq \alpha \leq \alpha_{max}$ and $\rho_0 \leq \rho \leq \rho_{i_{max}}$, and then projected onto the bound diatomic states at large R_λ from which the **R**, **S** and **P** matrices are obtained as discussed above.

For systems that are symmetric, namely A + BA $\rightarrow$ AB + A, the potential energy function is symmetric with respect to the line $\alpha = \alpha_{max}/2$ in configuration space, and the solutions are either even or odd with respect to reflection through that line: they can therefore be obtained separately, thereby decreasing the computational effort.

IV. RESULTS

A. Reaction Probability

Reaction probabilities for reactions (1)-(9) and their reverses, with reagents in their ground and first excited vibrational states are shown in Figs. 5-35. Partial reaction probabilities for reactions (1), (2), and (3), for the $v = 0$ to $v' = 0$, 1 and $v = 1$ to $v' = 0$, 1 reactive transitions, are shown in Figs. 7, 10, 11, 16 and 17. These results span the total energy range between 0.3 and 2 eV, with a 0.01 eV energy grid.

Every isotopic hydrogenic system shows similar pronounced oscillations at relative translational energies of about 0.6 eV and 1.0 eV. These oscillations are due to the quantum mechanical interference between direct reaction and dynamic resonant mechanisms, where energy is trapped in internal degrees of freedom of the system. For the 1.0 eV resonance, the trapping degree of freedom is due to the vibrational mode transverse to the minimum energy path,[24,39] while the lower energy one seems to be at least partially due to trapping of energy in a longitudinal mode, along the minimum energy path, with the repulsive walls of the skew axis acting as partial reflectors.[37,38] This corresponds to an asymmetric stetching vibration at the saddle point, while the 1.0 eV resonance is related to the symmetric stretching mode. These resonance can therefore be interpreted as virtual vibrational levels of the saddle point region, and the energies at which they occur can give information about the geometrical and energetic nature of the transition state. This effect can also be noticed in the partial reaction probabilities: for the H + H_2 system, the $0 \rightarrow 1$ probability goes through a peak at $E_{rel} = 0.60$ eV, while the $0 \rightarrow 0$ has a sharp dip over the same narrow energy range. (Fig. 7) This behavior occurs when the available energy equals the energy of a metastable excited state of the H_3 transition state, and a substantial amount of flux is diverted temporarily to this excited level and the corresponding vibrational states of the product diatom.[40]

Both of these resonances are nonadiabatic, internal "Feshbach" resonances. Schatz[41] attributes the 0.6 eV resonance to partial trapping of the energy in an asymmetric stretch of the transition state corresponding to the second symmetric vibrational eigenstate of the H_3 molecule, while the resonance at 1.0 eV could easily not be assigned to just a single virtual state.

Kaye and Kuppermann[42] performed collision lifetime matrix analysis on these two resonances to determine their positions, widths and lifetimes on the PK surface, and noted an important difference with respect to the participation of the newly opened vibrational state of the product: for the first resonance, the $v = 1$ state of the H_2 molecule makes a sizable contribution to the reactive scattering. Near the second resonance, however, the $v = 2$ does not contribute to the dynamics.

Isotope effects on the resonance structure of the colinear, symmetric hydrogenic systems have been studied by Dwyer,[43] who noticed a strong resonant oscillation in the region of the 0.6 eV resonance for the H + H_2 , D + HD and T + HT systems, and a gradual weakening of the structure for the H + DH, D + D_2 and H + TH systems. Systems with the lightest atom in the middle seemed to display the strongest resonances, and the effect of changing the end atoms was not significant.

These effects are verified in the present study as evident from Figures 5-35, heavy-light-heavy systems are found to exhibit the sharpest resonances for the $v = 0$ and $v = 1$ reaction probability.

A review of resonance effects in reaction dynamics can be found in Ref. (44).

B. Rate Constants

Rate constants for reactions (1)-(8) and their reverses were obtained using the equation:

$$\begin{aligned} k_r(n,T) &= \int_0^\infty F_T(E_n) v_{rel} P_n(E_n) dE_n \\ &= (2\pi\mu_{A,BC}\, kT)^{-1/2} \int_0^\infty P_n(E_n) exp(-E_n/kT) dEn, \end{aligned} \tag{49}$$

where k is Boltzmann's constant, T the absolute temperature, $P_n(E_n)$ is the reaction probability when the molecule is in vibrational state n with initial translational energy E_n, and $F_T(E_n)$ is given by:

$$F_T(E_n) = (2\pi\mu_{A,BC}\, kT)^{-1/2} \frac{1}{v_{rel}} exp(-E_n/kT). \tag{50}$$

For a thermal distribution of reagents vibrational levels, the total rate constant is:

$$k_r(T) = \sum_n k_r(n,T) p_n(T), \tag{51}$$

where p_n is the fraction of reagent molecules in vibrational state n:

$$p_n(T) = (Q^v)^{-1} exp[-(E_n^v - E_0^v)/kT]. \tag{52}$$

For the systems in this study it was sufficient to include only the ground and the first excited vibrational states. The integral in equation (49) was evaluated using Simpson's rule, and the probabilities for the 171 energies mentioned in the previous section. The logarithms of the rate constants are plotted as a function of $\frac{1}{T}$ in Figures 36-48. Both the $v = 0$ and $v = 1$ contributions are shown; the thermal rate constants, as expressed in Eq. (51), are almost identical to the $v = 0$ contribution for all thirteen hydrogenic systems.

C. Transition State Theory Results

This theory was first proposed by Pelzer and Wigner,[45] and extensively developed by Eyring and collaborators[46,47] and by Evans and Polanyi.[48] This

theory is based on the concept of a transition state separating reactants and products. The two most basic assumptions of transition state theory are the separation of electronic and nuclear motion, equivalent to the Born-Oppenheimer approximation in quantum mechanics, and the assumption that reactants and products are distributed among their internal states in accordance with the Maxwell-Boltzmann distribution. In addition, the following assumptions are required:

1. Systems that have crossed the transition state cannot turn around and form reactants.
2. Motion along the reaction coordinate can be separated from the internal degrees of freedom and treated classically.
3. The transition state complexes are also distributed among their states according to the Maxwell-Boltzmann laws.

Transition state theory can be derived using a quasi-equilibrium approach, which makes use of a "dividing surface" , and a dynamical approach, in which the flux through the transition state is evaluated, and equated to the reactive flux.[49] Both approaches lead to the following expression for the rate constant:

$$k_{TST} = \frac{kT}{h}\frac{Q^{\ddagger}}{Q_A Q_{BC}} exp(-E_0/kT), \tag{53}$$

where $Q^{\ddagger}$ is the partition function for the transition state and Q_A and Q_{BC} are the same functions for the reactants, and E_0 is the lowest level of the transition state relative to the zero-point energy of the reactants.

For the colinear case, this reduces to:

$$k_{TST} = \frac{kT}{h}\left(\frac{Q^{vs}}{Q^{rel}Q^{v}}\right) exp(-E_0/kT), \tag{54}$$

where Q^{rel} is the translational partition function:

$$Q^{rel} = \left(\frac{2\pi\mu_{A,BC}\,kT}{h^2}\right)^{1/2}, \tag{55}$$

and Q^{vs} and Q^{v} the vibrational partition functions for the symmetric stretch of the triatomic transition state and for the reactant molecule respectively. In order to find Q^{vs} the vibrational energies of the symmetric stretch must be obtained. A different procedure must be followed for symmetric and asymmetric reactions.

For symmetric ABA systems, the vibrational levels can be found by taking a cut along the line $R_1 = R_2$ on the potential energy surface. In Delves mass-scaled coordinates this corresponds to the line:

$$r_\alpha = \left(\frac{M m_B m_C}{m_A (2m_C + m_B)^2} \right)^{1/2} R_\alpha. \tag{56}$$

For the H_3 system this cut is shown in Figure 4. Two approaches can be used to estimate the vibrational levels supported by this well. In the first one, a harmonic approximation is made, where the second derivative at the minimum is found by numerical differentiation, and equated to the force constant k_e. The vibrational frequency is then:

$$\nu_e = \frac{1}{2\pi} \left(\frac{k_e}{\mu} \right)^{1/2}. \tag{57}$$

The reduced mass is given by Eq. (19).

A more accurate method involves solving for the eigenvalues of this potential by finite difference method. This includes anharmonicity effects, and has been used for the present TST results.

For asymmetric ABC systems, the procedure for finding the vibrational levels supported by the transition state is slightly more involved: the cut across the potential energy surface that represents the motion tranverse to the reaction coordinate has to be determined for each system. This cut no longer takes place along the line in Eq. (56), but rather along an arbitrary line of equation $r_\alpha = aR_\alpha + b$. This is obtained by carrying out a normal mode analysis:[50-52] first,

the bond displacements ΔR_1 and ΔR_2 are chosen as internal coordinates. The kinetic energy, after removal of the center of mass motion, is given by:

$$T = \frac{1}{2} \sum_{i,j} \mu_{ij} \Delta \dot{R}_i \Delta \dot{R}_j. \tag{58}$$

The potential energy has an analogous form:

$$V = \frac{1}{2} \sum_{i,j} f_{ij} \Delta R_i \Delta R_j. \tag{59}$$

The normal coordinates, q_k, of the triatomic are those for which there are no cross terms in either the kinetic or potential energy expressions:

$$T = \frac{1}{2} \sum_{k} \mu_k \dot{q}_k^2 \tag{60}$$

$$V = \frac{1}{2} \sum_{k} f_k {q_k}^2. \tag{61}$$

The normal coordinates are obtained from a transformation of the internal coordinates:

$$q_k = a_{1k} \Delta R_1 + a_{2k} \Delta R_2 \tag{62}$$

by simultaneous diagonalization of both T and V: The Hamiltonian for the system can be obtained by combining Equations (58) and (59) and expressing them in matrix form:

$$\mathbf{H} = (\overrightarrow{\Delta \dot{R}})^\dagger \, \mathbf{T} \, (\overrightarrow{\Delta \dot{R}}) + (\overrightarrow{\Delta R})^\dagger \, \mathbf{V} \, (\vec{\Delta R}). \tag{63}$$

Therefore, setting the secular determinant $det(V - \lambda T)$ equal to zero allows one to find the frequencies of the normal modes:

$$det \begin{pmatrix} f_{11} - \lambda \mu_{11}/2 & f_{12} - \lambda \mu_{12}/2 \\ f_{12} - \lambda \mu_{12}/2 & f_{22} - \lambda \mu_{22}/2 \end{pmatrix} = 0. \tag{64}$$

The force constants f_{11}, f_{12} and f_{22} are related to the second derivatives of the potential:

$$f_{ij} = \frac{1}{2}\frac{\partial^2 V}{\partial \Delta R_1 \partial \Delta R_2}. \tag{65}$$

The values of the force constants for the hydrogenic systems were found by numerically evaluating the second derivatives of the LSTH potential energy surface at the saddle point. For all isotopic systems, this results in $f_{11} = f_{22}$. The reduced masses in Equation (58) are found to be:

$$\mu_{11} = \frac{m_1(m_2+m_3)}{M}; \qquad \mu_{12} = \frac{m_1 m_3}{M}; \qquad \mu_{22} = \frac{m_3(m_2+m_1)}{M} \tag{66}$$

The eigenvalues λ_k are related to the frequencies by:

$$\lambda_k = 4\pi^2 {\nu_k}^2. \tag{67}$$

A positive and a negative eigenvalue are obtained. The negative one gives rise to an imaginary frequency, corresponding to the motion along the reaction path. Substitution of the eigenvalues into the set of linear equation allows the determination of the ratio a_{1k}/a_{2k}, and therefore the direction of the normal mode coordinate in R_1-R_2 space. Transformation to the Delves mass-scaled system of coordinates, yields a corresponding slope for the line, whose intercept can be determined using the coordinates of the saddle point, through which the line must pass. This line determines the cut along the mass-scaled potential that corresponds to the motion transverse to the minimum energy path, the "symmetric stretch" of the triatomic. The bound states of this well are the transition state vibrational levels to be used in the calculation of Q^{vs} in Equation (54). Exact quantum and transition state rate constants are tabulated in Tables 2-14, and shown in Figures 36-48. Exact transmission coefficients are obtained by dividing the quantum mechanical rate constants by the TST result. The excellent agreement between the forward and reverse exact transmission coefficients is a good test of the accuracy of the calculation.

V. DISCUSSION

A. Exact and Approximate Transmission Coefficients

In classical mechanics, the probability that a particle can cross a barrier of height E_b is zero for translational energies lower than E_b, and unity for energies higher than E_b. The reaction probability as a function of energy is therefore a step function. Quantum barrier permeabilities, on the other hand, are continuous functions of E_{trans}, with finite probabilities predicted for $E_{trans} \leq E_b$, a phenomenon known as tunnelling.

The purpose of this study has been to provide a complete compilation of exact quantum mechanical isotope effects, as well as to test the predictions of conventional transition state theory, and transition state theory with quantum corrections. Conventional transition state theory assumes no quantum correction due to tunnelling; the transmission coefficient in then set to 1.

Corrections to transition state theory can be found by approximating the two-mathematical dimensional barrier for the reaction by a one-mathematical dimensional barrier along the reaction coordinate.

The exact transmission coefficients are expressed in terms of the exact quantum mechanical transition probabilities, whereas the TST ones involve transmission probabilities across one-mathematical-dimensional barriers.

The usual method of obtaining corrected transition state rate constants is to calculate the conventional TST rate constant, k_0^{TST} assuming that the motion along the reaction path is classical, and the quantum correction κ_1, such that the actual TST rate constant is:

$$k^{TST}(T) = \kappa_1(T) k_0^{TST}. \tag{68}$$

The transmission coefficient κ_1 is given by:

$$\kappa_1 = \frac{\int_0^\infty T^{(1)}(E_{trans}) exp(-E_{trans}/kT) dE_{trans}}{\int_0^\infty T_{cl}^{(1)}(E_{trans}) exp(-E_{trans}/kT) dE_{trans}}, \tag{69}$$

where $T^{(1)}$ is the transmission probability through the 1-MD barrier that represents the potential energy of the system along the reaction path. This barrier is defined differently according to different models, as described later. $T_{cl}^{(1)}(E)$ is the classical transmission probability for the same barrier, namely 1 for energies greater than the barrier height, and 0 otherwise.

The easiest tunnelling correction to apply is the factor derived by Wigner,[53] for the case where the normal mode is separable at the saddle point. This correction factor is for a quadratic barrier, and is accurate to the second power of Planck's constant:

$$\kappa_W = 1 + \frac{1}{24}\left(\frac{h\nu_t}{kT}\right)^2, \tag{70}$$

where ν_t is the imaginary frequency associated with the reaction coordinate.

Several other approximate quantum treatments are possible.[9-11,54-58] In general, one of the following two models has been used: (1) conservation of transverse mode vibrational energy approximation (CVE), in which the barrier is the classical potential energy along the reaction path; (2) vibrational adiabaticity approximation, or conservation of vibrational quantum number, with no correction for reaction path curvature (VA), in which the local vibrational energy is assumed to adjust adiabatically along the reaction path. In other words, the initial vibrational quantum of reactant molecule BC is adiabatically transformed to a quantum of symmetric stretching vibrations of ABC in the transition state, and finally, to a vibrational quantum of the product AB.

In this case the barrier ${E_b}^{VA}$ is given by:

$$E_b^{VA} = E_b + E_0^{vs} - E_0^{v}, \tag{71}$$

where E_0^{vs} and E_0^{v} are the zero point energies associated with the symmetric stretching vibration of the transition state and the reactant molecule, respectively.

A simple method of evaluating tunnelling corrections is to replace the barrier by a truncated parabolic barrier. The quantum mechanical transmission probability through this barrier has been treated analytically by Bell[54,59] and others.[58,60–64] In this model, the curvature at the top of the barrier corresponds to a negative force constant and an imaginary frequency, ν_t as seen in the previous section.

Solution of this problem shows that the transmission probability for a particle of mass m and energy E_{trans} is given by:

$$T(E_{trans}) = \frac{1}{1 + exp[2\pi(E_b - E_{trans})/h\nu_t]}. \tag{72}$$

Another model potential for which an exact analytical solution is possible is the one worked out by Eckart[65] and Johnston and co-workers.[66,67] Besides the curvature at the top of the barrier, this model makes use of another parameter, which is adjusted to make the Eckart barrier resemble the actual barrier.

A third option is to treat the one-dimensional tunnelling problem numerically. The Schroedinger equation in one dimension is:

$$\left[-\frac{\hbar^2}{2\mu}\frac{d^2}{ds^2} + V(s) - E\right]\Psi_k(s) = 0, \tag{73}$$

where $V(s)$ is the effective potential energy function, along the reaction coordinate, which is defined depending on the model used, and E is the total energy of the system.

The distance s along the reaction path in normal coordinate space is calculated by numerical integration using a sufficiently fine grid. As $s \rightarrow -\infty$, the solutions of Eq. (73) go to an incident wave plus a reflected wave, and, for $s \rightarrow +\infty$, to a transmitted wave.

The asymptotic form of the solutions of the Schroedinger equation is:[2]

$$\Psi(s) \underset{s\rightarrow-\infty}{\sim} Ae^{iks} + Be^{-iks} \tag{74}$$

$$\Psi(s)\underset{s\to-\infty}{\sim} Fe^{iks} + Ge^{-iks}, \tag{75}$$

where $k = \frac{\sqrt{2\mu E}}{\hbar}$. The transmission probability for the barrier is given by the square of the absolute value of the ratio of F to A.

In order to test the validity of the one-dimensional barrier tunnelling corrections, three models were applied to the isotopic hydrogen exchange reaction results of this chapter. In the first model, a parabolic least-squares fit was determined for the reaction coordinate using the CVE approach. This path is shown in Figure 49. The reaction coordinate is along the minimum energy path in Delves mass-scaled configuration space. The barrier height was fixed at 0.4248 eV, the LSTH barrier), and the curvature was determined by a least squares fit, and used to obtain the imaginary frequency ν_t to use in Equation (72). Using the definition for the classical transmission probability, Eq. (69) can be expressed as:

$$\kappa_1(T) = (1/kT)e^{E_b/kT}\int_0^\infty T(E_{trans})exp(-E_{trans}/kT)dE_{trans}. \tag{76}$$

This integral was evaluated using a Simpson routine, with $T(E_{trans})$ given by Eq. (72).

Transmission coefficients for the parabolic approximation to the minimum energy path, κ_{par}^{CVE}, are tabulated in Tables 2-14.

The second model is a parabolic approximation to the vibrationally adiabatic path, shown in Figure 49. This path was obtained by finding the second derivative of the potential energy in the direction perpendicular to the minimum energy path, calculating the zero point energy of the transverse mode, and adding it to the potential energy at a thousand points along the reaction coordinate.

In this case, both the barrier height and the curvature were fit with a linear least-squares routine. The resulting transmission coefficients, κ_{par}^{VA} are shown in Tables 2-14.

The third model solves for the transmission probability through the actual vibrationally adiabatic barrier, by numerically integrating the one-dimensional Schroedinger equation. The transmission coefficients κ^{VA} obtained with this method are shown in Tables 2-14.

B. Comparison of Rate Constant Results

Exact transmission coefficients range between 30.8, for the H + H_2 case to 5.86, for the T + H_2 reaction.

For the H + H_2 reaction, conventional transition state theory predicts rate constants that are inaccurate by 15 % at 1000 K; at the highest temperature studied, 1600 K, the agreement is to within 4 %. At 700 K, TST predicts rate constants that are too low by 29 %, and the error rises to a factor of 30.8 at 200 K.

TST results are in better agreement with exact results for all other isotopic variants of the reaction, due to less tunnelling than in the H_3 system.

Conventional TST rate constants also tend to overestimate the thermal rate constants at high temperatures, due to the breakdown of the fundamental assumption of transition state theory, according to which the classical trajectories do not recross the transition state dividing surface.

As shown in Tables 2-14, and Figures 51-59, the parabolic approximation to the CVE model yields κ values ranging from a few hundred to several thousand. The overestimation of the tunnelling correction produced by this approximation is in accord with the fairly narrow barrier encountered along the minimum energy path (see Figure 49). If one considers a square barrier of height E_b and half-width a, as an example, the "well strength" is often characterized by the dimensionless parameter β, given by $\frac{a}{\hbar}(2\mu E_b)^{1/2}$. The higher and wider the barrier, the harder it is for the particle to make it through.

This is evidenced by the much lower transmission coefficients obtained for the much broader vibrationally adiabatic barrier. The parabolic approximation and the

exact one-dimensional barrier calculation yield similar transmission coefficients. A typical parabolic fit to the asymmetric system HHD is shown in Figure 50.

It is interesting to note that the VA treatment can yield tunnelling corrections that are less than unity. This effect was first observed by Truhlar,[69] who attributed it to the presence of more reflection above the barrier than transmission below the barrier for a system with a Boltzmann distribution of relative translational energies.

As far as the exact transmission coefficients are concerned, κ values less than one are observed in several systems as the temperature is increased. This is because, at sufficiently high temperatures, high translational energy values correspond to probabilities that are less than one.

The VA model is in better agreement with the quantum results, except at low temperatures, for the cases where tunnelling is expected to be significant. There are mainly two reasons why the the VA results can fail: (1) the separation of the transverse vibration is only partially justified; (2) neglect of curvilinear effects in treating the VA reaction path is a further approximation. This second problem involves two kinds of effects: first, centrifugal forces will cause the reaction path to lie off the minimum energy path. Second, the transmission probability was calculated by straightening out the path. It is the neglect of curvature that does not permit a true treatment of vibrationally adiabaticity.

The approximation made by separating out the transverse mode can be thought of as particles "cutting the corner," i.e., crossing the line perpendicular to the minimum energy path at the saddle point (the line $R_{AB} = R_{BC}$) in an nonadiabatic symmetric stretch vibrational state. It has been argued in the past that the centrifugal effect might tend to make the reaction coordinate lie on the convex side of the minimum energy path (sometimes called the "bobsled" effect), and, therefore, the two approximations might cancel out to some extent. Therefore,

it was believed that the validity of the VA approximation needed to be further evaluated for low temperatures, with the inclusion of curvature effects.

Wyatt[70] has studied curvilinear and angular momentum state effects on the rotating linear model for the H + H_2 reaction, within the VA approximation. He found that, at each energy, inclusion of reaction-path curvature lowers the reaction probability as does increasing the angular momentum quantum number. In other words, the zero-curvature approach predicts appreciable reaction at energies about 0.02-0.04 eV lower than models assuming vibrational adiabaticity, but not rectilinear motion. If this is indeed the case, the two effects would lead to partially compensating errors.

However, Marcus[71,72] pointed out that for the energy range below the VA barrier, the centrifugal effect can be negative, and cause the reaction coordinate to lie on the concave side of the minimum energy path. This amounts to corner-cutting, and confirms the expectations of McCullough and Wyatt,[12] who showed that an important reaction route for low energy particles is a diagonal cut across the center.

Russell and Light[73] also studied the effects of curvature on the reaction path, and noted that for low incident energies, the system must tunnel through an effective potential barrier that is higher than in the zero curvature approach. At higher energies, on the other hand, the curvature decreases the effective barrier. They also state that this effect is more pronounced for systems that involve an H atom transfer rather than a D or T atom transfer.

Since the effect of curvature is reversed for low temperatures versus high temperatures, the low T transmission coefficient will be lower for a tunnelling calculation that included curvature. Vice versa, κ will be higher at high temperatures than it is for a zero curvature calculation.

If this is indeed the case, the agreement of the low temperature VA transmission coefficients with the exact ones would get worse.

It wasn't until recently that probability current densities and streamlines for this reaction have confirmed the earlier predictions of corner cutting.[5,74] It seems therefore that the breakdown of the VA approximation is due mainly to tunnelling through a nonadiabatic portion of the potential energy surface, due to the failure of the separation of modes approximation.

The failure of one-dimensional theories at low energies has important implications for the future use of these calculations. At translational energies of 0.08-0.22 eV, the de Broglie wavelength for the relative motion of the H + H_2 is 1.2 to 1.6 Å, which is large compared to the range of internuclear distances near the saddle point over which the normal mode separation is valid.[66] The de Broglie wavelength for the heaviest system, THT, is still about 0.8 Å. In other words, at low energies, the separation of vibration and translation cannot be expected to be a good approximation, and a full treatment in two mathematical dimensions is necessary.

The correct formulation of the curvature correction is due to Marcus and Coltrin,[75] who developed a method that replaces the minimum energy path with a different path for which distances are shorter and the barrier thinner. The central idea of this work is that tunnelling is not along the reaction path, but rather along a curve that joins the points of maximum vibrational amplitude in the tranverse mode. This represents the system at the point when the bonds are stretched furthest, and is the shortest path to reaction.

This path has given the best fit to the quantum results for most hydrogenic systems.[76]

The breakdown of the VA approximation was verified by Bowman and co-workers,[77] who projected the exact scattering wavefunction onto the vibrational

levels along several cuts of the potential energy surface. At energies above the threshold region appreciable change of vibrational state is observed in the quantum reaction probabilities. This also violates the adiabatic approximation, especially for the region above the $v = 1$ vibrational level ($\sim$ 0.8 eV). However, in the region between the first and second thresholds, the reaction probability is greater for the reactive channel in which the vibrational quantum number is conserved, an indication of some adiabaticity.

In conclusion, the CVE approach deviates largely from the quantum mechanical approach; since this calculation is based on conservation of vibrational energy in the transverse mode as the system proceeds along the reaction path, one cannot expect it to accurately describe the dynamics of the reaction.

The VA model also fails to predict low energy reaction probabilities, by neglecting tunnelling in the nonadiabatic "corner" region of the potential energy surface. This results in too low a transmission coefficient at low temperatures.

C. Exact Isotope Effects

When an atom is replaced by one of its isotopes, there is no change in the potential energy surface for any reaction it might undergo: the reason there is a change in the rate is that there is a change in the average vibrational energy of the molecule and of the activated complex. The potential energy curve is the same, but the zero-point energies are different, meaning that H_2 , which has the highest vibrational frequency, will reach its dissociated state before HD or D_2 . The transition state expression is:

$$k^{TST} = \kappa \frac{kT}{h} \frac{Q^{\ddagger}}{Q_A Q_{BC}} e^{-E_b/kT}, \tag{77}$$

which, for the colinear case reduces to:

$$k^{TST} = \kappa \frac{kT}{h} \frac{Q^{vs}}{Q^{rel} Q^{v}} e^{-E_b/kT}, \tag{78}$$

where all but the frequency factor are mass dependent.

The isotope effects studied have been divided in four kinds. In the first, the effect of changing the reagent atom is studied. Four groups of reactions are identified: 1) H + H_2 , D + H_2 , T + H_2 ; 2) H + HD, D + HD, T + HD; 3) H + HT, D + HT, T + HT; 4) H + DH, D + DH.

The second set of reactions illustrates the effect of the end atom. In this category there are three groups of reactions: 1) H + H_2 , H + HD, H + HT; 2) D + H_2 , D + HD, D + HT; 3) T + H_2 , T + HD, T + HT.

The third effect to be considered is that of changing the middle atom, keeping the middle atom the same. Three examples can be found: 1) H + H_2 , H + DH, H + TH; 2) D + H_2 , D + DH; 3) H + HD, H + D_2 .

Finally there is a fourth category in which the reagent diatomic is turned around. The three cases are: 1) H + HD, H + DH; 2) H + HT, H + TH; 3) D + HD, D + DH.

The observed isotope effects for the quantum mechanical (QM), conventional transition state (TST), and the three one-dimensional models (CVE model, with parabolic fit, CVEp; VA model with parabolic fit, VAp; exact 1-D VA model, VA) are shown in Tables 15-27 for the cases mentioned above.

There are very few theories that try to explain the magnitudes of the isotope effects. Semiclassical isotope effects predictions can be made using the theories of Melander[55] and Westheimer.[68] They pointed out that for a symmetric reaction, isotopic substitution of the middle atom should have no effect on the vibrational frequency of the symmetric stretch. This is indeed the case for HHH, HDH and HTH in Table 1.

However, the imaginary frequency is isotope-dependent, and, since inclusion of the tunnelling corrections mentioned above is related to the reaction coordinate motion, κ will contain a contribution to the isotope effect.

For an unsymmetric system, on the other hand, the normal modes can no longer be referred to as symmetric or asymmetric; depending on the mass ratio, the middle atom will move in both normal vibrations.

Therefore both the real and imaginary frequencies can have an isotope effect.

Truhlar, Kuppermann and Adams calculated quantum mechanical probabilities and rate constants for the following isotopic systems: $H + H_2$, $D + H_2$, $H + D_2$ and $D + D_2$. Their results show the following trend: the larger the imaginary frequency the less steep the rise of the probability curve. Therefore the $H + H_2$ reaction has the least steep curve, and $D + D_2$ the steepest. This effect is in accord with expectations about tunnelling and nonclassical reflection at higher energies. Since the force constants don't vary significantly from one hydrogenic system to another (they increase by about 20 % as the skew angle is decreased), a higher frequency combined with a lower mass indicates more tunnelling at low energies.

The temperature dependence of the isotope effect can sometimes tell more than the magnitude itself. One cannot always expect a monotonic variation of $ln(k_1/k_2)$ with temperature. Often minima and maxima are observed in the dependence, especially in systems with small isotope effects.

An interpretation of the isotope effects observed in this work will be attempted in this section.

The results for the isotope effects in the reacting atom category (Tables 15-18) are very small, in the range of 1.7 to 0.3. For the first group of three reactions, the reactivity is as follows: $H > D \sim T$. Since transition state theory predicts the opposite trend, this effect can be entirely attributed to tunnelling. This is apparent also in the temperature dependence of the isotope effect, where the minimum is caused by low temperature tunnelling. A higher imaginary frequency

at the transition state signifies a higher probability of tunnelling; the frequency is decreased by the introduction of the heavy atom motion.

The next three groups in this category (Tables 16-18), show that T is more reactive than D, which is more reactive than H. The agreement with transition state theory is fairly good, an indication that the main contribution to the isotope effect comes from the difference in the symmetric stretch frequencies. In the two series the reactant zero point energy stays the same, while the ground vibrational level of the transition state is progressively lowered. The barrier changes from 0.2995 eV for H + HD to 0.2803 eV for D + HD, to 0.2724 eV for T + HD.

The end-atom isotope effects (Tables 19-21), are greater than the reacting atom ones. In all cases, having a hydrogen atom at the end accounts for a higher reactivity than having a deuterium or a tritium atom. The larger isotope effect in the case of the H + H_2 , H + HD and H + HT series is mostly due to the tunnelling contribution. Since TST predicts the correct trend, but smaller isotope effects than actually observed, the effect of changes in the zero point energies of both reactant and transition state, which results in a slightly higher barrier going from H + H_2 to H + HD to H + HT, is at least partially responsible for the trend observed. The barrier heights are 0.2815 eV, 0.2995 eV and 0.3058 eV for H + H_2 , H + HD and H + HT, respectively.

The series D + H_2 , HD, HT and T + H_2 , HD, HT are fairly well represented by conventional transition state theory. The exact transmission coefficients are very similar, and mostly cancel out. The barrier height increases down the D series, from 0.2638 eV to 0.2803 eV, to 0.2856 eV; the respective values for the T series are 0.2568 eV, 0.2724 eV and 0.2772 eV. These differences are believed to be responsible for the trend observed.

Middle-atom isotope effects are the largest in magnitude. In the series H + H_2 , H + DH , and H + TH , the imaginary frequency of the transition state drops

dramatically, while the symmetric stretch frequency is unchanged by middle atom substitution. The barrier is therefore raised as the reactant zero-point energy is decreased from H_2 to HD to HT: the barrier height for H + H_2 is 0.2815 eV, while for H + DH and H + TH it is 0.3173 eV and 0.3305 eV respectively. The tunnelling contribution is responsible for the effects being so large. A similar reasoning can be applied to the next two groups, D + H_2 , D + DH and H + HD and H + DD.

In the final category, two isotopes are substituted and the product diatomic is turned around. In all cases, the systems that have a hydrogen atom in the middle rather than a D or a T, are found to be more reactive. Conventional transition state theory more or less works as far as the observed trends are concerned, but the agreement in the magnitude of the isotope effects is poor. The basic difference in transition state zero-point energies accounts for the difference in reactivity. The symmetric HTH and HDH transition states have a higher stretching frequency than the HHT or the HHD cases. Also DDH has a higher stretching frequency than DHD.

D. Approximate Isotope Effects

The results for the H, D, T, + H_2 series are summarized in Table 15 and shown in Figure 60. Conventional transition state theory completely fails to predict the reactivity scale and the temperature dependence of the isotope effect. Using the VA correction doesn't improve the prediction of TST. It is somewhat surprising to see that the CVE approximation with parabolic fit to the barrier comes fairly close to the quantum results. It is also interesting to notice that whenever a model fails to predict the correct reactivity, it also fails in predicting the temperature dependence. Since the CVE barriers are essentially the same for all isotopic systems, (the zero-point energies of both the reactant and the transition state are neglected), the only difference in the predicted tunnelling is the reduced mass. The CVE approach tends

to overestimate the tunnelling correction for all cases, but partial cancellation of errors seems to occur for this series of reactions.

The results for the series H, D, T + HD (Table 16, Figure 61) and H, D, T + HT (Table 17, Figure 62) show surprisingly good agreement between the exact and the conventional transition state results. TST reproduces the kinetic isotope effect better than any of its corrected versions. Inspection of the rate constant tables shows very similar values of κ^{ex}, which very nearly cancel in the ratios. The CVE parabolic approximation fails badly in every case, while the VA model predicts the isotope effect trend correctly, but not the magnitude.

For the reactions H, D + DH, (Table 18, Figure 63) the VA approximation is closest to the exact results. Although the transmission coefficients are smaller than the exact ones, their relative magnitudes is similar.

All approximate models predict the reactivity scale and the temperature dependence of the isotope effect correctly for the end-atom isotope effects. Much smaller effects are predicted by conventional TST and the VA approximation, while the CVE approximation comes surprisingly close. It seems that, despite the excessive tunnelling observed through the CVE barrier, partial cancellation of errors occurs for the case of H + H_2 (Table 19, Figure 64).

In the next two series, D + H_2 , HD, HT (Table 20, Figure 65) and T + H_2 , HD, HT (Table 21, Figure 66), conventional TST comes closer than any of its corrected versions again.

The group of reactions that follow differs in the middle atom. For the series H + H_2 , H + DH , H + TH (Table 22, Figure 67), all of the approximate theories predict the reactivity scale correctly, but the magnitudes are wrong. The CVE model overestimates the isotope effect, while conventional transition state theory and TST with the VA correction underestimate the effect.

The next two groups of middle-atom isotope effects (Tables 23, 24, Figure 68, 69) show that the vibrationally adiabatic approximation improves the results of conventional transition state theory as far as the isotope effects are concerned.

Results for the fourth category (Tables 25-27, Figure 70-72) show all three corrections to TST to be incorrect. Conventional TST does a better job of reproducing the quantum results than the CVE of the VA approximation.

It might be worth to point out that the only cases for which the VA approximation predicts good isotope effects are those that include the HDD system as one of the two reactions The inclusion of heavier species might be responsible for a more adiabatic behavior. This is mostly speculative, and more reactions involving at least two of the heavier species have to be studied.

VI. SUMMARY

Exact colinear reaction probabilities and rate constants have been calculated for thirteen hydrogenic systems, using the method of hyperspherical coordinates. The results have been compared with the predictions of conventional transition state theory and transition state theory with tunnelling correction obtained using one-dimensional barriers. It was found that, although the vibrationally adiabatic method yields rate constants that are closer to the exact quantum results, it fails to predict isotope effects accurately. With the exception of the H_3 system, conventional TST leads to partial cancellation of errors in the isotope effects, while attempts to include the tunnelling correction worsen the predicted rate constant ratios. The failure of the CVE approximation comes as no surprise, since this method neglects zero-point energy contributions. The VA approximation fails to predict isotope ratios for light species, due to its neglect of tunnelling through the corner region of the potential energy surface.

It must be observed, however, that the VA approximation, in conjunction with the Marcus-Coltrin path has given results that are in very good agreement with both colinear[76] and 3-D[78] quantum mechanical calculations. The three-dimensional TST results with VA-MC corrections have also predicted isotope effects that are in good agreement with experimental findings.[79–84]

TABLE 1. Normal Mode Zero-Point Energies for the Transition State

TRANSITION STATE	E^{0s} (eV)	E^{0a} (eV)
HHH	0.1269	$0.0927i$
HHD	0.1092	$0.0880i$
HHT	0.1022	$0.0864i$
DHD	0.0899	$0.0847i$
DHT	0.0820	$0.0831i$
THT	0.0736	$0.0818i$
HDH	0.1269	$0.0757i$
HTH	0.1269	$0.0692i$
DDH	0.1091	$0.0696i$

TABLE 2. Comparison of Exact Quantum and Transition State Theory Thermal Rate Constants and Transmission Coefficients[a]

REACTION	T(K)	k(T) QM	TST	κ^{ex}	κ^{CVE}_{par}	κ^{VA}_{par}	κ^{VA}
$H+H_2$	200	1.56×10^{-1}	5.07×10^{-3}	30.8	[b]	2.76	2.01
	300	5.00	1.44	3.47	19.7	1.48	1.18
	400	5.48×10^{1}	2.52×10^{1}	2.17	3.52	1.24	1.04
	500	2.53×10^{2}	1.45×10^{2}	1.74	2.05	1.14	0.99
	600	7.26×10^{2}	4.74×10^{2}	1.53	1.61	1.10	0.97
	700	1.57×10^{3}	1.12×10^{3}	1.40	1.40	1.07	0.96
	800	2.85×10^{3}	2.17×10^{3}	1.31	1.29	1.05	0.96
	900	4.56×10^{3}	3.68×10^{3}	1.24	1.22	1.04	0.96
	1000	6.69×10^{3}	5.66×10^{3}	1.18	1.17	1.03	0.96
	1100	9.20×10^{3}	8.11×10^{3}	1.13	1.14	1.03	0.95
	1200	1.21×10^{4}	1.10×10^{4}	1.10	1.12	1.02	0.95
	1300	1.52×10^{4}	1.44×10^{4}	1.06	1.10	1.02	0.94
	1400	1.86×10^{4}	1.82×10^{4}	1.02	1.08	1.02	0.94
	1500	2.22×10^{4}	2.24×10^{4}	0.99	1.07	1.01	0.93
	1600	2.59×10^{4}	2.70×10^{4}	0.96	1.06	1.01	0.92

a) Rate constants in cm molecule^{-1} sec^{-1}.

b) Coefficient is too large to be meaningful.

TABLE 3. Comparison of Exact Quantum and Transition State Theory Thermal Rate Constants and Transmission Coefficients[a]

REACTION	T(K)	k(T) QM	TST	κ^{ex}	κ^{CVE}_{par}	κ^{VA}_{par}	κ^{VA}
H+HD	200	1.32×10^{-2}	1.67×10^{-3}	7.90	5104	2.21	3.59
	300	1.79	0.67	2.67	11.0	1.37	1.84
	400	2.58×10^{1}	1.41×10^{1}	1.83	2.82	1.19	1.46
	500	1.37×10^{2}	9.01×10^{1}	1.52	1.83	1.12	1.31
	600	4.30×10^{2}	3.17×10^{2}	1.36	1.49	1.08	1.23
	700	9.93×10^{2}	7.94×10^{2}	1.25	1.33	1.06	1.18
	800	1.88×10^{3}	1.60×10^{3}	1.18	1.24	1.04	1.14
	900	3.12×10^{3}	2.81×10^{3}	1.11	1.19	1.03	1.12
	1000	4.70×10^{3}	4.44×10^{3}	1.06	1.15	1.03	1.10
	1100	6.60×10^{3}	6.52×10^{3}	1.01	1.12	1.02	1.08
	1200	8.79×10^{3}	9.05×10^{3}	0.97	1.10	1.02	1.07
	1300	1.12×10^{4}	1.20×10^{4}	0.93	1.08	1.02	1.05
	1400	1.39×10^{4}	1.54×10^{4}	0.90	1.07	1.01	1.04
	1500	1.67×10^{4}	1.92×10^{4}	0.87	1.06	1.01	1.03
	1600	1.96×10^{4}	2.33×10^{4}	0.84	1.05	1.01	1.01

a) Rate constants in cm molecule^{-1} sec^{-1}.

TABLE 4. Comparison of Exact Quantum and Transition State Theory Thermal Rate Constants and Transmission Coefficients[a]

REACTION	T(K)	k(T) QM	TST	κ^{ex}	κ^{CVE}_{par}	κ^{VA}_{par}	κ^{VA}
$D+H_2$	200	9.15×10^{-2}	1.16×10^{-2}	7.89	5105	2.21	3.59
	300	6.17	2.33	2.65	11.0	1.34	1.84
	400	6.31×10^{1}	3.45×10^{1}	1.83	2.82	1.19	1.46
	500	2.72×10^{2}	1.79×10^{2}	1.52	1.83	1.12	1.31
	600	7.45×10^{2}	5.49×10^{2}	1.36	1.49	1.08	1.23
	700	1.56×10^{3}	1.25×10^{3}	1.25	1.33	1.06	1.18
	800	2.74×10^{3}	2.34×10^{3}	1.17	1.24	1.04	1.14
	900	4.29×10^{3}	3.87×10^{3}	1.11	1.19	1.03	1.12
	1000	6.19×10^{3}	5.85×10^{3}	1.06	1.15	1.03	1.10
	1100	8.38×10^{3}	8.28×10^{3}	1.01	1.12	1.02	1.08
	1200	1.08×10^{4}	1.12×10^{4}	0.96	1.10	1.02	1.07
	1300	1.35×10^{4}	1.44×10^{4}	0.94	1.08	1.02	1.05
	1400	1.64×10^{4}	1.81×10^{4}	0.91	1.07	1.01	1.04
	1500	1.93×10^{4}	2.22×10^{4}	0.87	1.06	1.01	1.03
	1600	2.24×10^{4}	2.66×10^{4}	0.84	1.05	1.01	1.01

a) Rate constants in cm molecule^{-1} sec^{-1}.

TABLE 5. Comparison of Exact Quantum and Transition State Theory Thermal Rate Constants and Transmission Coefficients[a]

REACTION	T(K)	k(T) QM	TST	κ^{ex}	κ^{CVE}_{par}	κ^{VA}_{par}	κ^{VA}
H+HT	200	6.62×10^{-3}	1.13×10^{-3}	5.86	3068	2.03	4.20
	300	1.12	0.51	2.20	8.69	1.33	2.05
	400	1.79×10^{1}	1.14×10^{1}	1.57	2.59	1.17	1.59
	500	1.01×10^{2}	7.58×10^{1}	1.33	1.75	1.10	1.39
	600	3.31×10^{2}	2.74×10^{2}	1.21	1.45	1.07	1.29
	700	7.85×10^{2}	6.99×10^{2}	1.12	1.31	1.05	1.23
	800	1.52×10^{3}	1.44×10^{3}	1.06	1.22	1.04	1.19
	900	2.56×10^{3}	2.54×10^{3}	1.01	1.17	1.03	1.15
	1000	3.90×10^{3}	4.07×10^{3}	0.96	1.14	1.02	1.13
	1100	5.53×10^{3}	6.02×10^{3}	0.92	1.11	1.02	1.11
	1200	7.42×10^{3}	8.41×10^{3}	0.88	1.09	1.02	1.09
	1300	9.53×10^{3}	1.12×10^{4}	0.85	1.08	1.01	1.07
	1400	1.18×10^{4}	1.45×10^{4}	0.81	1.07	1.01	1.06
	1500	1.43×10^{4}	1.81×10^{4}	0.79	1.06	1.01	1.04
	1600	1.68×10^{4}	2.21×10^{4}	0.76	1.05	1.01	1.03

a) Rate constants in cm molecule^{-1} sec^{-1}.

TABLE 6. Comparison of Exact Quantum and Transition State Theory Thermal Rate Constants[a]

REACTION	T(K)	k(T) QM	TST	κ^{ex}	κ_{par}^{CVE}	κ_{par}^{VA}	κ^{VA}
T+H_2	200	9.28×10^{-2}	1.58×10^{-2}	5.86	3068	2.03	4.20
	300	6.09	2.79	2.18	8.69	1.33	2.05
	400	6.07×10^{1}	3.86×10^{1}	1.57	2.59	1.17	1.59
	500	2.57×10^{2}	1.93×10^{2}	1.33	1.75	1.10	1.39
	600	6.97×10^{2}	5.77×10^{2}	1.21	1.45	1.07	1.29
	700	1.45×10^{3}	1.29×10^{3}	1.12	1.31	1.05	1.23
	800	2.53×10^{3}	2.39×10^{3}	1.06	1.22	1.04	1.19
	900	3.94×10^{3}	3.92×10^{3}	1.01	1.17	1.03	1.15
	1000	5.66×10^{3}	5.89×10^{3}	0.96	1.14	1.02	1.13
	1100	7.64×10^{3}	8.30×10^{3}	0.92	1.11	1.02	1.11
	1200	9.84×10^{3}	1.11×10^{4}	0.89	1.09	1.02	1.09
	1300	1.22×10^{4}	1.44×10^{4}	0.85	1.08	1.01	1.07
	1400	1.48×10^{4}	1.80×10^{4}	0.82	1.07	1.01	1.06
	1500	1.74×10^{4}	2.20×10^{4}	0.79	1.06	1.01	1.04
	1600	2.02×10^{4}	2.64×10^{4}	0.77	1.05	1.01	1.03

a) Rate constants in cm molecule^{-1} sec^{-1}.

TABLE 7. Comparison of Exact Quantum and Transition State Theory Thermal Rate Constants and Transmission Coefficients[a]

REACTION	T(K)	k(T) QM	TST	κ^{ex}	κ^{CVE}_{par}	κ^{VA}_{par}	κ^{VA}
D+HD	200	3.19×10^{-2}	4.05×10^{-3}	7.88	1334	1.79	1.12
	300	3.30	1.12	2.95	6.28	1.27	0.93
	400	3.99×10^{1}	1.96×10^{1}	2.04	2.30	1.14	0.90
	500	1.88×10^{2}	1.12×10^{2}	1.68	1.64	1.09	0.90
	600	5.43×10^{2}	3.71×10^{2}	1.46	1.39	1.06	0.91
	700	1.18×10^{3}	8.87×10^{2}	1.33	1.27	1.04	0.91
	800	2.12×10^{3}	1.74×10^{3}	1.22	1.20	1.03	0.92
	900	3.38×10^{3}	2.97×10^{3}	1.14	1.15	1.03	0.92
	1000	4.92×10^{3}	4.62×10^{3}	1.06	1.12	1.02	0.93
	1100	6.72×10^{3}	6.69×10^{3}	1.00	1.10	1.02	0.93
	1200	8.73×10^{3}	9.19×10^{3}	0.95	1.08	1.01	0.93
	1300	1.09×10^{4}	1.21×10^{4}	0.90	1.07	1.01	0.93
	1400	1.32×10^{4}	1.54×10^{4}	0.86	1.06	1.01	0.92
	1500	1.56×10^{4}	1.91×10^{4}	0.82	1.05	1.01	0.92
	1600	1.81×10^{4}	2.31×10^{4}	0.78	1.05	1.01	0.92

a) Rate constants in cm molecule^{-1} sec^{-1}.

TABLE 8. Comparison of Exact Quantum and Transition State Theory Thermal Rate Constants and Transmission Coefficients[a]

REACTION	T(K)	k(T) QM	TST	κ^{ex}	κ^{CVE}_{par}	κ^{VA}_{par}	κ^{VA}
D+HT	200	1.96×10^{-2}	2.83×10^{-3}	6.96	680	1.65	2.11
	300	2.41	0.87	2.77	5.04	1.23	1.45
	400	3.12×10^{1}	1.60×10^{1}	1.95	2.12	1.12	1.27
	500	1.53×10^{2}	9.51×10^{1}	1.61	1.57	1.08	1.19
	600	4.52×10^{2}	3.21×10^{2}	1.41	1.35	1.05	1.14
	700	9.92×10^{2}	7.84×10^{2}	1.27	1.25	1.04	1.11
	800	1.81×10^{3}	1.56×10^{3}	1.16	1.18	1.03	1.09
	900	2.89×10^{3}	2.70×10^{3}	1.07	1.14	1.02	1.07
	1000	4.23×10^{3}	4.24×10^{3}	1.00	1.11	1.02	1.06
	1100	5.79×10^{3}	6.20×10^{3}	0.93	1.09	1.02	1.05
	1200	7.53×10^{3}	8.57×10^{3}	0.88	1.08	1.01	1.04
	1300	9.41×10^{3}	1.14×10^{4}	0.83	1.06	1.01	1.03
	1400	1.14×10^{4}	1.45×10^{4}	0.79	1.05	1.01	1.02
	1500	1.34×10^{4}	1.81×10^{4}	0.74	1.05	1.01	1.01
	1600	1.55×10^{4}	2.20×10^{4}	0.70	1.04	1.01	1.00

a) Rate constants in cm molecule^{-1} sec^{-1}.

TABLE 9. Comparison of Exact Quantum and Transition State Theory Thermal Rate Constants and Transmission Coefficients[a]

REACTION	T(K)	k(T) QM	TST	κ^{ex}	κ^{CVE}_{par}	κ^{VA}_{par}	κ^{VA}
T+HD	200	3.97×10^{-2}	5.74×10^{-3}	6.92	680	1.65	2.11
	300	3.78	1.37	2.76	5.04	1.23	1.45
	400	4.32×10^{1}	2.21×10^{1}	1.95	2.12	1.12	1.27
	500	1.96×10^{2}	1.22×10^{2}	1.61	1.57	1.08	1.19
	600	5.50×10^{2}	3.91×10^{2}	1.41	1.35	1.05	1.14
	700	1.16×10^{3}	9.20×10^{2}	1.26	1.25	1.04	1.11
	800	2.06×10^{3}	1.78×10^{3}	1.16	1.18	1.03	1.09
	900	3.24×10^{3}	3.02×10^{3}	1.07	1.14	1.02	1.07
	1000	4.66×10^{3}	4.67×10^{3}	1.00	1.11	1.02	1.06
	1100	6.30×10^{3}	6.73×10^{3}	0.94	1.09	1.02	1.05
	1200	8.10×10^{3}	9.21×10^{3}	0.88	1.08	1.01	1.04
	1300	1.00×10^{4}	1.21×10^{4}	0.83	1.06	1.01	1.03
	1400	1.21×10^{4}	1.54×10^{4}	0.79	1.05	1.01	1.02
	1500	1.42×10^{4}	1.90×10^{4}	0.75	1.05	1.01	1.01
	1600	1.63×10^{4}	2.30×10^{4}	0.71	1.04	1.01	1.00

a) Rate constants in cm molecule^{-1} sec^{-1}.

TABLE 10. Comparison of Exact Quantum and Transition State Theory Thermal Rate Constants and Transmission Coefficients[a]

REACTION	T(K)	k(T) QM	TST	κ^{ex}	κ^{CVE}_{par}	κ^{VA}_{par}	κ^{VA}
T+HT	200	2.70×10^{-2}	4.08×10^{-3}	6.62	311	1.52	0.81
	300	2.98	1.06	2.81	4.06	1.19	0.79
	400	3.59×10^{1}	1.81×10^{1}	1.98	1.95	1.10	0.81
	500	1.67×10^{2}	1.03×10^{2}	1.62	1.50	1.06	0.83
	600	4.75×10^{2}	3.40×10^{2}	1.40	1.31	1.04	0.85
	700	1.01×10^{3}	8.14×10^{2}	1.24	1.22	1.03	0.86
	800	1.80×10^{3}	1.60×10^{3}	1.13	1.16	1.02	0.87
	900	2.83×10^{3}	2.75×10^{3}	1.03	1.12	1.02	0.88
	1000	4.07×10^{3}	4.29×10^{3}	0.95	1.10	1.02	0.89
	1100	5.49×10^{3}	6.24×10^{3}	0.88	1.08	1.01	0.90
	1200	7.05×10^{3}	8.60×10^{3}	0.82	1.07	1.01	0.90
	1300	8.70×10^{3}	1.14×10^{4}	0.76	1.06	1.01	0.90
	1400	1.04×10^{4}	1.45×10^{4}	0.72	1.05	1.01	0.90
	1500	1.22×10^{4}	1.80×10^{4}	0.68	1.04	1.01	0.90
	1600	1.39×10^{4}	2.19×10^{4}	0.63	1.04	1.01	0.90

a) Rate constants in cm molecule^{-1} sec^{-1}.

TABLE 11. Comparison of Exact Quantum and Transition State Theory Thermal Rate Constants and Transmission Coefficients[a]

REACTION	T(K)	k(T) QM	TST	κ^{ex}	κ^{CVE}_{par}	κ^{VA}_{par}	κ^{VA}
H+DH	200	6.26×10^{-3}	5.99×10^{-4}	10.5	1364	3.12	3.43
	300	1.01	0.34	2.97	6.33	1.54	1.62
	400	1.65×10^{1}	8.43	1.96	2.31	1.26	1.30
	500	9.56×10^{1}	5.95×10^{1}	1.61	1.64	1.16	1.18
	600	3.20×10^{2}	2.23×10^{2}	1.43	1.40	1.11	1.12
	700	7.75×10^{2}	5.85×10^{2}	1.32	1.27	1.08	1.08
	800	1.53×10^{3}	1.22×10^{3}	1.25	1.20	1.06	1.06
	900	2.62×10^{3}	2.18×10^{3}	1.20	1.15	1.05	1.05
	1000	4.07×10^{3}	3.51×10^{3}	1.16	1.12	1.04	1.03
	1100	5.87×10^{3}	5.22×10^{3}	1.12	1.10	1.03	1.02
	1200	8.02×10^{3}	7.32×10^{3}	1.10	1.08	1.03	1.01
	1300	1.05×10^{4}	9.80×10^{3}	1.07	1.07	1.02	1.00
	1400	1.32×10^{4}	1.26×10^{4}	1.05	1.06	1.02	0.99
	1500	1.62×10^{4}	1.58×10^{4}	1.03	1.05	1.02	0.98
	1600	1.94×10^{4}	1.93×10^{4}	1.01	1.05	1.01	0.97

a) Rate constants in cm molecule^{-1} sec^{-1}.

TABLE 12. Comparison of Exact Quantum and Transition State Theory Thermal Rate Constants and Transmission Coefficients[a]

REACTION	T(K)	k(T) QM	TST	κ^{ex}	κ^{CVE}_{par}	κ^{VA}_{par}	κ^{VA}
H+TH	200	2.45×10^{-3}	2.70×10^{-4}	9.07	407	3.07	3.72
	300	0.53	0.20	2.65	4.35	1.53	1.70
	400	1.02×10^{1}	5.56	1.83	2.01	1.26	1.34
	500	6.47×10^{1}	4.24×10^{1}	1.53	1.52	1.16	1.21
	600	2.30×10^{2}	1.68×10^{2}	1.37	1.33	1.10	1.14
	700	5.82×10^{2}	4.55×10^{2}	1.28	1.23	1.08	1.10
	800	1.19×10^{3}	9.74×10^{2}	1.22	1.17	1.06	1.08
	900	2.09×10^{3}	1.78×10^{3}	1.17	1.13	1.04	1.06
	1000	3.32×10^{3}	2.91×10^{3}	1.14	1.10	1.04	1.04
	1100	4.88×10^{3}	4.39×10^{3}	1.11	1.08	1.03	1.03
	1200	6.77×10^{3}	6.22×10^{3}	1.09	1.07	1.02	1.02
	1300	8.95×10^{3}	8.40×10^{3}	1.07	1.06	1.02	1.01
	1400	1.14×10^{4}	1.09×10^{4}	1.05	1.05	1.02	1.00
	1500	1.42×10^{4}	1.37×10^{4}	1.04	1.04	1.02	0.99
	1600	1.71×10^{4}	1.69×10^{4}	1.01	1.04	1.01	0.98

a) Rate constants in cm molecule^{-1} sec^{-1}.

TABLE 13. Comparison of Exact Quantum and Transition State Theory Thermal Rate Constants and Transmission Coefficients[a]

REACTION	T(K)	k(T) QM	TST	κ^{ex}	κ^{CVE}_{par}	κ^{VA}_{par}	κ^{VA}
D+DH	200	8.29×10^{-3}	1.33×10^{-3}	6.23	315	2.43	2.95
	300	1.20	0.53	2.25	4.07	1.42	1.56
	400	1.81×10^{1}	1.12×10^{1}	1.62	1.96	1.21	1.28
	500	9.85×10^{1}	7.14×10^{1}	1.38	1.50	1.13	1.17
	600	3.15×10^{2}	2.51×10^{2}	1.25	1.32	1.09	1.12
	700	7.40×10^{2}	6.29×10^{2}	1.18	1.22	1.06	1.08
	800	1.42×10^{3}	1.27×10^{3}	1.12	1.16	1.05	1.06
	900	2.40×10^{3}	2.23×10^{3}	1.08	1.13	1.04	1.05
	1000	3.66×10^{3}	3.52×10^{3}	1.04	1.10	1.03	1.04
	1100	5.22×10^{3}	5.17×10^{3}	1.01	1.08	1.02	1.02
	1200	7.04×10^{3}	7.17×10^{3}	0.98	1.07	1.02	1.01
	1300	9.11×10^{3}	9.52×10^{3}	0.96	1.06	1.02	1.01
	1400	1.14×10^{4}	1.22×10^{4}	0.93	1.05	1.02	1.00
	1500	1.39×10^{4}	1.52×10^{4}	0.91	1.04	1.01	0.99
	1600	1.65×10^{4}	1.85×10^{4}	0.89	1.04	1.01	0.98

a) Rate constants in cm molecule^{-1} sec^{-1}.

TABLE 14. Comparison of Exact Quantum and Transition State Theory Thermal Rate Constants and Transmission Coefficients[a]

REACTION	T(K)	k(T) QM	TST	κ^{ex}	κ^{CVE}_{par}	κ^{VA}_{par}	κ^{VA}
$H+D_2$	200	8.53×10^{-4}	1.37×10^{-4}	6.23	315	2.43	2.95
	300	0.28	0.13	2.15	4.07	1.42	1.56
	400	6.41	3.97	1.61	1.96	1.21	1.28
	500	4.47×10^{1}	3.25×10^{1}	1.38	1.50	1.13	1.17
	600	1.69×10^{2}	1.35×10^{2}	1.25	1.32	1.09	1.12
	700	4.46×10^{2}	3.79×10^{2}	1.18	1.22	1.06	1.08
	800	9.35×10^{2}	8.36×10^{2}	1.12	1.16	1.05	1.06
	900	1.68×10^{3}	1.56×10^{3}	1.08	1.13	1.04	1.05
	1000	2.70×10^{3}	2.60×10^{3}	1.04	1.10	1.03	1.04
	1100	4.01×10^{3}	3.99×10^{3}	1.01	1.08	1.02	1.02
	1200	5.59×10^{3}	5.72×10^{3}	0.98	1.07	1.02	1.01
	1300	7.43×10^{3}	7.81×10^{3}	0.95	1.06	1.02	1.01
	1400	9.49×10^{3}	1.02×10^{4}	0.93	1.05	1.02	1.00
	1500	1.17×10^{4}	1.30×10^{4}	0.90	1.04	1.01	0.99
	1600	1.42×10^{4}	1.61×10^{4}	0.88	1.04	1.01	0.98

a) Rate constants in cm molecule^{-1} sec^{-1}.

TABLE 15. Isotope Effects for the Reactions: 1) H + H_2; 2) D + H_2; 3) T + H_2

T(K)	k_1/k_2 (QM)	k_1/k_2 (TST)	k_1/k_2 (CVEp)	k_1/k_2 (VAp)	k_1/k_2 (VA)	k_1/k_3 (QM)	k_1/k_3 (TST)	k_1/k_3 (CVEp)	k_1/k_3 (VAp)	k_1/k_3 (VA)	k_2/k_3 (QM)	k_2/k_3 (TST)	k_2/k_3 (CVEp)	k_2/k_3 (VAp)	k_2/k_3 (VA)
200	1.70	0.44	1.30	0.55	0.25	1.68	0.32	1.58	0.43	0.15	0.99	0.73	1.21	0.80	0.62
400	0.87	0.73	0.91	0.76	0.52	0.90	0.65	0.88	0.69	0.43	1.04	0.89	0.97	0.91	0.82
900	1.06	0.95	0.98	0.96	0.81	1.16	0.94	0.98	0.95	0.79	1.09	0.99	1.00	0.99	0.96
1600	1.16	1.02	1.03	1.02	0.91	1.28	1.02	1.03	1.02	0.89	1.11	1.01	1.00	1.00	0.99

TABLE 16. Isotope Effects for the Reactions: 1) H + HD; 2) D + HD; 3) T + HD

T(K)	k_1/k_2 (QM)	k_1/k_2 (TST)	k_1/k_2 (CVEp)	k_1/k_2 (VAp)	k_1/k_2 (VA)	k_1/k_3 (QM)	k_1/k_3 (TST)	k_1/k_3 (CVEp)	k_1/k_3 (VAp)	k_1/k_3 (VA)	k_2/k_3 (QM)	k_2/k_3 (TST)	k_2/k_3 (CVEp)	k_2/k_3 (VAp)	k_2/k_3 (VA)
200	0.41	0.41	1.57	0.50	1.35	0.33	0.29	2.18	0.39	0.51	0.80	0.71	1.39	0.77	0.38
400	0.65	0.72	0.89	0.75	1.17	0.60	0.64	0.85	0.68	0.74	0.92	0.89	0.97	0.91	0.63
900	0.92	0.95	0.98	0.96	1.16	0.96	0.93	0.97	0.94	0.97	1.04	0.98	0.99	0.98	0.84
1600	1.08	1.01	1.02	1.01	1.11	1.20	1.01	1.02	1.01	1.02	1.11	1.00	1.00	1.00	0.92

TABLE 17. Isotope Effects for the Reactions: 1) H + HT; 2) D + HT; 3) T + HT

T(K)	k_1/k_2 (QM)	k_1/k_2 (TST)	k_1/k_2 (CVEp)	k_1/k_2 (VAp)	k_1/k_2 (VA)	k_1/k_3 (QM)	k_1/k_3 (TST)	k_1/k_3 (CVEp)	k_1/k_3 (VAp)	k_1/k_3 (VA)	k_2/k_3 (QM)	k_2/k_3 (TST)	k_2/k_3 (CVEp)	k_2/k_3 (VAp)	k_2/k_3 (VA)
200	0.34	0.40	1.80	0.49	0.80	0.25	0.28	2.76	0.37	1.45	0.73	0.69	1.51	0.75	1.80
400	0.57	0.71	0.87	0.74	0.89	0.50	0.63	0.84	0.67	1.24	0.87	0.88	0.96	0.90	1.41
900	0.89	0.94	0.97	0.95	1.01	0.90	0.92	0.96	0.93	1.20	1.02	0.98	0.99	0.98	1.19
1600	1.08	1.00	1.01	1.00	1.03	1.21	1.01	1.02	1.00	1.17	1.12	1.00	1.00	1.00	1.11

TABLE 18. Isotope Effects for the Reactions: 1) H + DH; 2) D + DH

T(K)	k_1/k_2 (QM)	k_1/k_2 (TST)	k_1/k_2 (CVEp)	k_1/k_2 (VAp)	k_1/k_2 (VA)
200	0.76	0.45	1.95	0.58	0.52
400	0.91	0.75	0.88	0.78	0.76
900	1.09	0.98	1.00	0.99	0.98
1600	1.18	1.04	1.05	1.04	1.03

TABLE 19. Isotope Effects for the Reactions: 1) H + H_2; 2) H + HD; 3) H + HT

T(K)	k_1/k_2 (QM)	k_1/k_2 (TST)	k_1/k_2 (CVEp)	k_1/k_2 (VAp)	k_1/k_2 (VA)	k_1/k_3 (QM)	k_1/k_3 (TST)	k_1/k_3 (CVEp)	k_1/k_3 (VAp)	k_1/k_3 (VA)	k_2/k_3 (QM)	k_2/k_3 (TST)	k_2/k_3 (CVEp)	k_2/k_3 (VAp)	k_2/k_3 (VA)
200	11.8	3.04	9.00	3.80	1.70	23.6	4.49	22.1	6.09	2.15	1.99	1.48	2.46	1.61	1.27
400	2.12	1.79	2.23	1.86	1.28	3.06	2.21	3.00	2.34	1.45	1.44	1.24	1.35	1.26	1.14
900	1.46	1.31	1.35	1.32	1.12	1.78	1.45	1.51	1.46	1.21	1.22	1.11	1.13	1.11	1.08
1600	1.32	1.16	1.17	1.16	1.06	1.54	1.22	1.23	1.22	1.09	1.17	1.05	1.05	1.05	1.03

TABLE 20. Isotope Effects for the Reactions: 1) D + H_2; 2) D + HD; 3) D + HT

T(K)	k_1/k_2 (QM)	k_1/k_2 (TST)	k_1/k_2 (CVEp)	k_1/k_2 (VAp)	k_1/k_2 (VA)	k_1/k_3 (QM)	k_1/k_3 (TST)	k_1/k_3 (CVEp)	k_1/k_3 (VAp)	k_1/k_3 (VA)	k_2/k_3 (QM)	k_2/k_3 (TST)	k_2/k_3 (CVEp)	k_2/k_3 (VAp)	k_2/k_3 (VA)
200	2.87	2.86	10.9	3.53	9.17	4.67	4.10	30.8	5.49	6.98	1.63	1.43	2.81	1.55	0.76
400	1.58	1.76	2.16	1.83	2.86	2.02	2.16	2.87	2.29	2.48	1.28	1.23	1.33	1.25	0.87
900	1.27	1.30	1.34	1.31	1.58	1.48	1.43	1.49	1.45	1.50	1.17	1.10	1.11	1.10	0.95
1600	1.24	1.15	1.16	1.15	1.26	1.45	1.21	1.22	1.21	1.22	1.17	1.05	1.05	1.05	0.97

TABLE 21. Isotope Effects for the Reactions: 1) T + H_2; 2) T + HD; 3) T + HT

T(K)	k_1/k_2 (QM)	k_1/k_2 (TST)	k_1/k_2 (CVEp)	k_1/k_2 (VAp)	k_1/k_2 (VA)	k_1/k_3 (QM)	k_1/k_3 (TST)	k_1/k_3 (CVEp)	k_1/k_3 (VAp)	k_1/k_3 (VA)	k_2/k_3 (QM)	k_2/k_3 (TST)	k_2/k_3 (CVEp)	k_2/k_3 (VAp)	k_2/k_3 (VA)
200	2.34	2.75	12.4	3.39	5.47	3.44	3.87	38.2	5.17	20.1	1.47	1.41	3.08	1.53	3.67
400	1.41	1.75	2.14	1.83	2.19	1.69	2.13	2.83	2.26	4.18	1.20	1.22	1.33	1.24	1.91
900	1.22	1.30	1.34	1.31	1.40	1.39	1.43	1.49	1.45	1.87	1.14	1.10	1.11	1.10	1.34
1600	1.24	1.15	1.16	1.15	1.18	1.45	1.21	1.23	1.21	1.38	1.17	1.05	1.05	1.05	1.17

TABLE 22. Isotope Effects for the Reactions: 1) H + H_2; 2) H + DH; 3) H + TH

T(K)	k_1/k_2 (QM)	k_1/k_2 (TST)	k_1/k_2 (CVEp)	k_1/k_2 (VAp)	k_1/k_2 (VA)	k_1/k_3 (QM)	k_1/k_3 (TST)	k_1/k_3 (CVEp)	k_1/k_3 (VAp)	k_1/k_3 (VA)	k_2/k_3 (QM)	k_2/k_3 (TST)	k_2/k_3 (CVEp)	k_2/k_3 (VAp)	k_2/k_3 (VA)
200	24.9	8.46	93.8	7.47	4.96	63.7	18.8	698	16.9	10.2	2.56	2.22	7.44	2.26	2.05
400	3.32	2.99	4.56	2.93	2.39	5.37	4.53	7.94	4.45	3.52	1.62	1.52	1.75	1.52	1.47
900	1.74	1.69	1.79	1.68	1.54	2.18	2.07	2.24	2.06	1.87	1.25	1.22	1.25	1.22	1.21
1600	1.34	1.40	1.42	1.39	1.33	1.51	1.60	1.64	1.60	1.50	1.13	1.14	1.15	1.14	1.13

TABLE 23. Isotope Effects for the Reactions: 1) D + H_2; 2) D + DH

T(K)	k_1/k_2 (QM)	k_1/k_2 (TST)	k_1/k_2 (CVEp)	k_1/k_2 (VAp)	k_1/k_2 (VA)
200	11.0	8.72	141	7.94	10.6
400	3.49	3.08	4.44	3.03	3.51
900	1.79	1.74	1.83	1.73	1.86
1600	1.36	1.44	1.46	1.44	1.48

TABLE 24. Isotope Effects for the Reactions: 1) H + HD; 2) H + D_2

T(K)	k_1/k_2 (QM)	k_1/k_2 (TST)	k_1/k_2 (CVEp)	k_1/k_2 (VAp)	k_1/k_2 (VA)
200	15.5	12.2	198	11.1	14.8
400	4.02	3.55	5.11	3.49	4.05
900	1.86	1.80	1.90	1.79	1.92
1600	1.38	1.45	1.47	1.45	1.49

TABLE 25. Isotope Effects for the Reactions: 1) H + HD; 2) H + DH

T(K)	k_1/k_2 (QM)	k_1/k_2 (TST)	k_1/k_2 (CVEp)	k_1/k_2 (VAp)	k_1/k_2 (VA)
200	2.11	2.79	10.4	1.97	2.92
400	1.56	1.67	2.04	1.57	1.88
900	1.19	1.29	1.33	1.28	1.38
1600	1.01	1.21	1.22	1.21	1.26

TABLE 26. Isotope Effects for the Reactions: 1) H + HT; 2) H + TH

T(K)	k_1/k_2 (QM)	k_1/k_2 (TST)	k_1/k_2 (CVEp)	k_1/k_2 (VAp)	k_1/k_2 (VA)
200	2.70	4.19	31.6	2.78	4.73
400	1.75	2.05	2.65	1.91	2.43
900	1.22	1.43	1.48	1.41	1.55
1600	0.98	1.31	1.32	1.30	1.38

TABLE 27. Isotope Effects for the Reactions: 1) D + HD; 2) D + DH

T(K)	k_1/k_2 (QM)	k_1/k_2 (TST)	k_1/k_2 (CVEp)	k_1/k_2 (VAp)	k_1/k_2 (VA)
200	3.85	3.05	12.9	2.25	1.16
400	2.20	1.75	2.06	1.65	1.23
900	1.41	1.33	1.36	1.32	1.17
1600	1.10	1.25	1.26	1.25	1.17

REFERENCES

1. R. D. Levine and R. B. Bernstein, *Molecular Reaction Dynamics and Chemical Reactivity*, (Oxford University Press, New York, 1987)
2. E. Merzbacher, *Quantum Mechanics*, (John Wiley and Sons, New York 1970) Chapter 11.
3. L. M. Delves, *Nucl. Phys.* **9**, 391 (1959).
4. L. M. Delves, *Nucl. Phys.* **20**, 275 (1960).
5. A. Kuppermann, *Theoretical Chemistry: Advances and Perspectives* **6A**, ed. D. Henderson (Academic Press, New York, 1981) pp. 79-164.
6. A. M. Lane and R. G. Thomas, *Rev. Mod. Phys.* **30**, 257 (1958).
7. E. M. Mortensen and K. S. Pitzer, *J. Chem. Soc., Spec. Publ.* **16**, 57 (1962).
8. D. J. Diestler and B. V. McKoy, *J. Chem. Phys.* **48**, 2951 (1968).
9. D. G. Truhlar and A. Kuppermann, *J. Chem. Phys.* **52**, 3841 (1970).
10. D. G. Truhlar and A. Kuppermann, *J. Chem. Phys.* **56**, 2232 (1972).
11. D. G. Truhlar A. Kuppermann and J. T. Adams, *J. Chem. Phys.* **59**, 395 (1973).
12. E. A. McCullough, Jr. and R. E. Wyatt *J. Chem. Phys.* **51**, 1253 (1969).
13. E. A. McCullough, Jr. and R. E. Wyatt *J. Chem. Phys.* **54**, 3578 (1971); *J. Chem. Phys.* **54**, 3592 (1971).
14. W. M. Sams and D. J. Kouri, *J. Chem. Phys.* **51**, 4809 (1969); *J. Chem. Phys.* **51**, 4815 (1969).
15. J. T. Adams, R. L. Smith and E. F. Hayes, *J. Chem. Phys.* **61**, 2193 (1974).
16. E. M. Mortensen and L. D. Gucwa, *J. Chem. Phys.* **51**, 5695 (1969).
17. A. Askar, A. S. Cakmak and H. A. Rabitz, *J. Chem. Phys.* **33**, 267 (1978).
18. C. C. Rankin and J. C. Light, *J. Chem. Phys.* **51**, 1701 (1969).

19. G. Miller and J. C. Light, *J. Chem. Phys.* **54**, 1635 (1971); *J. Chem. Phys.* **54**, 1643 (1971).

20. A. Kuppermann in *"Proceedings of the Conference on Potential Energy Surfaces in Chemistry"* (W. A. Lester, ed.), pp.121-124 (1970).

21. A. Kuppermann, *Proc. Int. Conf. Phys. Electron. At. Collisions, 7th*, 3 (1971).

22. D. J. Diestler, *J. Chem. Phys.* **54**, 4547 (1971).

23. J. C. Light and R. B. Walker, *J. Chem. Phys.* **65**, 4272 (1976).

24. G. C. Schatz and A. Kuppermann, *J. Chem. Phys.* **59**, 964 (1973).

25. G. C. Schatz, J. M. Bowman and A. Kuppermann, *J. Chem. Phys.* **58**, 4023 (1973).

26. G. C. Schatz, J. M. Bowman and A. Kuppermann, *J. Chem. Phys.* **63**, 674 (1975).

27. G. C. Schatz, J. M. Bowman and A. Kuppermann, *J. Chem. Phys.* **63**, 685 (1975).

28. M. Baer and D. J. Kouri, *Chem. Phys. Lett.* **24**, 37 (1974).

29. M. Baer, *Mol. Phys.* **27** 1429, (1974); *J. Chem. Phys.* **60**, 1057 (1974).

30. A. Kuppermann, J. A. Kaye and J. P. Dwyer, *Chem. Phys. Lett.* **74**, 257 (1980).

31. G. Haug, J. Manz and J. Römelt, *J. Chem. Phys.* **73**, 5040 (1980).

32. J. Römelt, *Chem. Phys. Lett.* **74**, 263 (1980).

33. J. A. Kaye and A. Kuppermann, *Chem. Phys. Lett.* **77**, 573 (1981).

34. J. Manz and J. Römelt, *Chem. Phys. Lett.* **81**, 179 (1981).

35. J. Manz and J. Römelt, *Chem. Phys. Lett.* **77**, 172 (1981).

36. J. A. Kaye and A. Kuppermann, *Chem. Phys. Lett.* **78**, 546 (1981).

37. A. Kuppermann and J. P. Dwyer, in: *Electronic and Atomic Collisions, 11th International Conference on the Physics of Electronic and Atomic Collisions,*

Kyoto, Japan (The Society for Atomic Collision Research, Tokyo, 1979) p.888.

38. A. Kuppermann, in: *Potential Energy Surfaces and Dynamics Calculations*, ed. by D. G. Truhlar (Plenum Press, New York, 1981) pp. 405, 414.
39. G. C. Schatz and A. Kuppermann, *Phys. Rev. Lett.* **35**, 1266 (1975).
40. G. C. Schatz in *The Theory of Chemical Reaction Dynamics* ed. by D. C. Clary, (D. Reidel Publishing Company, Dordrecht, Holland 1986) , p. 1-26.
41. G. C. Schatz, Ph.D. Thesis, California Institute of Technology, 1975.
42. J. A. Kaye and A. Kuppermann, *Chem. Phys.* **127**, 97 (1988).
43. J. P. Dwyer, Ph.D Thesis, California Institute of Technology, 1978.
44. *Resonances in Electron-Molecule Scattering, van der Waals Complexes, and Reactive Chemical Dynamics* ed. by D. G. Truhlar (American Chemical Society, Washington, D.C. 1984).
45. H. Pelzer and E. Wigner, *Z. Phys. Chem. (Leipzig)* **B15**, 445 (1932).
46. S. Glasstone, K. J. Laidler and H. Eyring, "Theory of Rate Processes", (Mc Graw-Hill, New York, 1940).
47. H. Eyring, *J. Chem. Phys.* **3**, 107 (1935).
48. M. G. Evans and M. Polanyi, *Trans. Faraday Soc.* **31**, 875 (1935).
49. J. I. Steinfeld, J. S. Francisco and W. L. Hase, "Chemical Kinetics and Dynamics" (Prentice Hall, Englewood Cliffs, New Jersey 1989), Chapter 10.
50. J. I. Steinfeld, "Molecules and Radiation" (Harper and Row, New York, NY, 1974), Chapter 8.
51. G. Herzberg, "Molecular Spectra and Molecular Structure II. Infrared and Raman Spectra of Polyatomic Molecules" (Van Nostrand Reinhold Company, New York, NY 1945), Chapter II.

52. I. N. Levine, "Molecular Spectroscopy" (J. Wiley and Sons, New York, NY 1975), Chapter 6.

53. E. P. Wigner, *Z. Phisik. Chem. (Leipzig)* **B19**, 203 (1932).

54. R. P. Bell, "The Proton in Chemistry," 2nd Ed. (Cornell University Press, Ithaca, NY, 1959), Chapter 12.

55. L. Melander and W. H. Saunders, Jr., "Reaction Rates of Isotopic Molecules," 2nd ed., (John Wiley and Sons, New York, 1979) pp. 13-17

56. K. J. Laidler, "Theories of Chemical Reaction Rates," (McGraw-Hill, New York, 1969) pp. 59-63.

57. H. S. Johnston, "Gas Phase Reaction Rate Theory" (Ronald, New York, 1966).

58. D. G. Truhlar and A. Kuppermann, *J. Am. Chem. Soc.* **93**, 1840 (1971).

59. R. P. Bell, *Trans. Faraday Soc.* **55**, 1 (1959).

60. J. Bigeleisen, F. S. Klein, R. E. Weston and M. Wolfsberg, *J. Chem. Phys.* **30**, 1340 (1959).

61. T. E. Sharp and H. S. Johnston, *J. Chem. Phys.* **37**, 1541 (1962).

62. R. E. Weston, *J. Chem. Phys.* **31**, 892 (1959).

63. R. E. Weston, *Discuss. Faraday Soc.* **44**, 163 (1968).

64. R. A. Marcus, *J. Chem. Phys.* **44**, 167 (1968).

65. C. Eckart, *Phys. Rev.* **35**, 1303 (1935).

66. H. S. Johnston and D. Rapp, *J. Am. Chem. Soc.* **83**, 1 (1961).

67. H. S. Johnston and J. Heicklen, *J. Phys. Chem.* **66**, 532 (1962).

68. F. H. Westheimer, *Chem. Rev.* **61**, 265 (1961).

69. D. G. Truhlar, Ph.D. Thesis, California Institute of Technology, 1970.

70. R. E. Wyatt, *J. Chem. Phys.* **51**, 3489 (1969).

71. R. A. Marcus *J. Chem. Phys.* **45**, 4493 (1966).

72. R. A. Marcus, *J. Chem. Phys.* **49**, 2617 (1969).

73. J. D. Russell and J. C. Light, *J. Chem. Phys.* **54**, 4881 (1971).

74. Y-S. M. Wu, Ph.D. Thesis, California Institute of Technology, 1992.

75. R. A. Marcus and M. E. Coltrin, *J. Chem. Phys.* **67**, 2609 (1977).

76. B. C. Garrett and D. G. Truhlar, *J. Phys. Chem.* **83**, 1079 (1979;).erratum *J. Phys. Chem.* **84**, 682 (1980).

77. J. M. Bowman, A. Kuppermann, J. T. Adams and D. G. Truhlar, *Chem. Phys. Lett.* **20**, 229 (1973).

78. B. C. Garrett and D. G. Truhlar, *J. Chem. Phys.* **72**, 3460 (1980).

79. A. A. Westenberg and N. de Haas, *J. Chem. Phys.* **47**, 1393 (1967).

80. W. R. Schultz and D. J. LeRoy *Can. J. Chem.* **42**, 2480 (1964).

81. D. N. Mitchell and D. J. LeRoy, *J. Chem. Phys.* **58**, 3449 (1973).

82. W. R. Schulz and D. J. LeRoy, *J. Chem. Phys.* **42**, 3869 (1965).

83. K. A. Quickert and D. J. LeRoy, *J. Chem. Phys.* **53**, 1325 (1970); erratun **54**, 5444 (1971).

84. D. J. LeRoy, B. A. Ridley and K. A. Quickert, *Discuss. Faraday Soc.* **44**, 92 (1968).

Figure Captions

Figure 1. Jacobi coordinates for a colinear triatomic reaction.

Figure 2. Potential energy contours for the generic A + BC reaction.

Figure 3. LSTH potential energy surface for the H + H_2 system. The solid curves are equipotential contours, and the total energies indicated by each contour are measured from the bottom of the H_2 well. The polar coordinates ρ and α of a general point P in the Delves mass-scaled configuration space are also shown.

Figure 4. Cut through the potential energy surface in mass-scaled coordinates, along the symmetric stretch of the H_3 transition state.

Figure 5. Reaction probability for the reaction H + H_2 ($v = 0$) $\rightarrow$ H_2 ($v' = 0$-3) + H, as a function of total energy and translational energy. The arrows indicate the opening of higher vibrational states of the product diatom.

Figure 6. Same as Figure 5, for the $v = 1$ state.

Figure 7. State-to-state reaction probabilities for the H + H_2 reaction; the bottom panel represents the 0-0 process, the middle panel the 0-1 process, and the top the 1-1 process.

Figure 8. Reaction probability for the reaction H + HD ($v = 0$) $\rightarrow$ H_2 ($v' = 0$-3) + D, as a function of total energy and translational energy. The arrows indicate the opening of higher vibrational states of the product diatom.

Figure 9. Same as Figure 8, for the $v = 1$ state.

Figure 10. State-to-state reaction probabilities for the H + HD reaction. The bottom panel represents the 0-0 transition, the top the 0-1 transition.

Figure 11. State-to-state reaction probabilities for the H + HD reaction. The bottom panel represents the 1-1 process, the top the 1-0 process.

Figure 12. Reaction probability for the reaction D + H_2 ($v = 0$) → DH ($v' = 0$-4) + H, as a function of total energy and translational energy. The arrows indicate the opening of higher vibrational states of the product diatom.

Figure 13. Same as Figure 12, for the $v = 1$ state.

Figure 14. Reaction probability for the reaction H + HT ($v = 0$) → H_2 ($v' = 0$-3) + T, as a function of total energy and translational energy. The arrows indicate the opening of higher vibrational states of the product diatom.

Figure 15. Same as Figure 14, for the $v = 1$ state.

Figure 16. State-to-state reaction probabilities for the H + HT reaction. The bottom panel represents the 0-0 transition, the top the 0-1 transition.

Figure 17. State-to-state reaction probabilities for the H + HT reaction. The bottom panel represents the 1-1 process, the top the 1-0 process.

Figure 18. Reaction probability for the reaction T + H_2 ($v = 0$) → TH ($v' = 0$-4) + H, as a function of total energy and translational energy. The arrows indicate the opening of higher vibrational states of the product diatom.

Figure 19. Same as Figure 18, for the $v = 1$ state.

Figure 20. Reaction probability for the reaction D + HD ($v = 0$) → DH ($v' = 0$-4) + D, as a function of total energy and translational energy. The arrows indicate the opening of higher vibrational states of the product diatom.

Figure 21. Same as Figure 20, for the $v = 1$ state.

Figure 22. Reaction probability for the reaction D + HT ($v = 0$) → DH ($v' = 0$-4) + T, as a function of total energy and translational energy. The arrows indicate the opening of higher vibrational states of the product diatom.

Figure 23. Same as Figure 22, for the $v = 1$ state.

Figure 24. Reaction probability for the reaction T + HD ($v = 0$) → TH ($v' = 0$-4) + D, as a function of total energy and translational energy. The arrows indicate the opening of higher vibrational states of the product diatom.

Figure 25. Same as Figure 24, for the $v = 1$ state.

Figure 26. Reaction probability for the reaction T + HT ($v = 0$) $\rightarrow$ TH ($v' = 0$-4) + T, as a function of total energy and translational energy. The arrows indicate the opening of higher vibrational states of the product diatom.

Figure 27. Same as Figure 26, for the $v = 1$ state.

Figure 28. Reaction probability for the reaction H + DH ($v = 0$) $\rightarrow$ HD ($v' = 0$-4) + H, as a function of total energy and translational energy. The arrows indicate the opening of higher vibrational states of the product diatom.

Figure 29. Same as Figure 28, for the $v = 1$ state.

Figure 30. Reaction probability for the reaction H + TH ($v = 0$) $\rightarrow$ HT ($v' = 0$-4) + H, as a function of total energy and translational energy. The arrows indicate the opening of higher vibrational states of the product diatom.

Figure 31. Same as Figure 30, for the $v = 1$ state.

Figure 32. Reaction probability for the reaction D + DH ($v = 0$) $\rightarrow$ D_2 ($v' = 0$-5) + H, as a function of total energy and translational energy. The arrows indicate the opening of higher vibrational states of the product diatom.

Figure 33. Same as Figure 32, for the $v = 1$ state.

Figure 34. Reaction probability for the reaction H + D_2 ($v = 0$) $\rightarrow$ HD ($v' = 0$-4) + D, as a function of total energy and translational energy. The arrows indicate the opening of higher vibrational states of the product diatom.

Figure 35. Same as Figure 34, for the $v = 1$ state.

Figure 36. Logarithm of the rate constants as a function of inverse temperature for the H + H_2 reaction. k_0 is the rate constant for the reaction from the $v = 0$ reactant state to all product vibrational states. k_1 is the rate constant for the reaction from the $v = 1$ reactant state to all product vibrational states. k_{TST} is the conventional transition state rate constant.

Figure 37. Same as Figure 36, for the H + HD reaction.

Figure 38. Same as Figure 36, for the D + H_2 reaction.

Figure 39. Same as Figure 36, for the H + HT reaction.

Figure 40. Same as Figure 36, for the T + H_2 reaction.

Figure 41. Same as Figure 36, for the D + HD reaction.

Figure 42. Same as Figure 36, for the D + HT reaction.

Figure 43. Same as Figure 36, for the T + HD reaction.

Figure 44. Same as Figure 36, for the T + HT reaction.

Figure 45. Same as Figure 36, for the H + DH reaction.

Figure 46. Same as Figure 36, for the H + TH reaction.

Figure 47. Same as Figure 36, for the D + DH reaction.

Figure 48. Same as Figure 36, for the H + D_2 reaction.

Figure 49. Potential energy curves for the H + H_2 reaction along the reaction coordinate. The lower curve represents the minimum energy path. The upper one is the vibrationally adiabatic potential energy along the minimum energy path. Negative distances refer to the reactant side, positive distances to the product side.

Figure 50. Vibrationally adiabatic potential energy curve along the minimum energy path for H + HD. Negative distances refer to the reactant side, positive distances to the product side. A parabolic fit to the barrier region is also shown.

Figure 51. Logarithmic plot of the transmission coefficient κ (top panel) and the rate constant ratio k^{approx}/k (bottom panel) as a function of inverse temperature for the H + H_2 reaction. The approximate methods are as follows: k^{TST} is the conventional transition state rate constant; k^{CVE} is the rate constant obtained with the conservation of vibrational energy

approximation with parabolic fit; k^{VA} is the vibrationally adiabatic rate constant. The classical value, $\kappa^{Cl} = 1$, is also shown.

Figure 52. Same as Figure 51, for the H + HD reaction or its reverse.

Figure 53. Same as Figure 51, for the H + HT reaction or its reverse.

Figure 54. Same as Figure 51, for the D + HD reaction.

Figure 55. Same as Figure 51, for the D + HT reaction or its reverse.

Figure 56. Same as Figure 51, for the T + HT reaction.

Figure 57. Same as Figure 51, for the H + DH reaction.

Figure 58. Same as Figure 51, for the H + TH reaction.

Figure 59. Same as Figure 51, for the D + DH reaction or its reverse.

Figure 60. Logarithmic plot of exact and approximate isotope effects for the following three reactions: 1) H + H_2 ; 2) D + H_2 ; 3) T + H_2 . k_i is the exact rate constant for reaction i, k_i^{CVE} is the rate constant obtained by the CVE approximation for reaction i, k_i^{VA} is the rate constant obtained using the VA approximation for reaction i, and k_i^{TST} is the conventional transition state rate constant for reaction i.

Figure 61. Same as Figure 60, for the following three reactions: 1) H + HD; 2) D + HD; 3) T + HD.

Figure 62. Same as Figure 60, for the following three reactions: 1) H + HT; 2) D + HT; 3) T + HT.

Figure 63. Same as Figure 60, for the following two reactions: 1) H + DH; 2) D + DH.

Figure 64. Same as Figure 60, for the following three reactions: 1) H + H_2 ; 2) H + HD; 3) H + HT.

Figure 65. Same as Figure 60, for the following three reactions: 1) D + H_2 ; 2) D + HD; 3) D + HT.

Figure 66. Same as Figure 60, for the following three reactions: 1) T + H_2 ; 2) T + HD; 3) T + HT.

Figure 67. Same as Figure 60, for the following three reactions: 1) H + H_2 ; 2) H + DH; 3) H + TH.

Figure 68. Same as Figure 60, for the following two reactions: 1) D + H_2 ; 2) D + DH.

Figure 69. Same as Figure 60, for the following two reactions: 1) H + HD; 2) H + D_2 .

Figure 70. Same as Figure 60, for the following two reactions: 1) H + HD; 2) H + DH.

Figure 71. Same as Figure 60, for the following two reactions: 1) H + HT; 2) H + TH.

Figure 72. Same as Figure 60, for the following two reactions: 1) D + HD; 2) D + DH.

Figure 1.

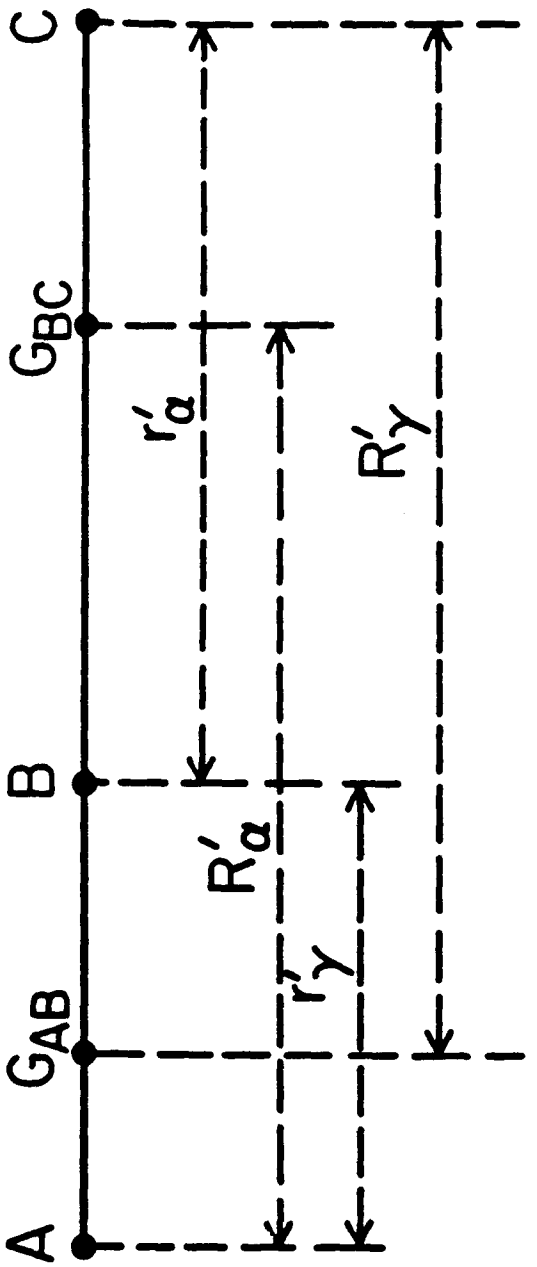

Figure 2.

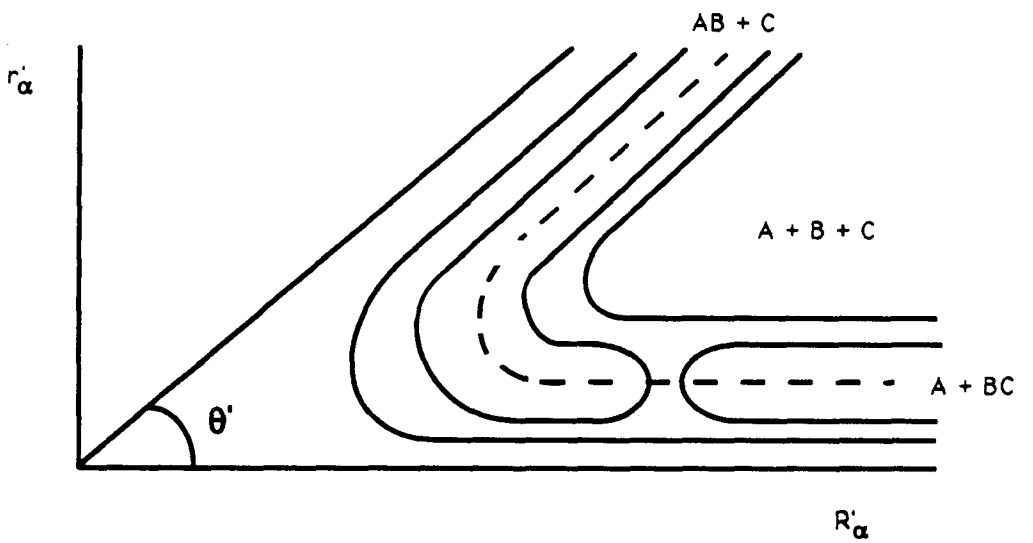

Figure 3.

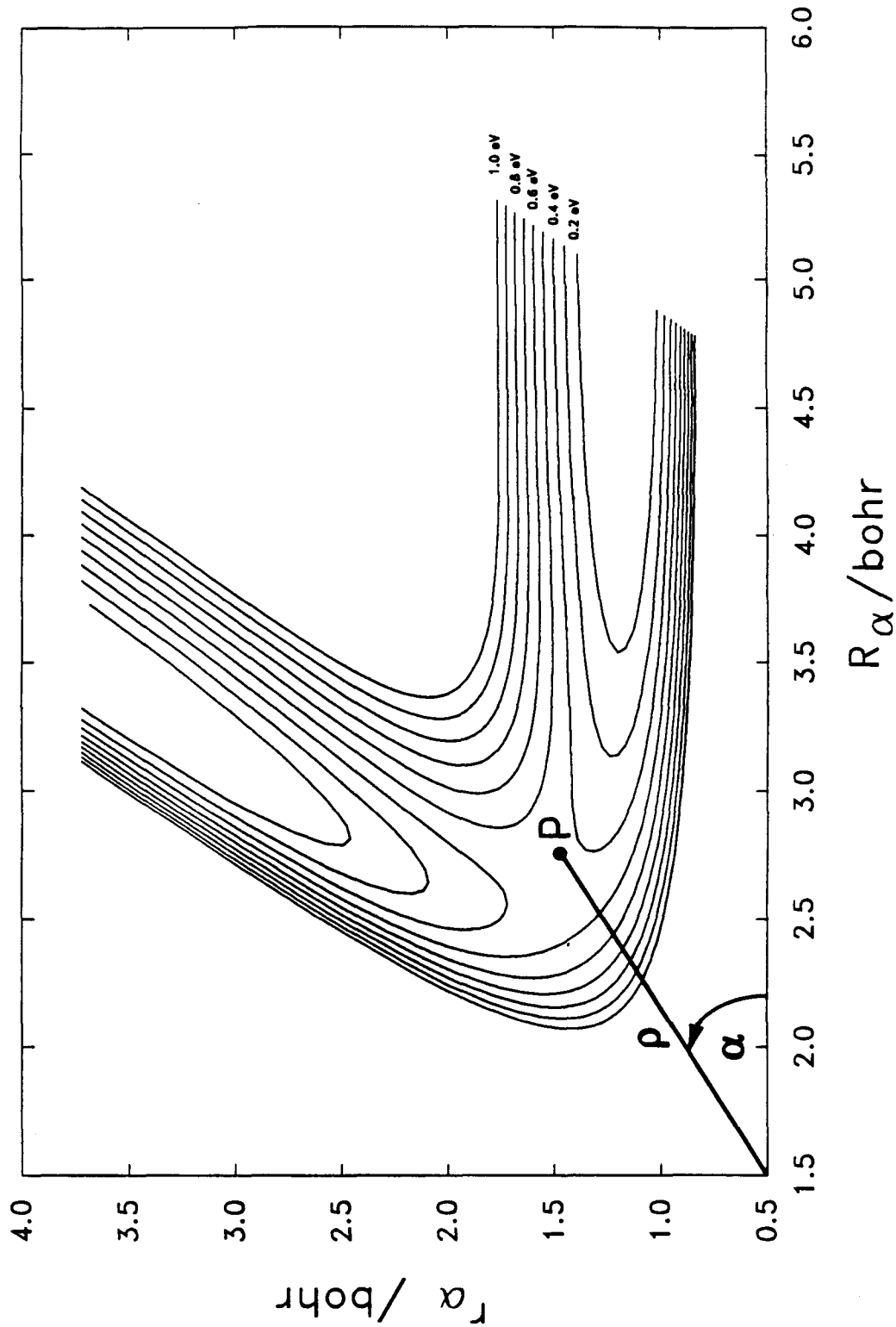
1.0 eV
0.8 eV
0.6 eV
0.4 eV
0.2 eV
P
ρ
α
r_α /bohr
R_α /bohr
4.0
3.5
3.0
2.5
2.0
1.5
1.0
0.5
1.5
2.0
2.5
3.0
3.5
4.0
4.5
5.0
5.5
6.0

Figure 4.

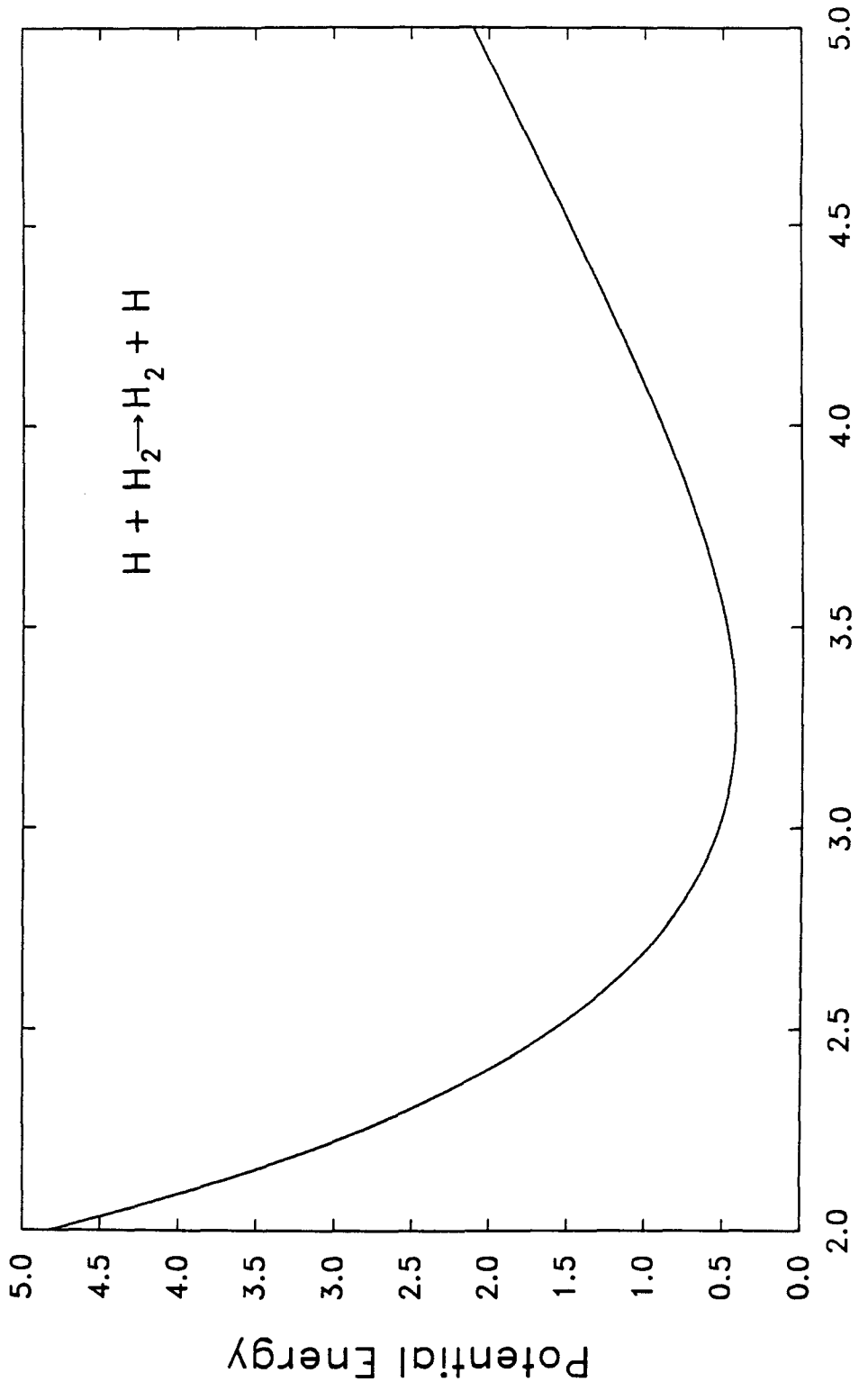
Potential Energy
ρ
H + H2→H2 + H
5.0
4.5
4.0
3.5
3.0
2.5
2.0
1.5
1.0
0.5
0.0
2.0
2.5
3.0
3.5
4.0
4.5
5.0

Figure 5.

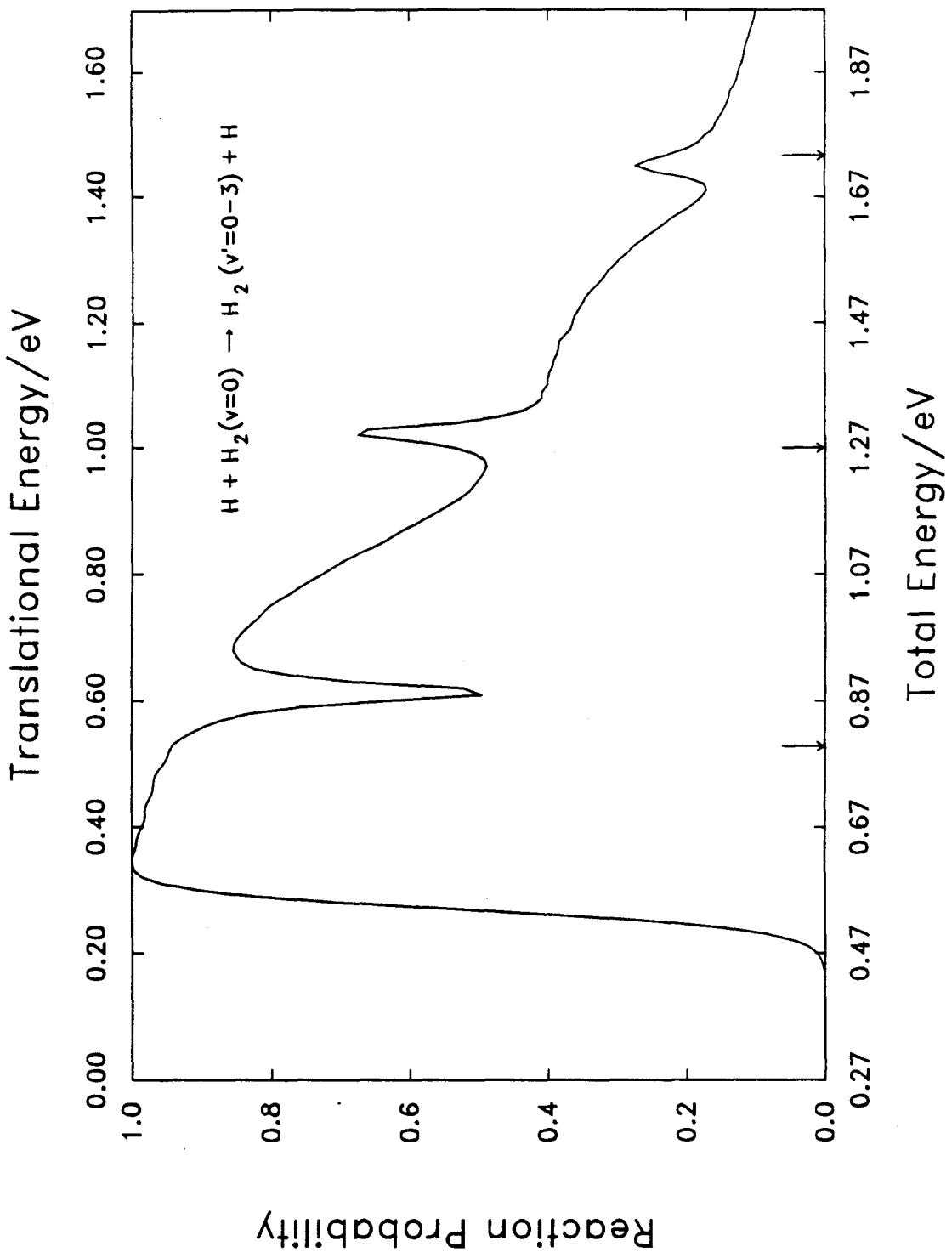
Translational Energy/eV
0.00
0.20
0.40
0.60
0.80
1.00
1.20
1.40
1.60
H + H2(v=0) → H2 (v'=0-3) + H
Reaction Probability
1.0
0.8
0.6
0.4
0.2
0.0
0.27
0.47
0.67
0.87
1.07
1.27
1.47
1.67
1.87
Total Energy/eV

Figure 6.

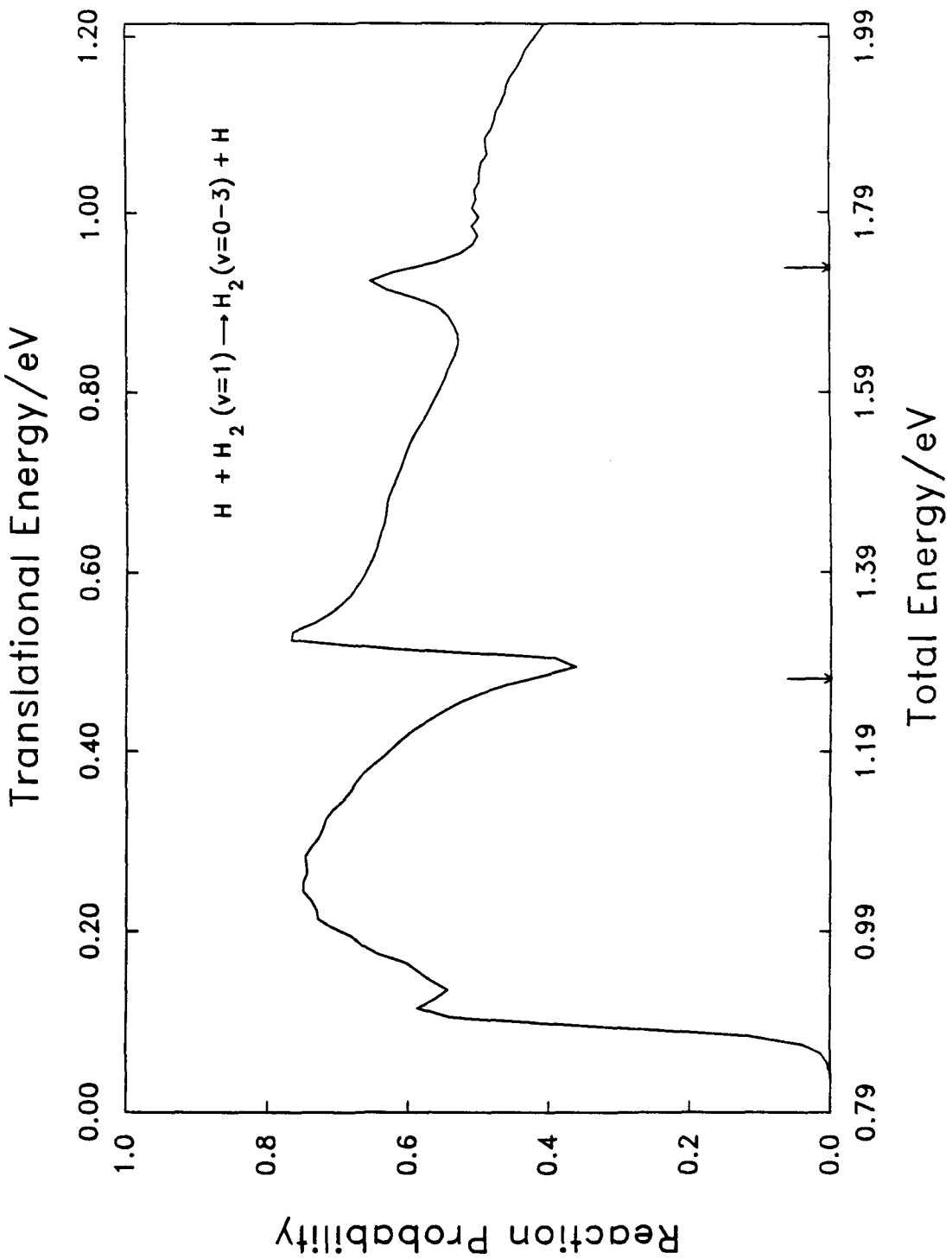
Translational Energy/eV
0.00
0.20
0.40
0.60
0.80
1.00
1.20
H + H2 (v=1) ⟶ H2 (v=0-3) + H
Reaction Probability
1.0
0.8
0.6
0.4
0.2
0.0
0.79
0.99
1.19
1.39
1.59
1.79
1.99
Total Energy/eV

Figure 7.

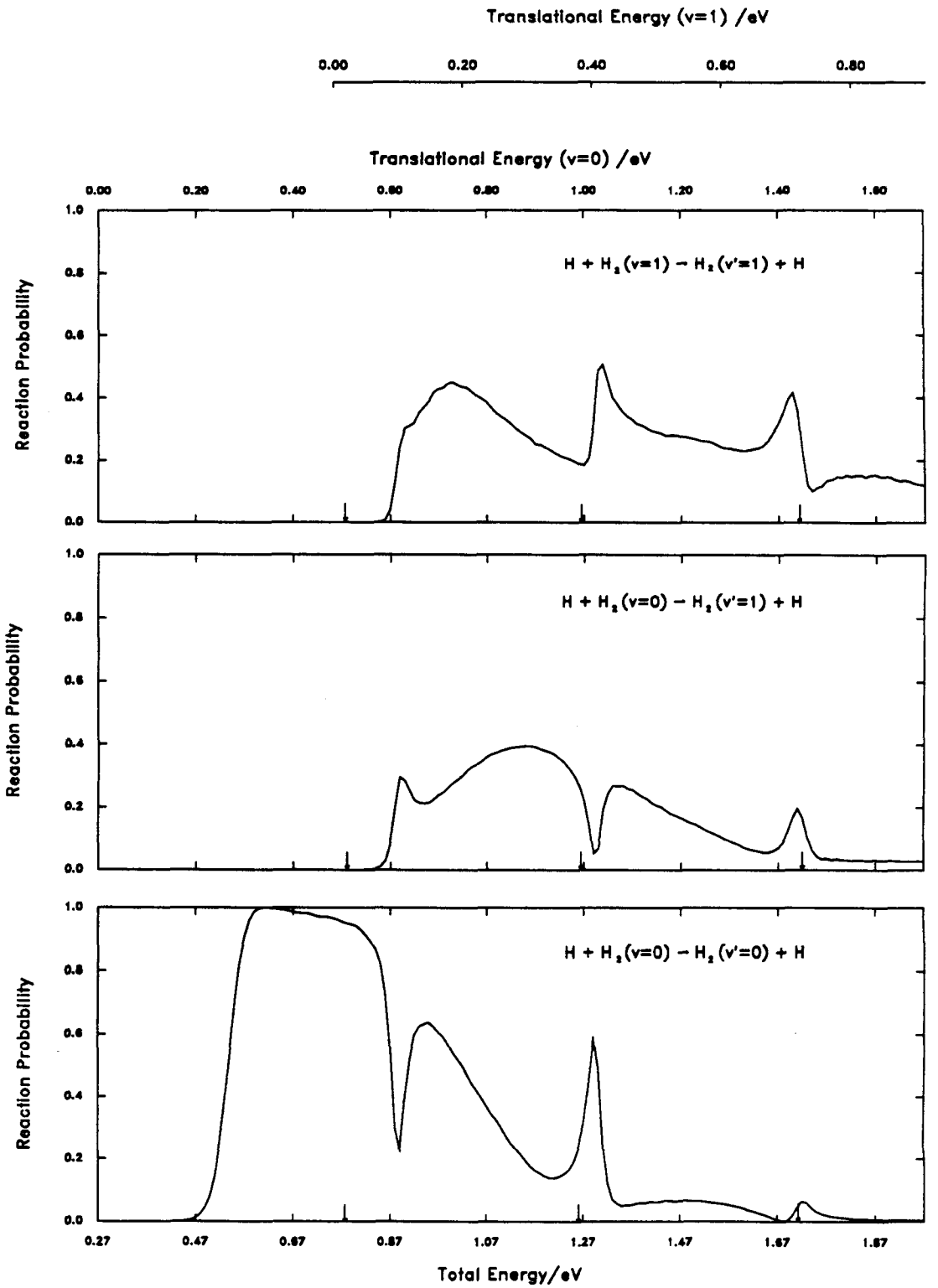
Translational Energy (v=1) /eV
0.00
0.20
0.40
0.60
0.80
Translational Energy (v=0) /eV
0.00
0.20
0.40
0.60
0.80
1.00
1.20
1.40
1.60
Reaction Probability
H + H2(v=1) → H2(v'=1) + H
H + H2(v=0) → H2(v'=1) + H
H + H2(v=0) → H2(v'=0) + H
0.0
0.2
0.4
0.6
0.8
1.0
0.27
0.47
0.67
0.87
1.07
1.27
1.47
1.67
1.87
Total Energy/eV

Figure 8.

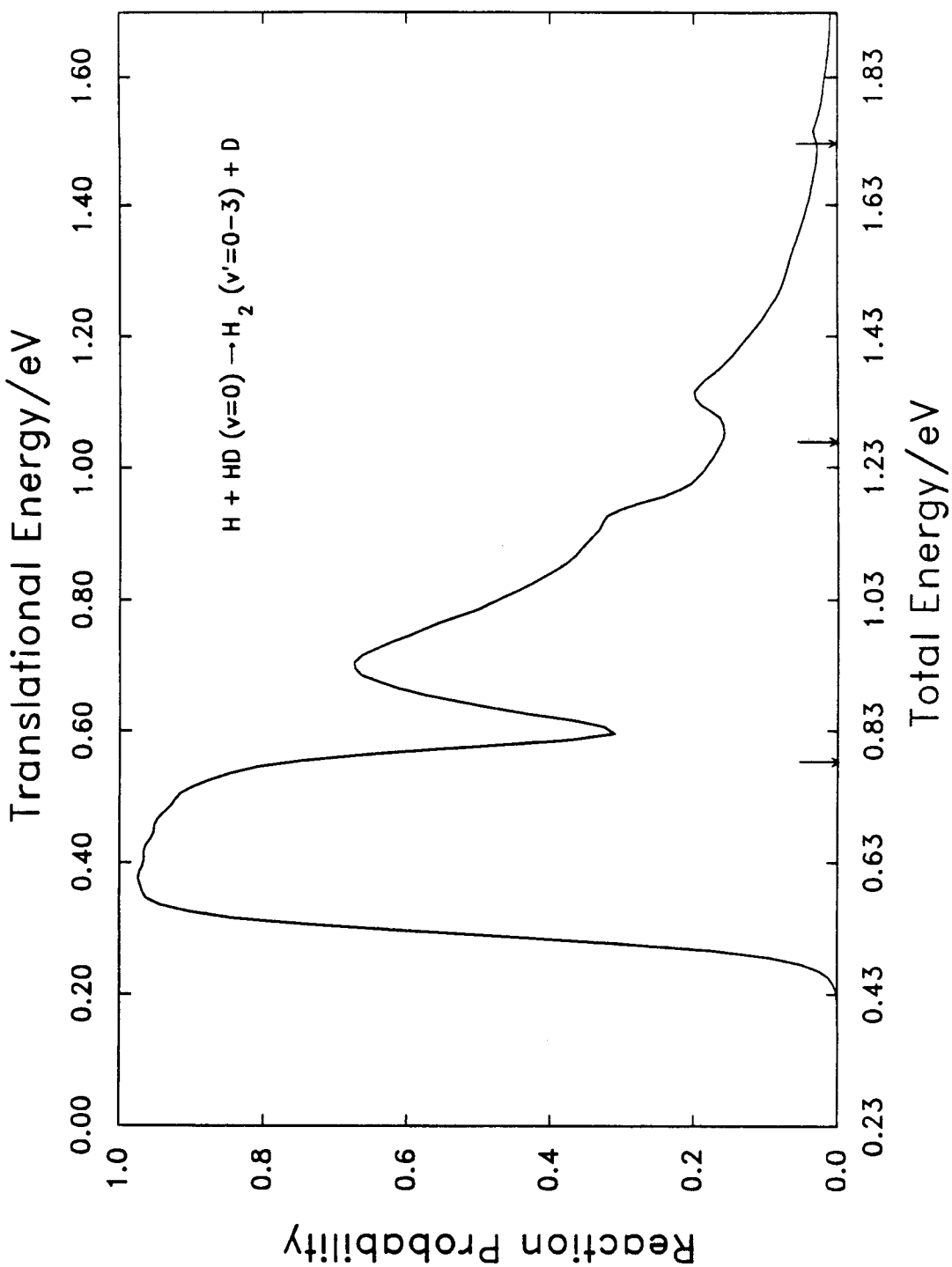
H + HD (v=0) → H2 (v'=0-3) + D
Reaction Probability
Translational Energy/eV
Total Energy/eV
0.00
0.20
0.40
0.60
0.80
1.00
1.20
1.40
1.60
1.0
0.8
0.6
0.4
0.2
0.0
0.23
0.43
0.63
0.83
1.03
1.23
1.43
1.63
1.83

Figure 9.

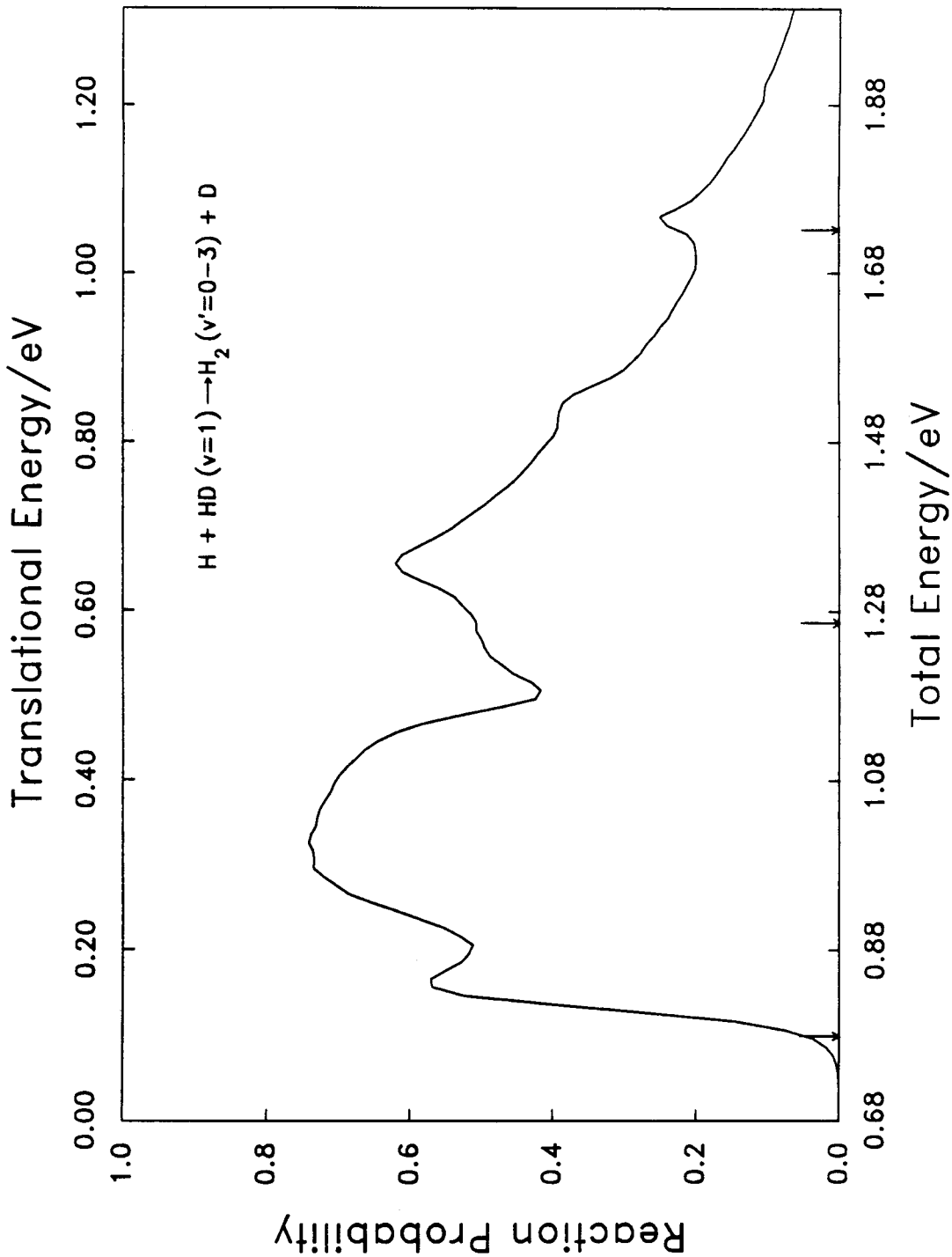
H + HD (v=1) → H2 (v'=0-3) + D
Reaction Probability
Translational Energy/eV
Total Energy/eV
0.0
0.2
0.4
0.6
0.8
1.0
0.00
0.20
0.40
0.60
0.80
1.00
1.20
0.68
0.88
1.08
1.28
1.48
1.68
1.88

Figure 10.

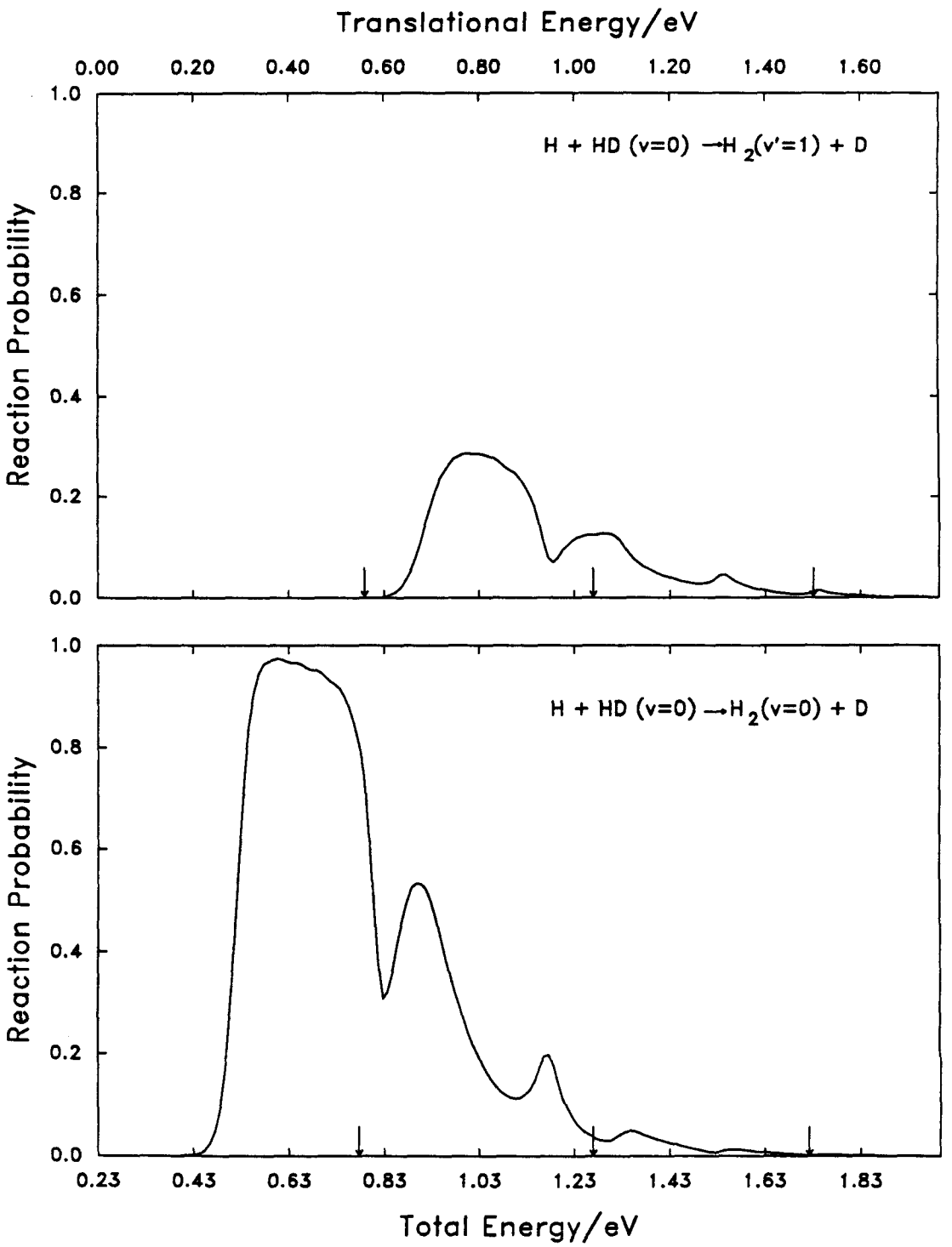
Translational Energy/eV
0.00
0.20
0.40
0.60
0.80
1.00
1.20
1.40
1.60
H + HD (v=0) → H2(v'=1) + D
Reaction Probability
1.0
0.8
0.6
0.4
0.2
0.0
H + HD (v=0) → H2(v=0) + D
Reaction Probability
0.23
0.43
0.63
0.83
1.03
1.23
1.43
1.63
1.83
Total Energy/eV

Figure 11.

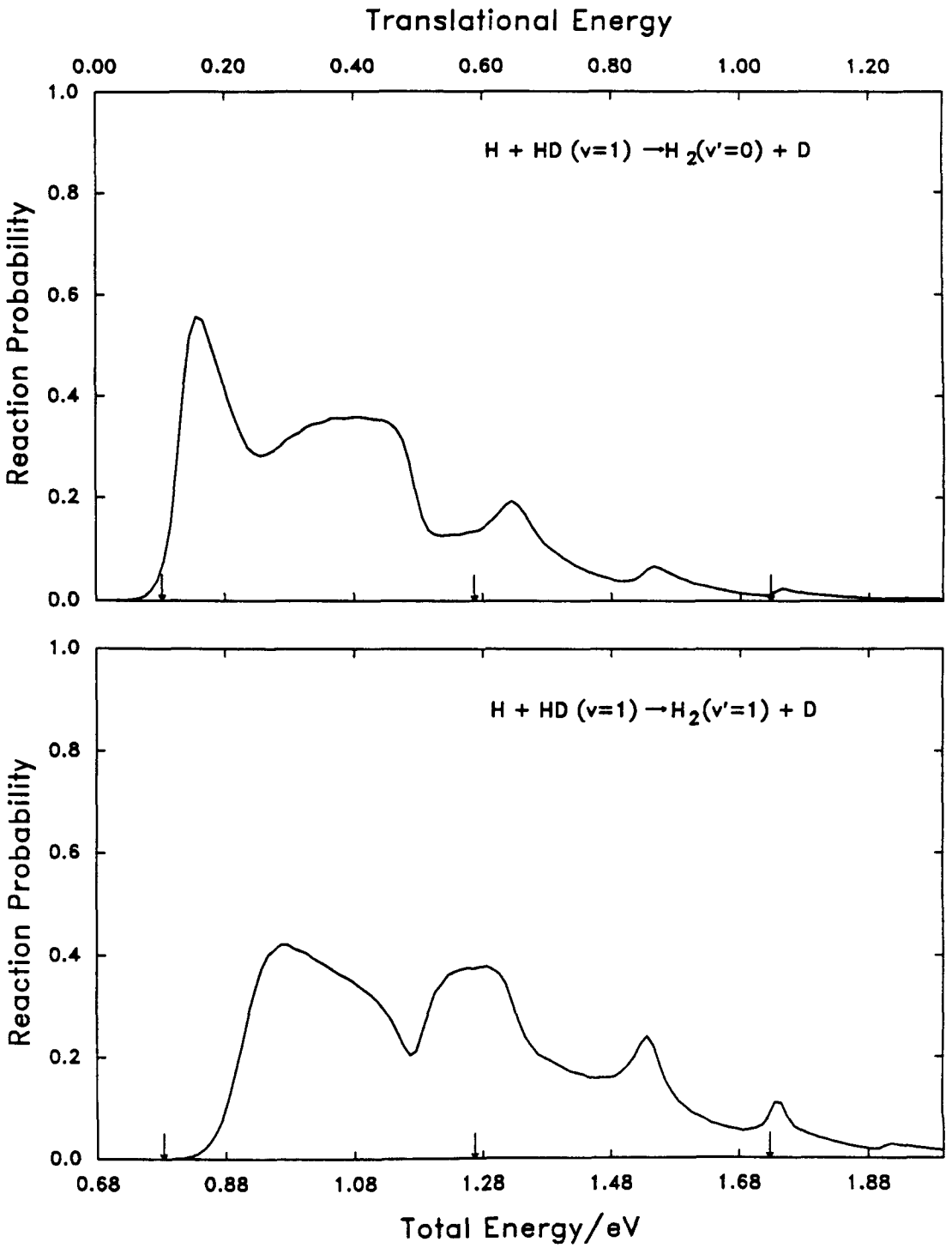
Translational Energy
0.00
0.20
0.40
0.60
0.80
1.00
1.20
H + HD (v=1) → H 2(v'=0) + D
Reaction Probability
1.0
0.8
0.6
0.4
0.2
0.0
H + HD (v=1) → H2(v'=1) + D
Reaction Probability
0.68
0.88
1.08
1.28
1.48
1.68
1.88
Total Energy/eV

Figure 12.

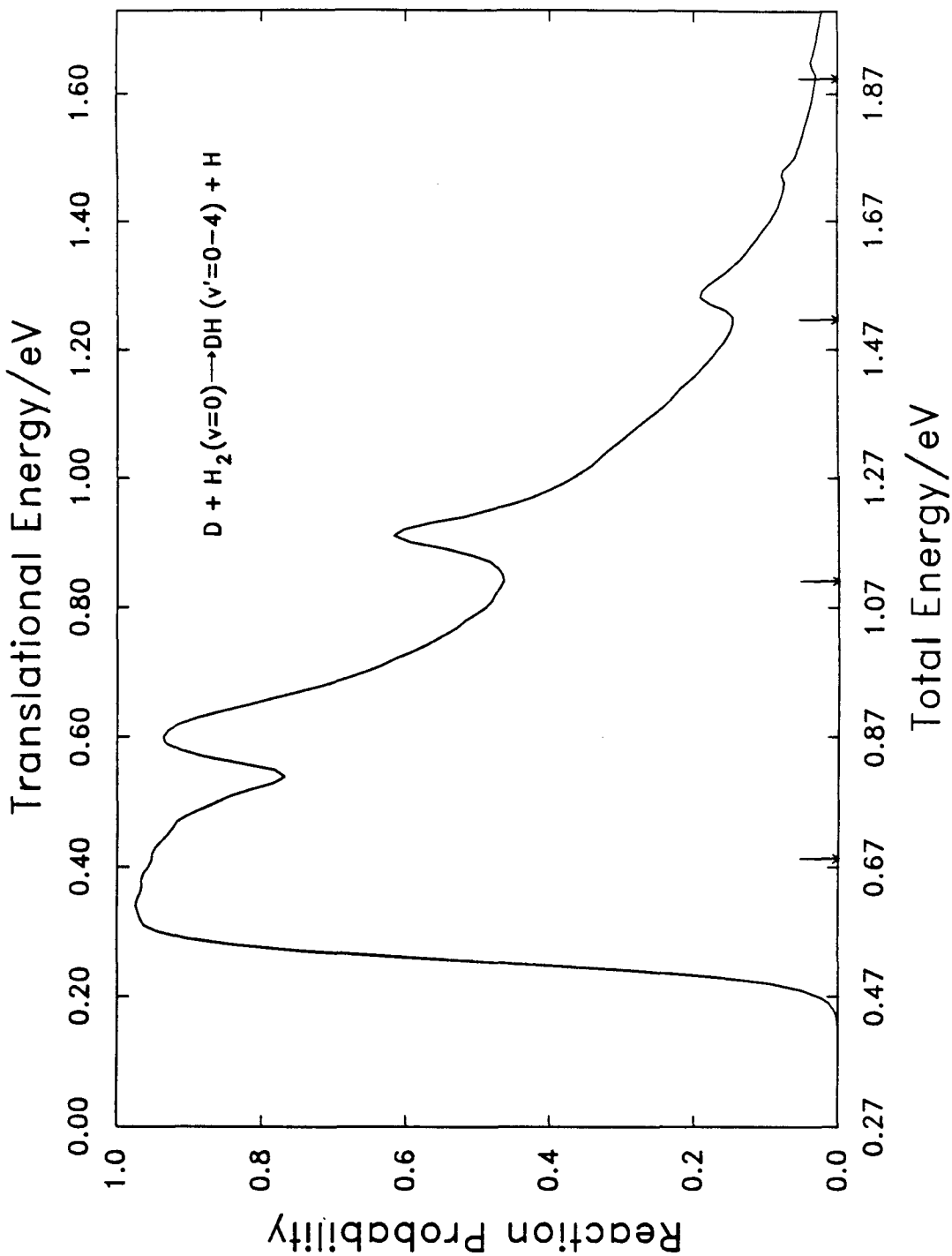
D + H2(v=0)⟶DH (v'=0−4) + H
Reaction Probability
Translational Energy/eV
Total Energy/eV
0.0
0.2
0.4
0.6
0.8
1.0
0.00
0.20
0.40
0.60
0.80
1.00
1.20
1.40
1.60
0.27
0.47
0.67
0.87
1.07
1.27
1.47
1.67
1.87

Figure 13.

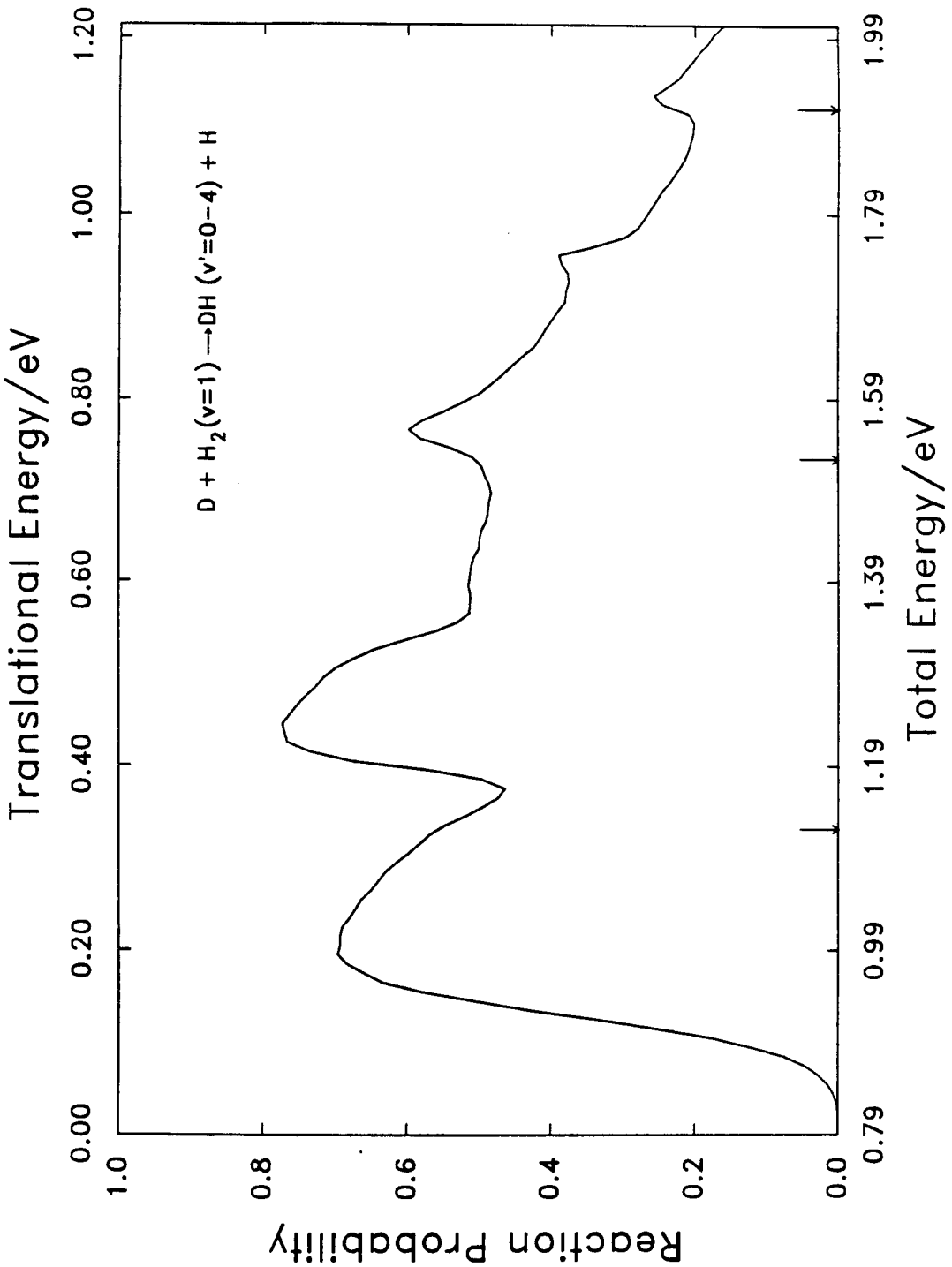
Translational Energy/eV
0.00
0.20
0.40
0.60
0.80
1.00
1.20
D + H2(v=1) → DH (v'=0-4) + H
Reaction Probability
1.0
0.8
0.6
0.4
0.2
0.0
0.79
0.99
1.19
1.39
1.59
1.79
1.99
Total Energy/eV

Figure 14.

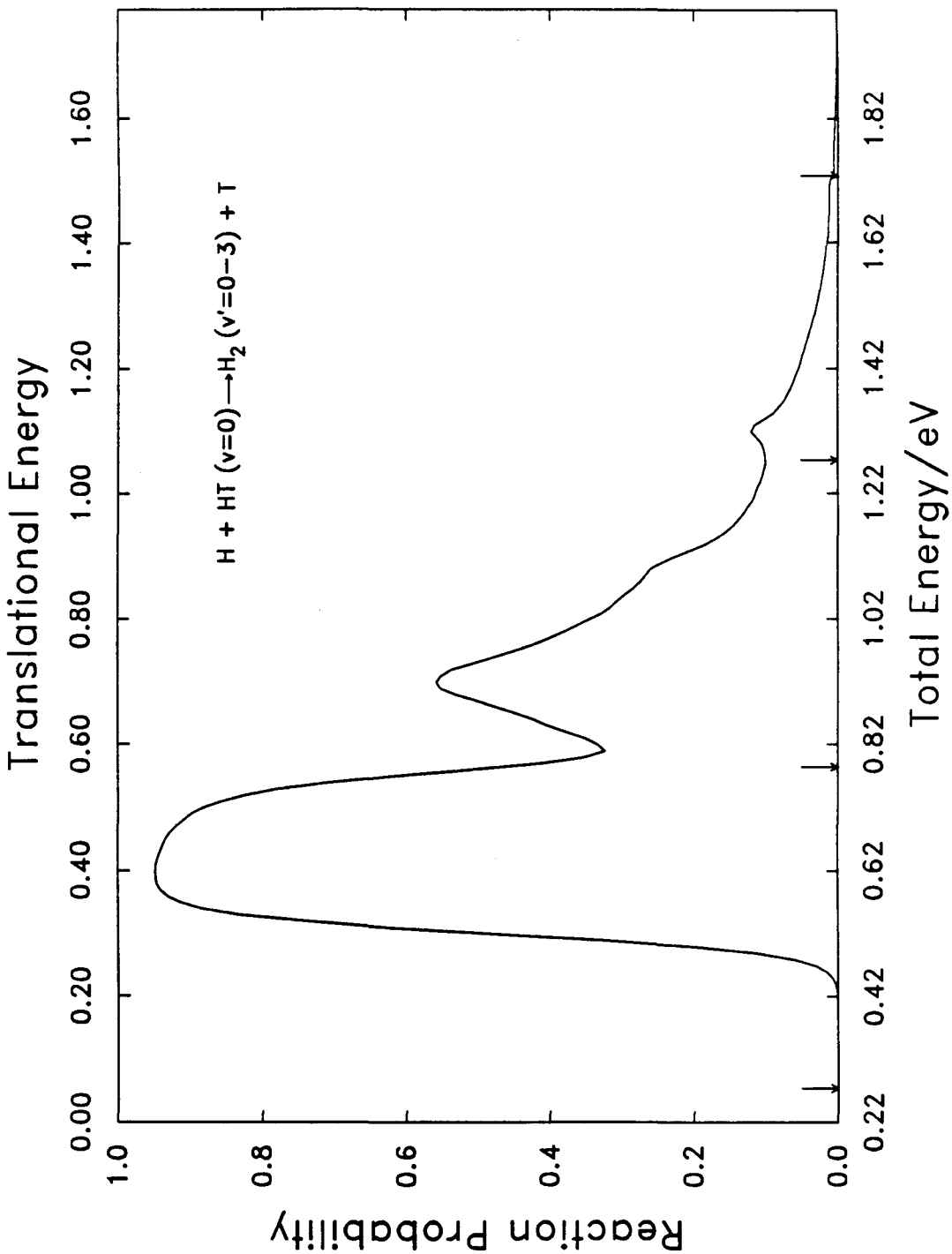
Translational Energy
0.00
0.20
0.40
0.60
0.80
1.00
1.20
1.40
1.60
H + HT (v=0)⟶H2 (v'=0-3) + T
Reaction Probability
1.0
0.8
0.6
0.4
0.2
0.0
0.22
0.42
0.62
0.82
1.02
1.22
1.42
1.62
1.82
Total Energy/eV

Figure 15.

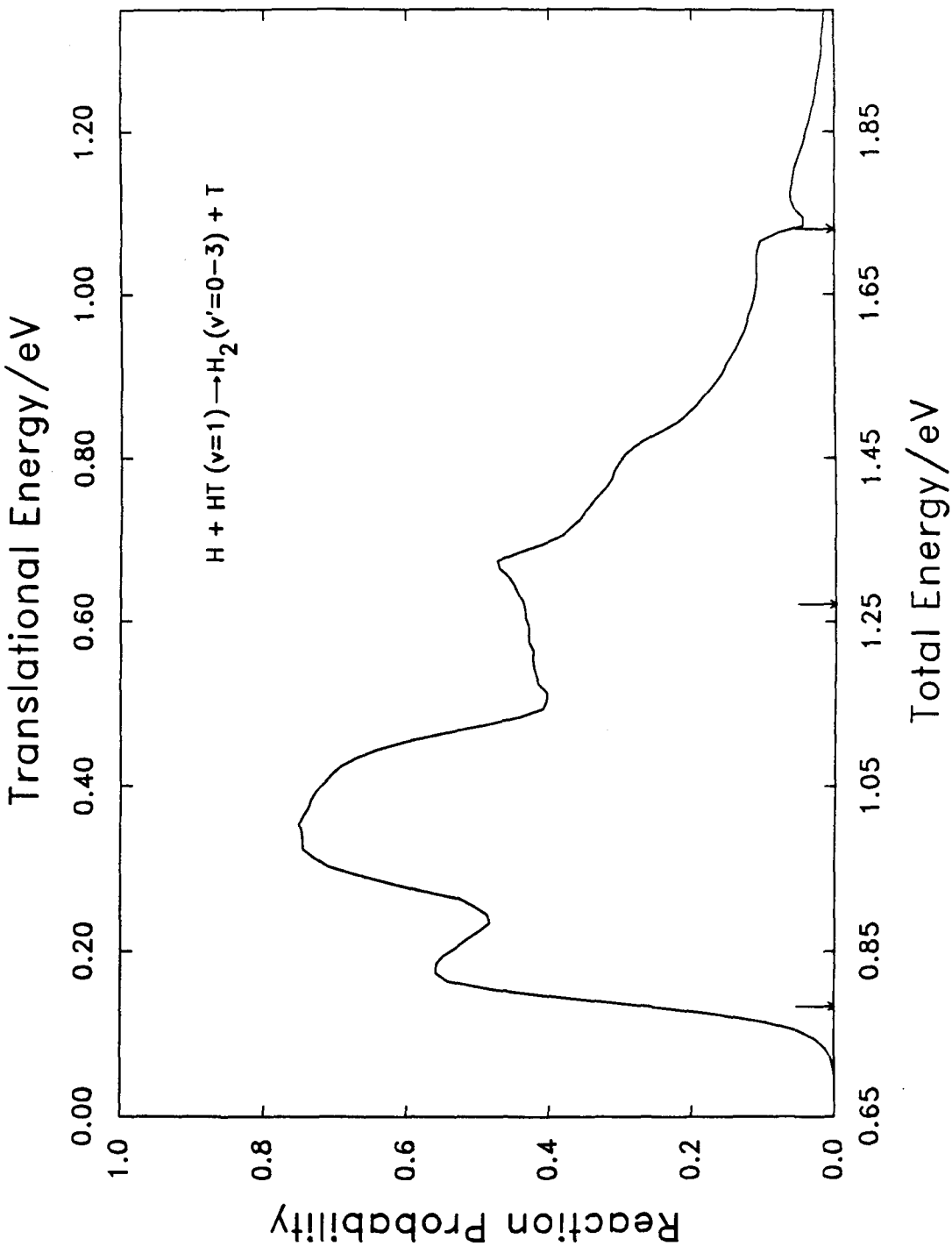
H + HT (v=1) → H2(v'=0-3) + T
Translational Energy/eV
0.00
0.20
0.40
0.60
0.80
1.00
1.20
Reaction Probability
1.0
0.8
0.6
0.4
0.2
0.0
Total Energy/eV
0.65
0.85
1.05
1.25
1.45
1.65
1.85

Figure 16.

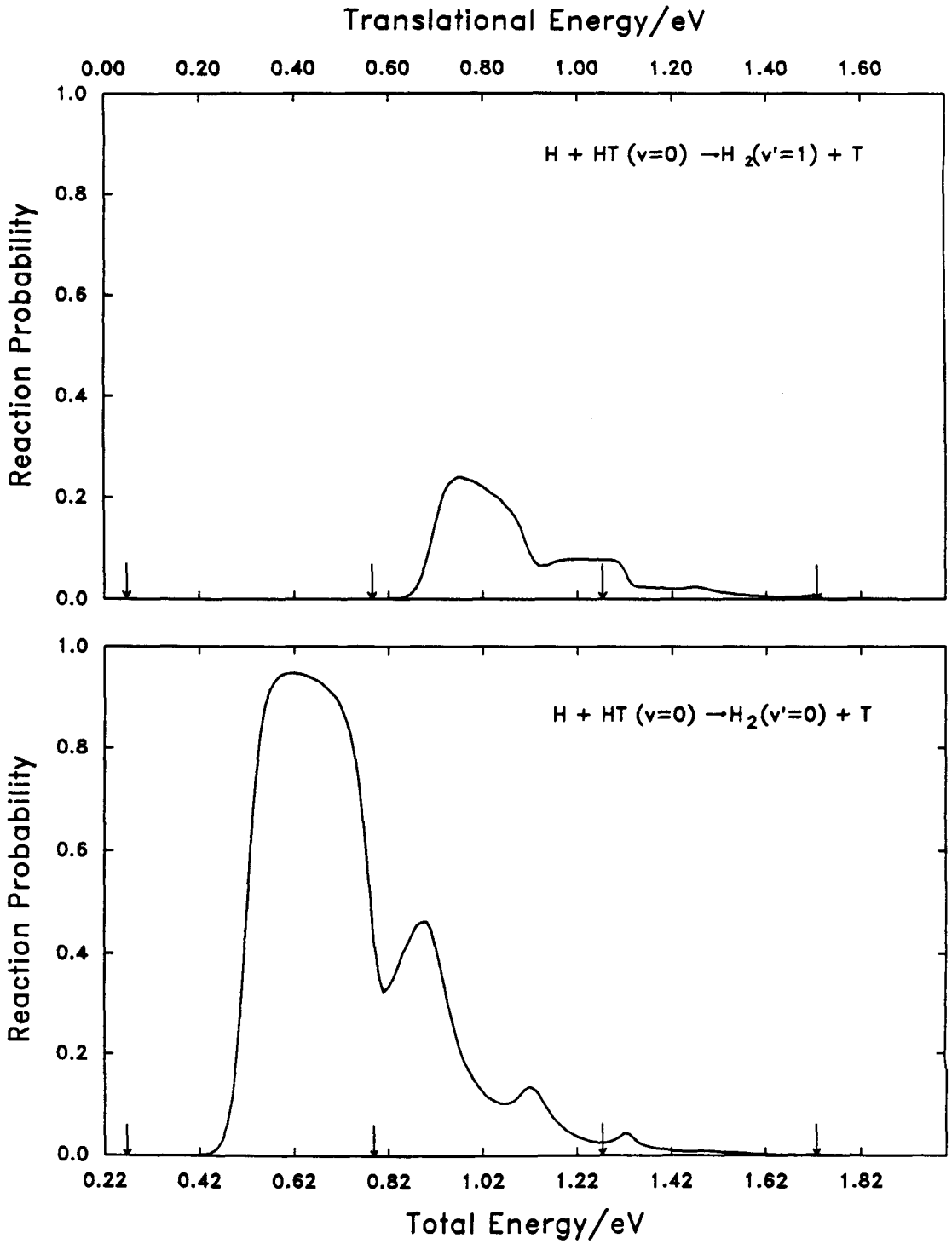
Translational Energy/eV
0.00
0.20
0.40
0.60
0.80
1.00
1.20
1.40
1.60
1.0
0.8
0.6
0.4
0.2
0.0
Reaction Probability
H + HT (v=0) →H 2(v'=1) + T
Reaction Probability
H + HT (v=0) →H2(v'=0) + T
0.22
0.42
0.62
0.82
1.02
1.22
1.42
1.62
1.82
Total Energy/eV

Figure 17.

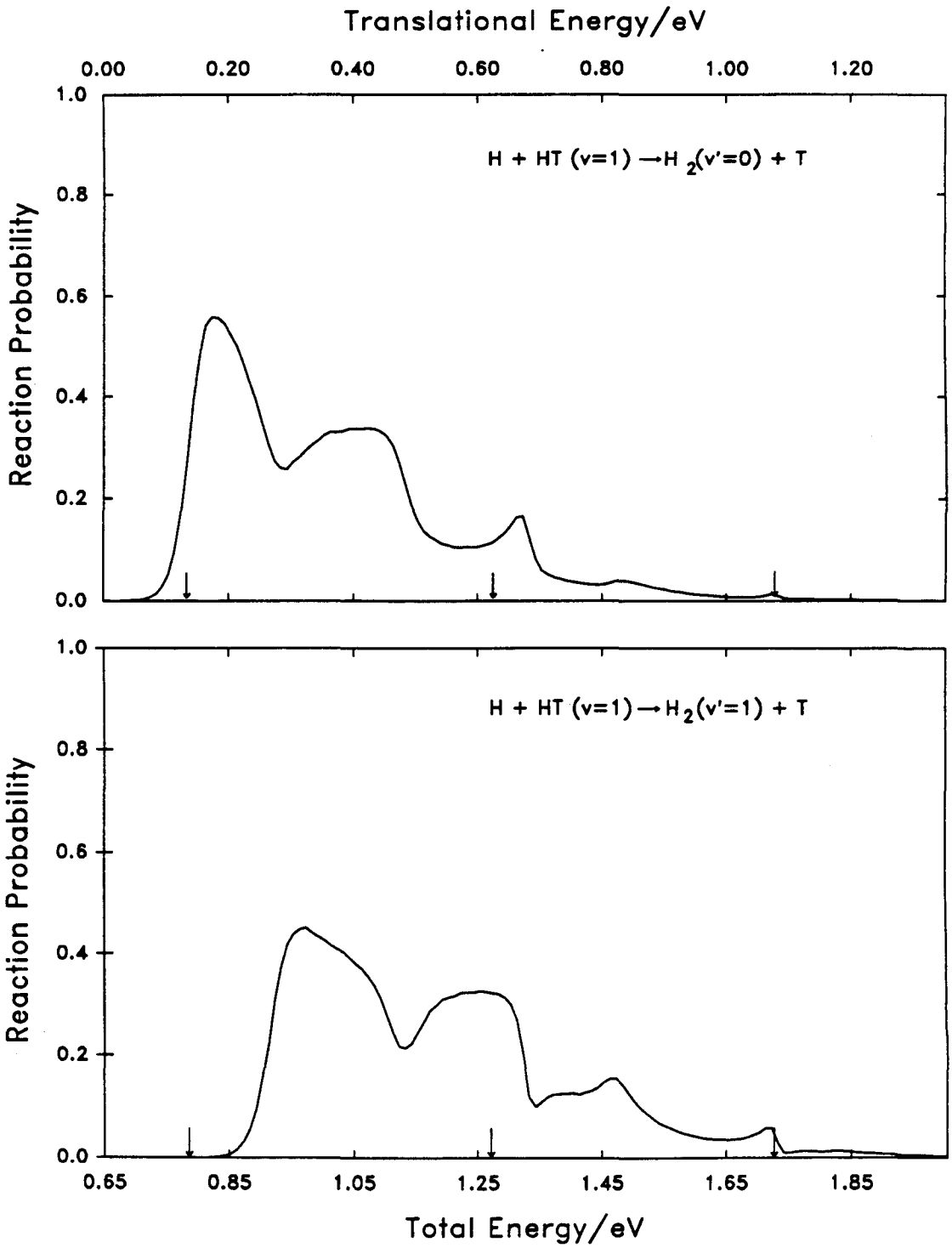
Translational Energy/eV
0.00
0.20
0.40
0.60
0.80
1.00
1.20
H + HT (v=1) → H 2(v'=0) + T
Reaction Probability
1.0
0.8
0.6
0.4
0.2
0.0
H + HT (v=1) → H2(v'=1) + T
Reaction Probability
0.65
0.85
1.05
1.25
1.45
1.65
1.85
Total Energy/eV

Figure 18.

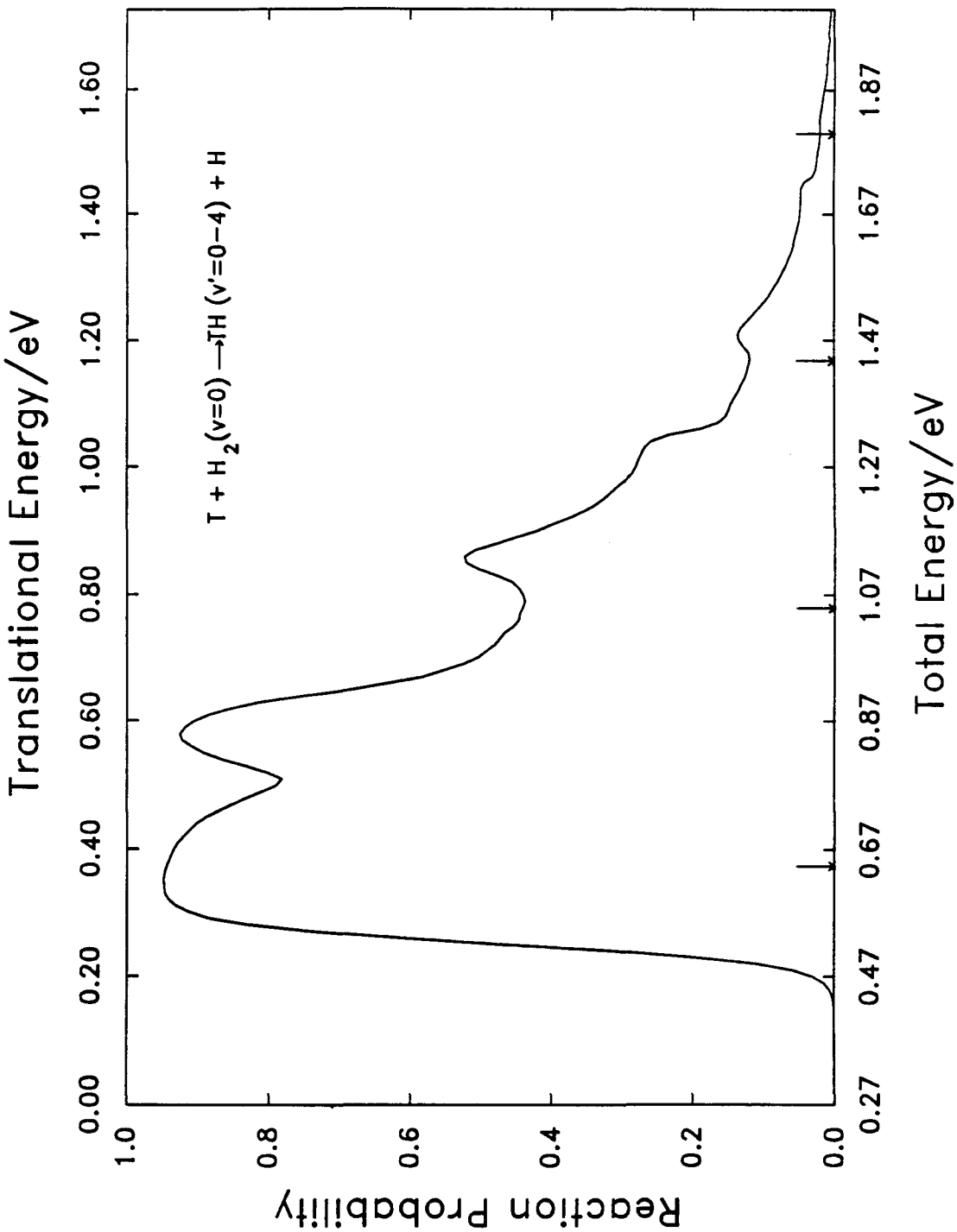
Translational Energy/eV
0.00
0.20
0.40
0.60
0.80
1.00
1.20
1.40
1.60
T + H2(v=0) ⟶ TH (v'=0–4) + H
Reaction Probability
1.0
0.8
0.6
0.4
0.2
0.0
Total Energy/eV
0.27
0.47
0.67
0.87
1.07
1.27
1.47
1.67
1.87

Figure 19.

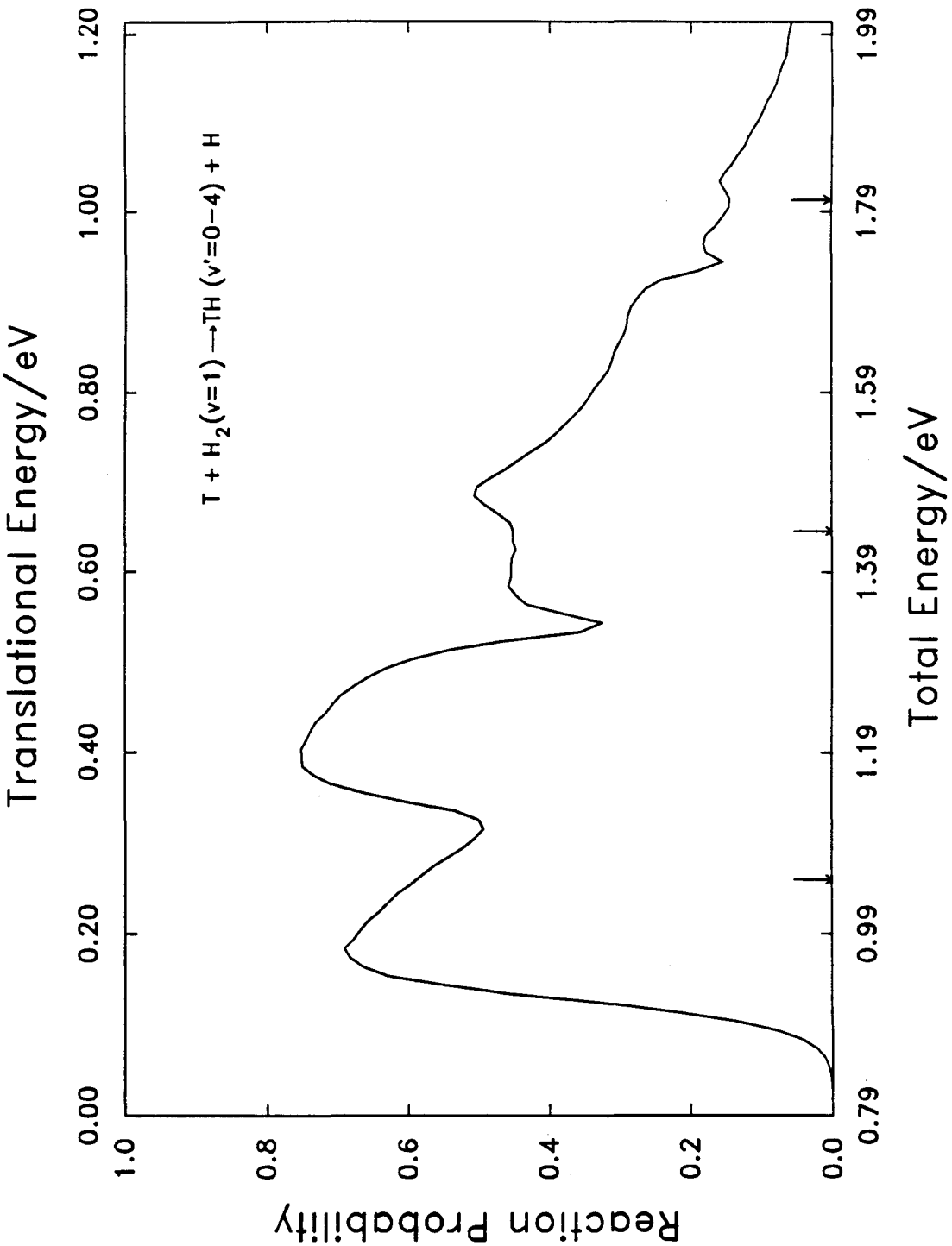
Translational Energy/eV
0.00
0.20
0.40
0.60
0.80
1.00
1.20
T + H2(v=1) → TH (v'=0–4) + H
Reaction Probability
1.0
0.8
0.6
0.4
0.2
0.0
0.79
0.99
1.19
1.39
1.59
1.79
1.99
Total Energy/eV

Figure 20.

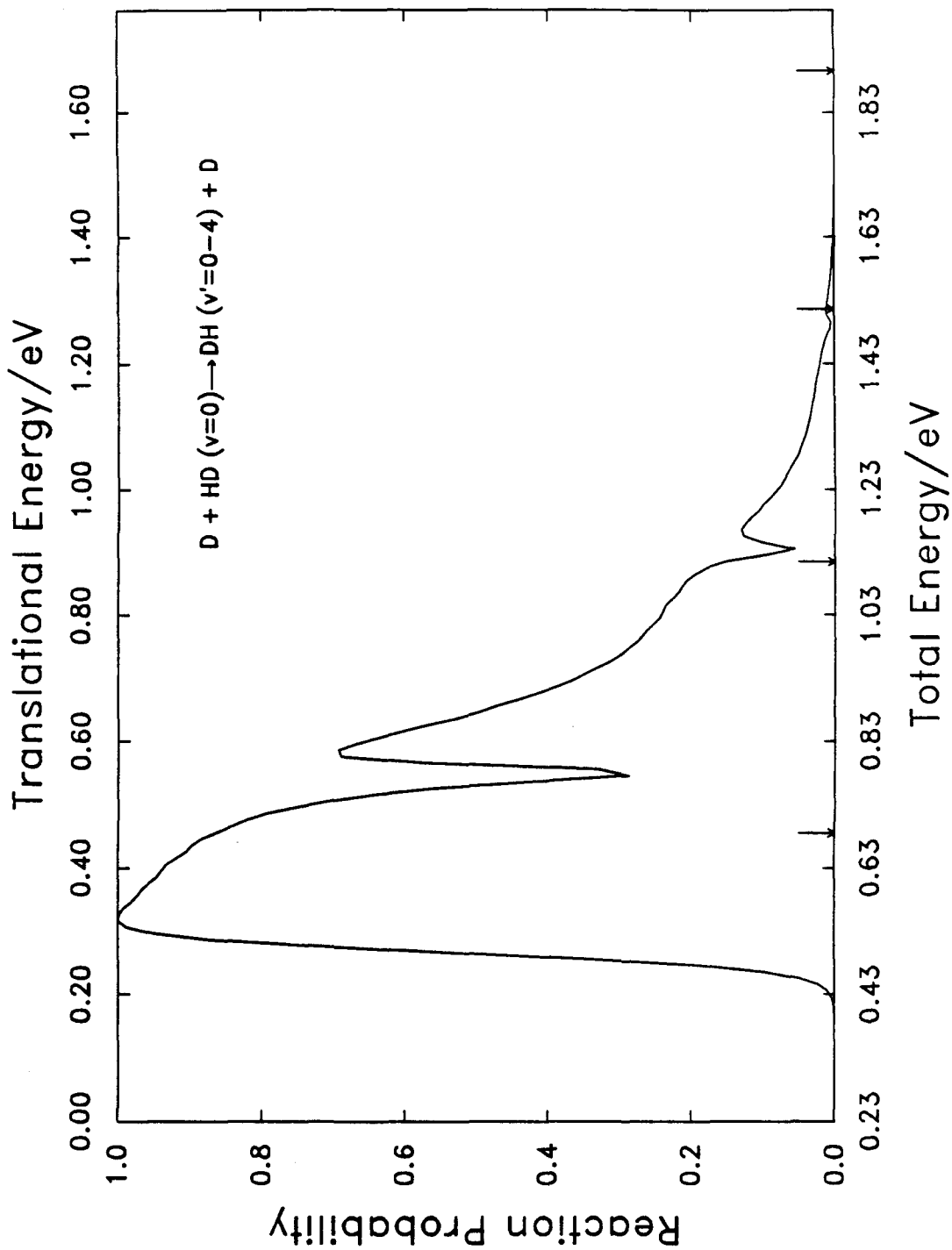
D + HD (v=0)⟶DH (v'=0−4) + D
Reaction Probability
1.0
0.8
0.6
0.4
0.2
0.0
Translational Energy/eV
0.00
0.20
0.40
0.60
0.80
1.00
1.20
1.40
1.60
Total Energy/eV
0.23
0.43
0.63
0.83
1.03
1.23
1.43
1.63
1.83

Figure 21.

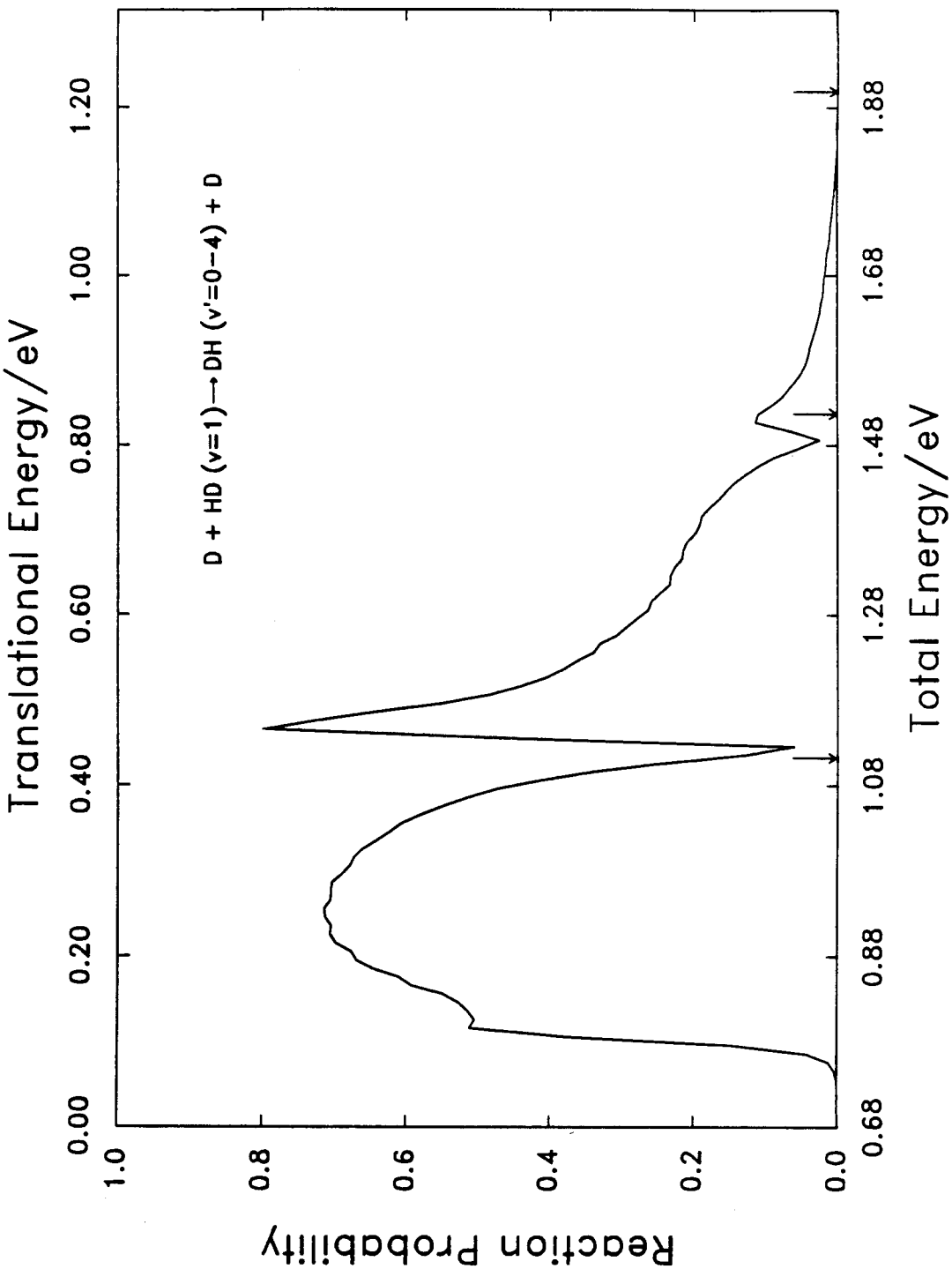
D + HD (v=1)⟶ DH (v'=0-4) + D
Translational Energy/eV
0.00
0.20
0.40
0.60
0.80
1.00
1.20
Reaction Probability
1.0
0.8
0.6
0.4
0.2
0.0
Total Energy/eV
0.68
0.88
1.08
1.28
1.48
1.68
1.88

Figure 22.

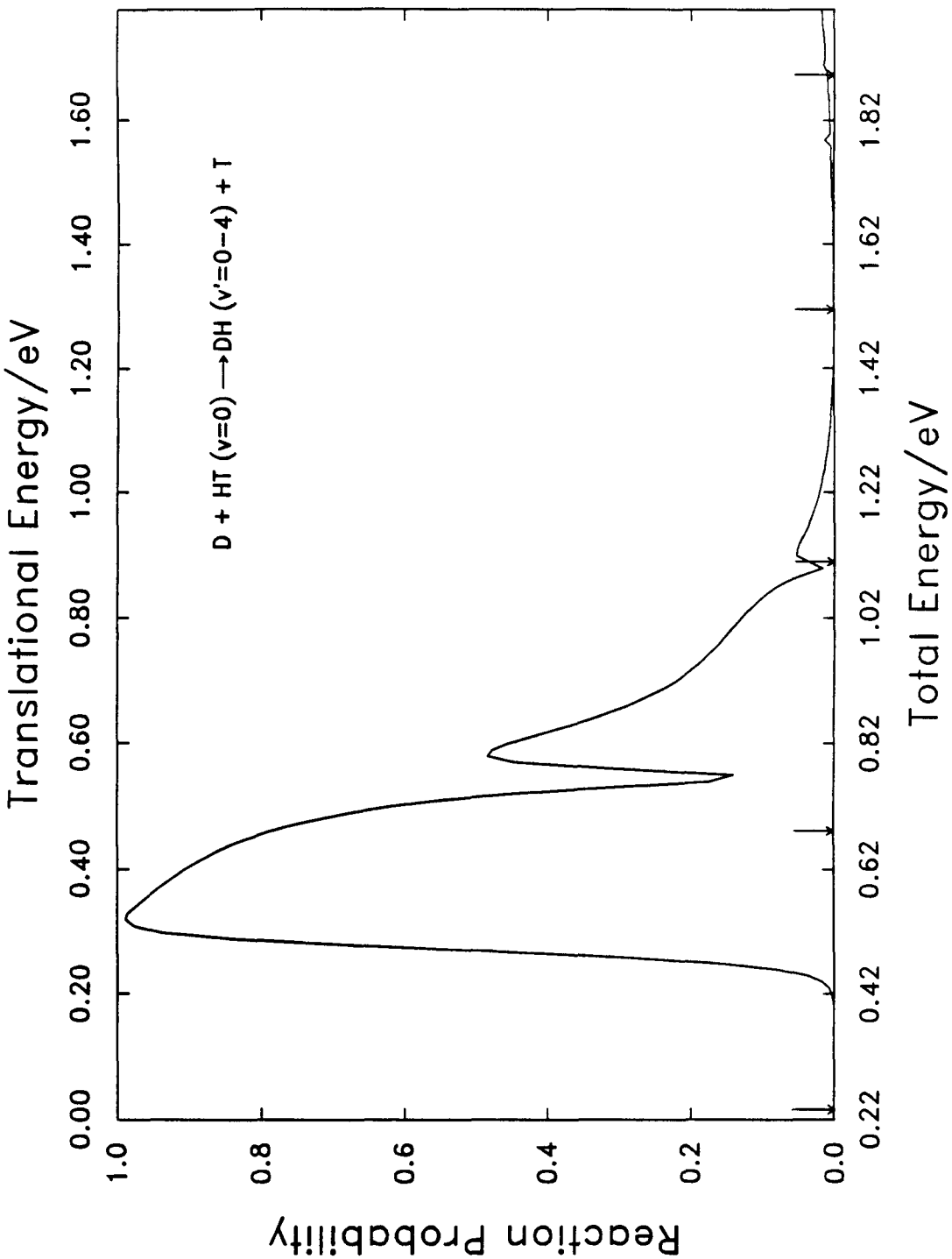
D + HT (v=0) ⟶ DH (v'=0–4) + T
Translational Energy/eV
0.00
0.20
0.40
0.60
0.80
1.00
1.20
1.40
1.60
Reaction Probability
1.0
0.8
0.6
0.4
0.2
0.0
Total Energy/eV
0.22
0.42
0.62
0.82
1.02
1.22
1.42
1.62
1.82

Figure 23.

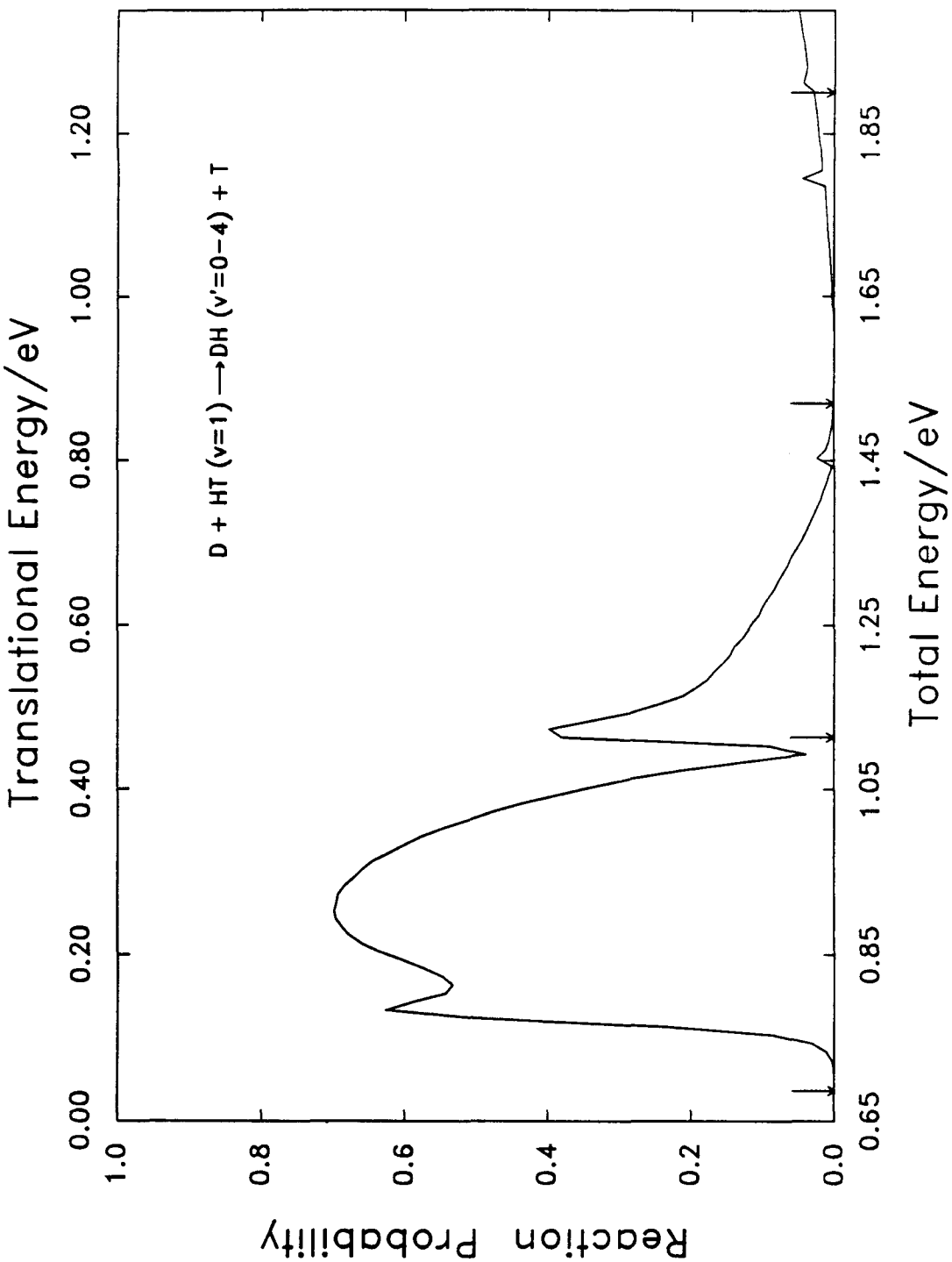
D + HT (v=1) ⟶ DH (v'=0-4) + T
Translational Energy/eV
0.00
0.20
0.40
0.60
0.80
1.00
1.20
Total Energy/eV
0.65
0.85
1.05
1.25
1.45
1.65
1.85
Reaction Probability
0.0
0.2
0.4
0.6
0.8
1.0

Figure 24.

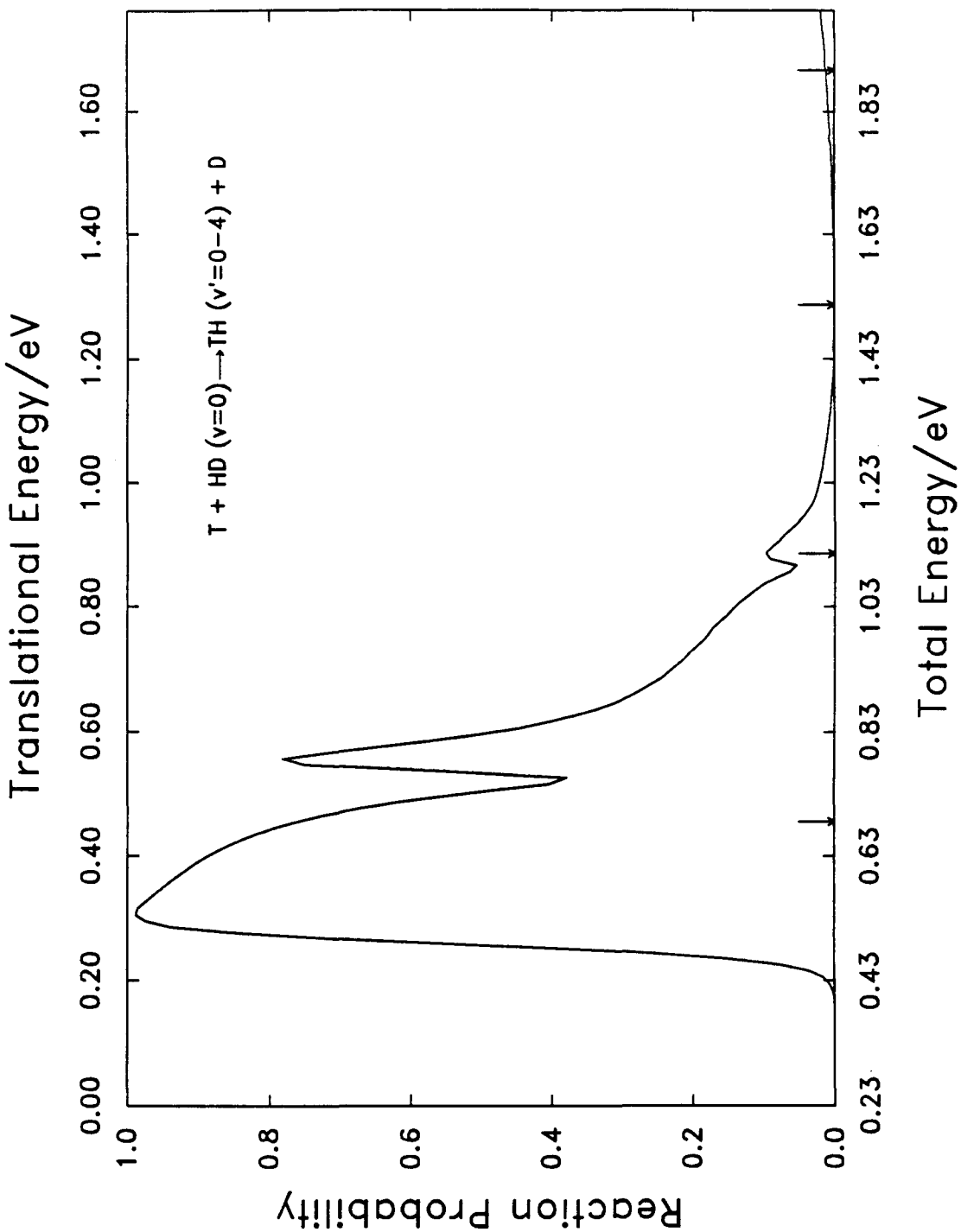
T + HD (v=0)⟶TH (v'=0-4) + D
Translational Energy/eV
0.00
0.20
0.40
0.60
0.80
1.00
1.20
1.40
1.60
Reaction Probability
1.0
0.8
0.6
0.4
0.2
0.0
Total Energy/eV
0.23
0.43
0.63
0.83
1.03
1.23
1.43
1.63
1.83

Figure 25.

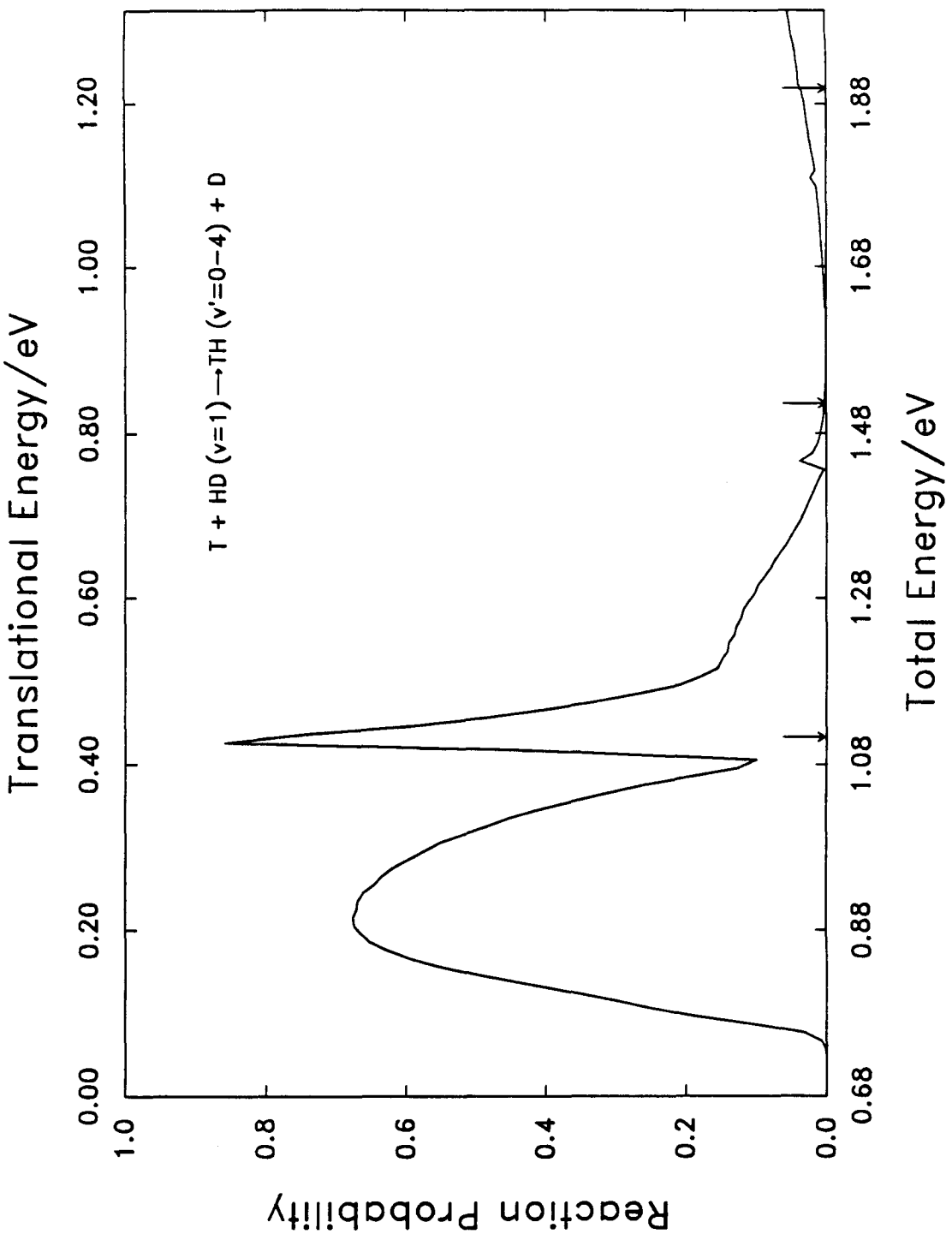
T + HD (v=1) ⟶ TH (v'=0−4) + D
Reaction Probability
Translational Energy/eV
Total Energy/eV
0.0
0.2
0.4
0.6
0.8
1.0
0.00
0.20
0.40
0.60
0.80
1.00
1.20
0.68
0.88
1.08
1.28
1.48
1.68
1.88

Figure 26.

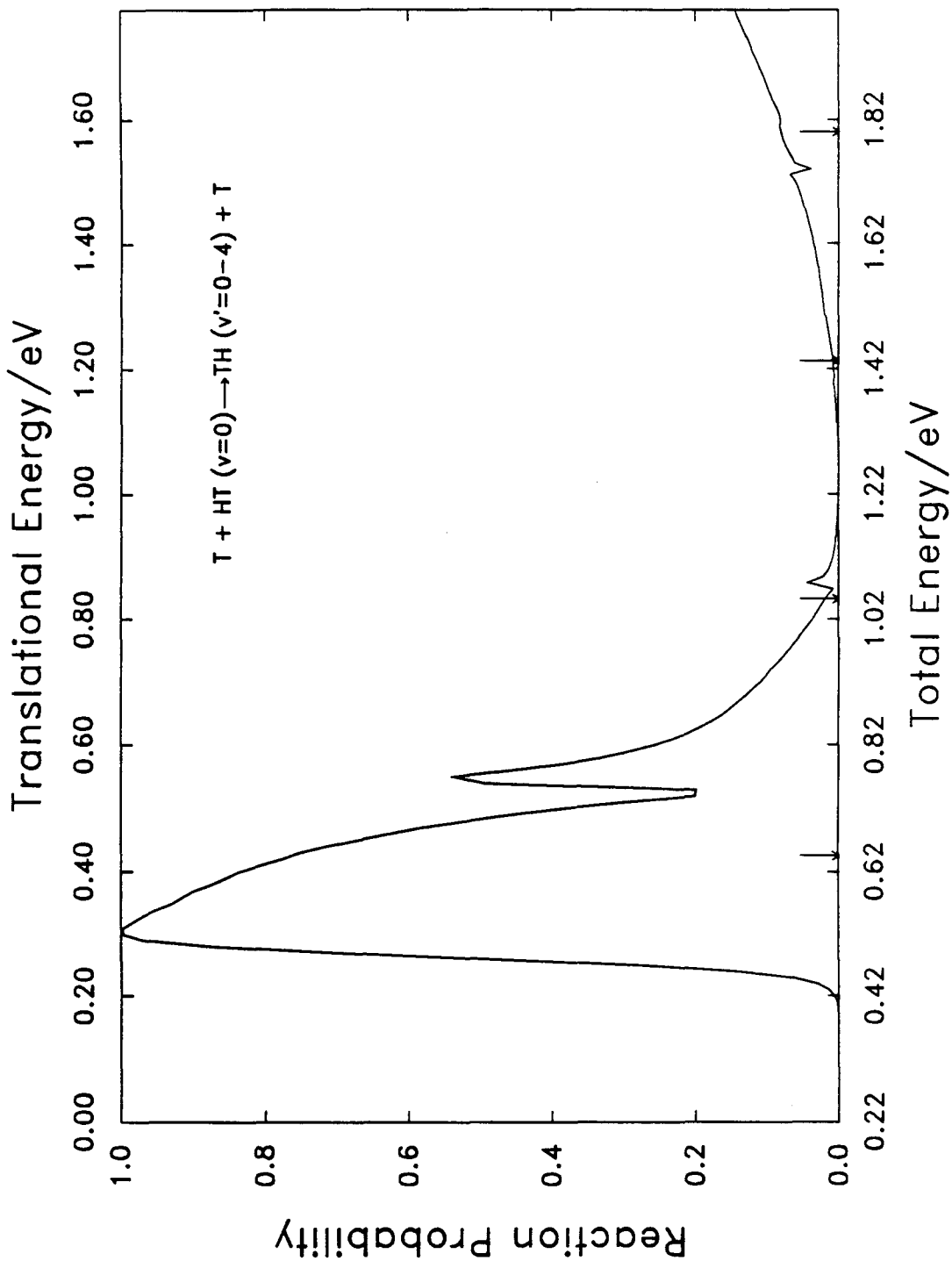
T + HT (v=0)⟶TH (v'=0-4) + T
Reaction Probability
Translational Energy/eV
Total Energy/eV
0.0
0.2
0.4
0.6
0.8
1.0
0.00
0.20
0.40
0.60
0.80
1.00
1.20
1.40
1.60
0.22
0.42
0.62
0.82
1.02
1.22
1.42
1.62
1.82

Figure 27.

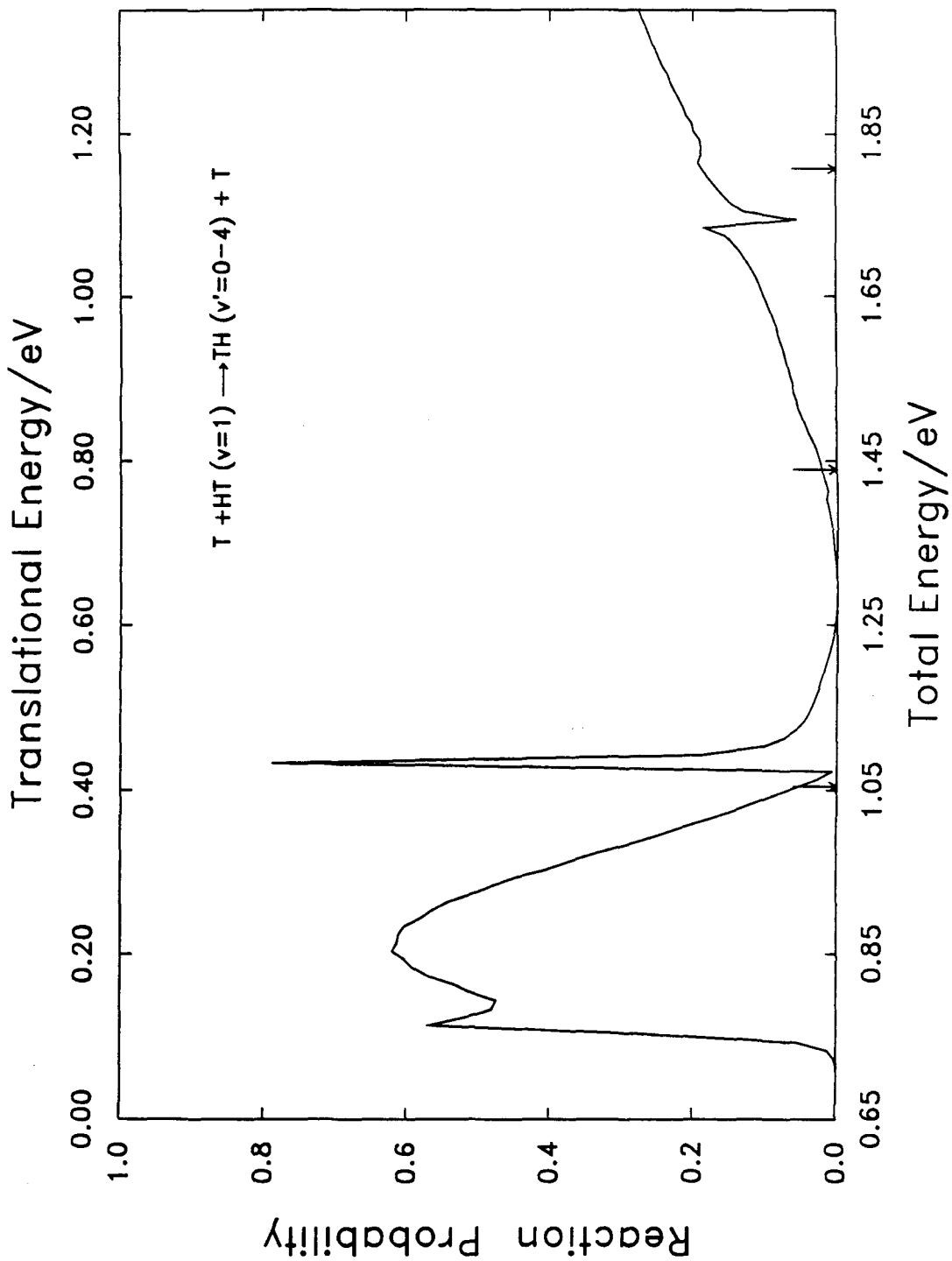
T +HT (v=1) ⟶TH (v'=0-4) + T
Translational Energy/eV
0.00
0.20
0.40
0.60
0.80
1.00
1.20
Reaction Probability
1.0
0.8
0.6
0.4
0.2
0.0
Total Energy/eV
0.65
0.85
1.05
1.25
1.45
1.65
1.85

Figure 28.

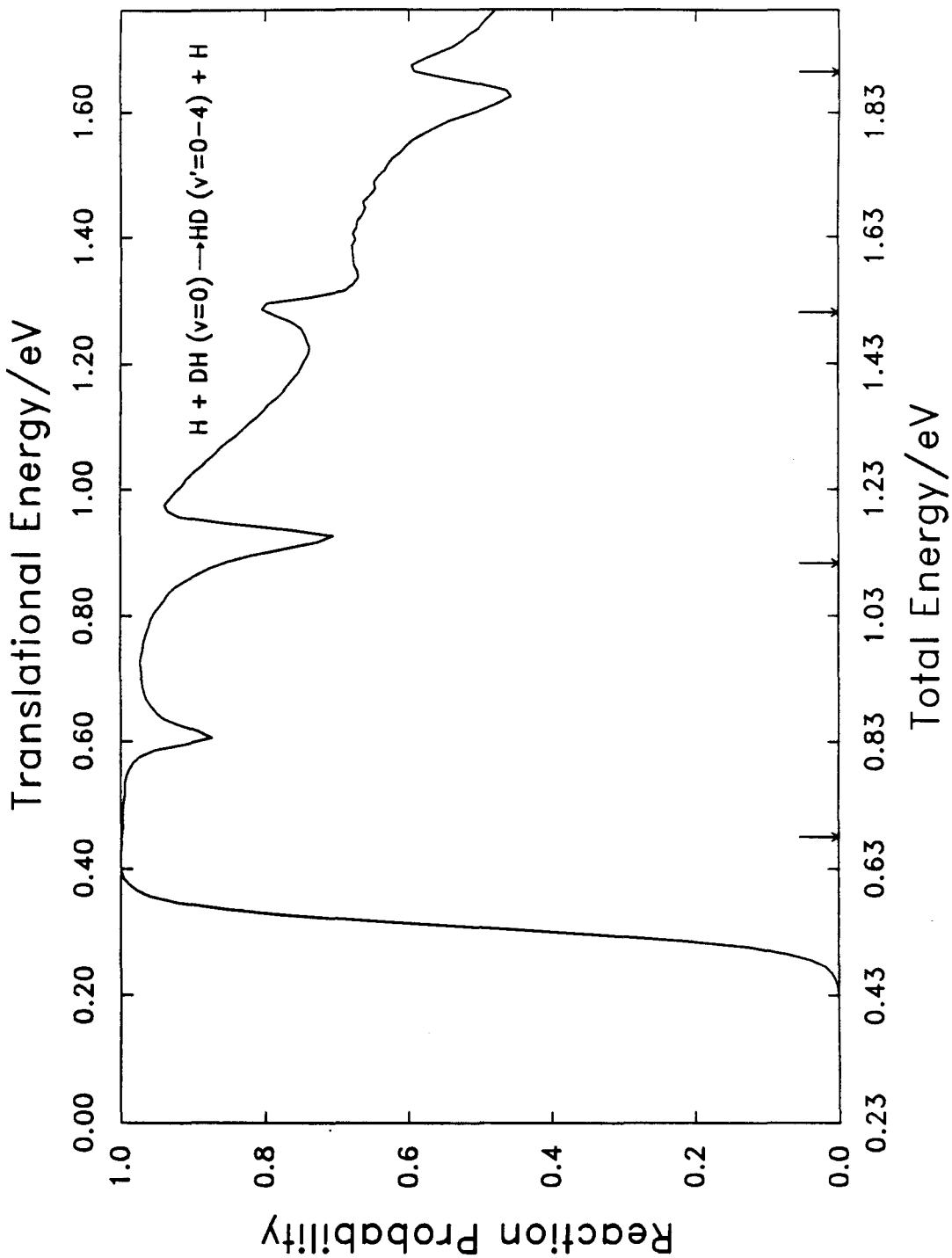
H + DH (v=0) → HD (v'=0–4) + H
Reaction Probability
Translational Energy/eV
Total Energy/eV
0.00
0.20
0.40
0.60
0.80
1.00
1.20
1.40
1.60
1.0
0.8
0.6
0.4
0.2
0.0
0.23
0.43
0.63
0.83
1.03
1.23
1.43
1.63
1.83

Figure 29.

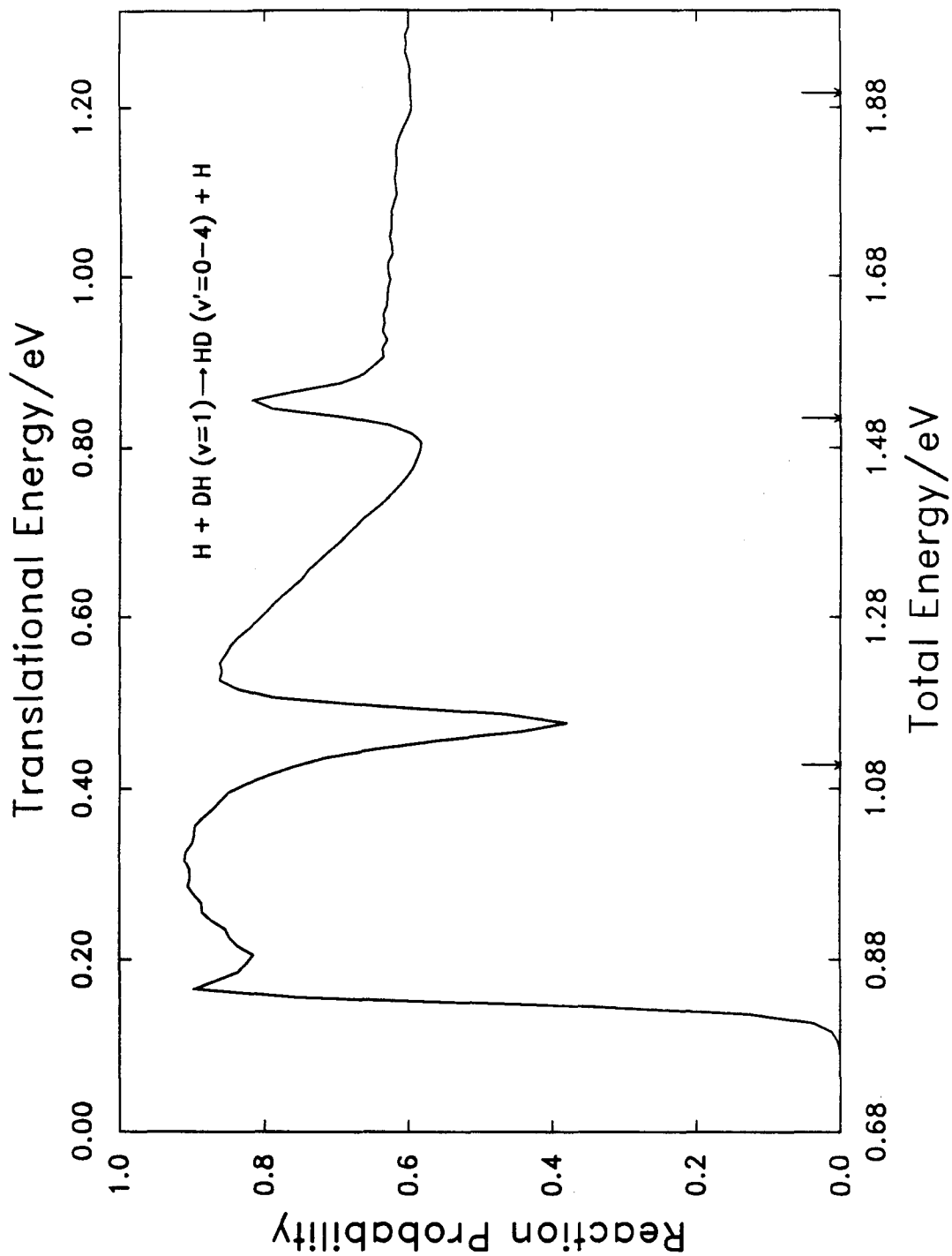
H + DH (v=1) ⟶ HD (v'=0−4) + H
Reaction Probability
Translational Energy/eV
Total Energy/eV
0.0
0.2
0.4
0.6
0.8
1.0
0.00
0.20
0.40
0.60
0.80
1.00
1.20
0.68
0.88
1.08
1.28
1.48
1.68
1.88

Figure 30.

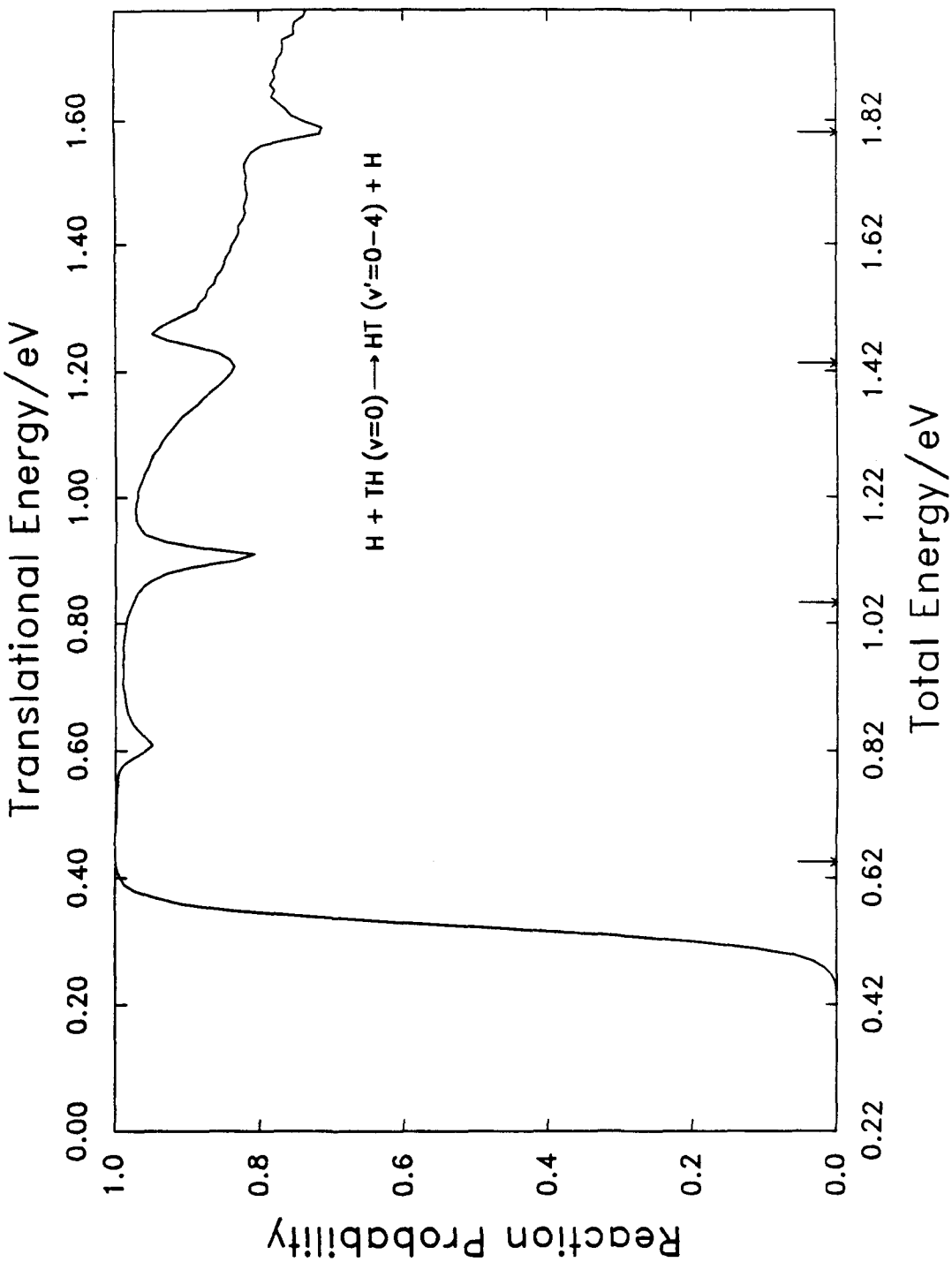
Translational Energy/eV
0.00
0.20
0.40
0.60
0.80
1.00
1.20
1.40
1.60
Reaction Probability
1.0
0.8
0.6
0.4
0.2
0.0
H + TH (v=0) ⟶ HT (v'=0-4) + H
0.22
0.42
0.62
0.82
1.02
1.22
1.42
1.62
1.82
Total Energy/eV

Figure 31.

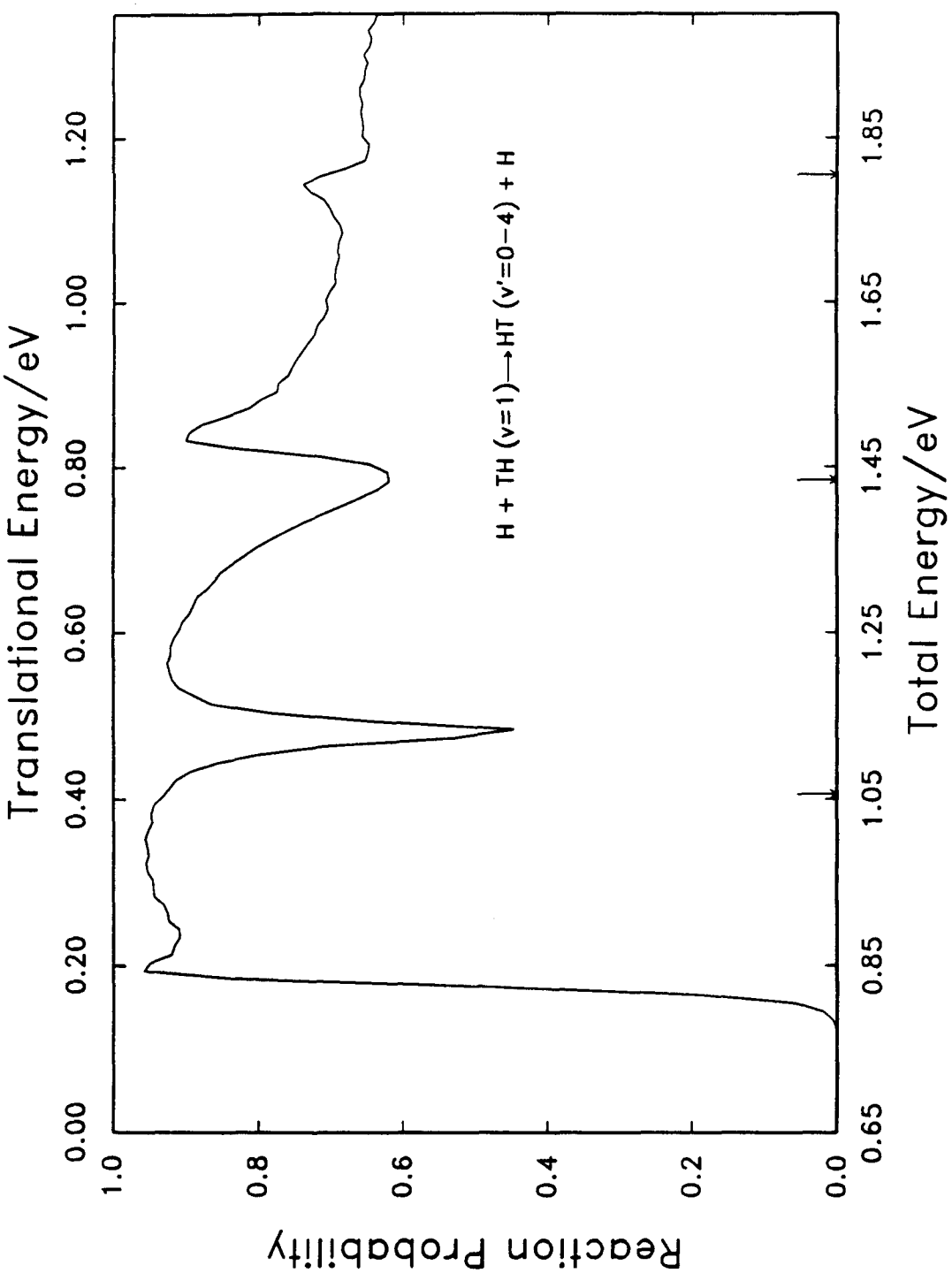
Translational Energy/eV
0.00
0.20
0.40
0.60
0.80
1.00
1.20
Total Energy/eV
0.65
0.85
1.05
1.25
1.45
1.65
1.85
Reaction Probability
1.0
0.8
0.6
0.4
0.2
0.0
H + TH (v=1)⟶HT (v'=0−4) + H

Figure 32.

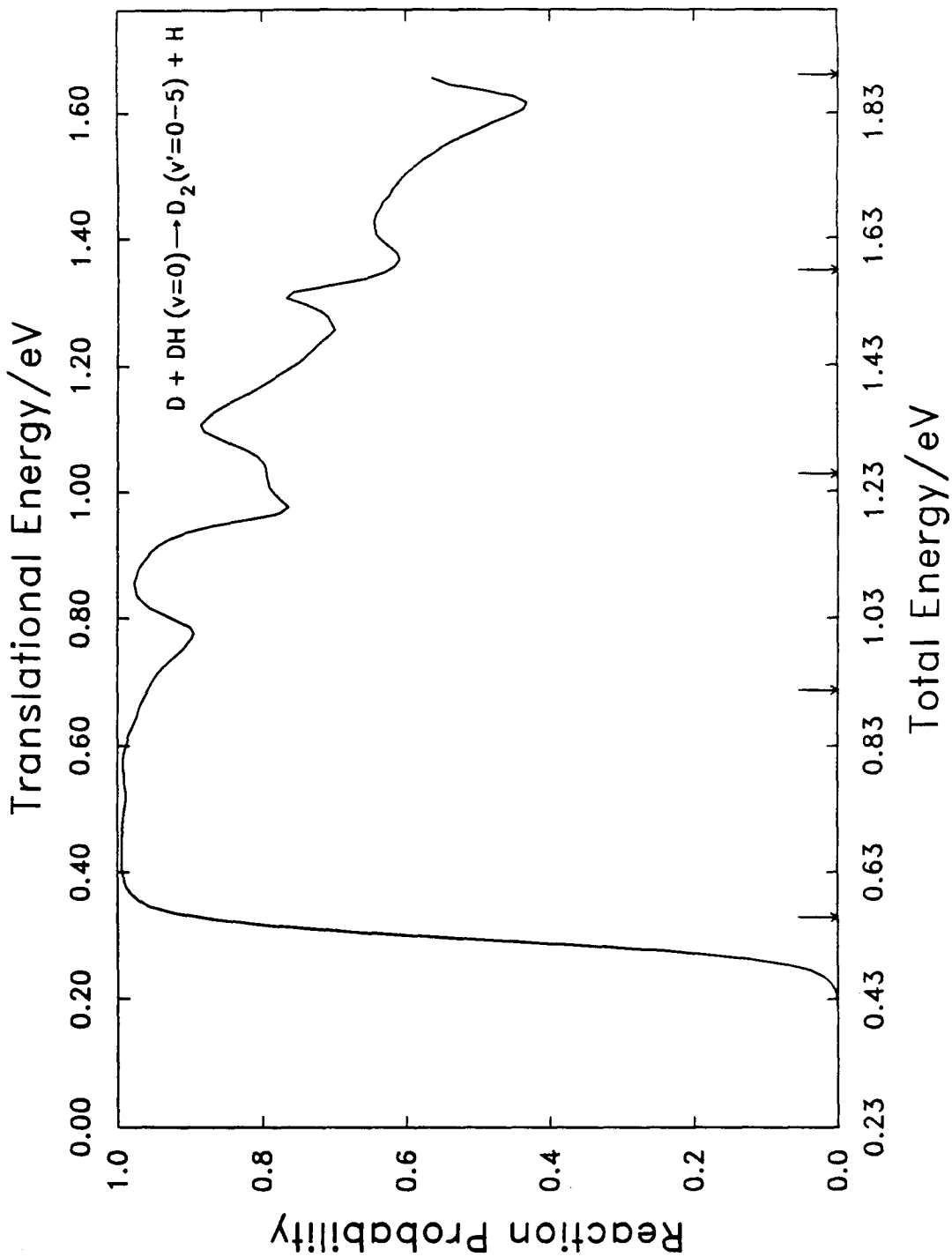
D + DH (v=0) → D2(v'=0-5) + H
Reaction Probability
Translational Energy/eV
Total Energy/eV
0.00
0.20
0.40
0.60
0.80
1.00
1.20
1.40
1.60
1.0
0.8
0.6
0.4
0.2
0.0
0.23
0.43
0.63
0.83
1.03
1.23
1.43
1.63
1.83

Figure 33.

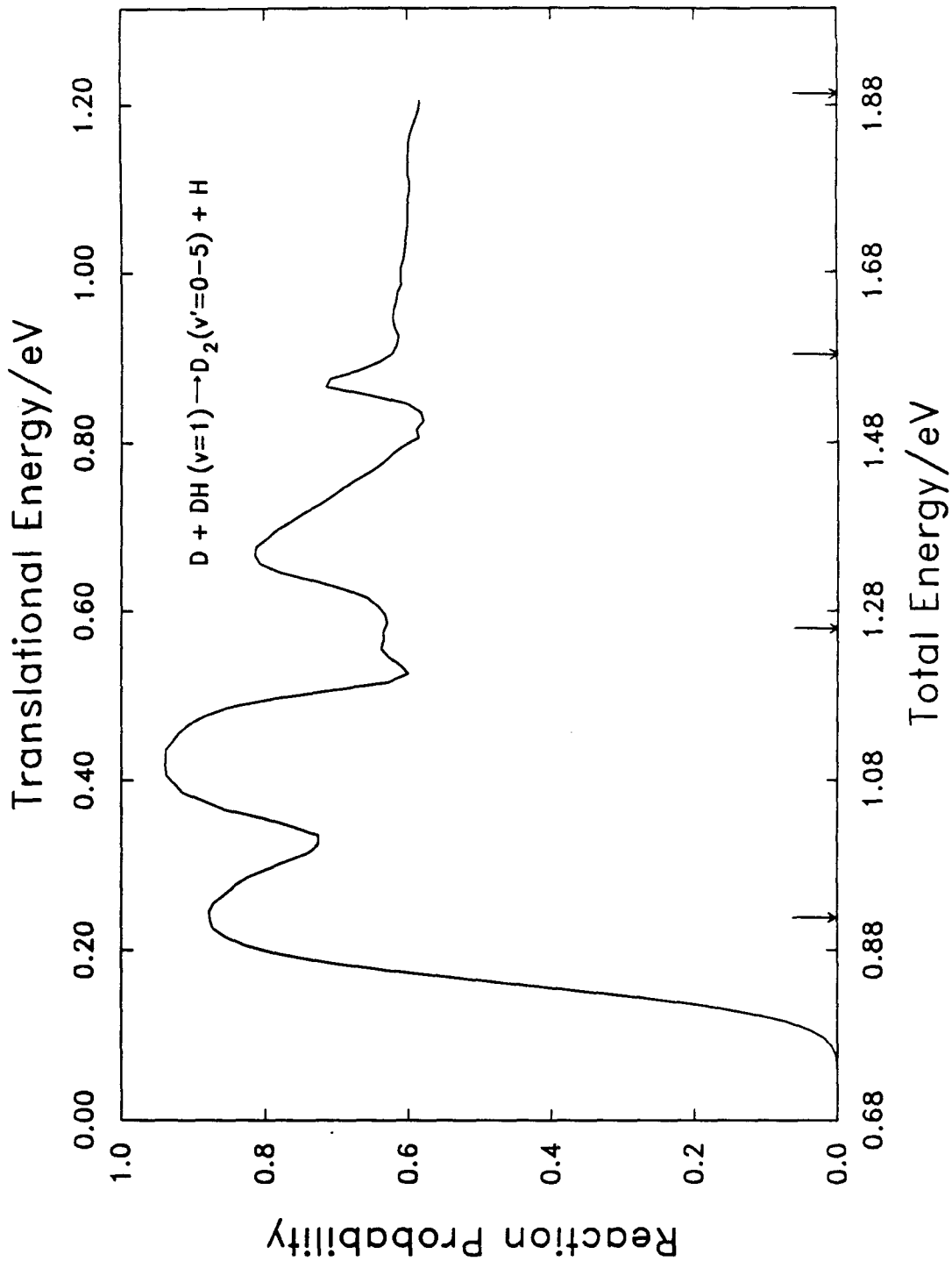
Translational Energy/eV
0.00
0.20
0.40
0.60
0.80
1.00
1.20
Reaction Probability
1.0
0.8
0.6
0.4
0.2
0.0
D + DH (v=1) → D2(v'=0-5) + H
0.68
0.88
1.08
1.28
1.48
1.68
1.88
Total Energy/eV

Figure 34.

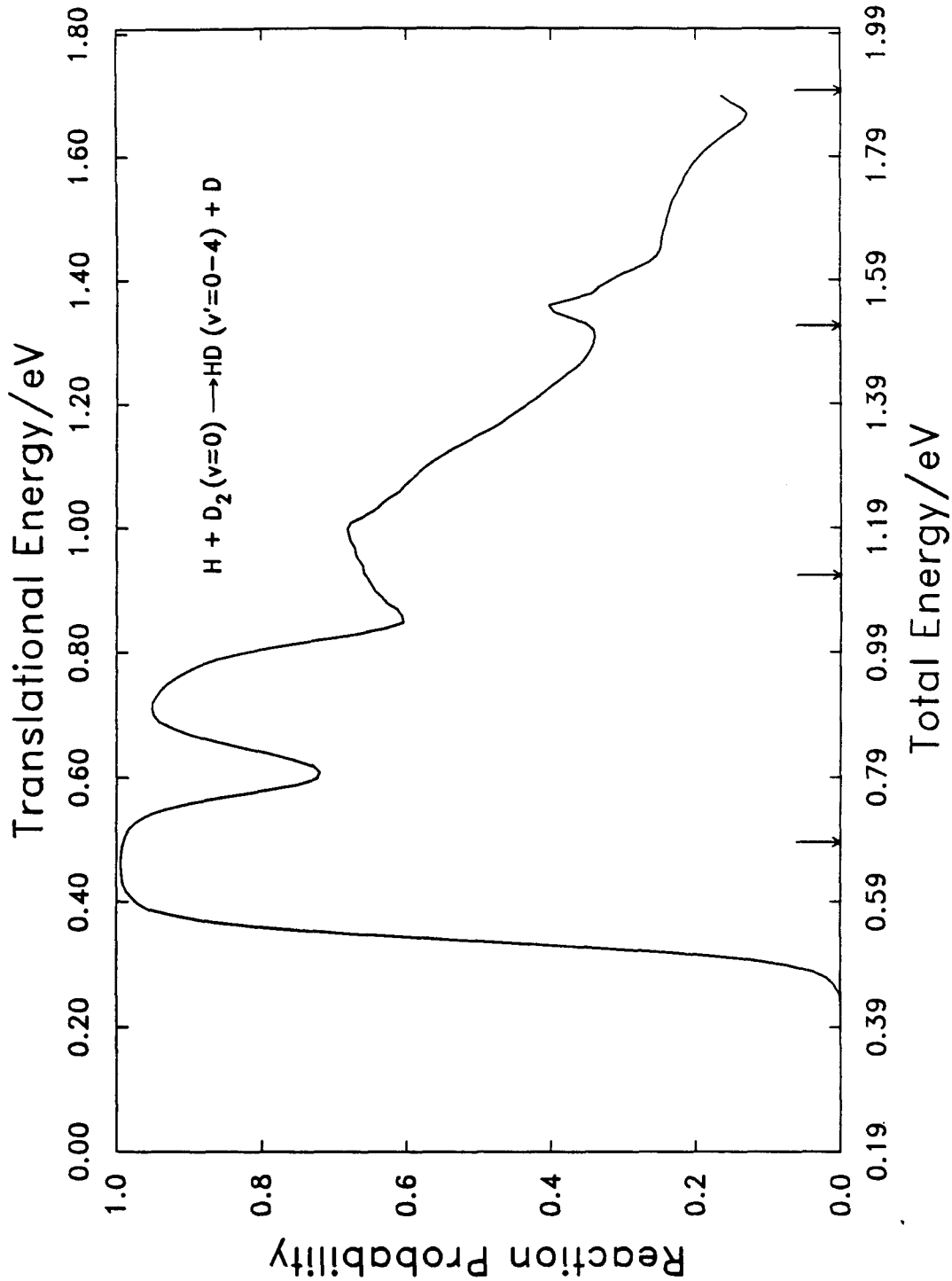
H + D2 (v=0) ⟶ HD (v'=0-4) + D
Translational Energy/eV
0.00
0.20
0.40
0.60
0.80
1.00
1.20
1.40
1.60
1.80
Total Energy/eV
0.19
0.39
0.59
0.79
0.99
1.19
1.39
1.59
1.79
1.99
Reaction Probability
1.0
0.8
0.6
0.4
0.2
0.0

Figure 35.

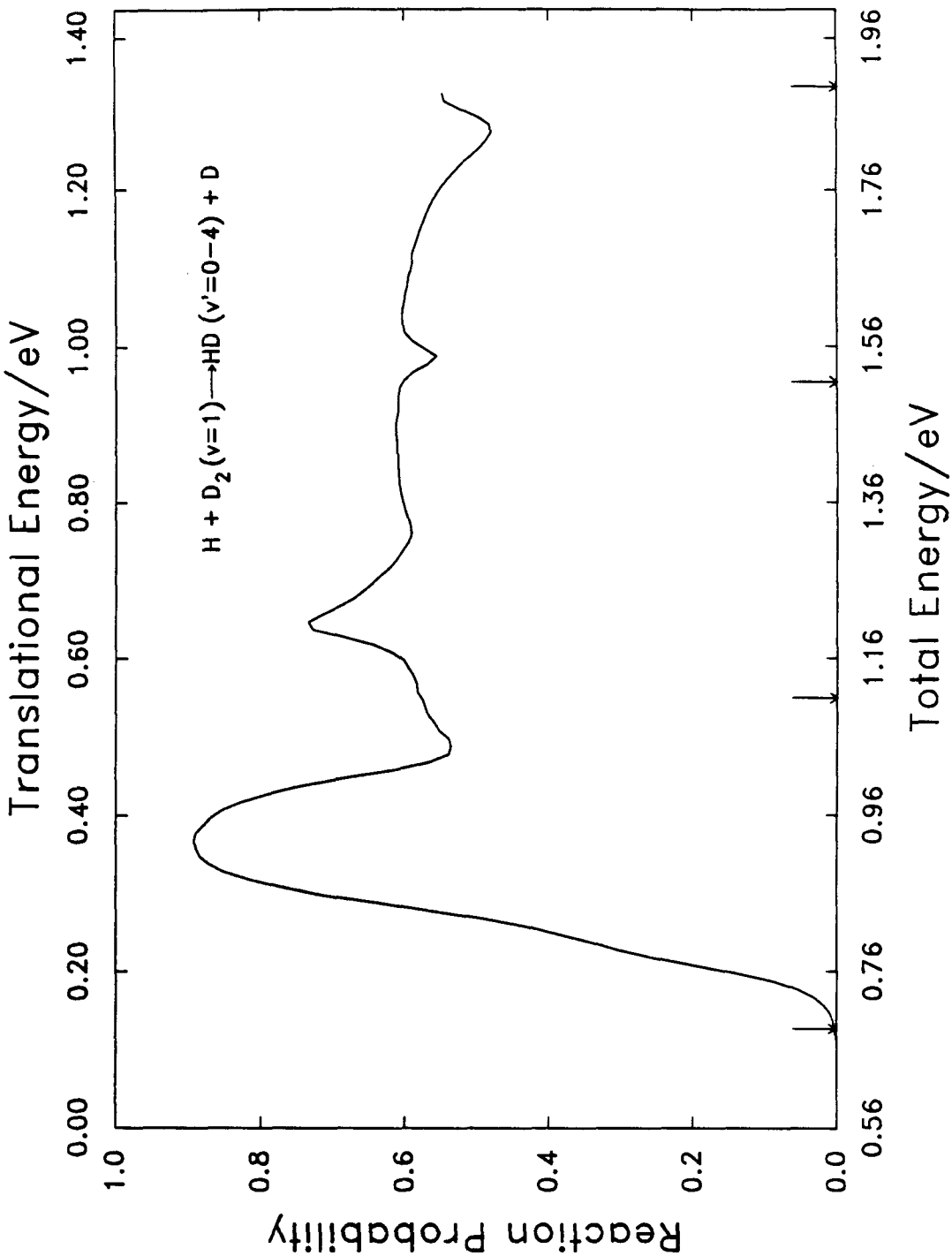
H + D2 (v=1)⟶HD (v'=0−4) + D
Translational Energy/eV
0.00
0.20
0.40
0.60
0.80
1.00
1.20
1.40
Total Energy/eV
0.56
0.76
0.96
1.16
1.36
1.56
1.76
1.96
Reaction Probability
0.0
0.2
0.4
0.6
0.8
1.0

Figure 36.

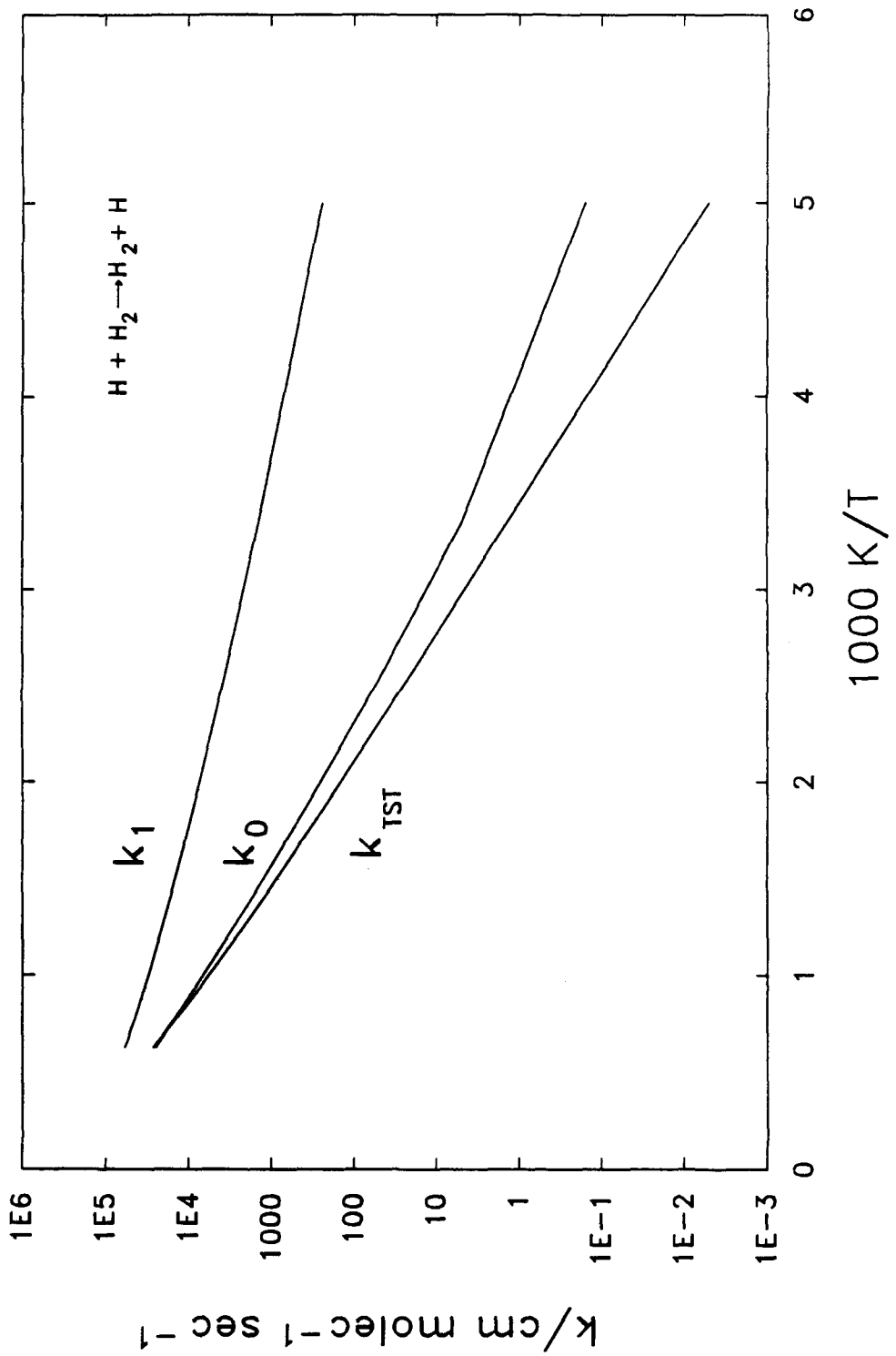
H + H2→H2+ H
k1
k0
kTST
k/cm molec−1 sec−1
1E6
1E5
1E4
1000
100
10
1
1E−1
1E−2
1E−3
0
1
2
3
4
5
6
1000 K/T

Figure 37.

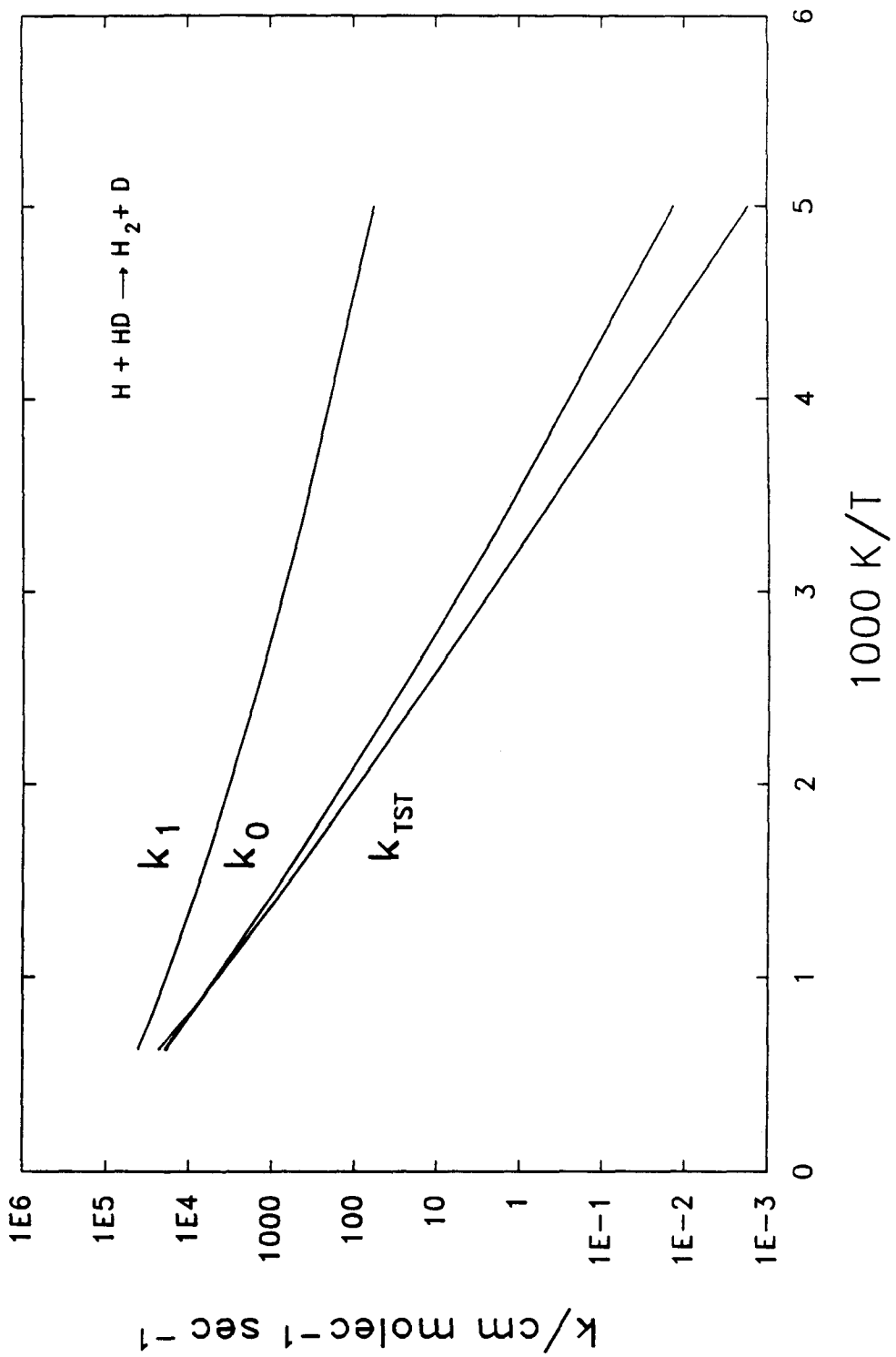
H + HD ⟶ H2 + D
k1
k0
kTST
k/cm mole−1 sec−1
1E6
1E5
1E4
1000
100
10
1
1E−1
1E−2
1E−3
0
1
2
3
4
5
6
1000 K/T

Figure 38.

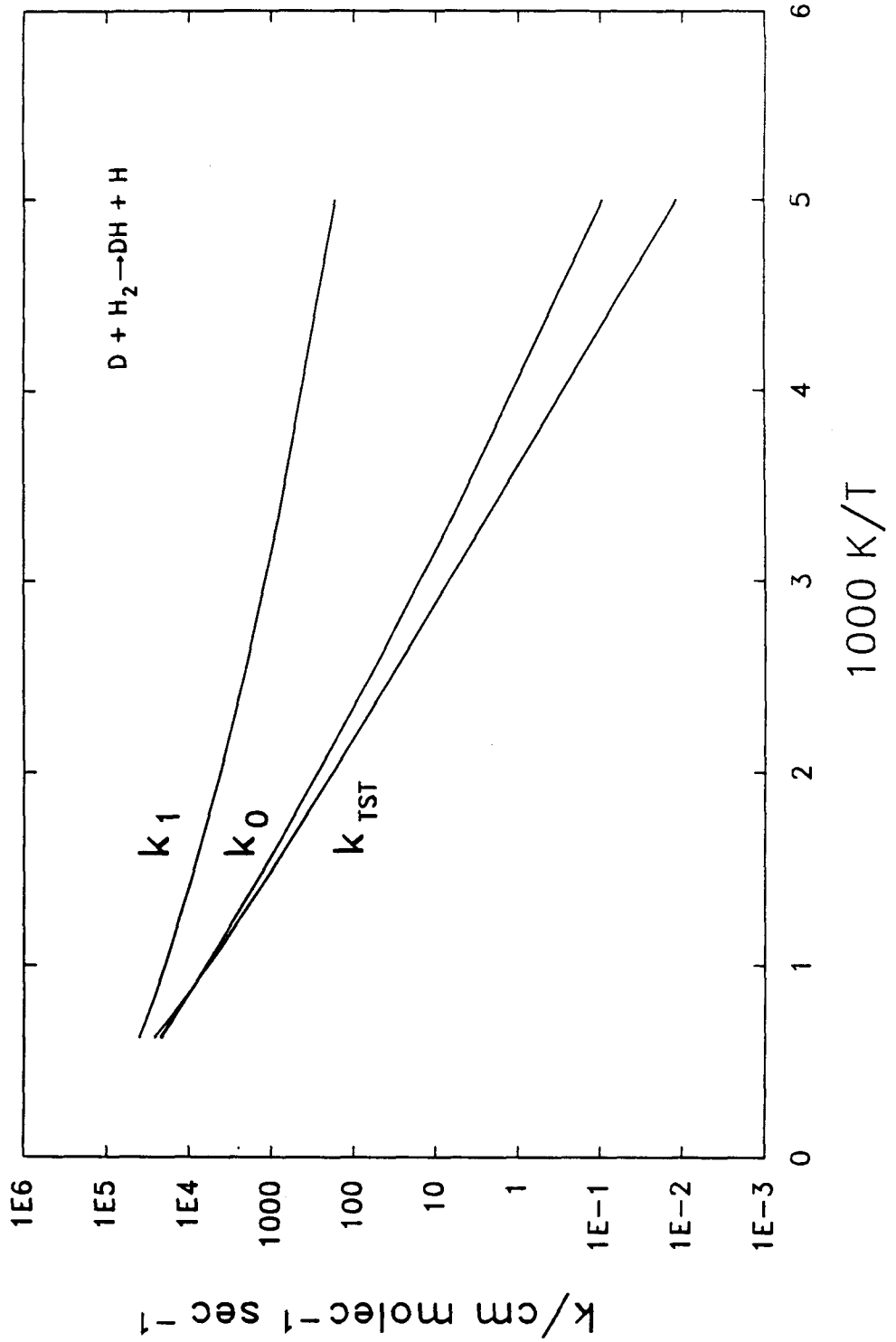
D + H2→DH + H
k1
k0
kTST
k/cm molec-1 sec-1
1E6
1E5
1E4
1000
100
10
1
1E-1
1E-2
1E-3
0
1
2
3
4
5
6
1000 K/T

Figure 39.

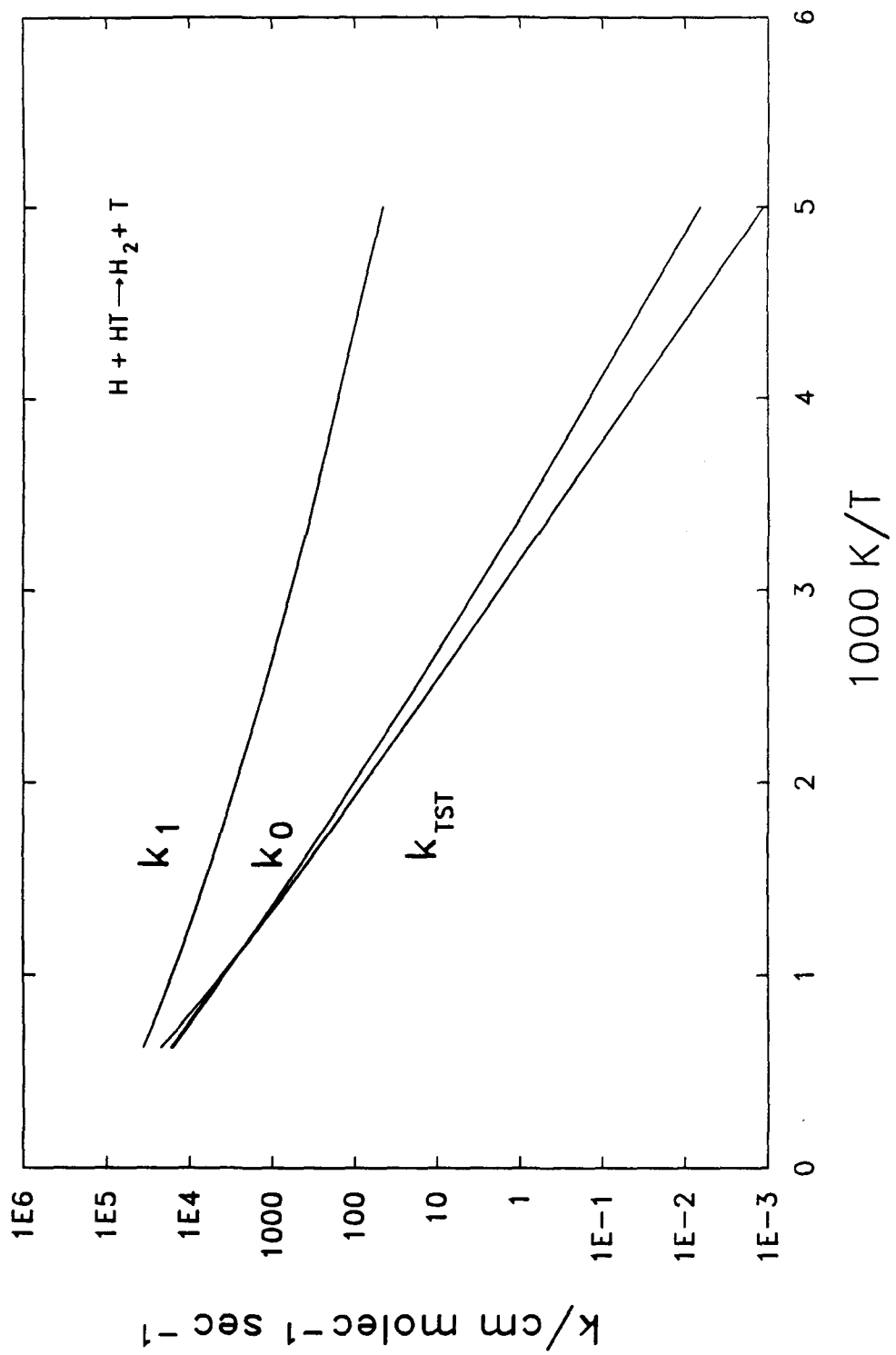
H + HT → H2 + T
k1
k0
kTST
k/cm molec-1 sec-1
1E6
1E5
1E4
1000
100
10
1
1E-1
1E-2
1E-3
0
1
2
3
4
5
6
1000 K/T

Figure 40.

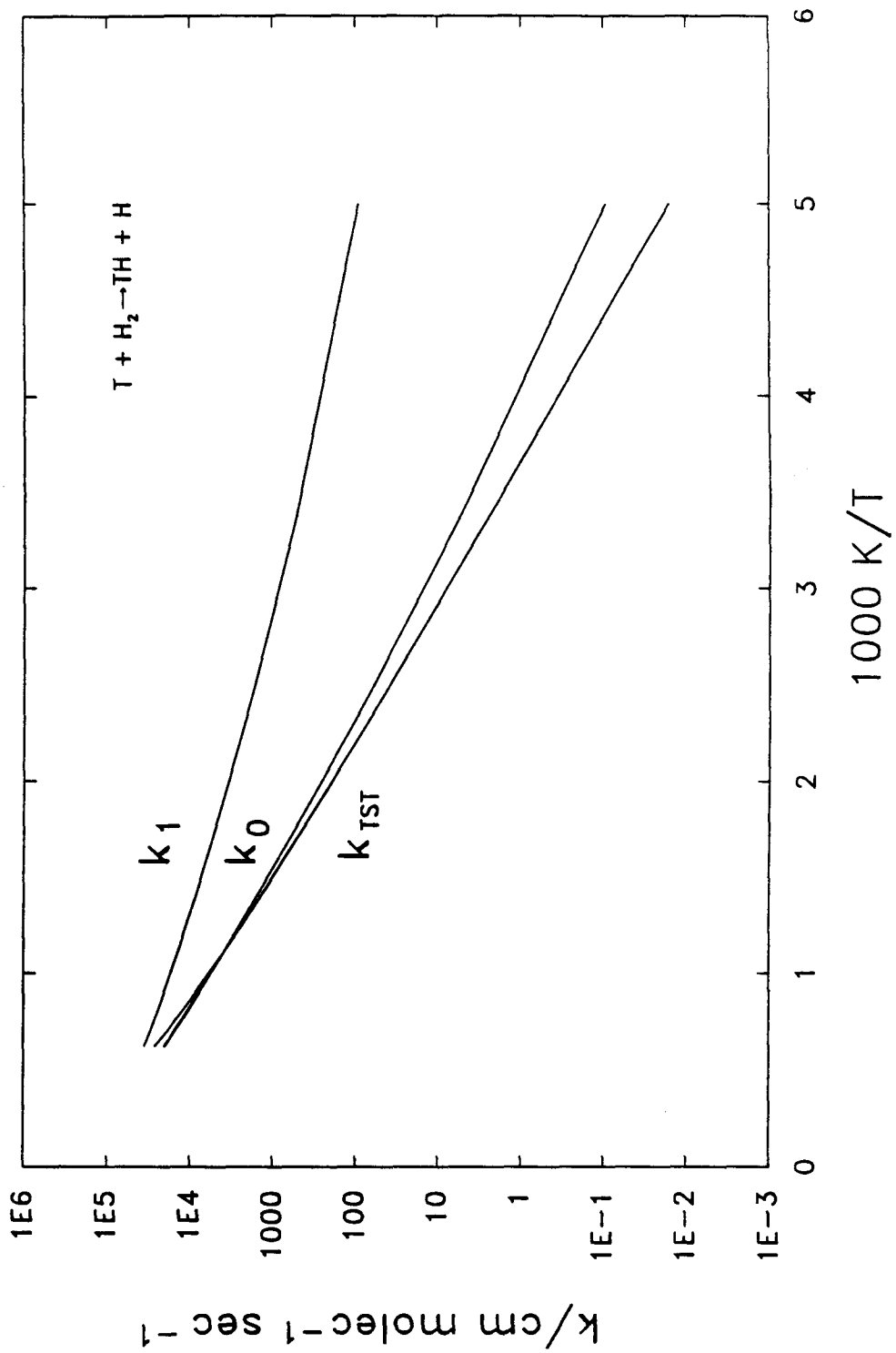
T + H2→TH + H
k1
k0
kTST
k/cm mole−1 sec−1
1E6
1E5
1E4
1000
100
10
1
1E−1
1E−2
1E−3
0
1
2
3
4
5
6
1000 K/T

Figure 41.

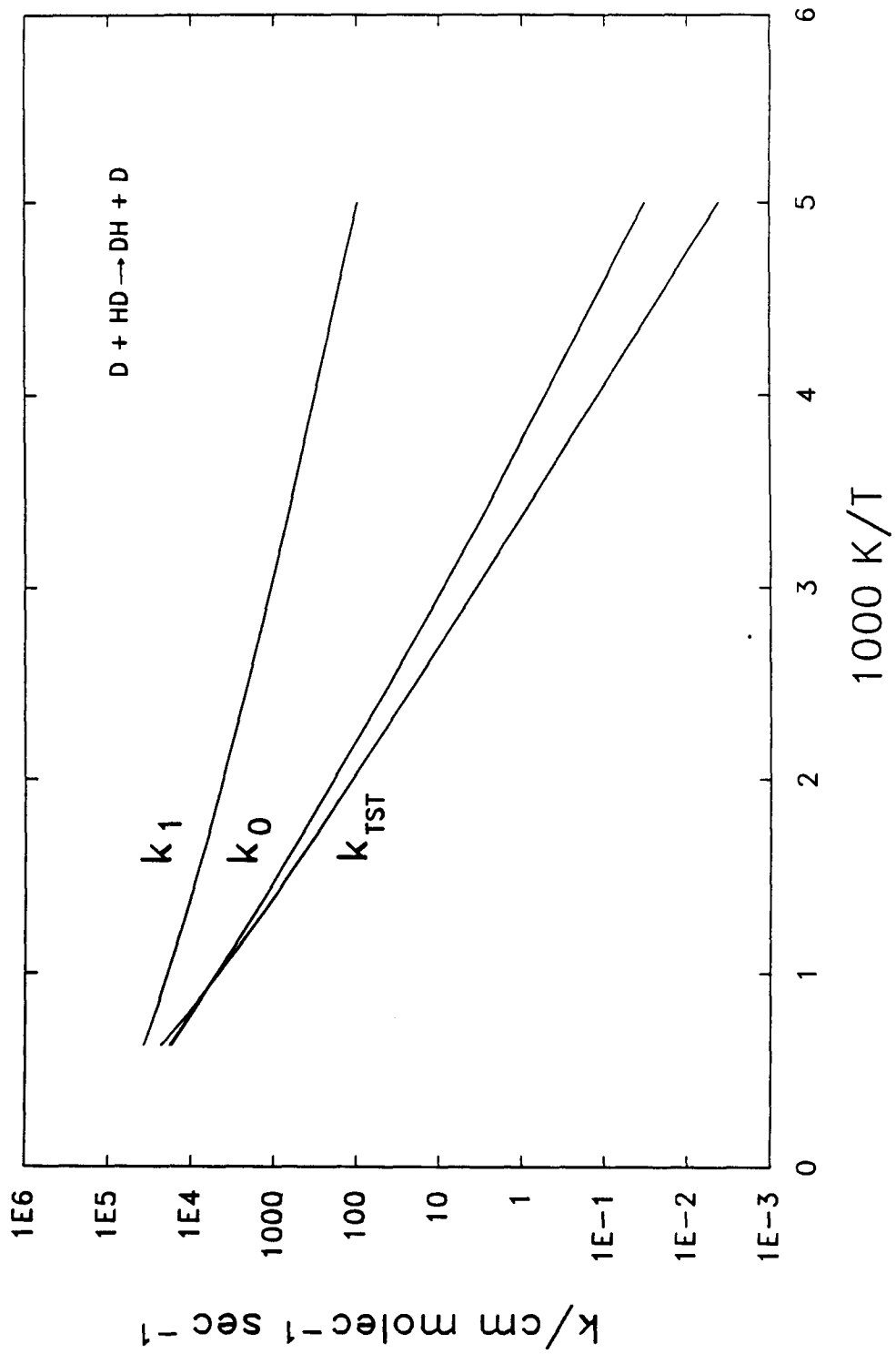
D + HD → DH + D
k_1
k_0
k_{TST}
k/cm mole^{-1} sec^{-1}
1E6
1E5
1E4
1000
100
10
1
1E−1
1E−2
1E−3
0
1
2
3
4
5
6
1000 K/T

Figure 42.

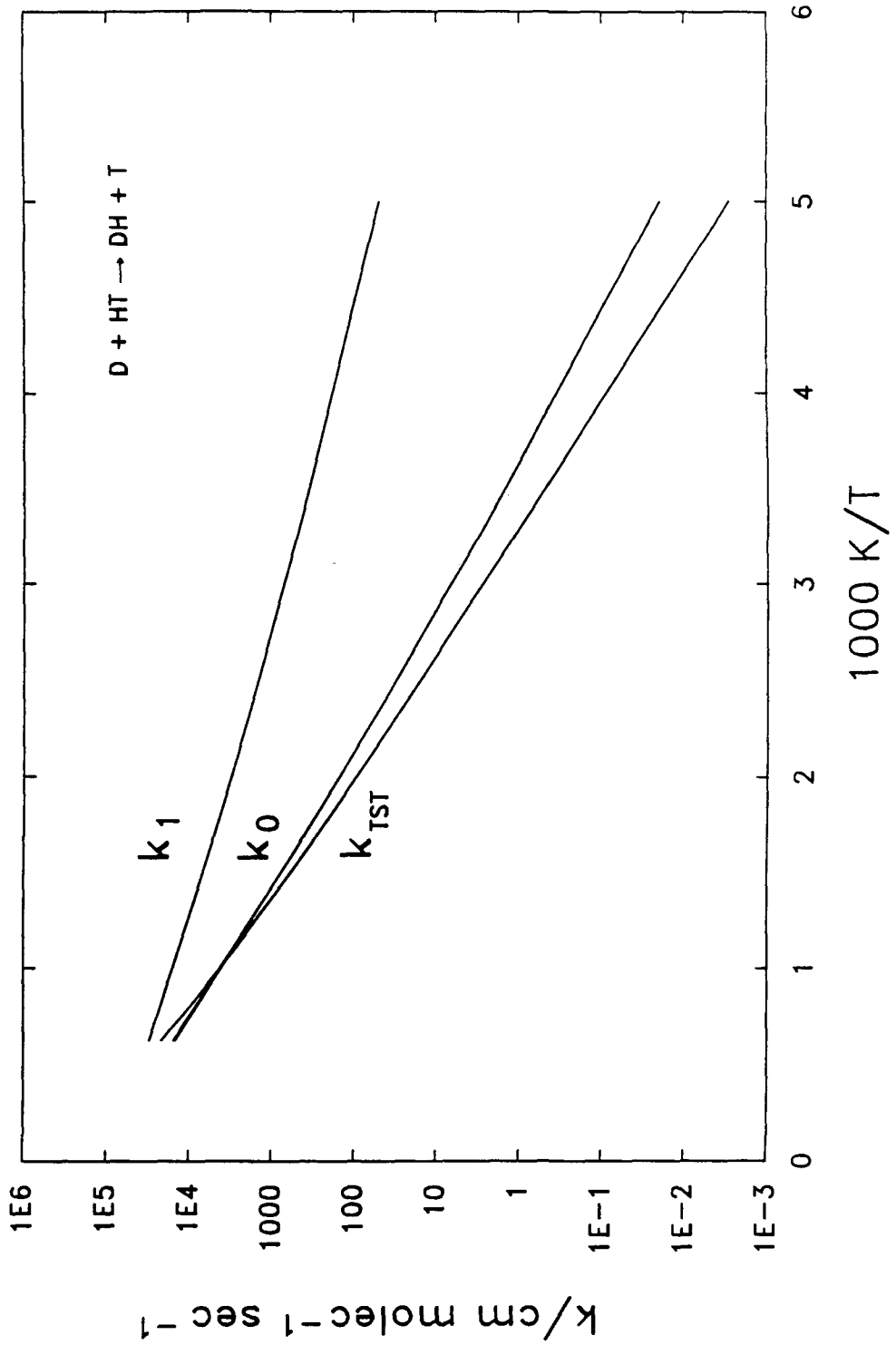
D + HT → DH + T
k_1
k_0
k_{TST}
k/cm mole^{-1} sec^{-1}
1E6
1E5
1E4
1000
100
10
1
1E-1
1E-2
1E-3
0
1
2
3
4
5
6
1000 K/T

Figure 43.

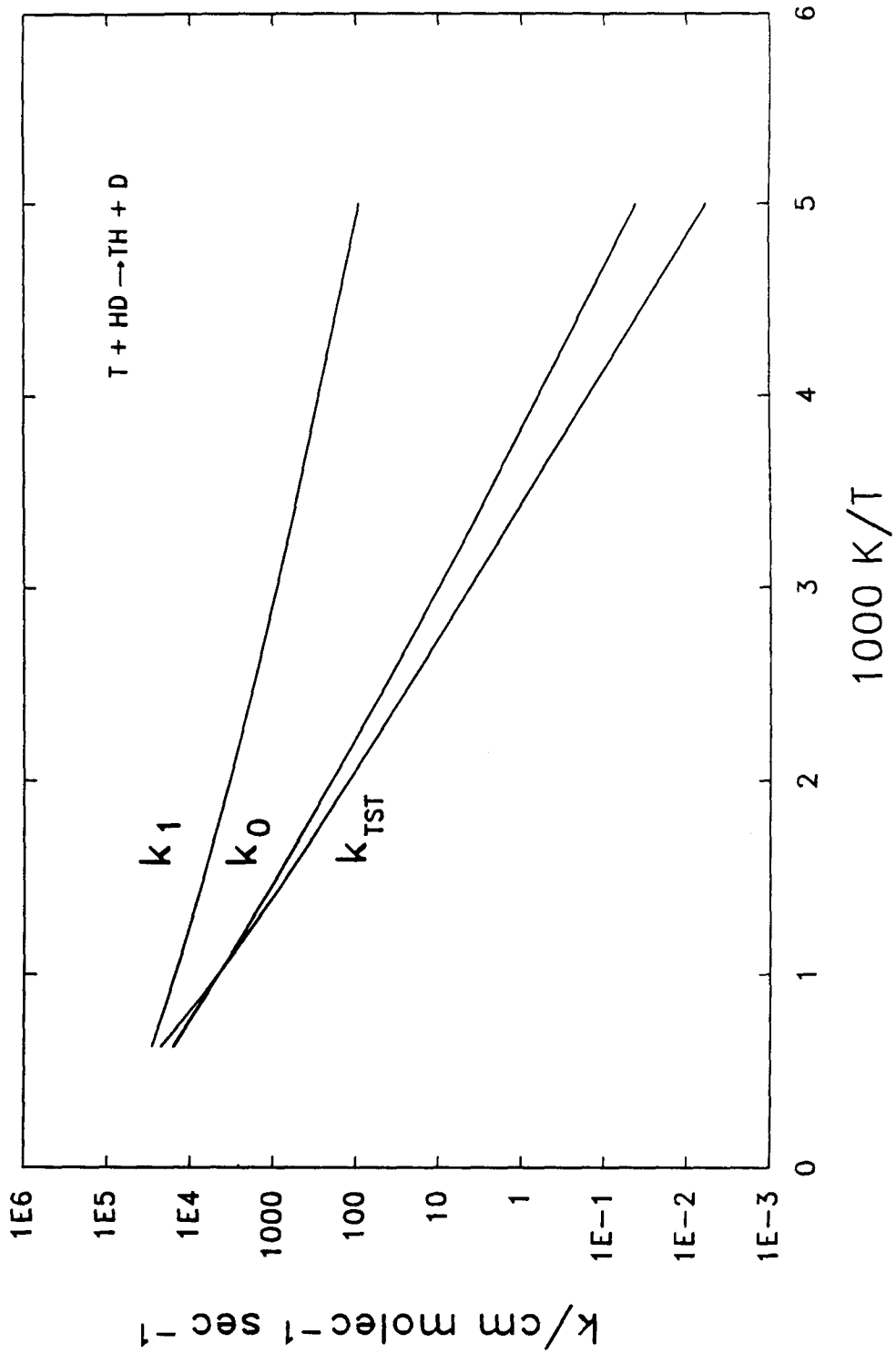
T + HD → TH + D
k_1
k_0
k_{TST}
k/cm mole^{-1} sec^{-1}
1E6
1E5
1E4
1000
100
10
1
1E−1
1E−2
1E−3
0
1
2
3
4
5
6
1000 K/T

Figure 44.

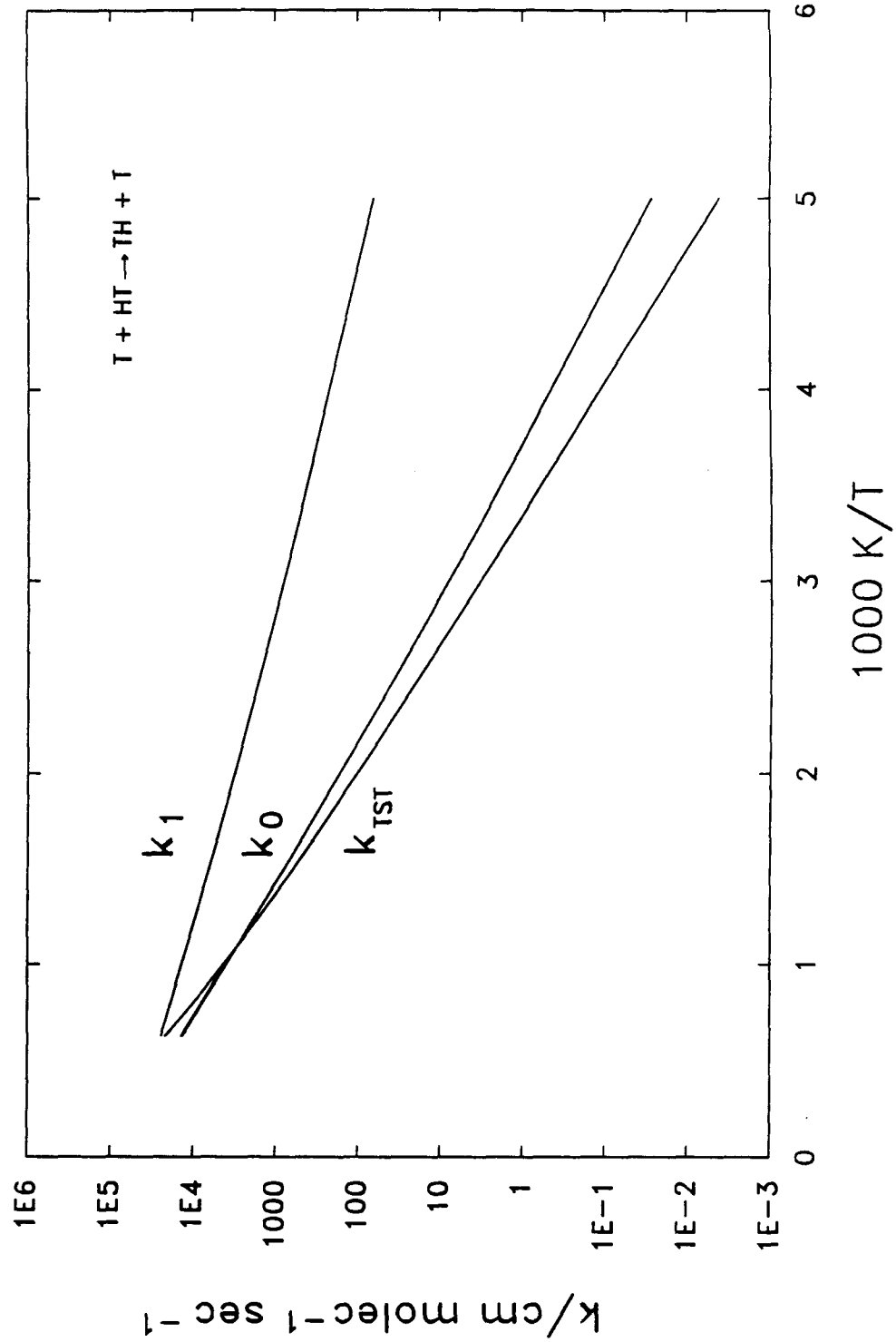
T + HT → TH + T
k 1
k 0
k TST
k/cm molec⁻¹ sec⁻¹
1E6
1E5
1E4
1000
100
10
1
1E-1
1E-2
1E-3
0
1
2
3
4
5
6
1000 K/T

Figure 45.

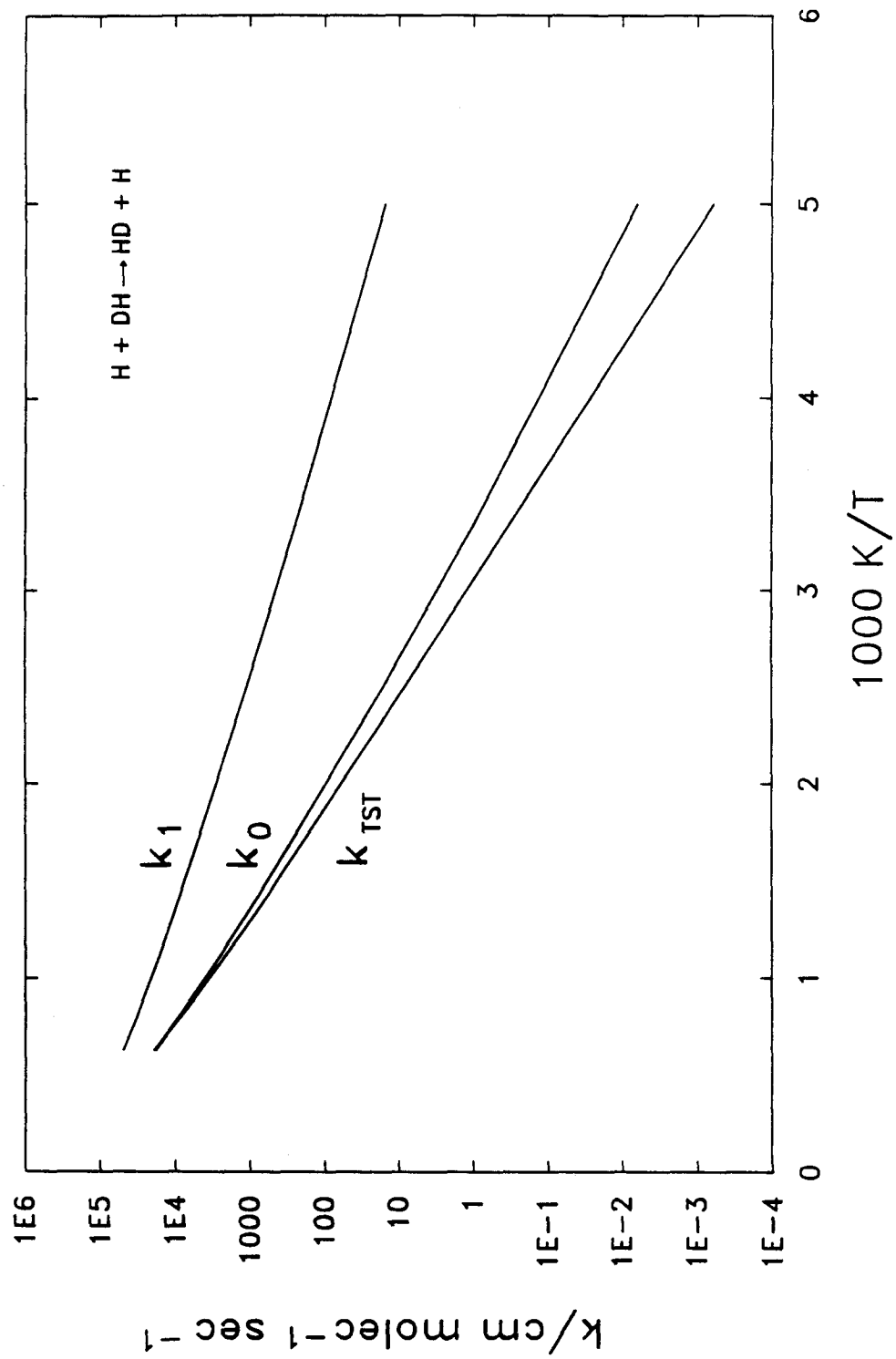
H + DH → HD + H
k 1
k 0
k TST
k/cm molec−1 sec −1
1E6
1E5
1E4
1000
100
10
1
1E−1
1E−2
1E−3
1E−4
0
1
2
3
4
5
6
1000 K/T

Figure 46.

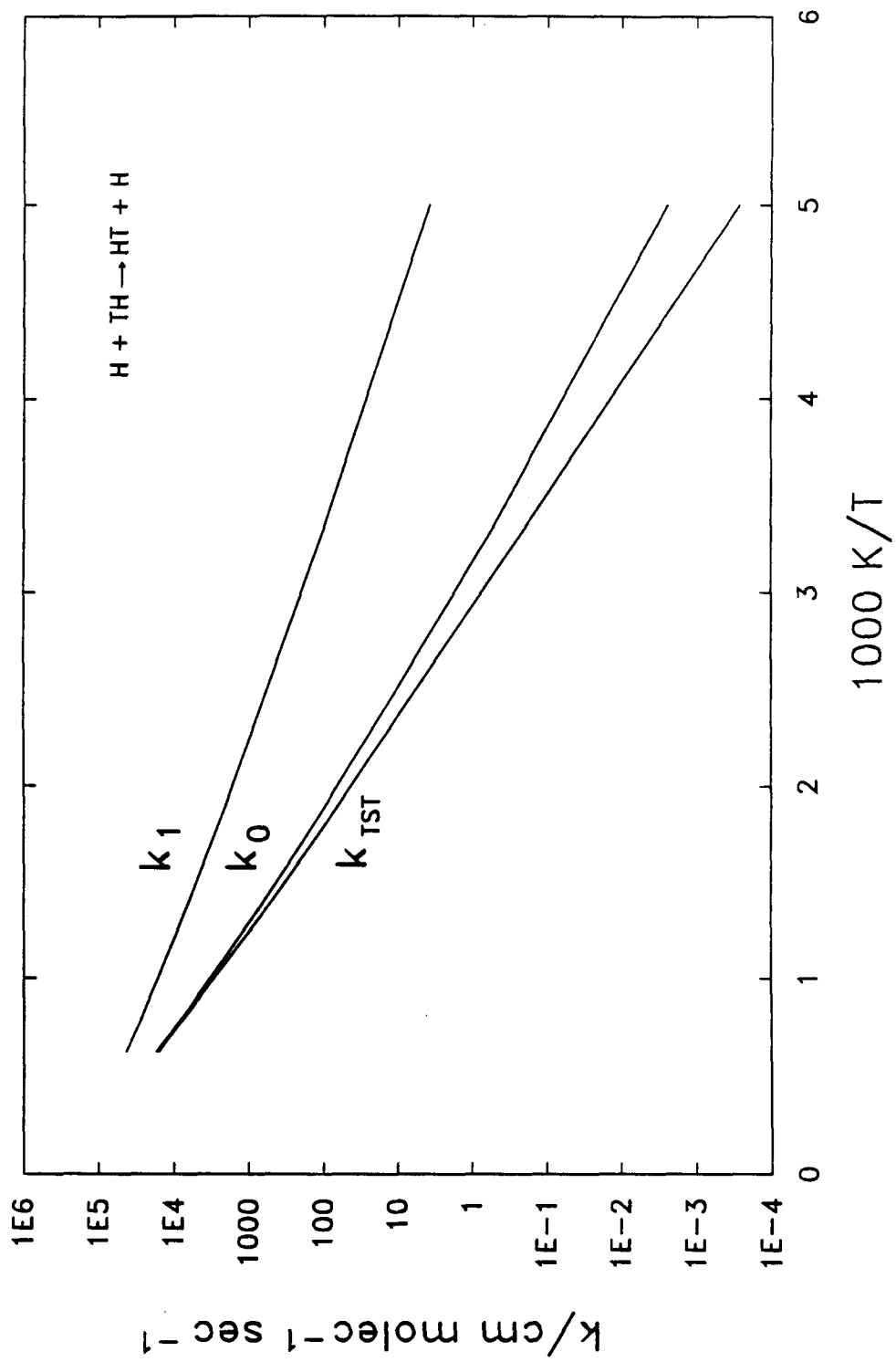
H + TH → HT + H
k_1
k_0
k_{TST}
k/cm mole⁻¹ sec⁻¹
1E6
1E5
1E4
1000
100
10
1
1E-1
1E-2
1E-3
1E-4
0
1
2
3
4
5
6
1000 K/T

Figure 47.

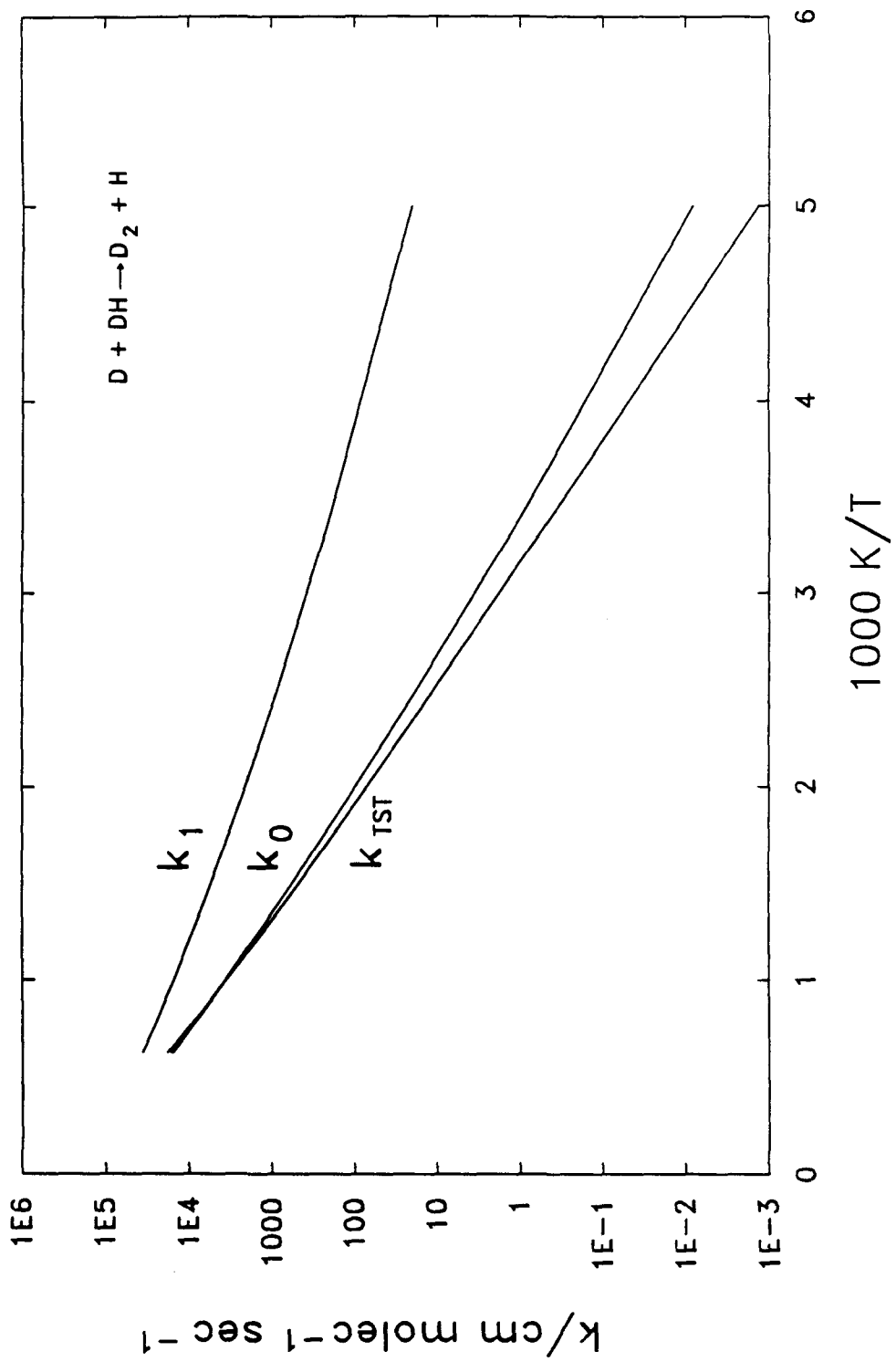
D + DH → D2 + H
k1
k0
kTST
k/cm molec-1 sec-1
1E6
1E5
1E4
1000
100
10
1
1E-1
1E-2
1E-3
0
1
2
3
4
5
6
1000 K/T

Figure 48.

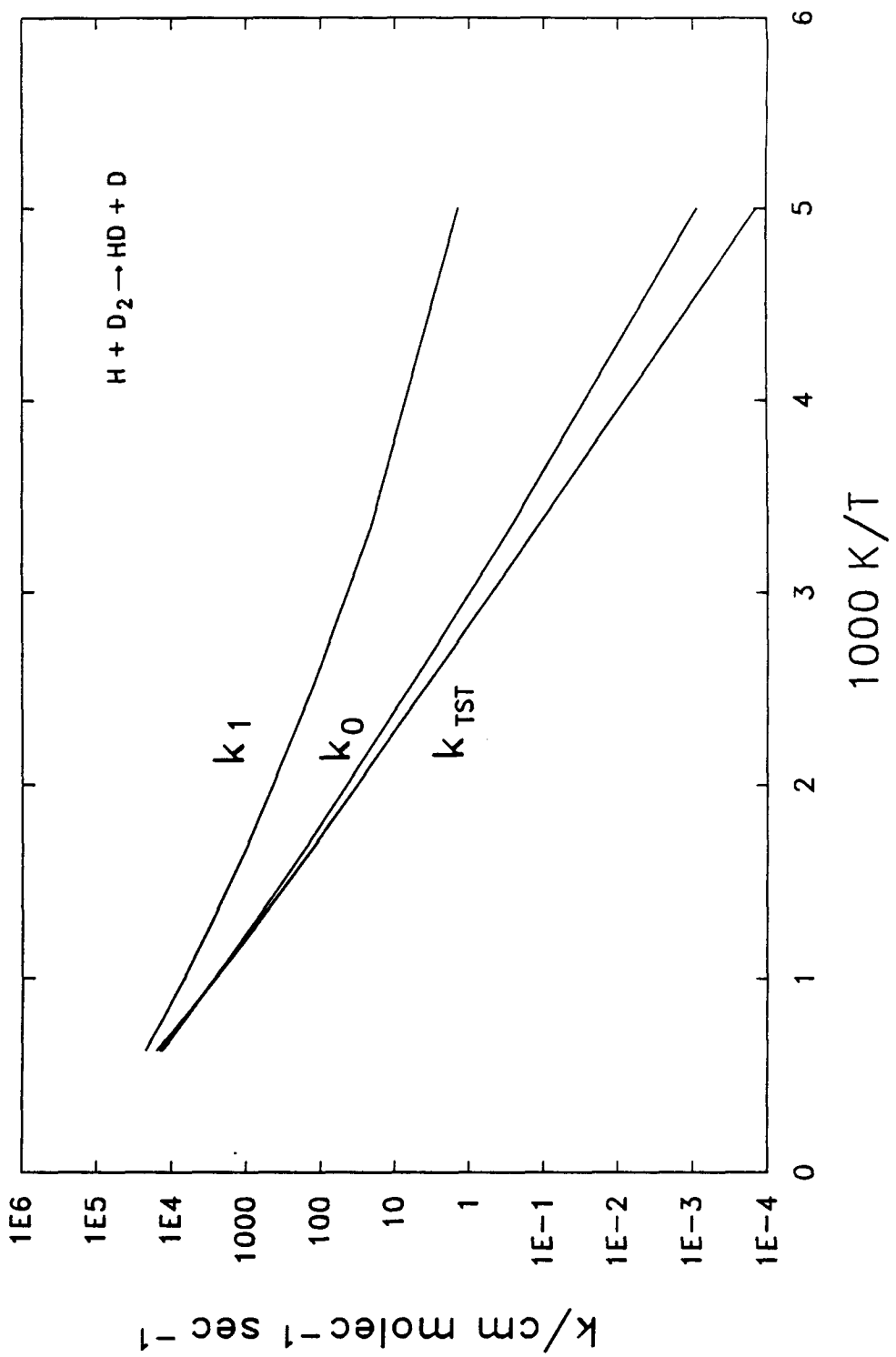
H + D2 → HD + D
k1
k0
kTST
k/cm molec−1 sec−1
1E6
1E5
1E4
1000
100
10
1
1E−1
1E−2
1E−3
1E−4
0
1
2
3
4
5
6
1000 K/T

Figure 49.

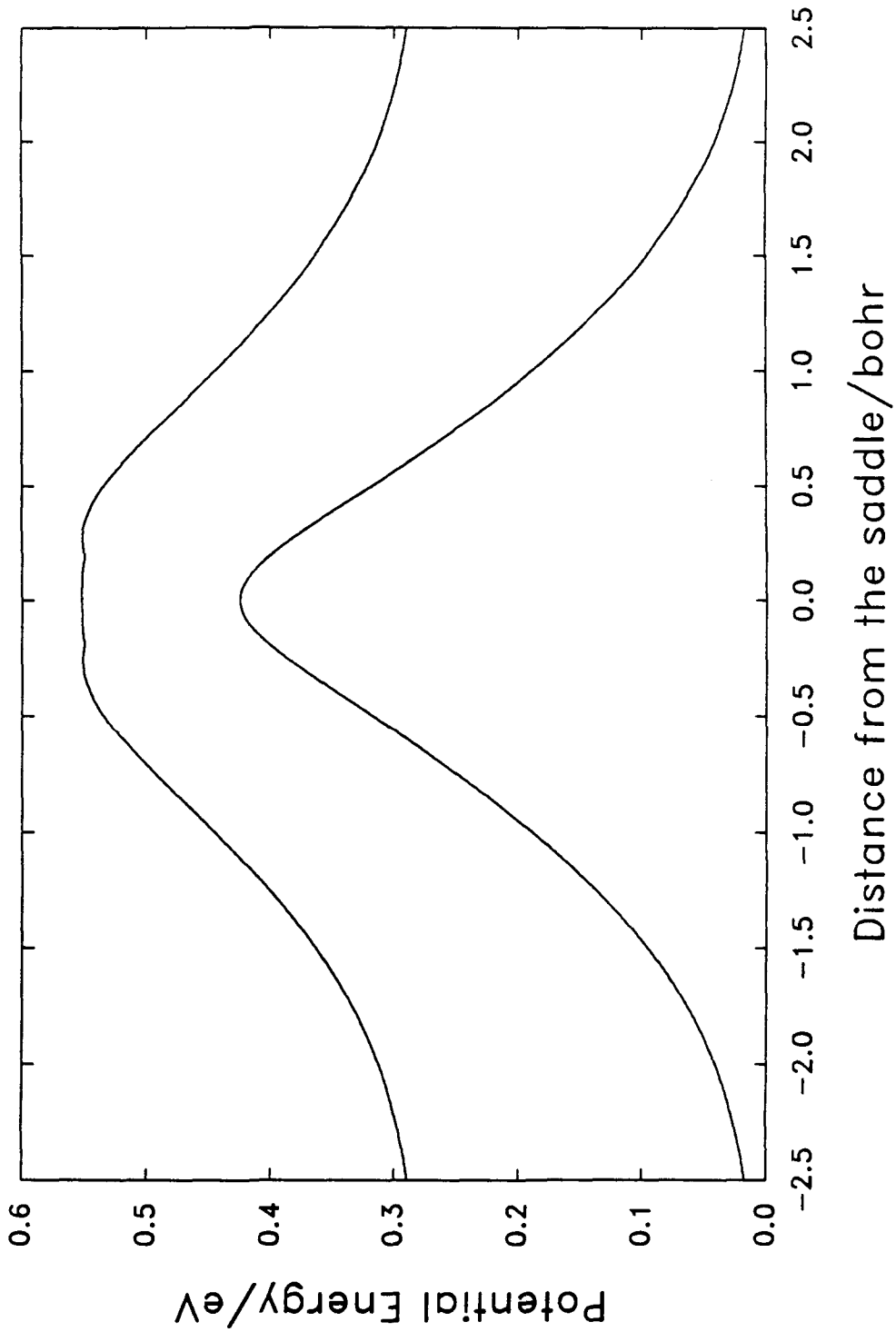
Potential Energy/eV
0.0
0.1
0.2
0.3
0.4
0.5
0.6
Distance from the saddle/bohr
-2.5
-2.0
-1.5
-1.0
-0.5
0.0
0.5
1.0
1.5
2.0
2.5

Figure 50.

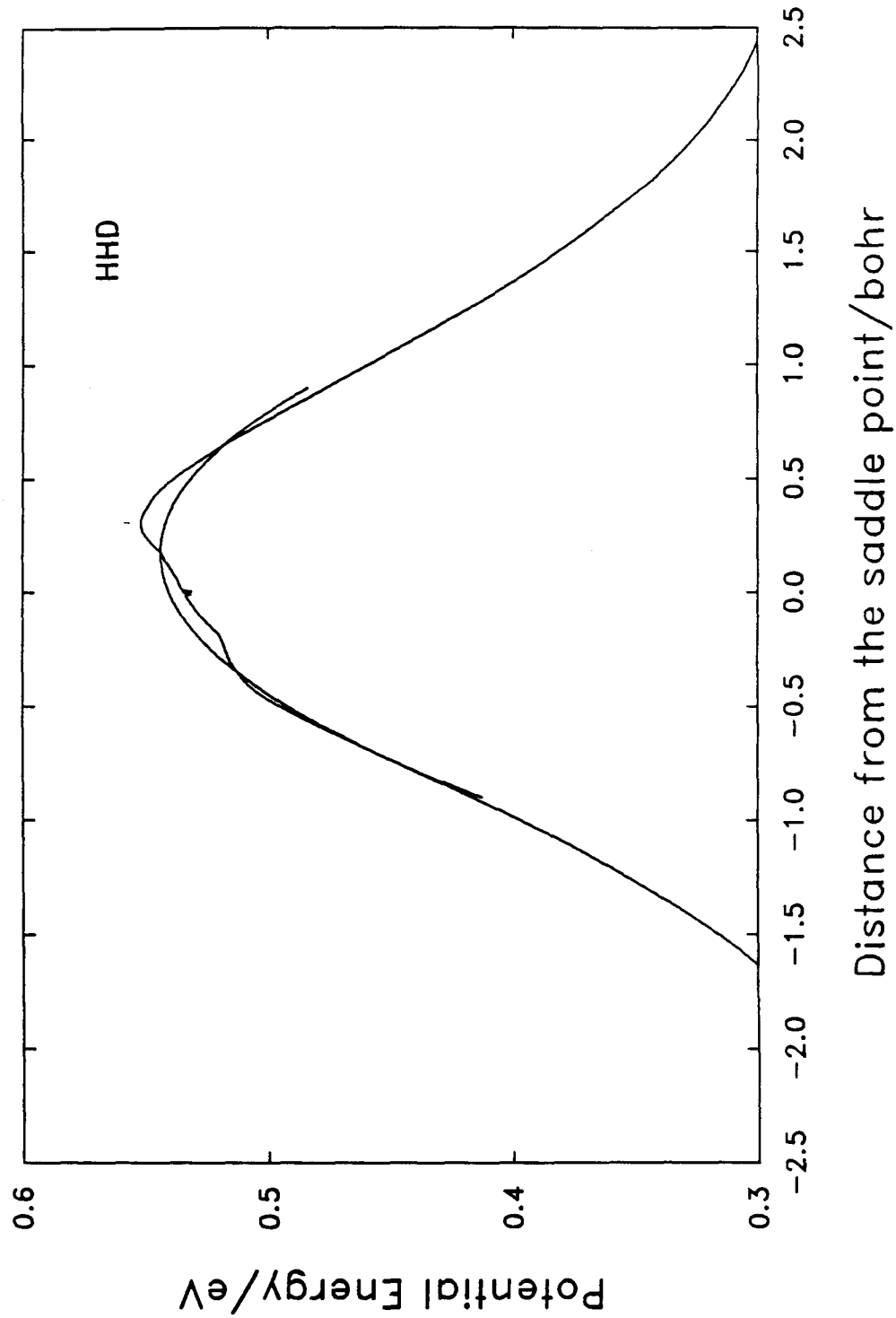
HHD
Potential Energy/eV
0.6
0.5
0.4
0.3
Distance from the saddle point/bohr
-2.5
-2.0
-1.5
-1.0
-0.5
0.0
0.5
1.0
1.5
2.0
2.5

Figure 51.

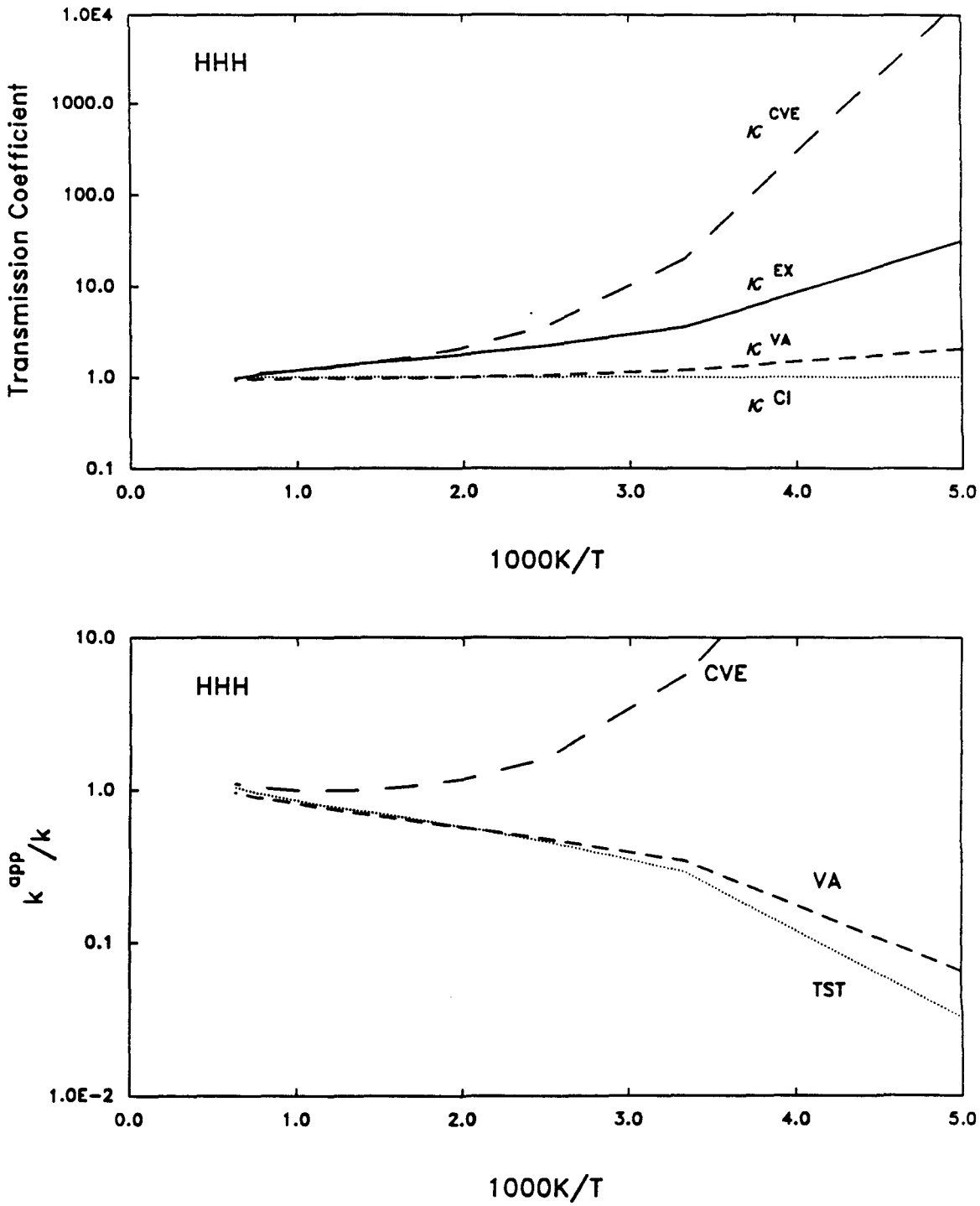
HHH
Transmission Coefficient
1.0E4
1000.0
100.0
10.0
1.0
0.1
0.0
1.0
2.0
3.0
4.0
5.0
1000K/T
κ CVE
κ EX
κ VA
κ CI
HHH
10.0
1.0
0.1
1.0E-2
k app /k
CVE
VA
TST
0.0
1.0
2.0
3.0
4.0
5.0
1000K/T

Figure 52.

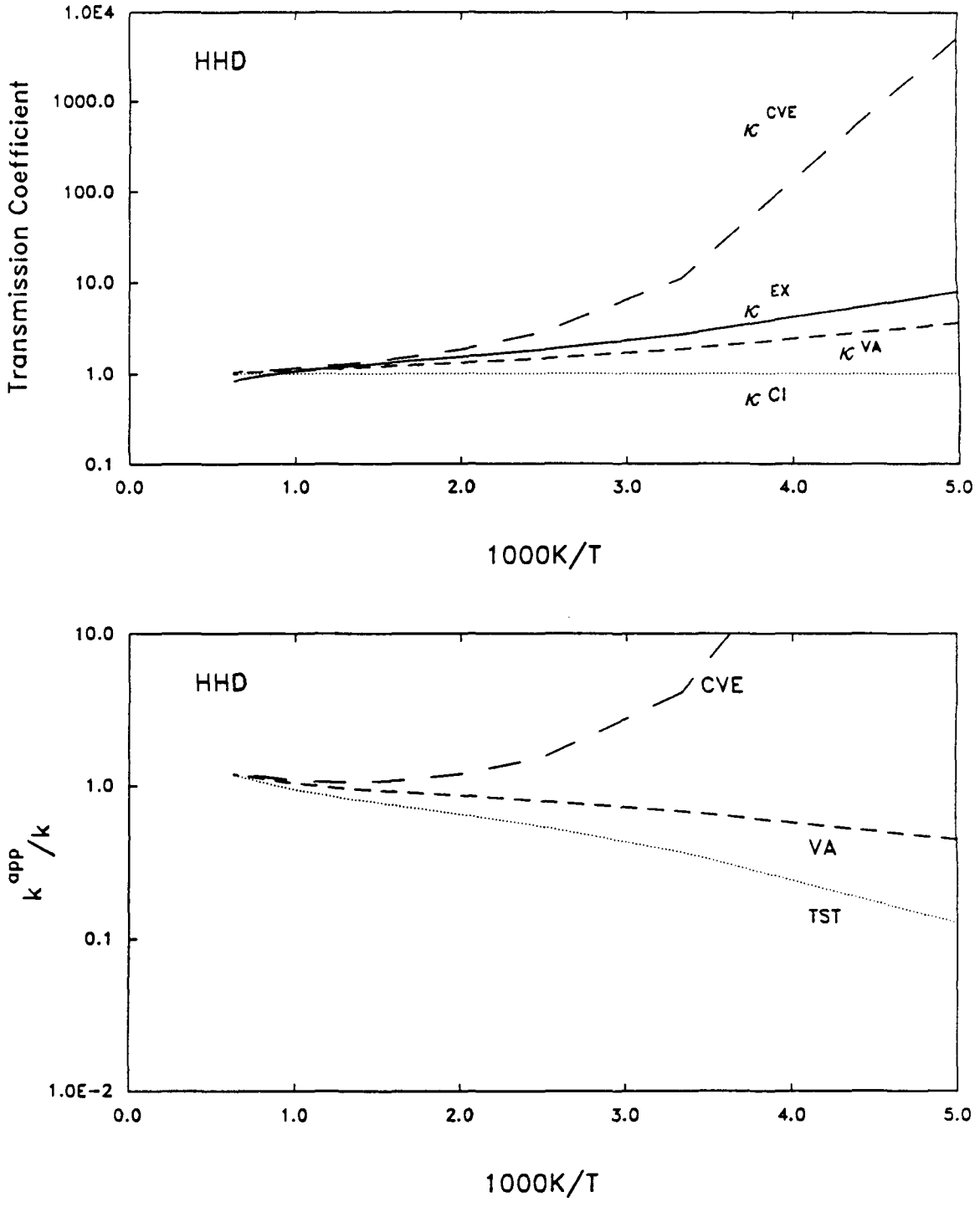
HHD
Transmission Coefficient
1.0E4
1000.0
100.0
10.0
1.0
0.1
κ CVE
κ EX
κ VA
κ CI
0.0
1.0
2.0
3.0
4.0
5.0
1000K/T
HHD
CVE
VA
TST
k app /k
10.0
1.0
0.1
1.0E-2
0.0
1.0
2.0
3.0
4.0
5.0
1000K/T

Figure 53.

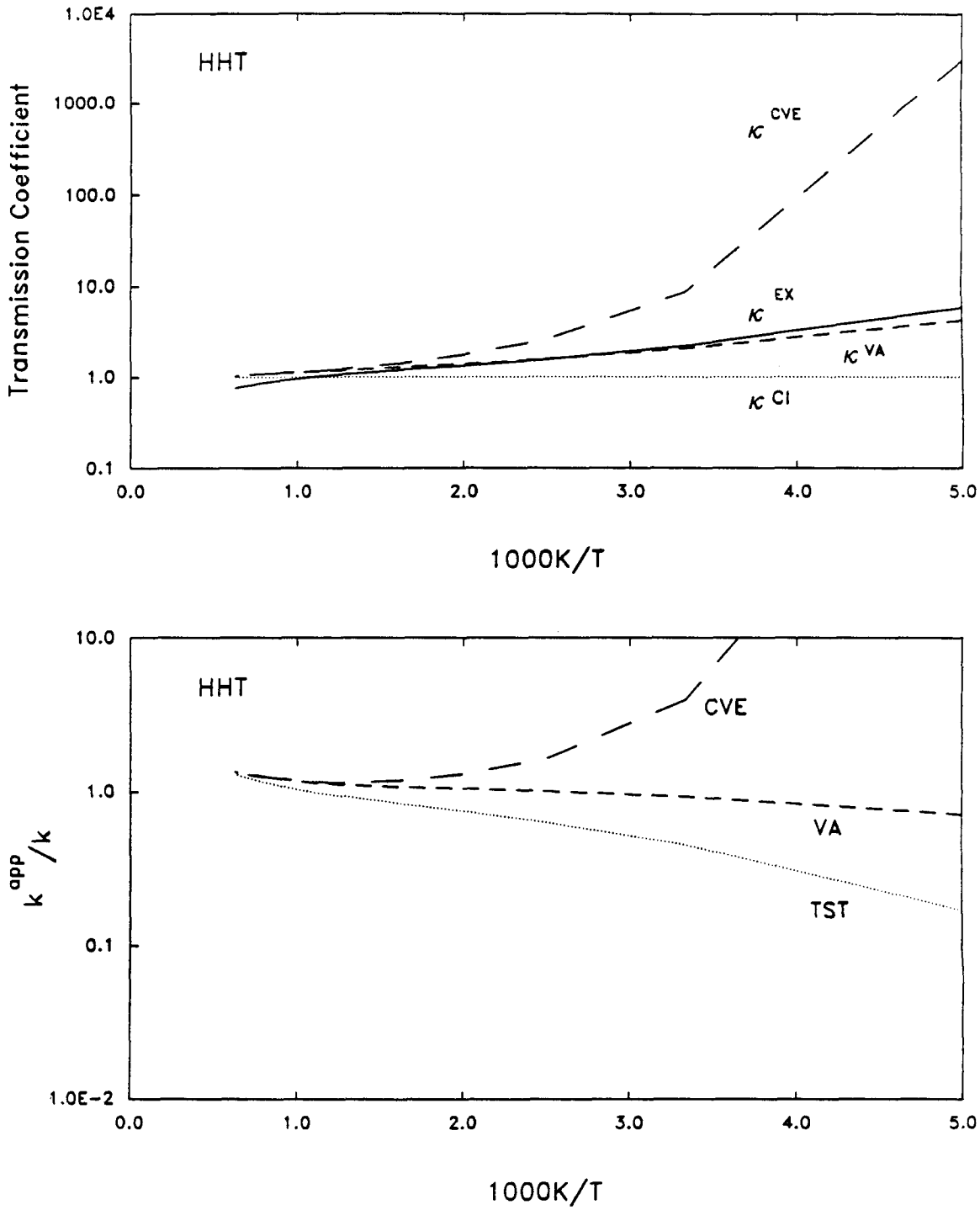
HHT
Transmission Coefficient
1.0E4
1000.0
100.0
10.0
1.0
0.1
0.0
1.0
2.0
3.0
4.0
5.0
1000K/T
κ CVE
κ EX
κ VA
κ CI
HHT
k app /k
10.0
1.0
0.1
1.0E-2
CVE
VA
TST

Figure 54.

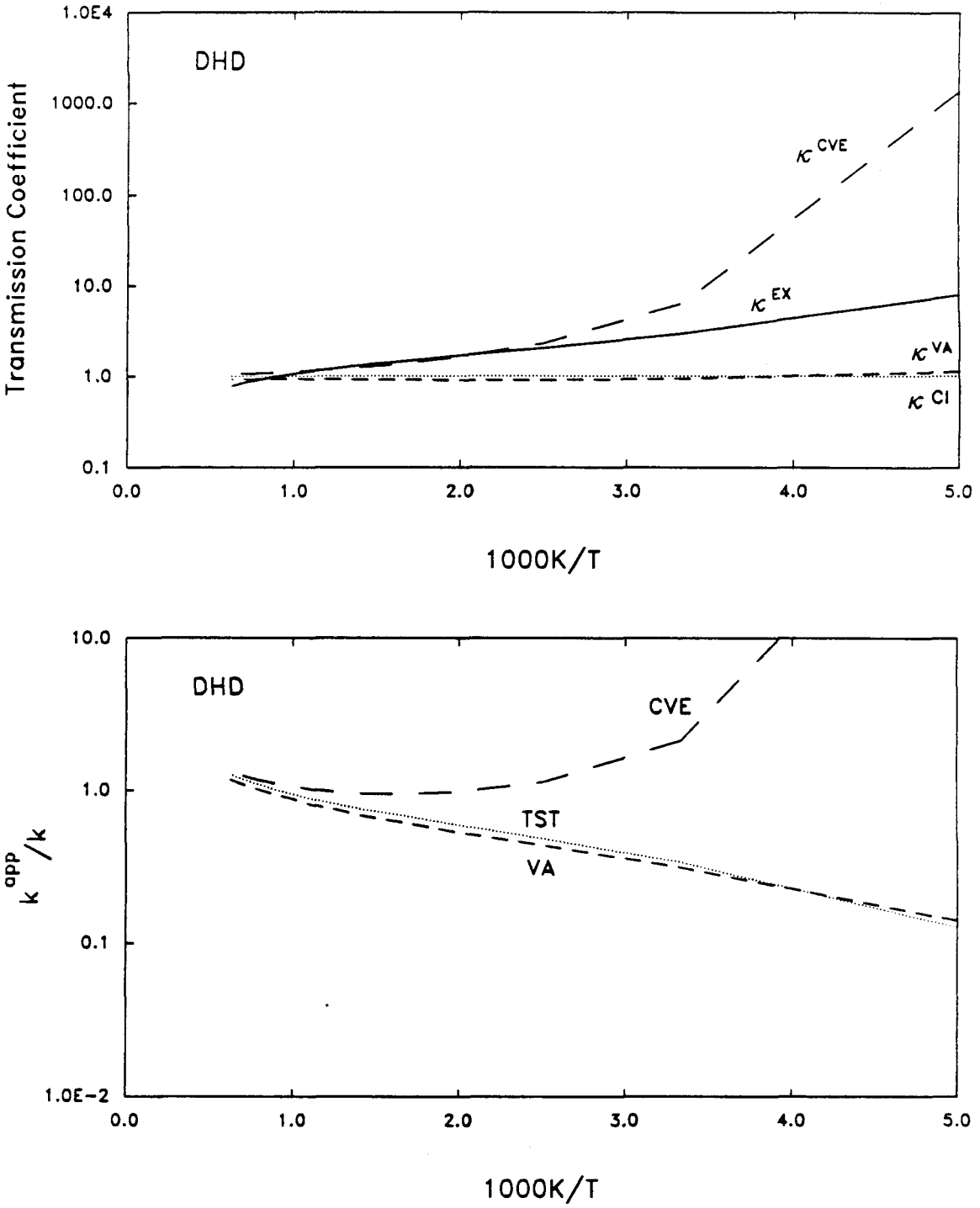
DHD
Transmission Coefficient
1.0E4
1000.0
100.0
10.0
1.0
0.1
0.0
1.0
2.0
3.0
4.0
5.0
1000K/T
κ CVE
κ EX
κ VA
κ CI
DHD
k app /k
10.0
1.0
0.1
1.0E-2
CVE
TST
VA

Figure 55.

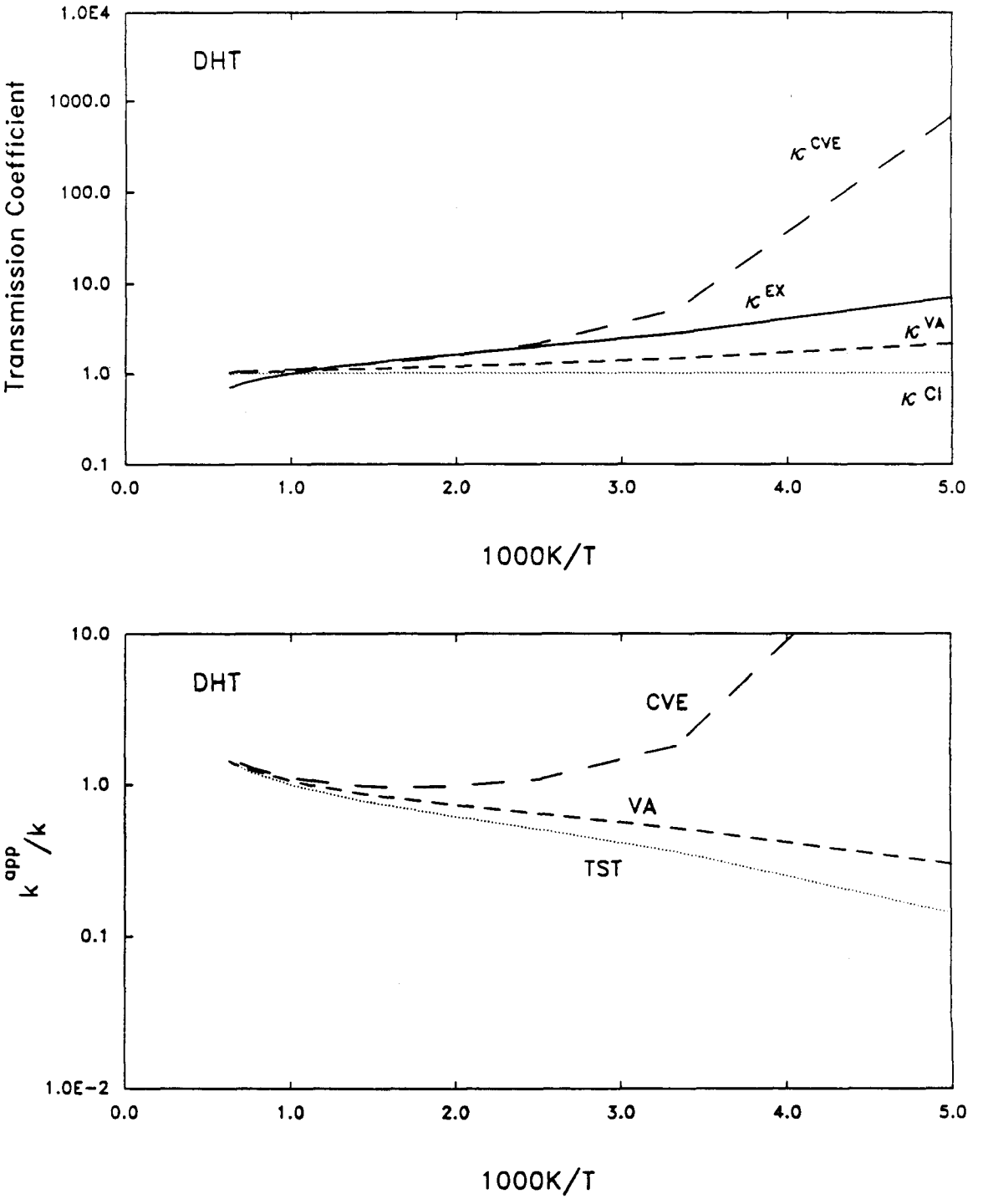
DHT
Transmission Coefficient
1.0E4
1000.0
100.0
10.0
1.0
0.1
κ^{CVE}
κ^{EX}
κ^{VA}
κ^{CI}
0.0
1.0
2.0
3.0
4.0
5.0
1000K/T
DHT
k^{app}/k
10.0
1.0
0.1
1.0E-2
CVE
VA
TST
0.0
1.0
2.0
3.0
4.0
5.0
1000K/T

Figure 56.

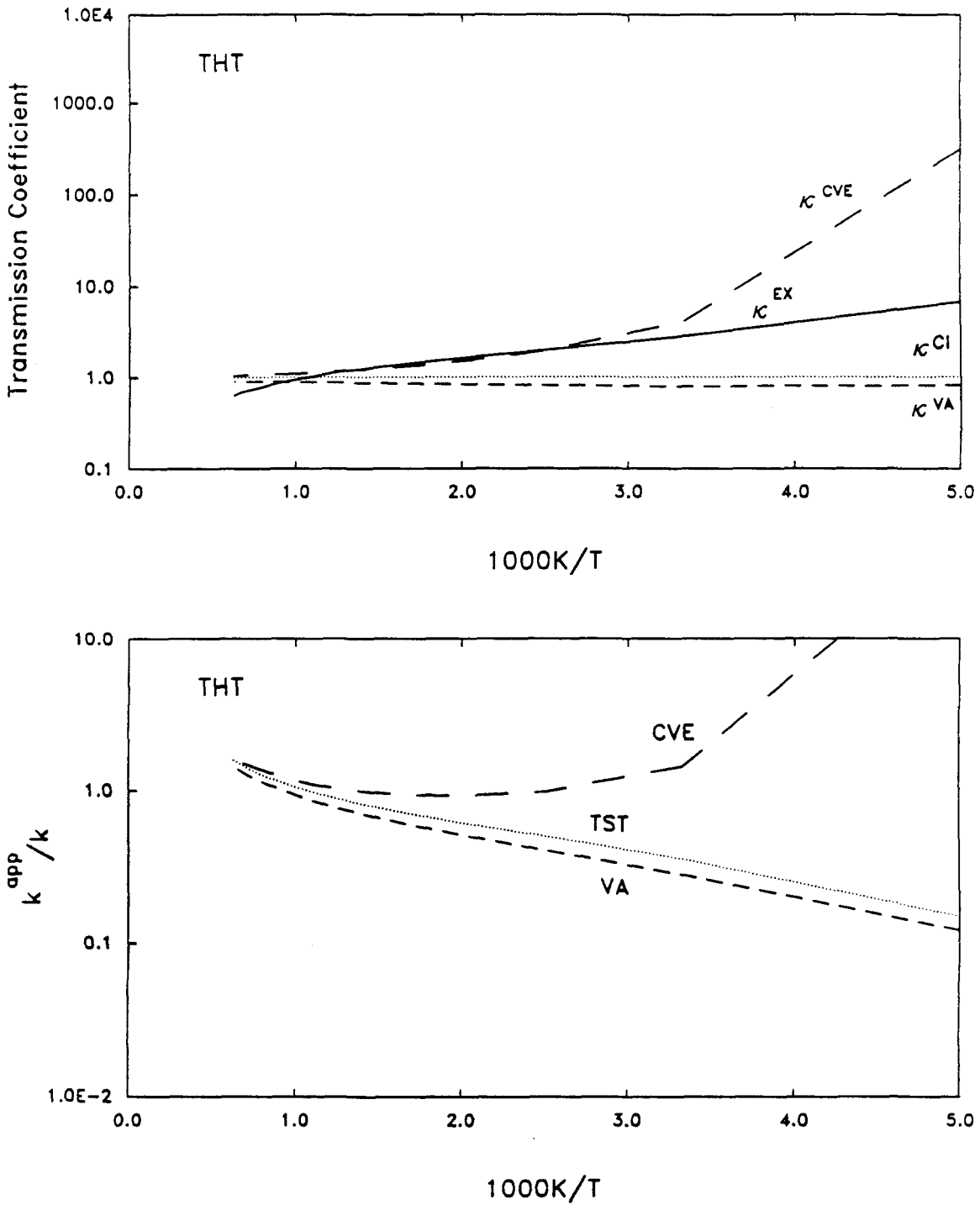
THT
Transmission Coefficient
1.0E4
1000.0
100.0
10.0
1.0
0.1
0.0
1.0
2.0
3.0
4.0
5.0
1000K/T
κ CVE
κ EX
κ CI
κ VA
THT
CVE
TST
VA
k app /k
10.0
1.0
0.1
1.0E-2
0.0
1.0
2.0
3.0
4.0
5.0
1000K/T

Figure 57.

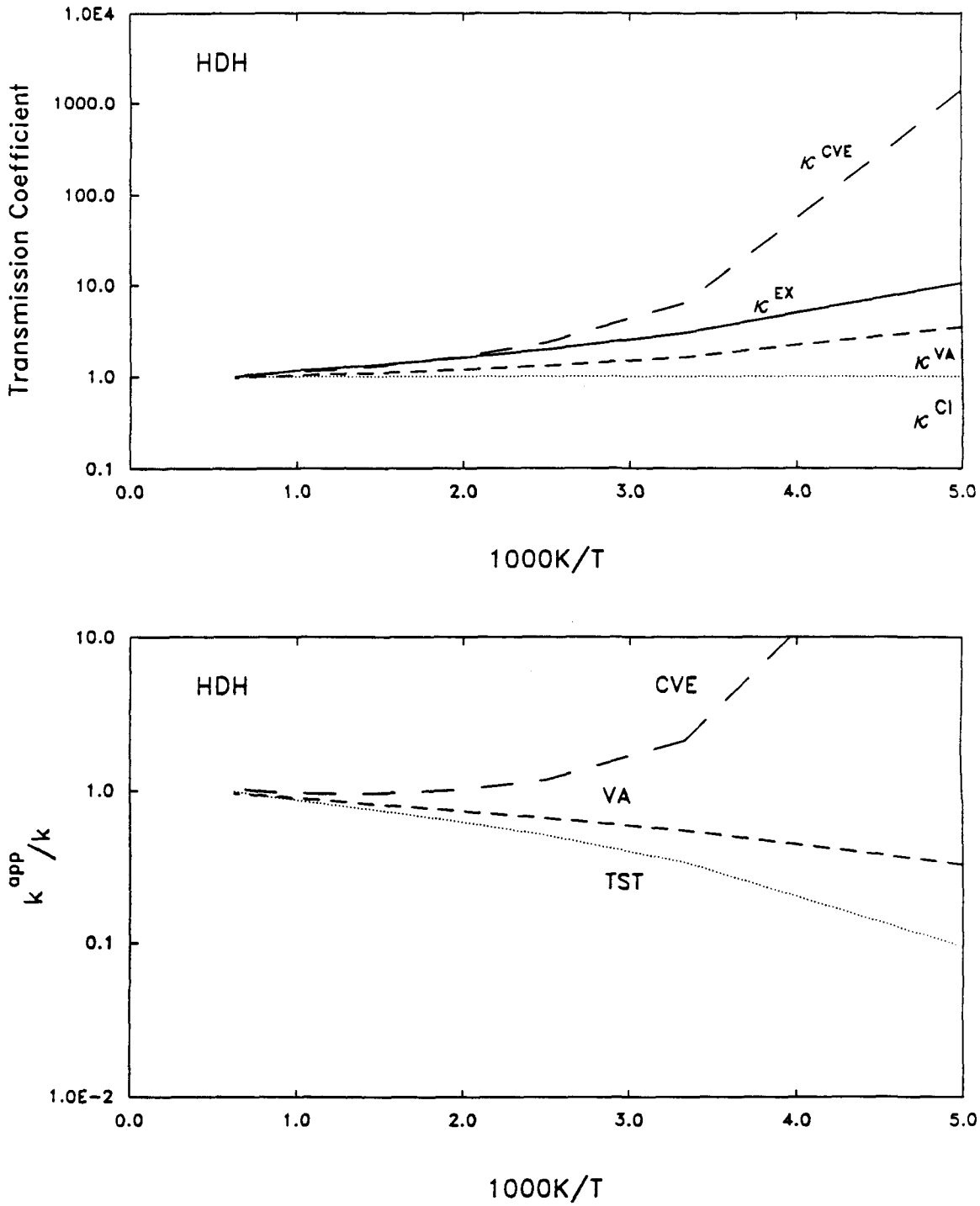
HDH
Transmission Coefficient
1.0E4
1000.0
100.0
10.0
1.0
0.1
0.0
1.0
2.0
3.0
4.0
5.0
1000K/T
κ CVE
κ EX
κ VA
κ CI
HDH
CVE
VA
TST
k app /k
10.0
1.0
0.1
1.0E-2
0.0
1.0
2.0
3.0
4.0
5.0
1000K/T

Figure 58.

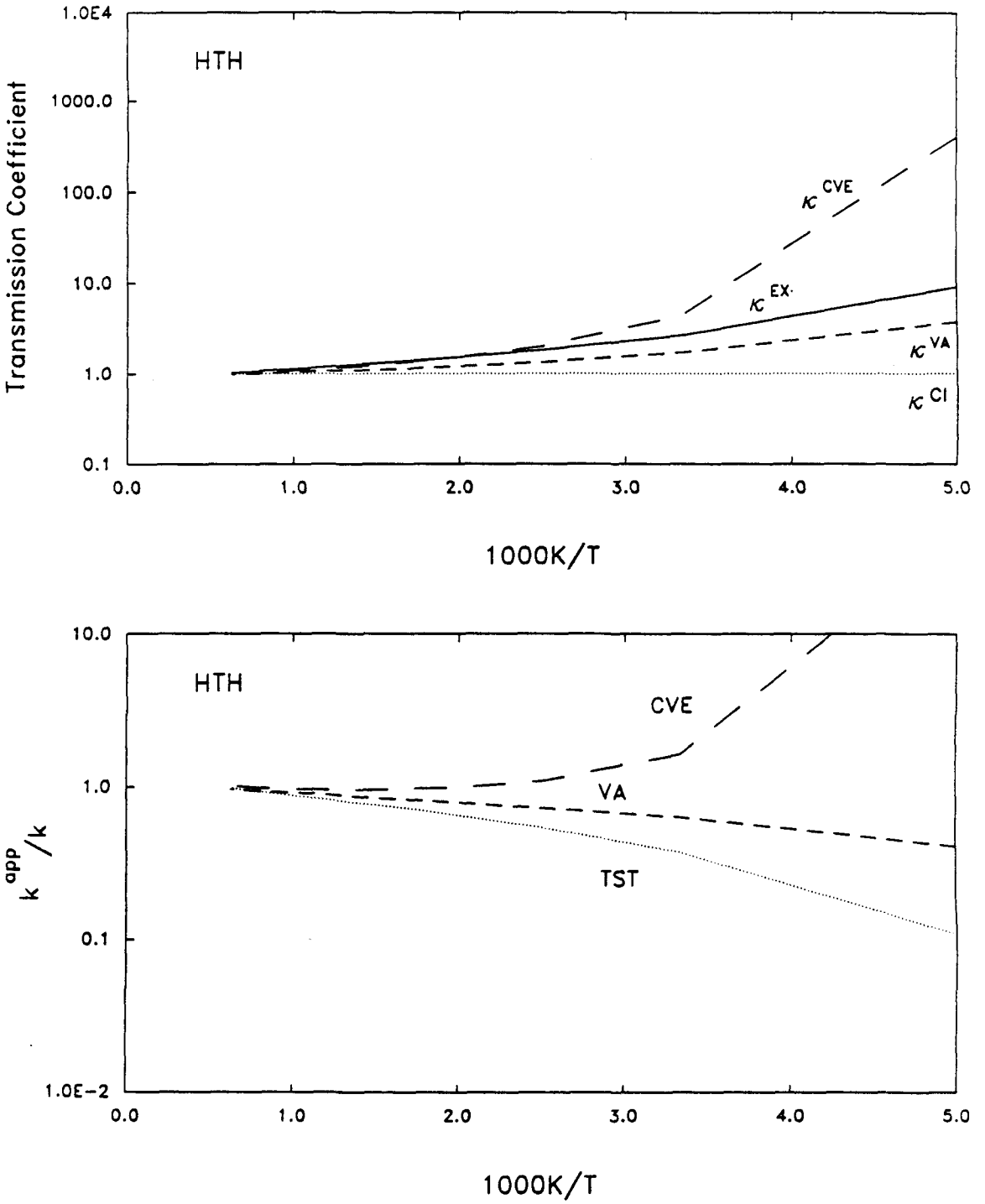
HTH
Transmission Coefficient
1.0E4
1000.0
100.0
10.0
1.0
0.1
0.0
1.0
2.0
3.0
4.0
5.0
1000K/T
κ CVE
κ EX.
κ VA
κ CI
HTH
CVE
VA
TST
k app /k
10.0
1.0
0.1
1.0E-2
0.0
1.0
2.0
3.0
4.0
5.0
1000K/T

Figure 59.

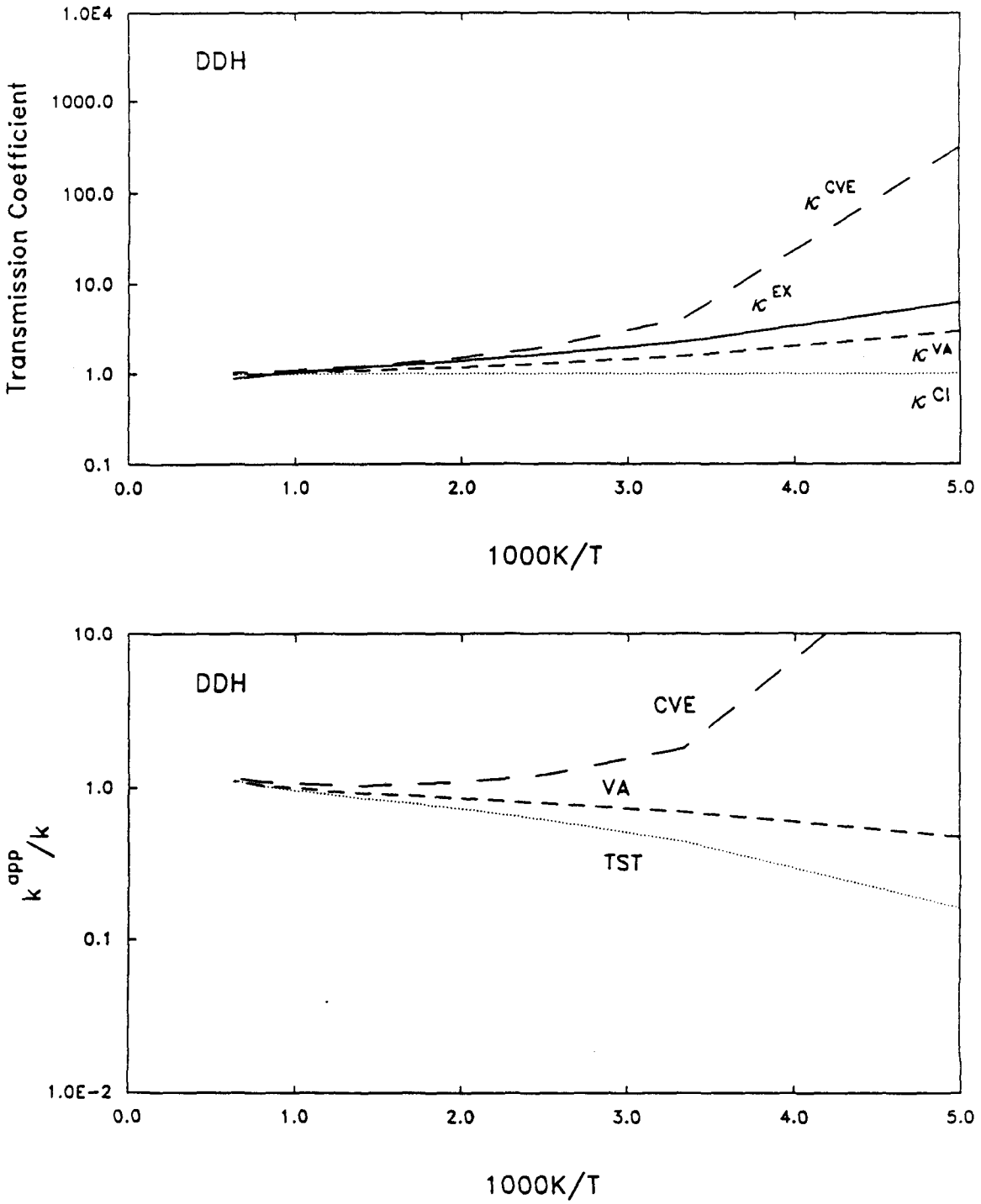
DDH
Transmission Coefficient
1.0E4
1000.0
100.0
10.0
1.0
0.1
κ CVE
κ EX
κ VA
κ CI
0.0
1.0
2.0
3.0
4.0
5.0
1000K/T
DDH
k app /k
10.0
1.0
0.1
1.0E-2
CVE
VA
TST
0.0
1.0
2.0
3.0
4.0
5.0
1000K/T

Figure 60.

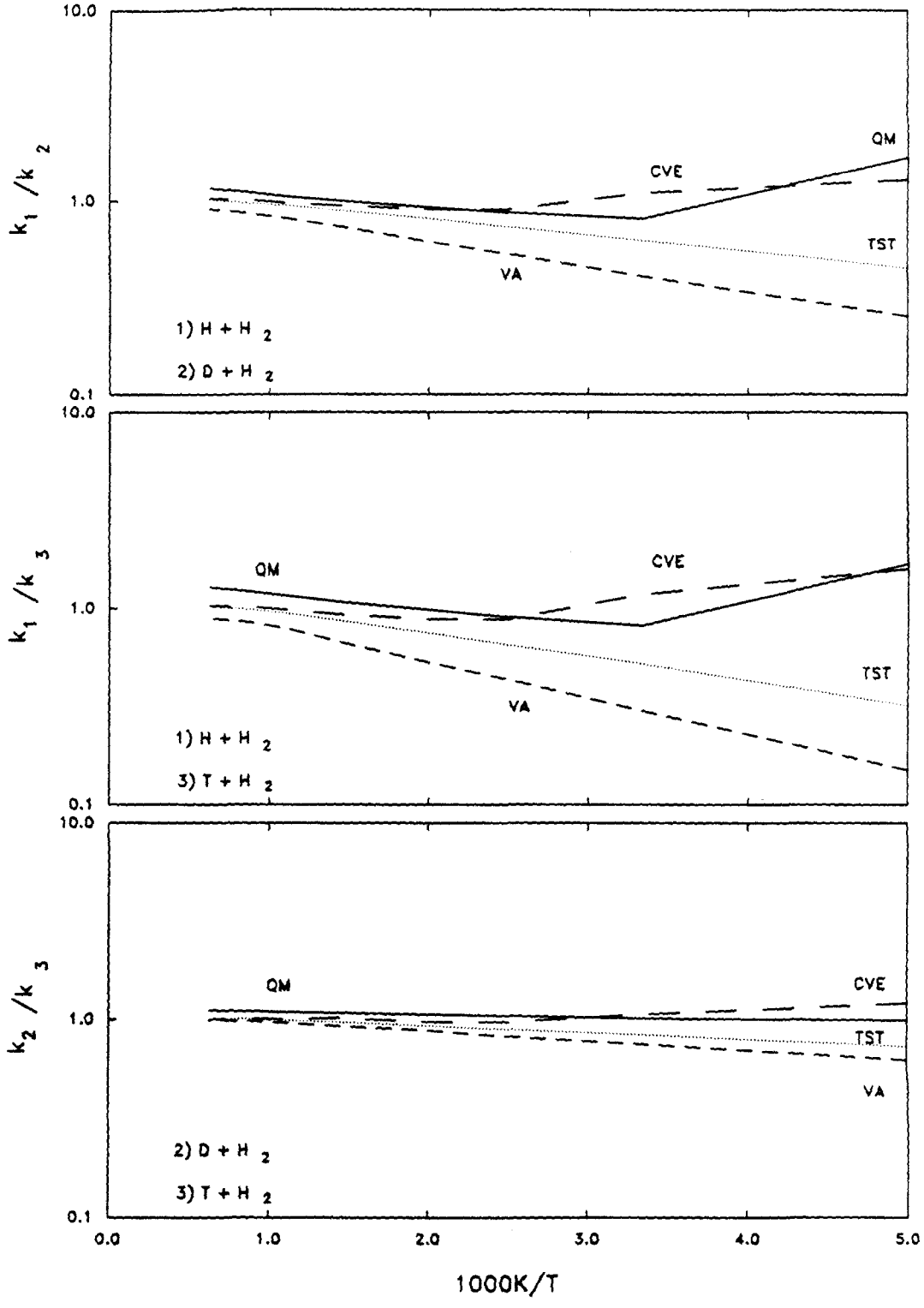
10.0
1.0
0.1
k_1/k_2
QM
CVE
TST
VA
1) H + H 2
2) D + H 2
10.0
1.0
0.1
k_1/k_3
QM
CVE
TST
VA
1) H + H 2
3) T + H 2
10.0
1.0
0.1
k_2/k_3
QM
CVE
TST
VA
2) D + H 2
3) T + H 2
0.0
1.0
2.0
3.0
4.0
5.0
1000K/T

Figure 61.

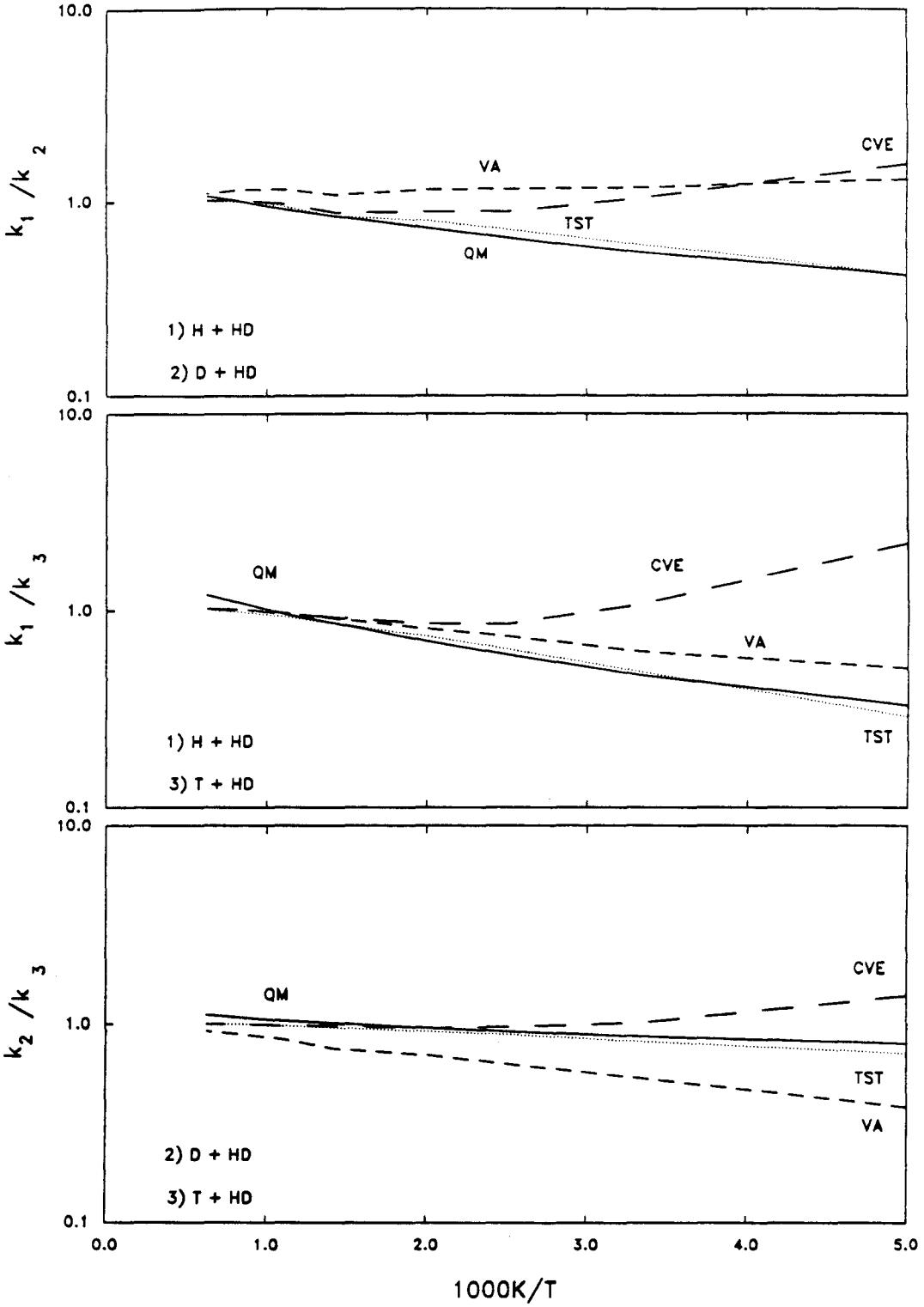
10.0
1.0
0.1
k_1/k_2
VA
CVE
TST
QM
1) H + HD
2) D + HD
10.0
1.0
0.1
k_1/k_3
QM
CVE
VA
TST
1) H + HD
3) T + HD
10.0
1.0
0.1
k_2/k_3
QM
CVE
TST
VA
2) D + HD
3) T + HD
0.0
1.0
2.0
3.0
4.0
5.0
1000K/T

Figure 62.

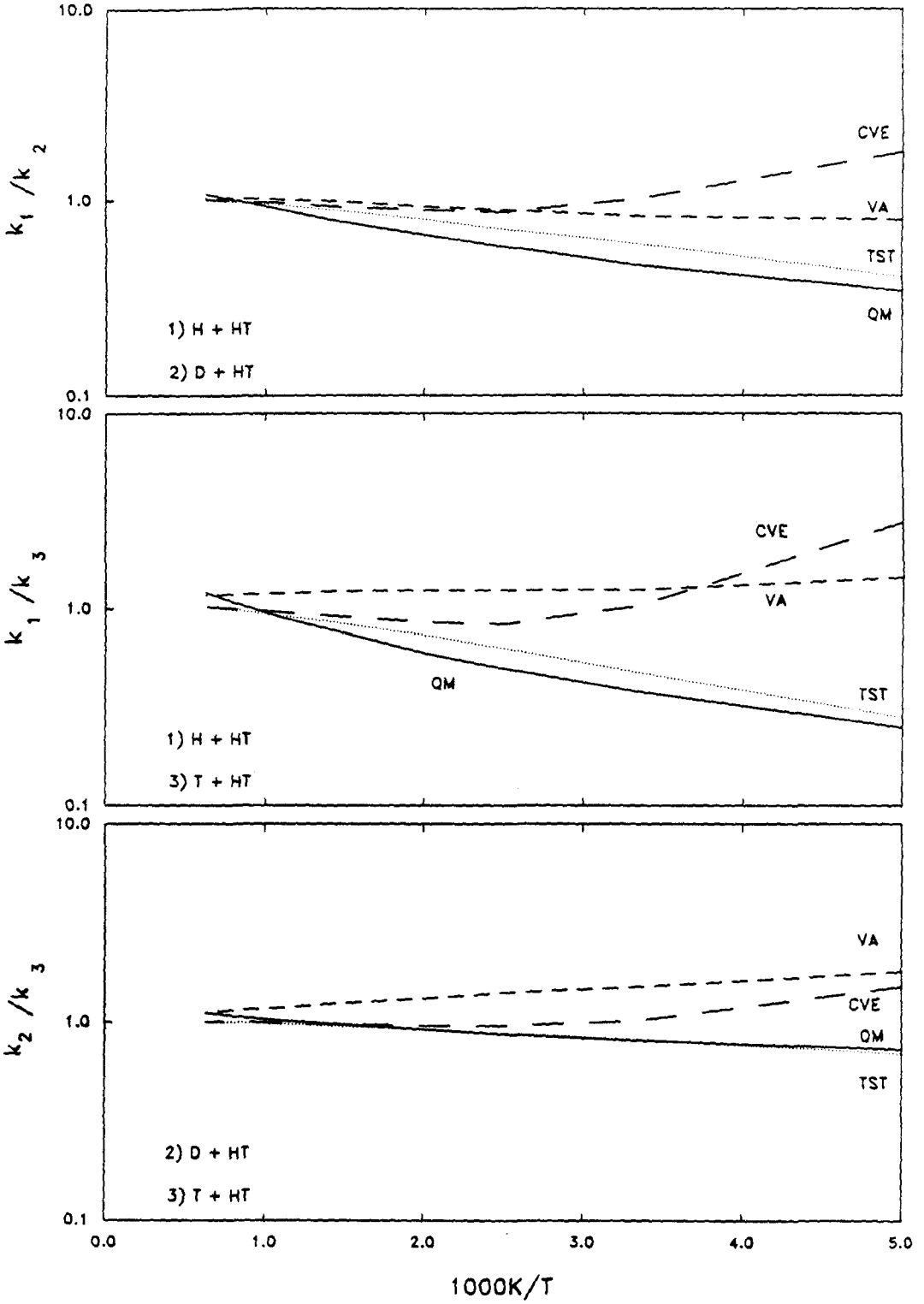
10.0
1.0
0.1
k_1/k_2
CVE
VA
TST
QM
1) H + HT
2) D + HT
10.0
1.0
0.1
k_1/k_3
CVE
VA
QM
TST
1) H + HT
3) T + HT
10.0
1.0
0.1
k_2/k_3
VA
CVE
QM
TST
2) D + HT
3) T + HT
0.0
1.0
2.0
3.0
4.0
5.0
1000K/T

Figure 63.

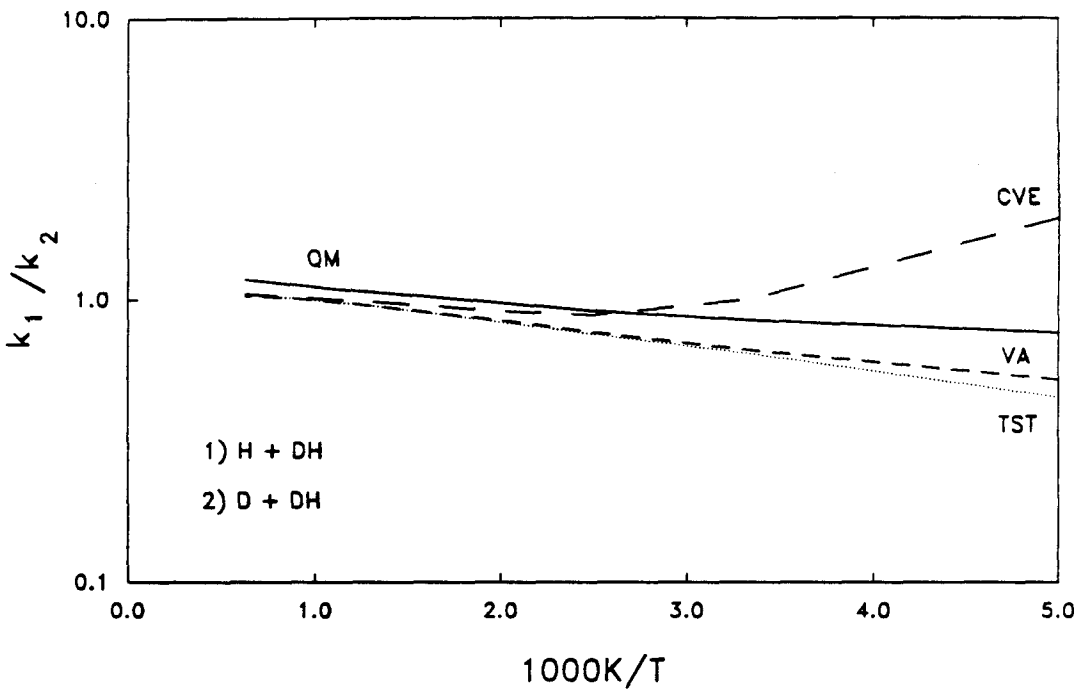

Figure 64.

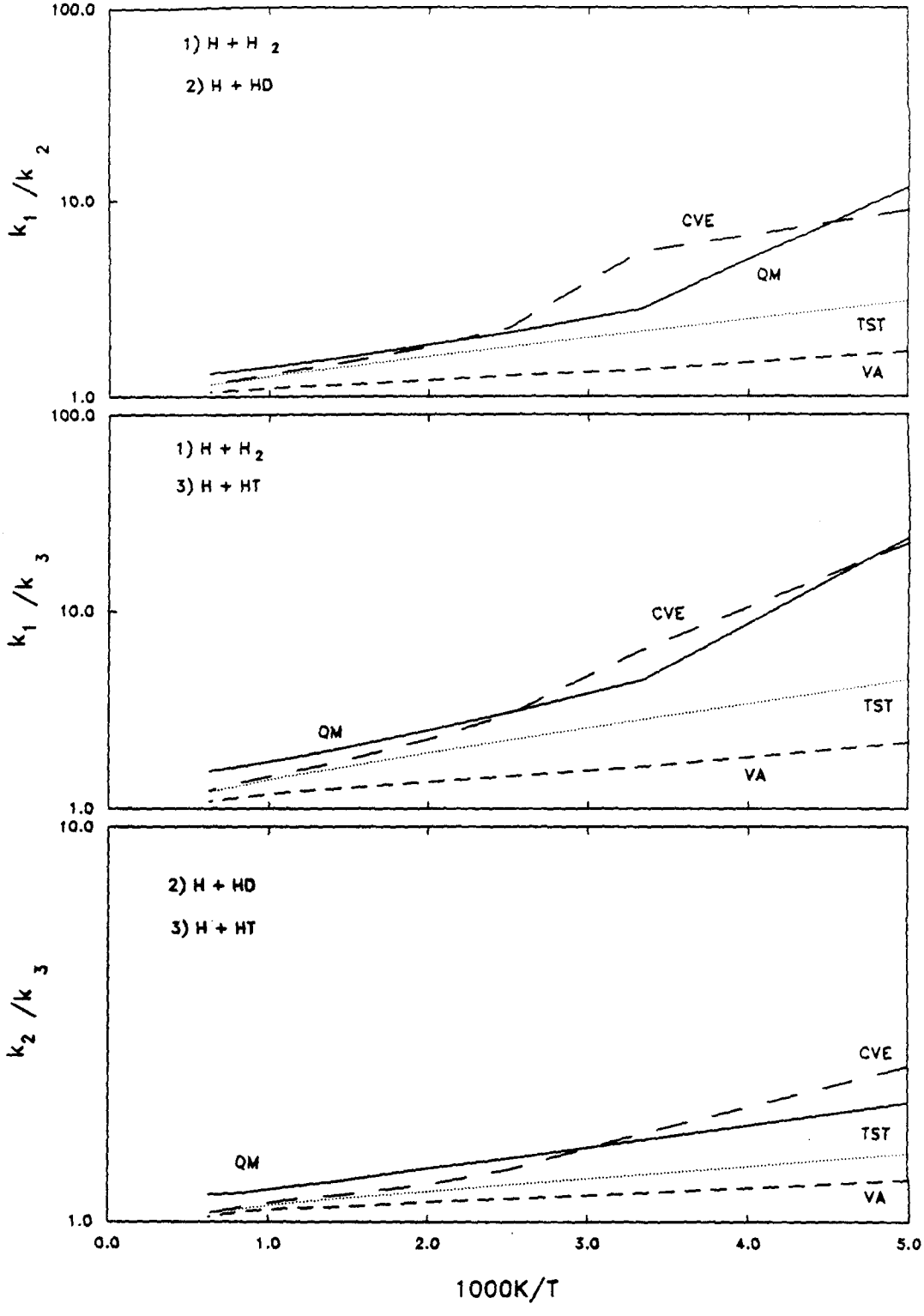
100.0
1) H + H 2
2) H + HD
k1 /k 2
10.0
CVE
QM
TST
VA
1.0
100.0
1) H + H2
3) H + HT
k1 /k 3
10.0
CVE
QM
TST
VA
1.0
10.0
2) H + HD
3) H + HT
k2 /k 3
CVE
TST
QM
VA
1.0
0.0
1.0
2.0
3.0
4.0
5.0
1000K/T

Figure 65.

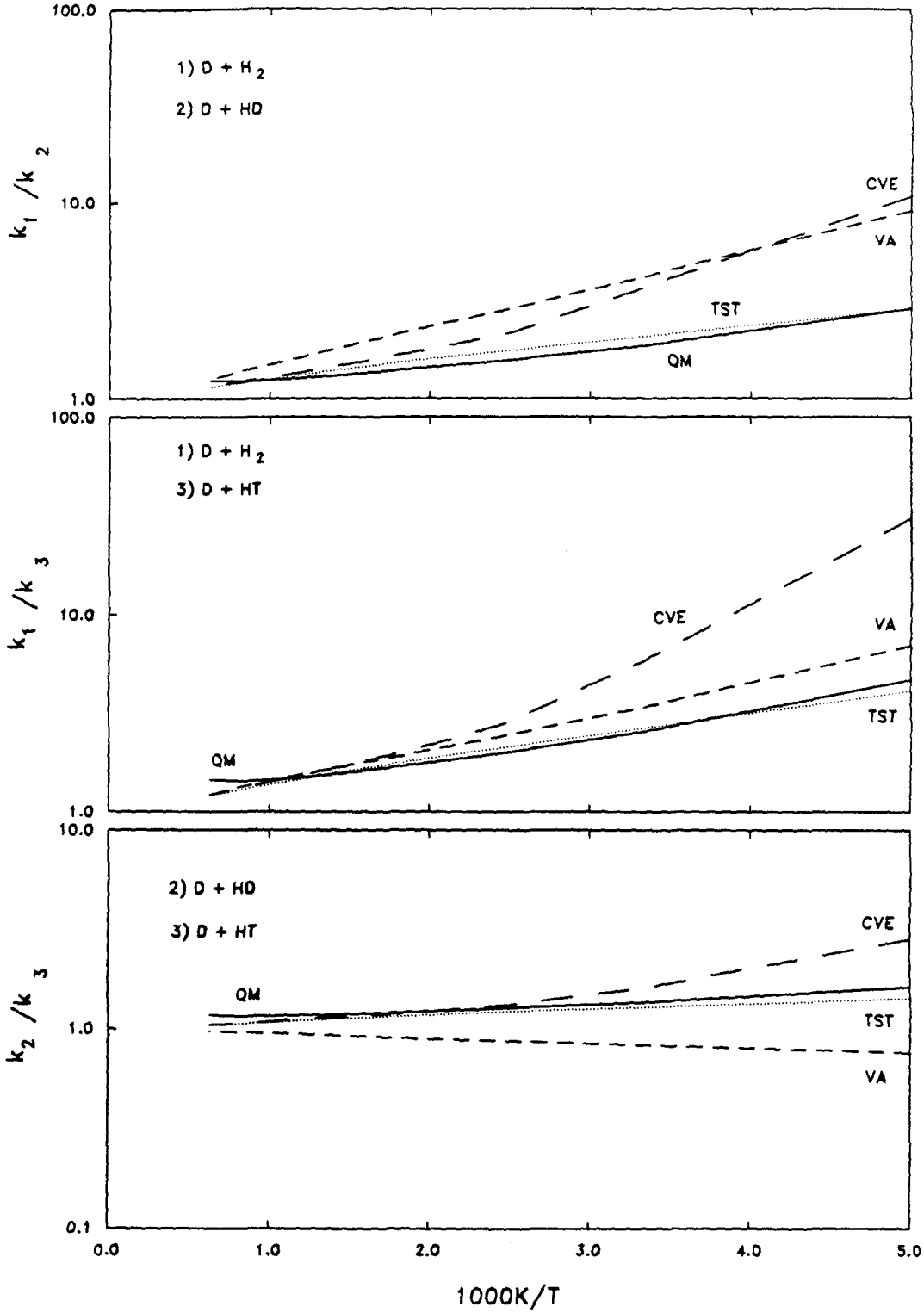
100.0
10.0
1.0
1) D + H 2
2) D + HD
k 1 /k 2
CVE
VA
TST
QM
100.0
10.0
1.0
1) D + H 2
3) D + HT
k 1 /k 3
CVE
VA
TST
QM
10.0
1.0
0.1
2) D + HD
3) D + HT
k 2 /k 3
QM
CVE
TST
VA
0.0
1.0
2.0
3.0
4.0
5.0
1000K/T

Figure 66.

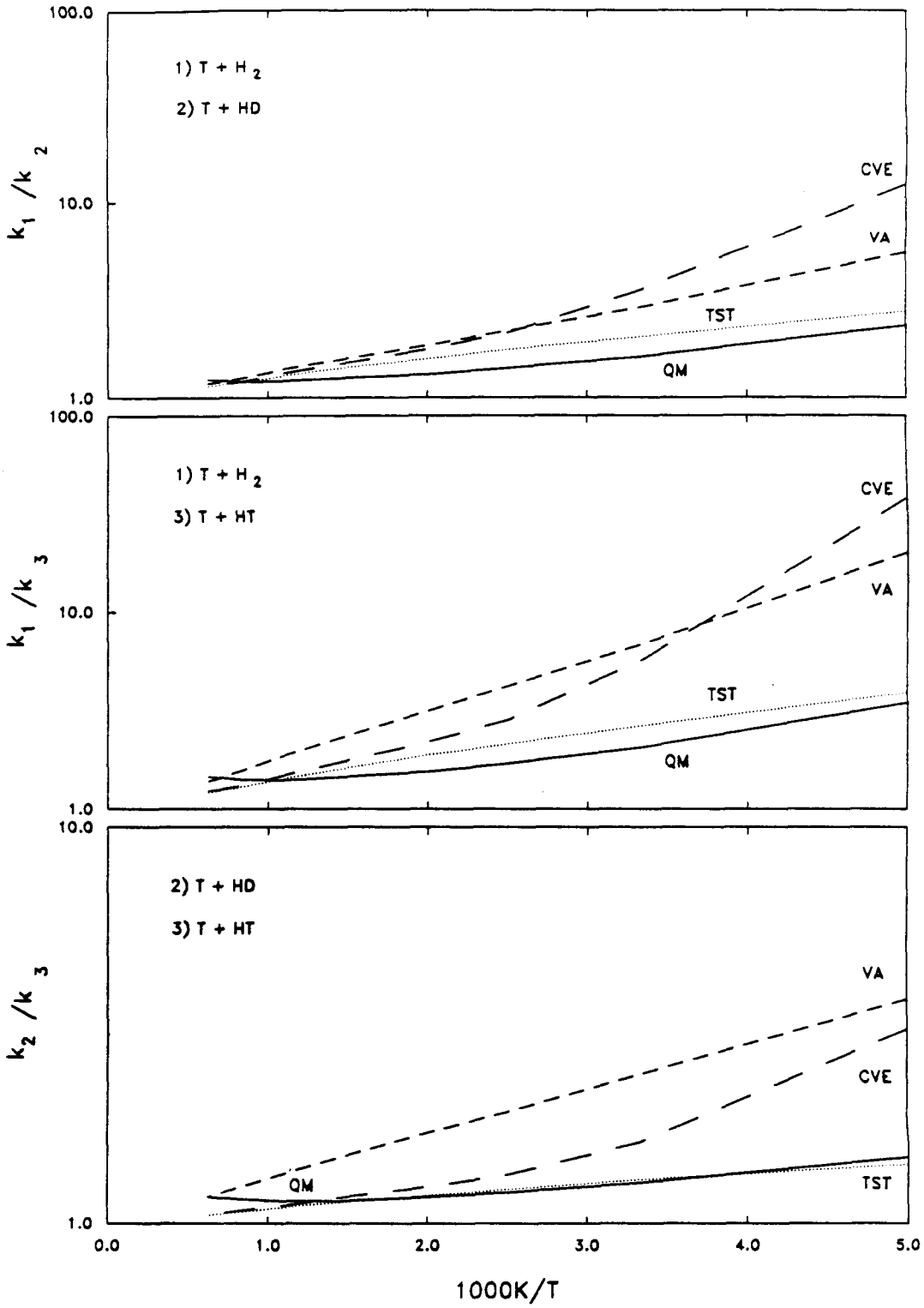
100.0
1) T + H 2
2) T + HD
k1 /k 2
10.0
CVE
VA
TST
QM
1.0
100.0
1) T + H 2
3) T + HT
k1 /k 3
10.0
CVE
VA
TST
QM
1.0
10.0
2) T + HD
3) T + HT
k2 /k 3
VA
CVE
QM
TST
1.0
0.0
1.0
2.0
3.0
4.0
5.0
1000K/T

Figure 67.

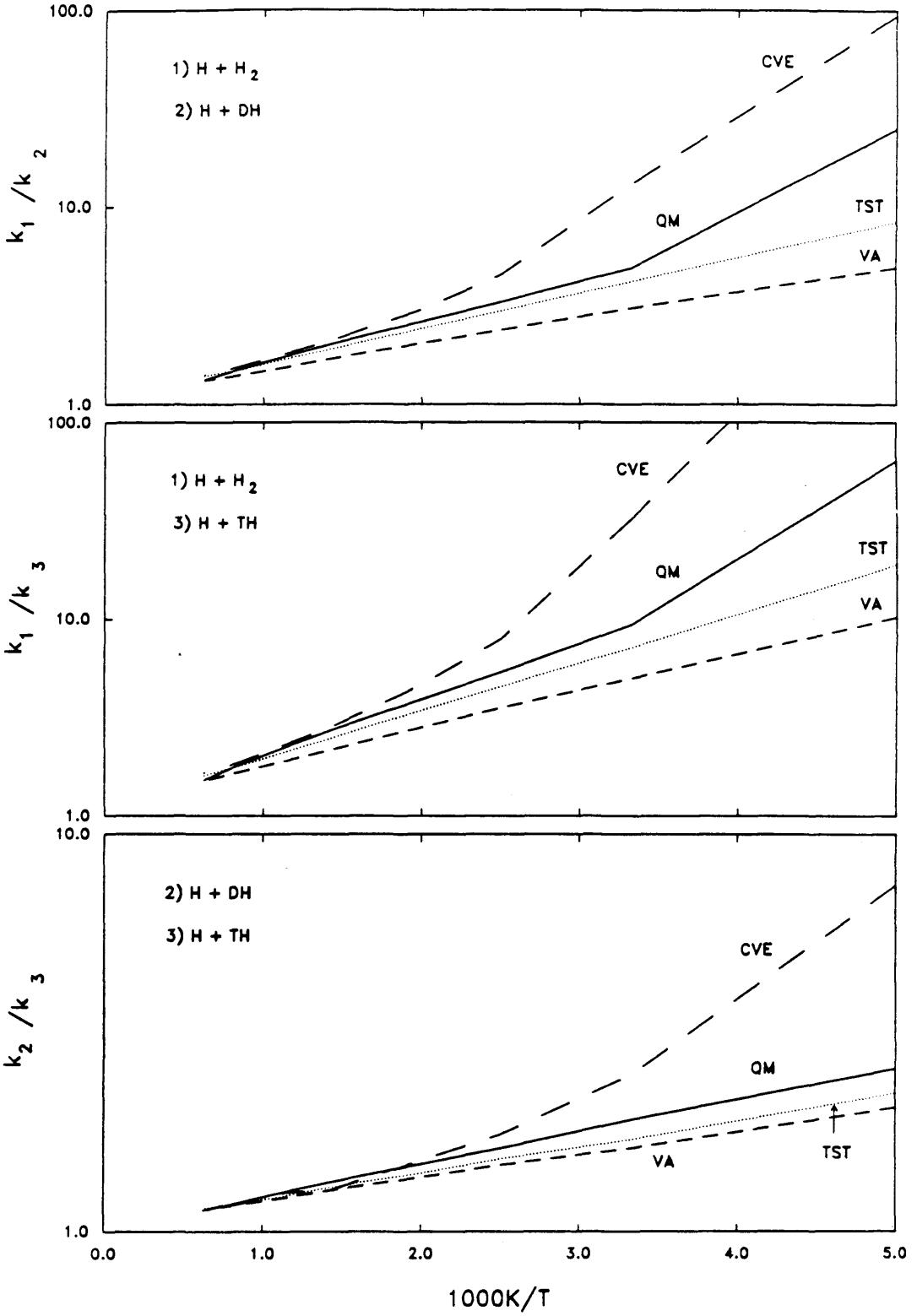
100.0
10.0
1.0
k_1 / k_2
1) H + H_2
2) H + DH
CVE
QM
TST
VA
100.0
10.0
1.0
k_1 / k_3
1) H + H_2
3) H + TH
CVE
QM
TST
VA
10.0
1.0
k_2 / k_3
2) H + DH
3) H + TH
CVE
QM
VA
TST
0.0
1.0
2.0
3.0
4.0
5.0
1000K/T

Figure 68.

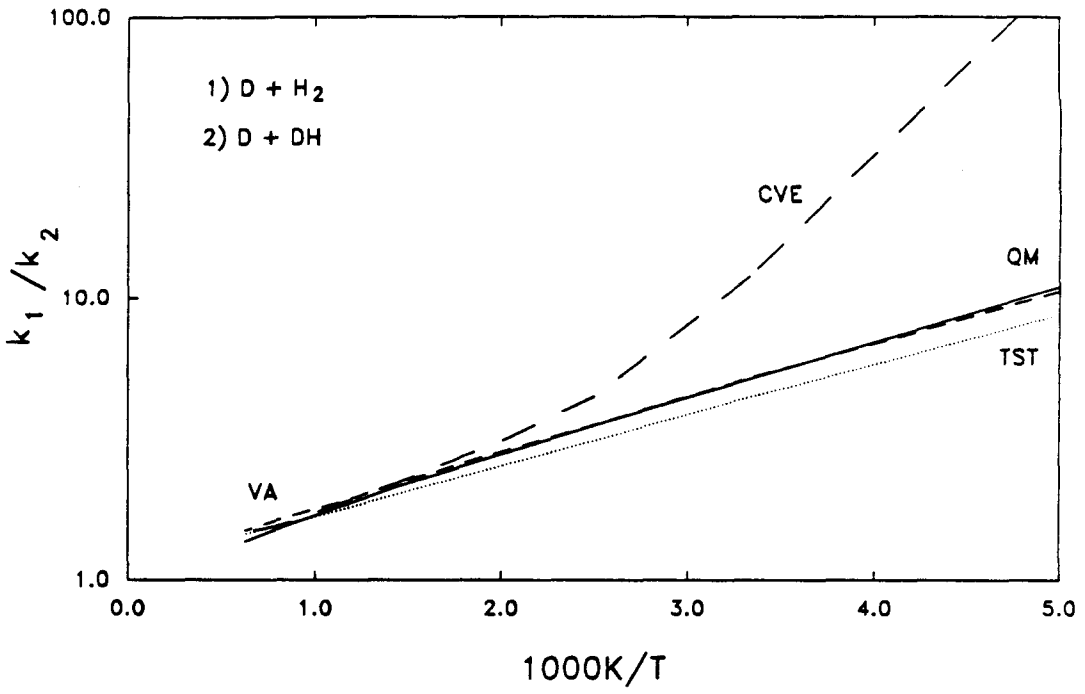

Figure 69.

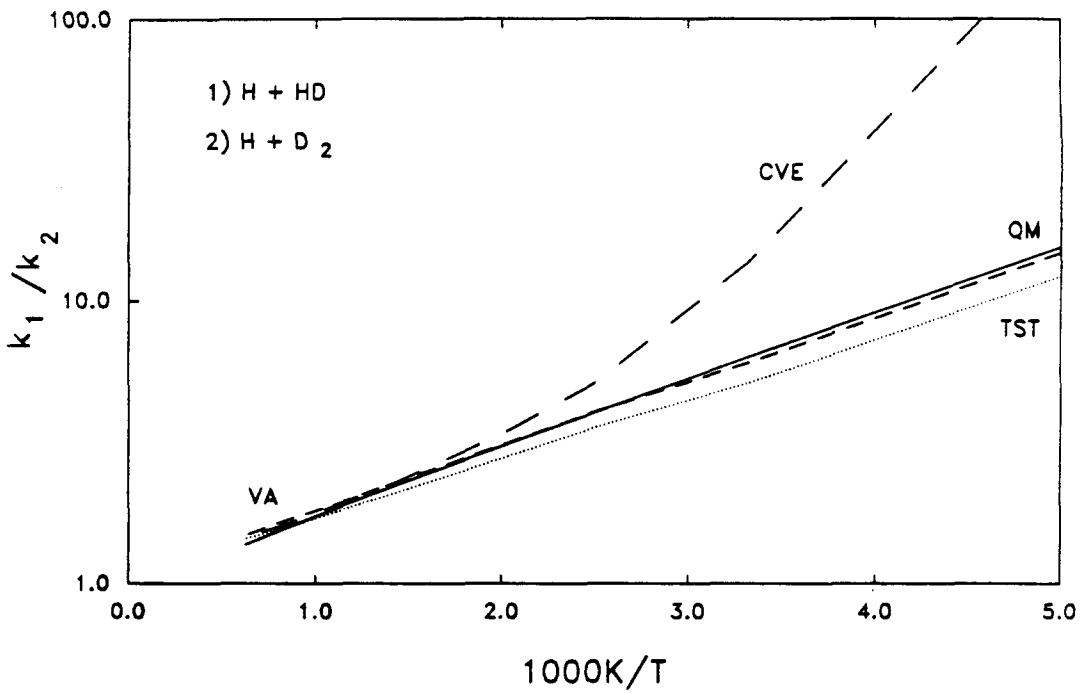

Figure 70.

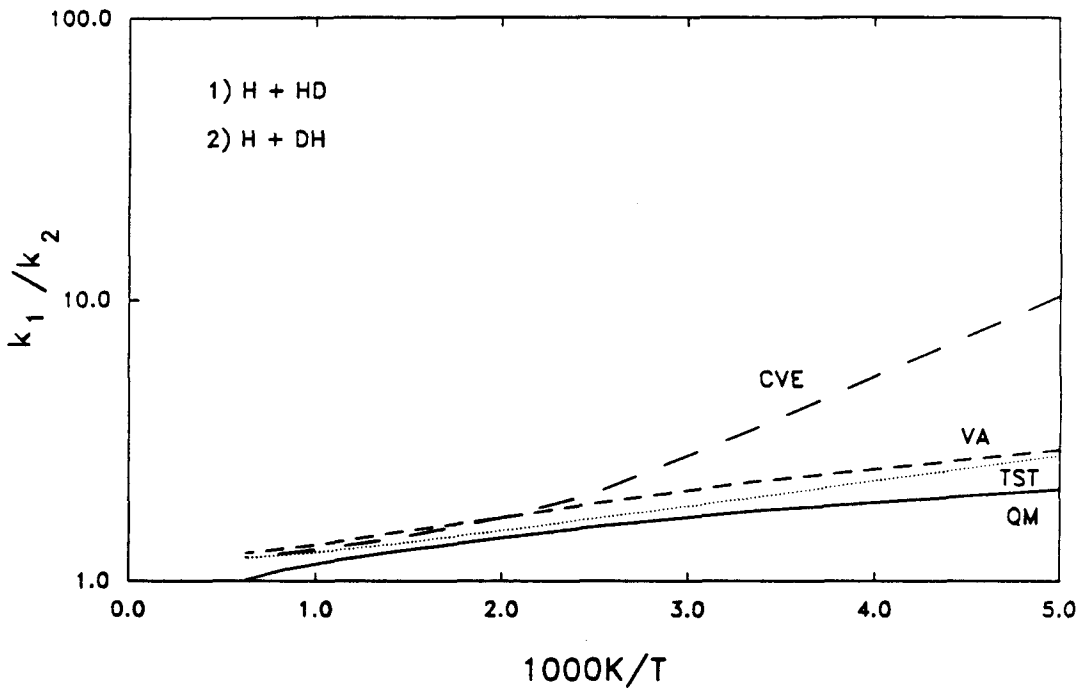

Figure 71.

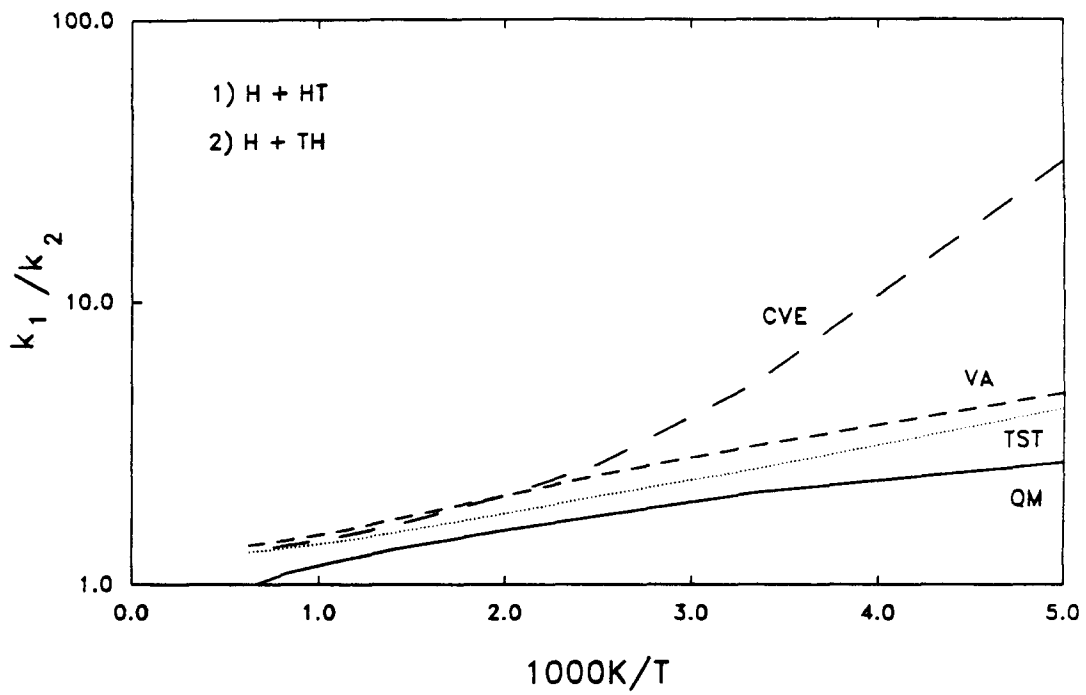

Figure 72.

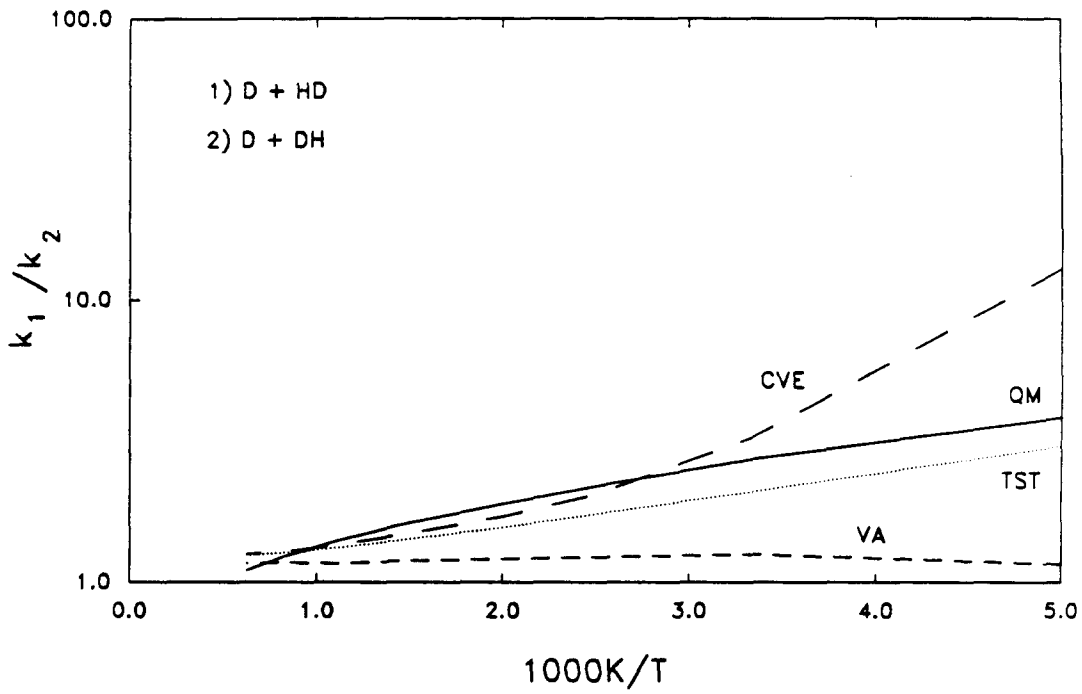

CHAPTER IV

GENERATION OF VACUUM ULTRAVIOLET RADIATION BY THIRD-HARMONIC GENERATION

I. INTRODUCTION

The field of nonlinear optics has expanded tremendously since the advent of high power lasers, and has made vital contributions to such diverse fields as high-resolution atomic and molecular spectroscopy, optical microscopy, signal processing and combustion analysis. The concept of a nonlinear process, however, preceded the invention of the laser: the simultaneous absorption of two photons was theoretically described as early as 1931 by M. Goeppert-Mayer.[1] Nonlinear optical interactions, however, are orders of magnitude weaker than linear ones, and their eperimental verification had to wait for the intense radiation fields provided by a laser.

The nonlinear interactions of radiation with matter are characterized by an induced polarization that depends on the second- and higher-order powers of the optical field. The familiar linear phenomena, such as linear absorption, refraction and scattering, on the other hand, all arise from oscillating polarizations in the medium that are proportional to the first power of the field. The various types of nonlinear processes can be classified according to two broad categories, involving inelastic and elastic interactions with the medium. In the first case, energy is transferred from the field to the medium; the phenomena of stimulated Raman scattering and multiphoton absorption and emission are examples of such effects. The elastic type of interaction consists of an energy exchange between the different optical waves, with no net energy gain or loss to the material: optical harmonic generation and frequency mixing belong to this category.

The optical properties of materials are determined by the response of their component electrons and ions to the incident field. Light impinging on a medium induces an oscillating dipole moment in the electron cloud; the induced dipole then radiates a second optical field which interferes with the incident one. The electrons or ions in many materials can be described as vibrating about their equilibrium positions in a harmonic potential well. However, for large enough displacements (as

induced by strong enough fields), the potential becomes sufficiently anharmonic, and the polarization will depend on the higher powers of the field. This model has been used by Bloembergen[2] to estimate the second- and third-order coefficients.

The lowest-order process, three-wave-mixing, involves the interaction of two photons to create a third field with frequency $\omega_3 = \omega_1 \pm \omega_2$; the degenerate case, $\omega_3 = 2\omega_1$ was first demonstrated by Franken *et al.*[3] who doubled the output of a ruby laser with a quartz crystal. Four-wave mixing (FWM) processes are the next highest-order processes. In this case, three waves interact to form a fourth one, whose frequency is given by $\omega_4 = \omega_1 \pm \omega_2 \pm \omega_3$. The degenerate case, in which $\omega_4 = 3\omega_1$, is third-harmonic-generation (THG), first observed by Maker and Terhune[4] in crystals and glasses, as well as liquids. Ward and New[5] later showed its existence in gaseous media. Higher-order processes, such as fifth- or seventh-harmonic generation have extended the wavelength range down into the soft X-ray region.[6] Nonlinear phenomena have also been the subject of extensive theoretical work: in most cases, the electric field is described classically, while the atomic and molecular systems are treated quantum mechanically. The first studies by Dirac[7] and Goeppert-Mayer[1] applied perturbation theory to explain the effect of the field on the medium.

Both three-wave and four-wave interactions have been treated semiclassically by Armstrong *et al.*[8] and Kleinman and co-workers;[9,10] their treatment can also be found in standard quantum electronics textbooks.[11] Many groups have later extended the theory of third- and higher-order phenomena.[12–16] This chapter will attempt to review the main results of the theory and focus on the experimental aspects of third-harmonic-generation.

II. THEORY OF FOUR-WAVE MIXING PROCESSES

A. Nonlinear Optical Phenomena

The theory of nonlinear phenomena has been extensively reviewed in the recent books by Reintjes[17] and Shen;[18] only the principal results will be summarized here.

The propagation of an optical wave through a medium is described by Maxwell's equations:[19]

$$\nabla \times \mathcal{H} = \frac{1}{c}\frac{\partial \mathcal{D}}{\partial t}, \tag{1}$$

$$\nabla \times \mathcal{E} = -\frac{1}{c}\frac{\partial \mathcal{B}}{\partial t}, \tag{2}$$

and, in the absence of currents and free charges:

$$\nabla \cdot \mathcal{B} = 0, \tag{3}$$

$$\nabla \cdot \mathcal{D} = 0, \tag{4}$$

where $\mathcal{D}$ and $\mathcal{B}$ are the electric displacement and magnetic induction vectors; the response of the medium can be accounted for by defining the electric and magnetic polarization vectors $\mathcal{P}$ and $\mathcal{M}$:

$$\mathcal{D} = \mathcal{E} + 4\pi\mathcal{P}, \tag{5}$$

$$\mathcal{B} = \mathcal{H} + 4\pi\mathcal{M}. \tag{6}$$

Substituting Eqs. (5) and (6) into Maxwell's equations, and ignoring magnetic effects, one obtains the wave equation relating the polarization to the electric field:

$$\nabla^2\mathcal{E} - \frac{1}{c^2}\frac{\partial^2\mathcal{E}}{\partial t^2} = \frac{4\pi}{c^2}\frac{\partial^2\mathcal{P}}{\partial t^2}. \tag{7}$$

The slowly varying envelope approximation is usually invoked to justify the representation of the electric field as a product of two components, one whose

time variations occur on a much slower scale than the optical frequency, and the other oscillating at the optical frequency ω:

$$\mathcal{E}(r,z,t) = \frac{1}{2}\left[E(r,z,t)e^{-i(\omega t - kz)} + c.c.\right], \tag{8}$$

where the z direction has been chosen as the direction of propagation. In problems involving nonlinear processes, the presence of more than one optical frequency is anticipated by expressing the resulting field as a sum of terms:

$$\mathcal{E}(r,z,t) = \frac{1}{2}\sum_i \left[E_i(r,z,t)e^{-i(\omega_i t - k_i z)} + c.c.\right]. \tag{9}$$

A similar expression exists for the resulting polarization:

$$\mathcal{P}(r,z,t) = \frac{1}{2}\sum_j \left[\mathbf{P}_j(r,z,t)e^{-i(\omega_j t - k_j^P z)} + c.c.\right]. \tag{10}$$

For sufficiently weak fields, the polarization can be separated into a linear component, proportional to the field, and a nonlinear contribution:

$$\mathcal{P} = \chi^{(1)}\mathcal{E} + \mathcal{P}^{NL}. \tag{11}$$

Substituting Eqs. (9), (10) and (11) into the wave equation, and invoking the slowly varying envelope approximation, one obtains a set of coupled equations for the electric field amplitudes in terms of the nonlinear polarizations:

$$\nabla_\perp^2 E_j + 2ik_j\frac{\partial E_j}{\partial z} + \frac{2in_j{}^2\omega_j}{c^2}\frac{\partial E_j}{\partial t} = -\frac{4\pi\omega_j{}^2}{c^2}\mathbf{P_j}^{NL}e^{-i\Delta k_j z}. \tag{12}$$

$\Delta k_j = k_j - k_j^P$ is known as the wave vector mismatch for the jth wave. The relationship between the linear susceptibility and the index of refraction has also been used in deriving Eq. (12):

$$n_j{}^2 = (1 + 4\pi\chi_j^{(1)}). \tag{13}$$

Transformation to a coordinate system which propagates at the group velocity common to all waves eliminates the time derivative on the left side of Equation (12), and the resulting equation is of the same form as those that represent interactions with steady-state fields:

$$\nabla_{\perp}^2 E_j + 2ik_j \frac{\partial E_j}{\partial z} = -\frac{4\pi {\omega_j}^2}{c^2} \mathbf{P_j}^{NL} e^{-i\Delta k_j z}. \tag{14}$$

In general, the time-dependent polarizations needed in Eq.(14) can be quite complicated. In cases not involving saturation, breakdown or resonant behavior, the nonlinear polarization, ignoring higher multipole terms, can be expressed as a power series in the incident field:

$$\mathcal{P}^{NL} = \chi^{(2)} {\mathcal{E}_T}^2 + \chi^{(3)} {\mathcal{E}_T}^3 + ... \tag{15}$$

$\mathcal{P}^{NL}$ has components at frequencies not present in the original fields. For the general nth order process, $\omega_q = \omega_1 + \omega_2 + ... + \omega_n$, the nonlinear polarization amplitude is given by:[17]

$$P^{NL}(\omega_q) = \frac{g}{2^{n-1}} \chi^{(n)}(-\omega_q, \omega_1, ..., \omega_n) E_1 E_2 ... E_n, \tag{16}$$

where g indicates the degeneracy of the process. For the process employed in this thesis, third-harmonic generation, Equation (16) becomes:

$$P_i(\omega_4 = 3\omega_1) = \frac{1}{4} \chi^{(3)}_{ijkl}(-\omega_3, \omega_1, \omega_1, \omega_1) E_j^{\omega_1} E_k^{\omega_1} E_l^{\omega_1}. \tag{17}$$

B. Four-wave Mixing

An expression describing the total energy output of a four-wave mixing process using three incident Gaussian laser beams in a TEM_{00} mode has been derived by Bjorklund[12] using a Fourier decomposition. The procedure consists of specifying the spatial dependence of the driving polarization, and decomposing it into its

constituent frequency terms. The sum of the generated fields is then obtained. The resulting energy for the sum-frequency mixing process is found to be:[20]

$$E_4 = \frac{16384\,\pi^5\, ln2\,\sigma^2 \left|N\chi^{(3)}\right|^2 k_0}{\lambda_1\lambda_2\lambda_3\lambda_4 n_4 c^2 k'} \times \frac{E_1 E_2 E_3 \tau_4}{\tau_1\tau_2\tau_3} \times \Phi, \tag{18}$$

where σ is the degeneracy factor (1/4 for THG), $\chi^{(3)}$ is the atomic third-order nonlinear susceptibility tensor, N is the number density of the medium, n_4 is the index of refraction at the generated wavelength λ_4 and τ_i is the full-width at half-maximum pulse width of the ith laser beam. Φ is a dimensionless quantity termed the phase matching factor which contains all of the parameters relating to the experimental geometry, for example the length of the medium, the location of the foci, the confocal parameters and the wavevector mismatch Δk. The efficiency of the process therefore depends on three different aspects: the first term in Eq. (18) depends on the medium chosen, and with the sole exception of the number density N, it is subject to the choice of λ_4 desired. The second term incorporates the pump source requirements of power and pulse width. The phase matching factor, on the other hand, contains the geometrical requirements of the process, and can be adjusted to some extent.

1. Third-order Nonlinear Susceptibility

In isotropic media, the third-order nonlinear susceptibility is the first nonlinear nonzero term in the polarizability expansion; this tensor has 81 components, only 21 of which are nonzero due to the property of inversion symmetry. Each component of the susceptibility tensor can be evaluated from the density matrix approach.[17,21,22] The result for third-harmonic generation in the dipole approximation is:

$$\chi^{(3)}_{ijkl}(-3\omega,\omega,\omega,\omega) = \frac{(ea_0)^4}{\hbar c^3}\sum_{\alpha,\beta,\gamma}(\mathbf{r}_{0\alpha})_l(\mathbf{r}_{\alpha\beta})_k(\mathbf{r}_{\beta\gamma})_j(\mathbf{r}_{\gamma 0})_i$$
$$\times\left[\frac{1}{(\omega_{\alpha 0}-\omega)(\omega_{\beta 0}-2\omega)}\left(\frac{1}{\omega_{\gamma 0}-3\omega}+\frac{1}{\omega^*_{\gamma 0}+\omega}\right)\right. \tag{19}$$
$$\left.+\frac{1}{(\omega^*_{\alpha 0}+\omega)(\omega^*_{\beta 0}+2\omega)}\left(\frac{1}{\omega^*_{\gamma 0}+3\omega}+\frac{1}{\omega_{\gamma 0}-\omega}\right)\right],$$

where the transition frequencies between states a and b, $\omega_{ab} = (E_b - E_a)/\hbar - i\Gamma_{ab}$, are in reciprocal centimeters, and the transition dipole moments, $\mathbf{r}_{ab} = \langle a|\mathbf{r}|b\rangle$, are in bohrs. The indices i, j, k, l are for the three cartesian directions, while α, β, γ stand for all discrete or continuum states within the atom or molecule. Eq. (19) suggests that the third-order nonlinear susceptibility is largest whenever the transition dipole moments between the intermediate states are large. Also, $\chi^{(3)}$ varies rapidly in the vicinity of one-, two-, or three-photon resonances, becoming large and imaginary. This phenomenon is referred to as resonance-enhancement of the nonlinear process.

Accurate calculations of $\chi^{(3)}$ can be very complex: wavefunctions must be calculated accurately for many states, and the sum over states must be replaced by an integral for the continuum region.

2. Phase Matching Factor

The second factor that can greatly influence the efficiency of the third-order process is the phase-matching factor Φ. For three collimated Gaussian laser beams with the same confocal parameters and foci, this factor is given by:[12]

$$\Phi = \frac{4L^2}{b^2}\frac{sin^2(L\Delta k/2 + 2L/b)}{L\Delta k/2 + 2K/b)^2}, \tag{20}$$

where L is the length of the medium, b the confocal parameter and Δk the wave vector mismatch . Perfect phase-matching is achieved when the wave vector of the generated radiation equals that of the driving polarization. It is a characteristic of

Gaussian laser beams to have the optimum Δk not at zero, but at a negative value given by $-4/b$, the maximum of the function in Eq.(20).

A different situation is encountered for beams that are focused tightly inside the medium. In this case the phase matching factor is nonzero only for negative Δk, in which case it is given by:[12]

$$\Phi = (\pi b \Delta k)^2 e^{b\Delta k}, \tag{21}$$

and has a maximum value at $\Delta k = -2/b$.

From this section it is apparent that Δk places restrictions on the choice of nonlinear medium; by definition $\Delta k = k_4 - k'$, where k' is the wave vector of the driving polarization, $k' = k_1 + k_2 + k_3$:

$$\Delta k = 2\pi \left(\frac{n_{\lambda_4} - n_{\lambda_1}}{\lambda_1} + \frac{n_{\lambda_4} - n_{\lambda_2}}{\lambda_2} + \frac{n_{\lambda_4} - n_{\lambda_3}}{\lambda_3} \right). \tag{22}$$

Phase mismatches arise from the dispersion in the refractive indeces between the incident and the generated frequencies. Below the first excited level, the dispersion is positive and n increases with frequency. In the vicinity of a resonance, the dispersion varies rapidly from large positive to large negative values, a phenomenon known as anomalous dispersion. Choice of appropriate wavelengths arranged about a dispersive resonance is possible, but this requires several pump lasers. Multicomponent gas mixtures are widely used for phase matching. In this method, a gas with positive Δk is mixed with one with a negative one. Varying the ratio can provide a broad range of Δk's.

By far the simplest method of providing the required phase matching is to vary the number density of the medium. This method requires a gas with negative Δk, since the pressure variation can only change the magnitude, not the sign of Δk. Calculation of Δk is possible if the linear refractive indeces are known; n_{λ_i} is

found from the linear susceptibility $\chi^{(1)}$ by Eq.(13)[23] and the oscillator strengths of the medium:[24]

$$n-1=2\pi N\chi^{(1)}=\frac{N\lambda^2}{2\pi}\left[\alpha^2 a_0\sum_{i=1}^{n_d}\frac{\lambda^2 f_i}{\lambda^2-{\lambda_i}^2}+\frac{1}{\pi}\int_0^{\lambda_{IP}}\frac{\sigma(\lambda_i)d\lambda_i}{\lambda^2-\lambda_i^2}\right]. \qquad (23)$$

Here α is the fine structure constant,a_0 the Bohr radius, f_i the oscillator strength of the i'th transition, σ the absorption cross section and N the number density. The summation is over all discrete states (n_d), and the integral over the continuum region. Mahon *et al.*[25] calculated the refractive indeces for Ar, Kr and Xe using this method.

III. EXPERIMENTAL APPROACH

The purpose of the experiments in this thesis was to detect molecular hydrogen using the technique of laser-induced fluorescence from the first excited electronic state $\tilde{B}\ ^1\Sigma_u^+$ to the ground state $\tilde{X}\ ^1\Sigma_g^+$. This requires an excitation wavelength around 110 nm. No three-wave process can generate radiation at this short a wavelength, so the technique of third-harmonic generation was used.

A detailed discussion of the development of the VUV laser source used for these experiments can be found in the thesis by G. R. Parker, Jr.[20] Only the principal criteria for the choice of medium will be reviewed here. From the results of the previous chapter, the two dominant factors for the choice of a nonlinear medium are the wave vector mismatch Δk and the third-order nonlinear susceptibility $\chi^{(3)}$. The refractive index and Δk for THG in Ar, Kr and Xe were calculated[20,25] using Eqs. (22) and (23). Ref. (20) makes use of the most recent published oscillator strengths,[26-36] high resolution absorption and photoionization spectra[37-40] and recent compilations of continuum absorption cross sections.[41-43] The wave vector mismatch Δk was found to be positive for all wavelengths above 106.7 nm in Ar, thus excluding the possibility of using Ar as a nonlinear medium. Xe and Kr were both found to have regions of negative Δk, with Kr having a fairly wide window between 109.55 nm and 116.4867 nm. The results for the three rare gases were found to agree well with both calculations[25] and experiments.[44-49]

Obtaining an estimate of $\chi^{(3)}$ is a significantly more complicated problem than calculating Δk. Exact dipole matrix elements are difficult to obtain, since accurate wavefunctions are required. A few observation about the process in Kr can however be made from spectroscopic considerations.[20] No resonance enhancement is expected in the wavelength region considered. For a tripling wavelength of 330 nm the virtual states populated by the one- and two- photon processes will lie several thousands of wavenumbers away from allowed excited states of Kr. Both

the magnitude and the phase of the matrix elements are needed for a calculation of $\chi^{(3)}$. For the case of Kr, several states are expected to contribute to the triple sum in Eq. (19), so the expression does not lend itself to much simplification. The magnitude of the dipole matrix elements is given by:[50]

$$|(\mathbf{r}_{ab})_i| = \mathcal{Z}_{Jl}\left(\frac{g_a f_{ab}}{E_b - E_a}\right)^{1/2}, \tag{24}$$

where f_{ab} is the oscillator strength for the transition from state a to state b, g_a is the degeneracy of state a, and $\mathcal{Z}_{Jl}$ is an angular momentum term, which depends on the coupling between the states and the polarization of the incident radiation. The six strongest transitions, in order of decreasing wavelength,are to the $5s[3/2]_1^o$, $5s'[1/2]_1^o$, $4d[1/2]_1^o$, $4d[3/2]_1^o$, $6s[3/2]_1^o$, and the $5d[3/2]_1^o$ excited states); their dipole matrix elements have relative magnitudes of 1.00 : 0.93 : 0.14 : 0.54 : 0.76 : 0.68, those are the states most likely to contribute to $\chi^{(3)}$, provided the phases do not interfere destructively.

IV. APPARATUS

A. Laser System and Optics

All of the VUV work described in this thesis makes use of a Quanta-Ray DCR-2A Nd:YAG laser, a PDL-2 dye laser and a WEX-1 wavelength extension unit. A detailed description of this laser system can be found in Appendix 1 of Reference (20). Briefly, this laser is a diffractio-coupled resonator plus amplifier, which produces a donut-shaped beam at 1064.1 nm; the second harmonic at 532 nm is generated by doubling in a type II KD*P crystal. The various beams are separated in a prism harmonic separator (PHS) composed of a Pellin-Broca prism, a Porro prism, and two right-angle turning prisms. The polarization of the output beam is rotated by a $\lambda/2$ plate to vertical just before input to the dye laser. This laser operates at a preferred repetition rate of 20 Hz, and achieves peak powers of 360 mJ at 532 nm.

The dye laser is of the Hänsch design, with a transversely pumped preamplifier and longitudinally pumped amplifier stages. This laser is controlled by an Intel SBC 80/20 microcomputer whose hardware and software is described in the theses of R. Rianda,[51] D. J. Moll[52] and G. R. Parker, Jr.;[20] the software is written in 8080 assembly language.

The wavelength-extension unit WEX-1 is equipped with seven KD*P crystals to cover the range 217-432 nm; both doubling and mixing with the 1064 nm beam is possible. Optimum phase-matching is maintained by a servo-mechanism that uses a pair of photodiodes to keep the output uniform as the dye-laser is scanned. The residual visible light is removed by a Schott UG-11 UV filter at the output of the WEX.

In order to generate VUV radiation at 110 nm, the visible output of the dye laser at 660 nm is doubled by the WEX doubling crystal to 330 nm, then tripled to 110 nm by the THG process. All of the experiments in this thesis use Exciton laser

dye DCM (4-(dicyano-methylene)-2-methyl-6-(p-dimethylaminostyryl)-4H-pyran) in methanol/DMSO (50:50 v:v). The addition of DMSO shifts the DCM lasing maximum to 650 nm, with an efficiency of 21 %

The configuration of the laser table for third-harmonic generation experiments is illustrated in Figure 1. The 330 nm beam goes through a right angle prism and is focused into the cell by a 10 cm focal length Suprasil lens. The UV energy output is monitored by splitting off a small portion of the beam and sending it to a Laser Precision Corporation Rjp-735 pyroelectric joulemeter. The temporal profile of the beam can be monitored by a photodiode (HP 5082-4220). Taking into account spherical aberration and diffraction, the lens is expected to focus the 2.4 mm radius beam to a 4.8 microns spot size.[20]

B. Experimental Cell

The cell used for the VUV experiments is illustrated in Figure 2. The first compartment holds the nonlinear medium: it is a stainless steel tube 4.25 in. long and 1.5 inches in diameter. The laser beam enters through a 1/16 in. thick Suprasil window and exits through a 1 mm thick VUV grade LiF window into the middle compartment, which houses the sample/reaction cell. This is a 5 in. long 1.5 in. in diameter stainless steel cell bolted to the first compartment. This cell contains a series of aluminum apertures to minimize scattered light, as shown in Fig. 2. The photomultiplier used for fluorescence detection is mounted perpendicular to the cell axis 2 in. from the LiF entrance window, and 2 in. away from the laser beam axis. All inside surfaces of the first and second compartments are painted flat black, while the aluminum apertures are black anodized.

A second LiF window separates the second and third compartment. This is also a 1.5 in. diameter stainless steel tube, 7.75 in. long, with a second Suprasil window at the exit. This part of the cell is used as an ionization cell to monitor the intensity of the VUV radiation.

All three compartments are fitted with vacuum line connections; the cell is evacuated for about 48 hours between experiments on a glass vacuum line pumped by a 2 in. oil diffusion pump with utlimate vacuum of the order of 2×10^{-7} torr. During experiments, the cell is pumped by a small glass vacuum line placed on the laser table which uses a mechanical pump and a liquid nitrogen pump.

The use of ionization cells for VUV detection is discussed by Carver and Mitchell,[53] who investigated several gases: nitric oxide, acetone, carbo disulphide, ethyl bromide and ethyl chloride. Experiments in this dissertation have used both NO and acetone.

The ionization cell makes use of a parallel plate arrangement of 15.8 cm by 1.7 cm Ni plates, 0.08 cm thick. The outer side is coverd with 0.025 cm thick platinum foil to minimize photoelectron emission by the UV beams in the cell. The two electrodes are mounted on two Teflon spacers at the two ends and the assembly is wrapped in teflon tape to prevent contact with the stainless steel walls of the cell.

The photoabsorption cross section for NO has been extensively studied.[54–60] In order to ionize NO, photons of wavelengths below 133.83 nm are required.

The far UV spectroscopy of acetone is somewhat less well documented in the literature: the region up to 7.5 eV has been studied extensively.[61–68] Rydberg series are found converging to the lowest IP (9.71 eV, 127.70 nm, adiabatic), while the region above 10 eV is found to have only broad features.[68]

The response of the ionization cell is expressed in terms of the total charge collected per laser pulse:[69]

$$Q = \kappa e \phi \times \left(1 - e^{-N\sigma z_2}\right) \times e^{-N\sigma z_1}, \tag{25}$$

where κ is the electron detection efficiency, e is the electron charge, ϕ the ionization quantum yield, N the number density, σ the absorption cross section, and z_1 and z_2 the electrode length and the distance from the window to the electrode.

This formula can be analyzed in terms of the three different contributions to the ionization process: the first term represents the fraction of photons absorbed which lead to ionization; the second term gives the fraction of photons absorbed, while the third is the fraction by which the incoming beam is attenuated by the gas before the electrode assembly. The number density can be optimized by differentiating the above equation:

$$N_{opt} = \frac{1}{\sigma z_2}\left(\frac{z_2 + z_1}{z_1}\right). \tag{26}$$

The average absorption cross section[56] for NO is 4.811×10^{-18} cm^2 over the range 109.0-112.0 nm. For this ionization cell, $z_2 = 15.8$ cm and $z_1 = 2.0$ cm, which gives $N_{opt} = 2.88 \times 10^{16}$ molecules/cm^3, or 0.889 torr at room temperature. Using this number, together with the average cross section, and a photoionization yield of 0.81,[53] the average response of the NO ionization cell is 8.67×10^{-8} pC/photon.

The absorption cross section and photoionization yields for acetone have been measured by Person and Nicole.[70] The average cross section is 4.742×10^{-17} cm^2 over the same range of wavelengths, while the photoionization yield is 0.2426, which gives an optimum number density $N_{opt} = 2.92 \times 10^{15}$ molecules/cm^3, and an optimum pressure of 0.0901 torr. The average response of the cell is then 2.61×10^{-8} pC/photon.

V. EXPERIMENTAL RESULTS FOR THG

A. Procedure

99.995 % Kr form Alpha Products was used as the nonlinear medium. The Kr compartment was filled on the small vacuum line on the laser table without further purification.

The ionization cell gas (NO or acetone) was usually prepared in a mixture with He. 99.0 % NO from Matheson gas products was purified by trap-to-trap distillation: after several freeze-pump-thaw cycles in liquid nitrogen, NO was distilled from an isopentane/liquid nitrogen slush (90 K), to remove the heavier nitrogen oxides. Spectral grade acetone was subjected to three freeze-pump-thaw cycles and used without further purification.

Mixtures with He were prepared, in order to insure a more accurate pressure reading for the quantities specified in the previous section. Approximately 9 torr of a 10 % mixture of NO, or a 1 % mixture of acetone in He, provide number densities near the optimum value determined in the previous section.

The signal from the ionization cell is sent to a charge-sensitive preamplifier described in Ref. (20), with a sensitivity of 20.90 ± 0.33 mV/pC and 22.90 ± 0.31 mv/pC for the inverted and noninverted outputs respectively.

The UV output of the Quanta-Ray laser system was monitored by a pyroelectric joulemeter. Both the ionization cell and the PEJM signal were integrated by a pair of Molectron model 112 Differential Gated Integrators, the DC outputs of which were digitized by an Analog Devices RTI-1200 real time interface. The data was collected by the Intel SBC 80/20 single board computer and stored on 8 in. floppy disks. The programs used for data conversion and analysis were originally written by G. R. Parker, Jr., for the Chemistry Division VAX computer.

B. VUV Tuning Curve

As mentioned several times before, the VUV source used in this thesis was developed by G. R. Parker, Jr.: a complete study of the pressure dependence and UV pulse energy dependence of the VUV output is contained in his dissertation.[20] All of the experiments in this thesis used Kr pressures in the range 700-850 torr. The VUV tuning curves for NO and acetone are shown in figures 4 and 5.

The sructure observed in the curves show two intense dips at 111.07 nm and 109.97 nm, which have been attributed to Xe impurities in the Kr, or even XeKr dimers.[20]

The generation of coherent tunable VUV radiation by frequency mixing in gases is now a well established technique: VUV sources of this type are widely used in spectroscopic studies today,[71–79] and have made possible novel experiments in atomic molecular and plasma physics.

REFERENCES

1. M. Goeppert-Mayer, *Ann. Phys. (Leipzig)* **9**, 273 (1931).
2. N. Bloembergen, "Nonlinear Optics" (Benjamin, New York, NY 1965).
3. P. A. Franken, A. E. Hill, C. W. Peters and G. Weinreich, *Phys. Rev. Lett.* **7**, 118 (1961).
4. P. D. Maker and R. W. Terhune, *Phys. Rev.* **137**, 801 (1965).
5. G. H. C. New and J. F. Ward, *Phys. Rev. Lett.* **19**, 556 (1967); J. F. Ward and G. H. C. New, *Phys. Rev.* **185**, 57 (1969).
6. J. Reintjes, C. Y. She and R. C. Eckardt, *IEEE J. Quantum Electron.* **QE-14**, 581 (1978).
7. P. A. M. Dirac, *Proc. Roy. Soc.* **A-114**, 143 (1927).
8. J. A. Armstrong, N. Bloembergen, J. Ducuing and P. S. Pershan *Phys. Rev.* **127**, 1918 (1962).
9. D. A. Kleinman, *Phys. Rev.* **128**, 1761 (1962).
10. D. A. Kleinman, A. Ashkin and G. D. Boyd, *Phys. Rev.* **145**, 145 (1966).
11. A. Yariv, "Quantum Electronics," 3rd edition (John Wiley & Sons, New York, 1989).
12. G. C. Bjorklund, *IEEE J. Quantum Electron.* **QE-11**, 287 (1975).
13. I. V. Tomov and M. C. Richardson, *IEEE J. Quantum Electron.* **QE-12**, 521 (1976).
14. H. B. Puell and C. R. Vidal, *IEEE J. Quantum Electron.* **QE-14**, 364 (1978).
15. Y. M. Yiu, T. J. McIlrath and R. Mahon, *Phys. Rev.* **A-20**, 2470 (1979).
16. N. Nayak, *IEEE J. Quantum Electron.* **QE-16**, 843 (1980).
17. J. F. Reintjes, "Nonlinear Optical Parametric Processes in Liquids and Gases," (Academic Press, New York, 1984).
18. Y. R. Shen, "Principles of Nonlinear Optics," (J. Wiley, New York, 1984).

19. J. D. Jackson, "Classical Electrodynamics," 2nd edition, (J.!Wiley, New York, 1975).

20. G. R. Parker, Jr., Ph.D. Thesis, California Institute of Technology, 1988, Chapters 3 and 4.

21. N. Bloembergen, H. Lotem and R. T. Lynch, Jr., *Indian J. Pure Appl. Phys.* **16**, 151 (1978).

22. M. D. Levenson and S. K. Kano, "Introduction to Nonlinear Laser Spectroscopy," (Academic Press, New York, 1988).

23. M. Born and E. Wolf, "Principles of Optics," 6th edition, (Pergamon Press, New York, 1980).

24. P. L. Smith, M. C. E. Huber and W. H. Parkinson, *Phys. Rev.* **A-13**, 1422 (1976).

25. R. Mahon, T. J. McIlrath, V. P. Myerscough and D. W. Koopman, *IEEE J. Quantum Electron.* **QE-15**, 444 (1979).

26. J. Berkowitz, "Photoabsorption, Photoionization and Photoelectron Spectroscopy," (Academic Press, New York, 1979).

27. G. M. Lawrence, *Phys. Rev.* **175**, 40 (1968).

28. W. B. Westerweld, Th. F. A. Mulder and J. van Eck, *J. Quant. Spectrosc. Radiat. Transfer* **21**, 533 (1979).

29. A. Delâge and J.-D. Carette, *Phys Rev.* **A-14**, 1345 (1976); *J. Phys.* **B-9**, 2399 (1976).

30. J. Geiger, *Z. Physik* **A-282**, 129 (1977).

31. J. M. Vaughan, *Phys. Rev.* **166**, 13 (1968).

32. E. Matthias, R. A. Rosenberg, E. D. Poliakoff, M. G. White, S.-T. Lee and D. A. Shirley, *Chem. Phys. Lett.* **52**, 239 (1977).

33. K. T. Lu, *Phys. Rev.* **A-4**, 579 (1971).

34. P. G. Wilkinson, *J. Quant. Spectrosc. Radiat. Transfer* **6**, 823 (1966).

35. G. I. Chashchina and E. Ya. Shreider, *Opt. Spectrosc. (USSR)* **20**, 283 (1966).

36. W. Wieme and P. Mortier, *Physica* **65**, 198 (1973).

37. K. Yoshino, *J. Opt. Soc. Am.* **60**, 1220 (1970).

38. K. Yoshino and Y. Tanaka, *J. Opt. Soc. Am.* **69**, 159 (1979).

39. K. Yoshino and D. E. Freeman, *J. Opt. Soc. Am.* **B-2**, 1268 (1985).

40. R. E. Huffman, Y. Tanaka and J. C. Larrabee, *Appl. Opt.* **2**, 947 (1963); *J. Chem. Phys.* **39**, 902 (1963).

41. G. V. Marr and J. B. West, *Atom. Dat. Nucl. Dat. Tab.* **18**, 497 (1976).

42. J. B. West and J. Morton, *Atom. Dat. Nucl. Dat. Tab.* **22**, 103 (1978).

43. A. Kumar and W. J. Meath, *Can. J. Chem.* **63**, 1616 (1985).

44. R. Hilbig and R. Wallenstein, *Applied Optics* **21**, 913 (1982).

45. R. Hilbig and R. Wallenstein, *IEEE J. Quantum Electron.* **QE-17**, 1566 (1981).

46. F. J. Northrup, J. C. Polanyi, S. C. Wallace and J. M. Williamson, *Chem. Phys. Lett.* **105**, 34 (1984).

47. D. Cotter *Opt. Commun.* **31**, 397 (1979); *Opt. Lett.* **5**, 134 (1979).

48. E. E. Marinero, C. T. Rettner, R. N. Zare and A. H. Kung, *Chem. Phys. Lett.* **95**, 486 (1983).

49. R. Hilbig and R. Wallenstein, *Opt. Comm.* **44**, 283 (1983).

50. E. U. Condon and G. H. Shortly, "The Theory of Atomic Spectra," (Cambridge University Press, Cambridge, 1970).

51. R. Q. Rianda, Ph.D. Thesis, California Institute of Technology, Pasadena, CA 1982.

52. D. J. Moll, Ph.D. Thesis, California Institute of Technology, Pasadena, CA, 1983.

53. J. H. Carver and P. Mitchell *J. Sci. Instrum.* **41**, 555 (1964).

54. E. Miescher, *Can. J. Phys.* **54**, 2074 (1976).

55. J. A. Guest and L. C. Lee, *J. Phys.* **B-14**, 3401 (1981).

56. K. Watanabe, F. M. Matsunaga and H. Sakai, *Appl. Opt.* **6**, 391 (1967).

57. P. H. Metzger, G. R. Cook and M. Ogawa, *Can. J. Phys.* **45**, 203 (1967).

58. D. Vichon, R. I. Hall, F. Gresteau and J. Mazeau, *J. Mol. Spectrosc.* **69**, 341 (1978).

59. R. P. Frueholz, R. Rianda and A. Kuppermann, *Chem. Phys.* **31**, 315 (1978).

60. R. J. Stubbs, T. A. York and J. Comer, *Chem. Phys.* **106**, 161 (1986).

61. N. L. Allinger, T. W. Stuart and J. C. Tai, *J. Am. Chem. Soc.* **90**, 2809 (1968).

62. E. H. Van Veen, W. L. Van Dijk and H. H. Brongersma, *Chem. Phys.* **16**, 337 (1976).

63. R. H. Staley, L. B. Harding, W. A. Goddard and J. L. Beauchamp, *Chem. Phys. Lett.* **36**, 589 (1975).

64. R. Huebner, R. J. Celotta, S. R. Mielczarek and C. E. Kuyatt, *J. Chem. Phys.* **59**, 5434 (1973).

65. W. M. St. John, R. C. Estler and J. P. Doering, *J. Chem. Phys.* **61**, 763 (1974).

66. J. P. Doering and R. McDiarmid, *J. Chem. Phys.* **76**, 1838 (1982).

67. A. Gedanken *J. Phys. Chem.* **89**, 3781 (1985).

68. K. N. Walzl, C. F. Koerting and A. Kuppermann, *J. Chem. Phys.* **87**, 3796 (1987).

69. S. D. Kramer, C. H. Chen, M. G. Payne, G. S. Hurst and B. E. Lehman, *Appl. Opt.* **22**, 3271 (1983).

70. J. C. Person and P. P. Nicole, Argonne National Laboratory, Radiological Physics Division Annual Report, July 1969-June 1970. ANL-7760, p.97.

71. J. C. Miller, R. N. Compton and C. D. Cooper, *J. Chem. Phys.* **76**, 3967 (1982).

72. M. P. McCann, C. H. Chen and M. G. Payne, *J. Chem. Phys.* **89**, 5429 (1988).

73. K. D. Bonin and T. J. McIlrath, *J. Opt. Soc. Am.* **B-2**, 527 (1985).

74. C. R. Vidal, *Appl. Opt.* **19**, 3897 (1980).

75. T. Trickl, M. J. J. Vrakking, E. Cromwell, Y. T. Lee and A. H. Kung, *Phys. Rev.* **A-39**, 2948 (1989).

76. W. Ubachs, L. Tashiro and R. N. Zare, *Chem. Phys.* **130**, 1 (1989).

77. T. Tsuchizawa, K. Yamanouchi and S. Tsuchiya, *J. Chem Phys.* **93**, 111 (1990); *J. Chem. Phys.* **92**, 1560 (1990).

78. D. J. Hart and O. L. Bourne, *Chem. Phys.* **133**, 103 (1989).

79. R. G. Tonkyn, J. W. Winniczek and M. G. White, *J. Chem. Phys.* **91**, 6632 (1989).

FIGURE CAPTIONS

Figure 1. Scale laser table layout for VUV generation experiments:[20] the following symbols are used: A- aperture, BS- beam splitter, PEJM- pyroelectric joulemeter, P-right angle prism, PD- photodiode.

Figure 2. Scale diagram of the experimental cell:[20] the first compartment holds the nonlinear medium for THG, the second is the reaction cell and the third the VUV detector.

Figure 3. Electronics for the VUV experiment:[20] the dotted lines correspond to digital control signals, the $- \cdot -$lines to analog control signals, and the solid lines to analog data signals.

Figure 4. VUV detection with NO ionization cell: the top panel is the output of the pyroelectric joulemeter. and the bottom the ionization cell signal in pC.

Figure 5. Same as Figure 4 but with acetone as the ionization cell medium.

Figure 1.

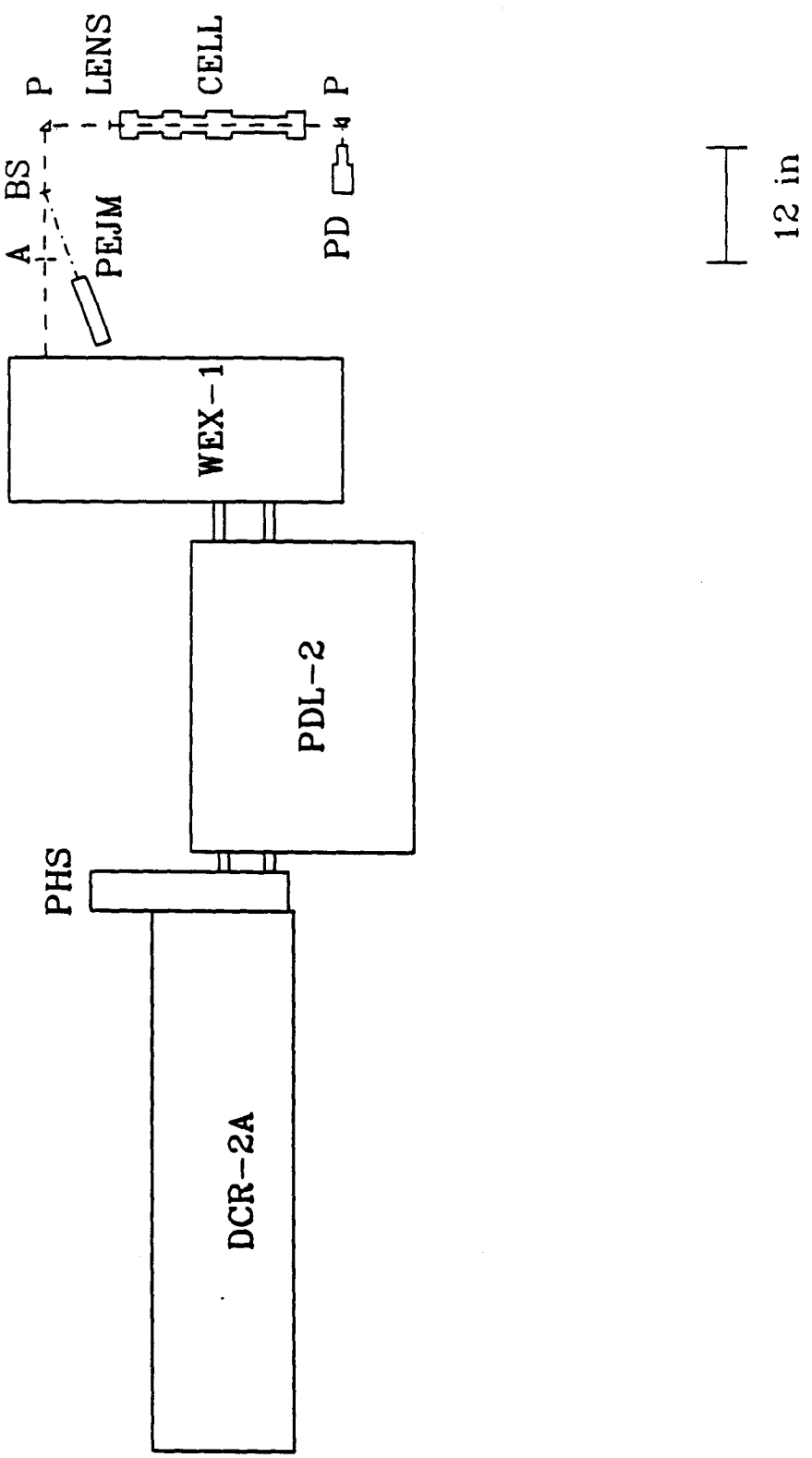

Figure 2.

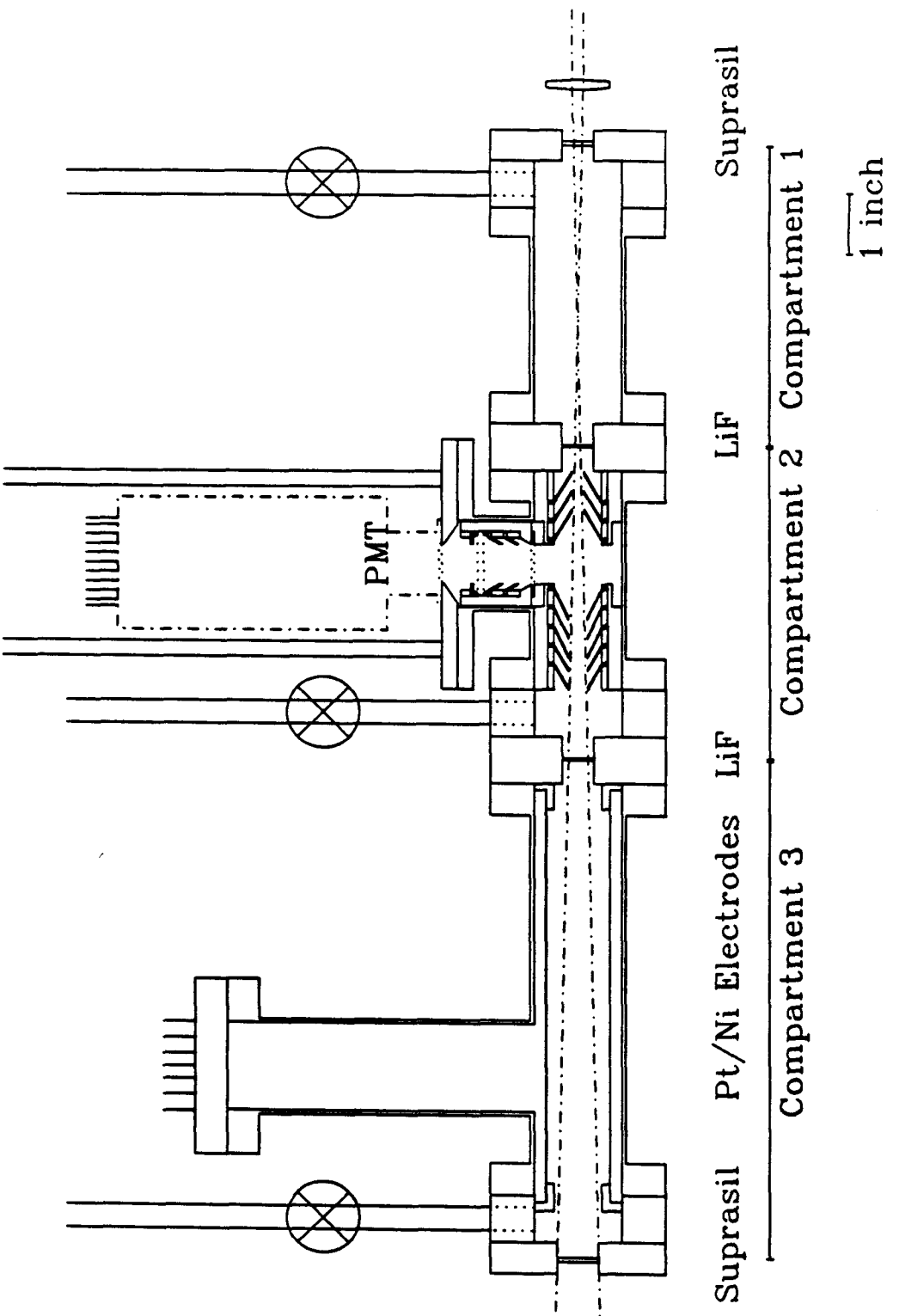
PMT
Suprasil
LiF
Compartment 1
Compartment 2
Pt/Ni Electrodes
LiF
Compartment 3
Suprasil
1 inch

Figure 3.

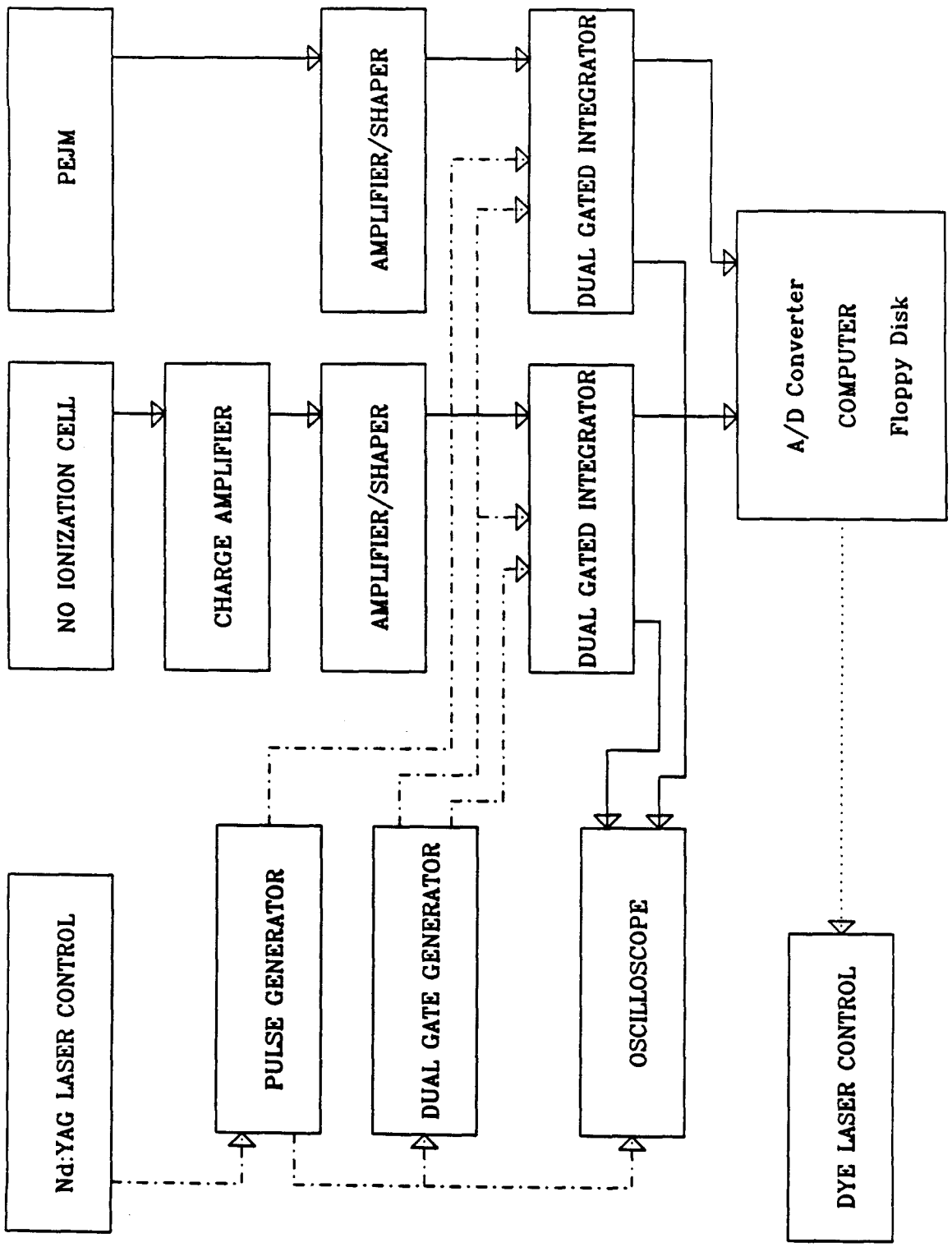
PEJM
AMPLIFIER/SHAPER
DUAL GATED INTEGRATOR
NO IONIZATION CELL
CHARGE AMPLIFIER
AMPLIFIER/SHAPER
DUAL GATED INTEGRATOR
A/D Converter
COMPUTER
Floppy Disk
Nd:YAG LASER CONTROL
PULSE GENERATOR
DUAL GATE GENERATOR
OSCILLOSCOPE
DYE LASER CONTROL

Figure 4.

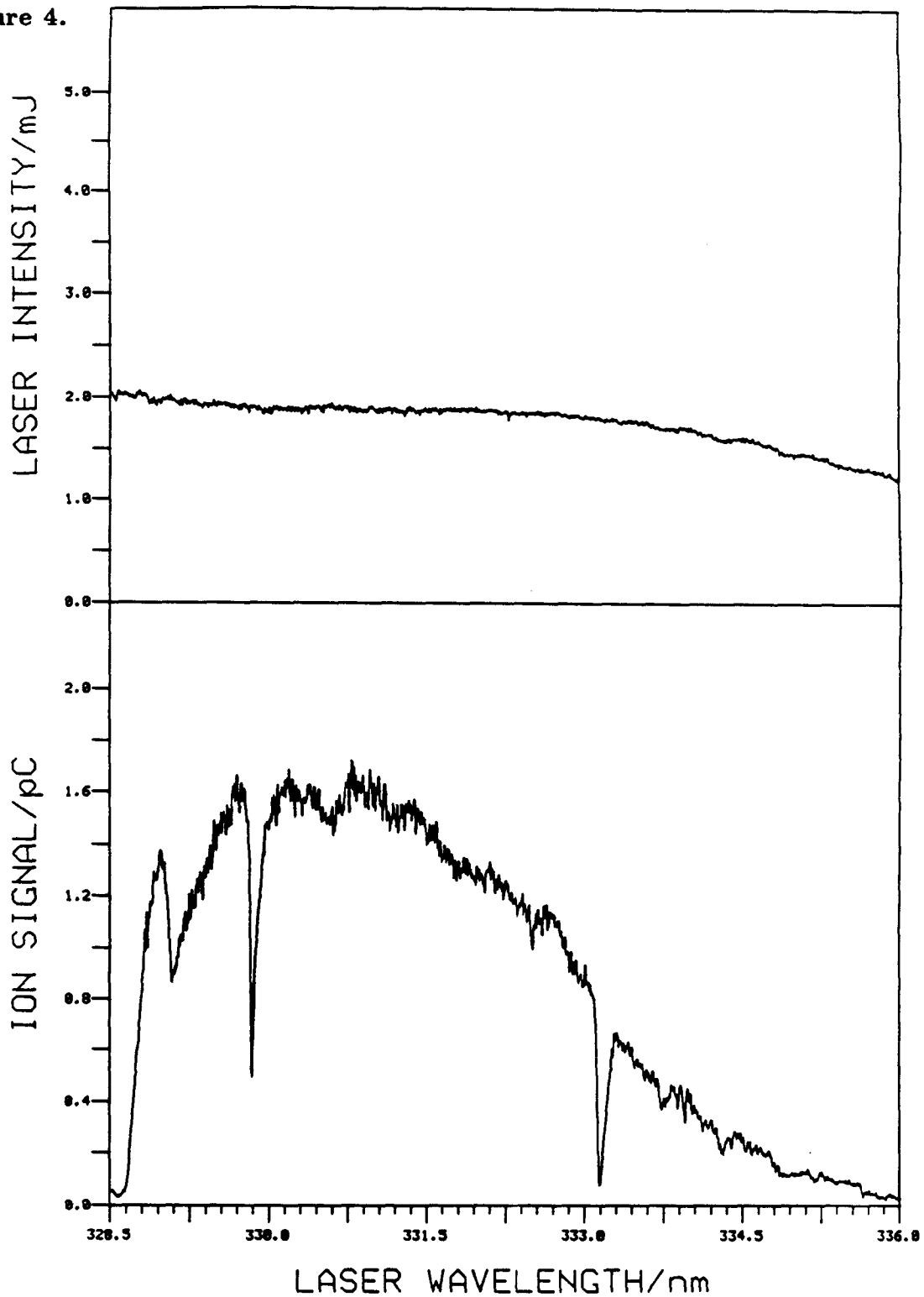
LASER INTENSITY/mJ
5.0
4.0
3.0
2.0
1.0
0.0
ION SIGNAL/pC
2.0
1.6
1.2
0.8
0.4
0.0
328.5
330.0
331.5
333.0
334.5
336.0
LASER WAVELENGTH/nm

Figure 5.

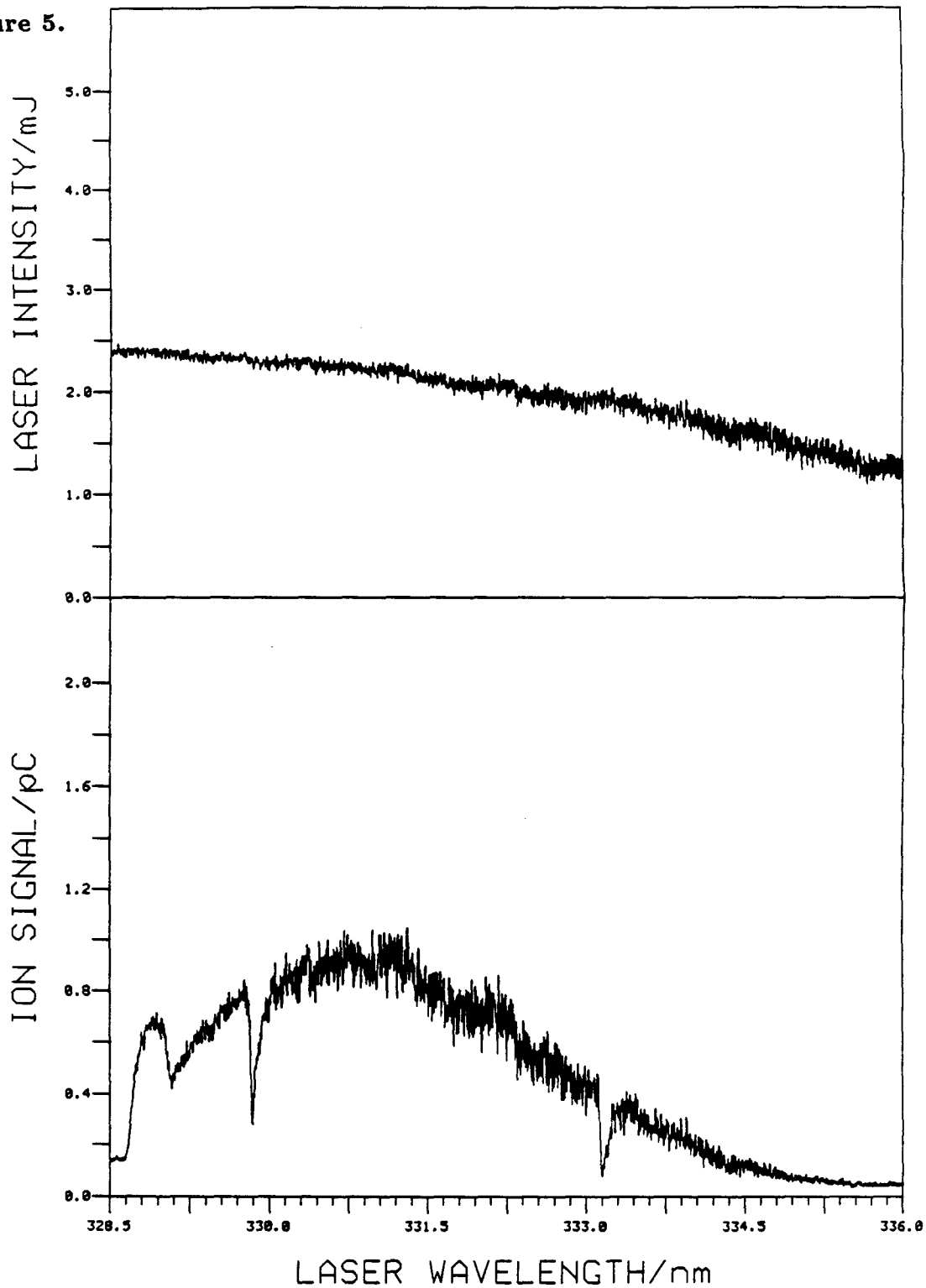
LASER INTENSITY/mJ
5.0
4.0
3.0
2.0
1.0
0.0
ION SIGNAL/pC
2.0
1.6
1.2
0.8
0.4
0.0
328.5
330.0
331.5
333.0
334.5
336.0
LASER WAVELENGTH/nm

CHAPTER V

DETECTION OF MOLECULAR HYDROGEN BY LASER INDUCED FLUORESCENCE

I. INTRODUCTION

This chapter illustrates the state-specific detection of H_2 by laser induced fluorescence (LIF) in the vacuum-ultraviolet. The relevant equations for the fluorescence signal are derived, and the sensitivity is compared to the results of Coherent-Anti-Stokes-Raman spectroscopy (CARS) and Multiphoton Ionization (MPI).

The hydrogen molecule has been extensively studied both theoretically and experimentally: an accurate electronic potential energy surface was determined by Kolos and Wolniewicz,[1-5] and the method was later extended to several excited states.[6-12] A wealth of information about H_2 and its isotopic counterparts in their ground state has been obtained using Raman,[13] quadrupole ro-vibrational [14-19] and pure rotational spectroscopy.[20,21] Both the ground and the excited states have been extensively studied by emission[22-26] and absorption[28-39] techniques.

The ground state electronic configuration is $(1s\sigma)^2\,\tilde{X}\,^1\Sigma_g^+$ in the one electron molecular orbital approximation.[40] Its equilibrium bond distance is 0.741 Å, its bond dissociation energy[5] is 36 118.3 cm^{-1}, and its ionization potential[41] is 124 418.4 cm^{-1}

The first excited state of H_2 is $(1s\,\sigma)(2p\,\sigma)\tilde{B}\,^1\Sigma_u^+$. Its minimum lies 89 404.7 cm^{-1} above the $v = 0$ level of the ground state. The second electronic excited state is $(1s\sigma)(2p\pi)\tilde{C}\,^1\Pi_u$, at an energy of 97 813.1 cm^{-1} above the ground vibrational level of the $\tilde{X}$ state. The three potential energy curves for these states are shown in Figure 1.

The $\tilde{B} \leftrightarrow \tilde{X}$ transitions constitute the Lyman band system, while the $\tilde{C} \leftrightarrow \tilde{X}$ transitions are commonly referred to as the Werner bands. The Lyman system is a $^1\Sigma_u^+ \leftrightarrow {}^1\Sigma_g^+$ transition, therefore it possesses an R and a P branch, with no Q branch. The P and R branches are shifted to lower energy, so the highest energy

transition is the R(0) line. The $^1\Pi_u \leftrightarrow {}^1\Sigma_g^+$ Werner system has P, Q, and R branches, also shifted to lower energy.[42]

As can be seen in Figure 1, the difference between the equilibrium bond distances for the $\tilde{X}$ and $\tilde{B}$ states indicates small Franck-Condon factors for the 0-0 transition and larger ones for $|\Delta v| \gg 0$. On the other hand, the equilibrium internuclear separations of the $\tilde{C}$ and the $\tilde{X}$ states are fairly close. It is therefore expected that favorable Franck-Condon factors will exist for small $|\Delta v|$'s.

The band oscillator strength for H_2 has been determined by photoabsorption[43-46] and inelastic electron scattering.[47-49] Allison and Dalgarno[50,51] have calculated band oscillator strengths and transition probabilities for all $\tilde{B} \leftrightarrow \tilde{X}$ and $\tilde{C} \leftrightarrow \tilde{X}$ transitions in H_2 , HD and D_2 , and obtained good agreement with experiment.

Laser induced fluorescence of hydrogen in the vacuum ultraviolet was first observed by Marinero *et al.*;[52] XUV radiation between 97.3 nm and 102.3 nm was generated in a pulsed argon source by third-harmonic generation; the estimated photon flux was $\sim 7 \times 10^9$ photons/pulse, and the detection sensitivity 5×10^8 states/cm^3, at a signal to noise ratio of 3.

Polanyi and co-workers[53] generated VUV radiation between 105.8 nm and 106.8 nm in a Xe cell, and estimated an intensity around 10^9 photons/pulse. LIF spectra of H_2 , HD and D_2 were obtained at various pressures, and their detection sensitivity was estimated at 3.3×10^9 states/cm^3, at the same signal to noise ratio as the previous work.

Meier *et al.*[54,55] obtained a beam intensity of $\sim 10^{10}$ photons/pulse at 110 nm in Kr, or at 106 nm in Xe; their study focused on the collisional relaxation of vibrationally excited H_2 and D_2 by various gases. Their detection sensitivity was not reported.

In conclusion, excitation of H_2 from the ground state to the $\tilde{B}$ and $\tilde{C}$ states requires photons of energies above $\sim 90\,000\,\mathrm{cm}^{-1}$ (111.1 nm) and $\sim 100\,000\,\mathrm{cm}^{-1}$

(100 nm) respectively. The $\tilde{B}$ state will fluoresce with a 0.54 ns lifetime[50] at wavelengths significantly longer than the excitation wavelength ($\sim$ 130 nm). The $\tilde{C}$ state, on the other hand, fluoresces with a 0.85 ns lifetime at wavelengths around 105 nm.

II. MECHANISM OF LASER INDUCED FLUORESCENCE

In this technique, a laser beam is used to excite a molecule from an initial state $|\Sigma\Lambda pvJm\rangle$ to an excited state $|\Sigma'\Lambda'p'v'J'm'\rangle$, which then decays to a final state $|\Sigma''\Lambda''p''v''J''m''\rangle$, with emission of a photon. Σ describes the spin state of the molecule, Λ the electronic state, p the parity, v the vibrational quantum number, J the total angular momentum quantum number, and m its projection along a laboratory fixed axis.

The oscillator strength of a transition is given by:[56,57]

$$f_{\Sigma\Lambda pvJm}^{\Sigma'\Lambda'p'v'J'm'} = \frac{32\pi^3\epsilon_0 m_e \nu_0}{3he^2 g} \times |\langle\Sigma'\Lambda'p'v'J'm'|\vec{\mu}|\Sigma\Lambda pvJm\rangle|^2, \qquad (1)$$

where ϵ_0 is the permittivity of vacuum, m_e the mass of an electron, e the electron charge, ν_0 the transition frequency, g the degeneracy and $\vec{\mu}$ the transition dipole operator. In the abscence of fields, the spin states and the m sublevels are equally populated, and the oscillator strength becomes:

$$f_{\Lambda pvJ}^{\Lambda'p'v'J'} = \frac{32\pi^3\epsilon_0 m_e \nu_0}{3he^2 g} \times |\langle\Lambda'p'v'J'|\vec{\mu}|\Lambda pvJ\rangle|^2, \qquad (2)$$

where the degeneracy g is equal to $(2S+1)(2J+1)$. It is customary to separate the matrix element into its electronic-vibrational component and a rotational term. This separation was first performed by Hönl and London:[58]

$$|\langle\Lambda'p'v'J'|\vec{\mu}|\Lambda pvJ\rangle|^2 = |\langle\Lambda'p'v'|\vec{\mu}|\Lambda pv\rangle|^2 \times S_{\Lambda J}^{\Lambda' J'}. \qquad (3)$$

The matrix element $S_{\Lambda J}^{\Lambda' J'}$ is called the Hönl=London factor, or the rotational line strength. Tables of Hönl-London factors are avilable in the literature.[59,60]

The Einstein A and B coefficients can be expressed in terms of the oscillator strengths:[61]

$$(B_{abs})_{\Sigma\Lambda pvJm}^{\Sigma'\Lambda'p'v'J'm'} = \frac{e^2 n}{4\epsilon_0 m_e c} \times f_{\Sigma\Lambda pvJm}^{\Sigma'\Lambda'p'v'J'm'}, \qquad (4)$$

$$(B_{em})_{\Sigma\Lambda pvJm}^{\Sigma'\Lambda'p'v'J'm'} = \frac{e^2 n}{4\epsilon_0 m_e c} \times \frac{g}{g'} \times f_{\Sigma\Lambda pvJm}^{\Sigma'\Lambda'p'v'J'm'}, \tag{5}$$

$$A_{\Sigma\Lambda pvJm}^{\Sigma'\Lambda'p'v'J'm'} = \frac{2\pi e^2 n^3 {\nu_0}^2}{\epsilon_0 m_e c^3} \times \frac{g}{g'} \times f_{\Sigma\Lambda pvJm}^{\Sigma'\Lambda'p'v'J'm'}, \tag{6}$$

where c is the speed of light, and n the refractive index of the medium.

The rate of absorption, stimulated emission and spontaneous emission are then:

$$k_{abs} = B_{abs} I(\nu_L) g(\nu_L - \nu_0), \tag{7}$$

$$k_{stim} = B_{em} I(\nu_L) g(\nu_L - \nu_0), \tag{8}$$

$$k_{spont} = A, \tag{9}$$

where $I(\nu_L)$ is the laser photon flux and $g(\nu_L - \nu_0)$ is the normalized lineshape function.

The LIF technique has been reviewed extensively.[62-69] The main processes can be illustrated as follows:

$$|\Lambda v J\rangle + h\nu_L \xrightarrow{k_1} |\Lambda' v' J'\rangle$$

$$|\Lambda' v' J'\rangle + h\nu_L \xrightarrow{k_2} |\Lambda v J\rangle + 2h\nu_L$$

$$|\Lambda' v' J'\rangle \xrightarrow{k_3} |\Lambda'' v'' J''\rangle + h\nu$$

$$|\Lambda' v' J'\rangle \xrightarrow{k_4} \text{other.}$$

The first reaction is the absorption step, the second the competing stimulated emission, the third the fluorescence process and the fourth represents other competing processes, such as dissociation, ionization, or transitions to other states.

Assuming that stimulated emission, repopulation of the ground state, and collisional relaxation processes, contribute little to the overall reaction scheme,[70]

only reactions 1, 3 and 4 are important. If n_0 is the initial state population, the following set of differential equations describes the kinetics:

$$\frac{dn_{|\Lambda v J\rangle}}{dt} = -k_1\, n_{|\Lambda v J\rangle} \tag{10}$$

$$\frac{dn_{|\Lambda' v' J'\rangle}}{dt} = k_1 + n_{|\Lambda v J\rangle} - (k_3 + k_4)\, n_{|\Lambda' v' J'\rangle} \tag{11}$$

$$dn_{|\Lambda'' v'' J''\rangle} dt = (k_3)_i\, n_{|\Lambda' v' J'\rangle}. \tag{12}$$

For a square laser pulse of width τ, the number density in the final state long after the end of the laser pulse is given by:

$$n_{|\Lambda'' v'' J''\rangle} = \frac{n_0 (k_3)_i}{k_3 + k_5} \times (1 - e^{k_1 \tau}). \tag{13}$$

In other words, the final population density is the product of n_0 times the fraction of molecules that absorb a photon, times the fraction that decay to state i, as opposed to other states.

If the photomultiplier detector subtends a solid angle $\frac{\Omega}{4\pi}$, and the quantum efficiency of the photocathode is $Q(\nu_i)$, then the signal at the PMT will be:

$$SIGNAL(\nu_i) = \frac{\Omega}{4\pi} Q(\nu_i) G e n_o V \frac{(k_3)_i}{k_3 + k_5} \times (1 - e^{k_1 \tau}), \tag{14}$$

where V is the volume and G is the PMT gain. Since the product $k_1 \tau$ is on the order of 10^{-5}, the approximation $1 - e^{-x} \sim x$ can be used. Also, $(k_3)_i$ is the emission rate from state i, namely A_i, and the total spontaneous emission rate is $k_3 = \sum A_i$. Similarly, k_1 is related to the the Einstein coefficient for absorption by

$$k_1 = B_{abs} I(\nu_L) g(\nu_L - \nu_0). \tag{15}$$

Substituting this and the equation for k_3 into Eq. (14), and expressing the laser intensity as:

$$I(\nu_L) = \frac{N_{\nu_L}}{\tau \pi r^2}, \tag{16}$$

the PMT signal at frequency ν_i becomes:

$$SIGNAL(\nu_i) = \frac{\Omega Gen_0 l B_{abs} N_{\nu_L} g(\nu_L - \nu_0)}{4\pi(A + k_4)} \times A_i Q(\nu_i), \tag{17}$$

where l is the length of the volume probed by the VUV laser.

The total fluorescence signal is then:

$$SIGNAL_{tot} = \frac{\Omega Gen_0 l B_{abs} N_{\nu_L} g(\nu_L - \nu_0)}{4\pi(A + k_4)} \times \sum_i (A_i Q(\nu_i)). \tag{18}$$

The form of the normalized lineshape function is described in Refs. (70-72): two cases are generally studied: in the first case, the molecules are assumed to have a thermal distribution, and the lineshape function, including laser linewidth effects, is given by a Gaussian. In the case of molecules produced by a photodissociation, the particles are nearly monoenergetic , and their velocity distribution resembles a delta function. The lineshape function is found to depend on the anisotropy of the angular distribution,[72] and can have a much more complicated form.

III. DETECTION OF H_2 BY LIF

A. Apparatus

The apparatus used to generate VUV light at 110 nm has been described in Chapter 4. A diagram of the laser table set-up is shown in Figure 2. The Quanta-Ray dye laser output at 660 nm is is doubled in the Wavelenght Extension unit (WEX-1), and focused into the Kr cell. The dye laser uses dye DCM in a mixture of DMSO and methanol, which shifts the maximum of the tuning curve to about 650 nm. Typical output powers in the visible are in the range of 60-70 mJ/pulse, when pumped by 310 mJ/pulse of the doubled Nd:YAG frequency. UV conversion efficiencies are in the range of 10 %, or 6-7 mJ/pulse at 330 nm. A Schott UG-11 filter is used to separate the visible from the UV, and a 10 cm lens is used to focus the beam for third-harmonic generation. A diagram of the cell is shown in Figure 3; the cell compartments have been described in detail in Chapter 4, and in Ref. (70). The electronics used in these experiments are shown in Figure 4. The PMT output is considered to be the "SIGNAL". The PMT signal processing electronics are described in Appendix 1. The output of the ionization cell is the "LASER INTENSITY" channel. Research purity (99.995 %) Kr gas from Alpha Products is used in the VUV compartment, at pressures in the range of 700-800 torr. The ionization cell is filled with acetone or NO, as described in Chapter 4.

H_2 pressures of the order of $10^{-4} - 10^{-5}$ torr are needed for the LIF experiments: in order to measure the H_2 pressure accurately, a "Primary Standard" ultra-high purity mixture of $100\pm$ 1 ppm of H_2 in He was purchased from MG Industries.

B. Procedure

The procedure for obtaining the LIF spectrum of H_2 is fairly straightforward. After optimization of the Nd:YAG laser, the dye laser and the frequency doubling unit, the cell, which has been previously evacuated to $\sim 3 \times 10^{-7}$ torr, is filled

with acetone (or NO), placed on the laser table, and aligned with the UV laser beam. The gated integrators are set to collect data from the ionization cell and the photomultiplier, and H_2 is allowed into the sample cell.

The dye laser is tuned to an H_2 line, the gates are positioned, and final alignment adjustments are made to minimize scattered background. Several scans are then taken and averaged together: the scans are taken in both directions, which helps correct for sample pressure fluctuations.

The cell is taken apart and the windows cleaned after every day of experiments. The cell is pumped for at least 3 days in between experiments. Although not necessary for the H_2 LIF runs, pumping becomes crucial when HI is used, as illustrated in the next chapter.

C. LIF Spectrum

Figure 5 shows a raw room temperature spectrum. The pressure was 2.63 $\times 10^{-4}$ torr of H_2 , the scan was 13 nm in the visible (from 109.5 nm to 111.67 nm in the VUV) at a rate of 0.5 nm/min. Data was acquired at a density of 333 points/nm, and the integrator time constant, RC, was 1 $\times 10^{-7}$ seconds. From Appendix 1, this results in an overall time constant of 0.05 seconds, for a gate width of 100 ns (see Appendix 1, Section III).

The spectral features are easily assignable from published line positions.[36,73] The spectrum shows two overlapping bands, the (0-0) and the (1-0) bands, where the quantum munber of the upper state is given first. Table 1 gives the assignments and line positions.

The weakest line observed in this spectrum is the (1-0) R(5) line at 90,534.8 wavenumbers. This state has a population of 0.0963 % corresponding to 3.12 $\times 10^{13}$ states/cm^3 torr. Since the H_2 partial pressure was 2.63 $\times 10^{-4}$, the number density of the J = 5 level is 8.21 $\times 10^9$ states/cm^3 at a signal-to-noise ratio of about 3:1.

IV. DISCUSSION

The H_2 lines in Figure 5 are assigned in Table 1. Deviations from literature line positions range between -1.8 and 1.8 wavenumbers, which amounts to as much as four steps of the dye laser stepping motor. This cannot be entirely due to poor calibration of the dye laser, since the shifts are both positive and negative. Despite the slight inaccuracy in line positions, H_2 spectra are still easily assignable.

The detection sensitivity observed in these experiments is a factor of 10 lower than the sensitivity reported in Ref.(70), in which the same equipment was used. The difference is attributed to deterioration of the Quanta-Ray laser optics and doubling crystal efficiency, observed in the past four years. Several optical components in the dye laser have suffered radiation damage, and the WEX-1 doubling crystal auto-tracking system has become less efficient, and less stable during the duration of a scan. This effect is evidenced in Figure 5, where the VUV intensity (top panel) is observed to fluctuate greatly. This is, however, not the case for the VUV tuning curves shown in Chapter IV, determined almost two years earlier. It is believed that an overhaul of the PDL-2 dye laser can restore the original detection sensitivity of this apparatus. Taking into consideration the decrease in VUV intensity, the sensitivity is only a factor of 2 smaller than that reported in Ref. (70).

The detection sensitivity of LIF is still far greater than that of Coherent Anti-Stokes Raman Spectroscopy (CARS);[74] typical CARS detection limits are on the order of $\sim 10^{12}$ states/cm^3. The sensitivity observed with this apparatus is, however, comparable to that achieved by Marinero *et al.*,[52] and Polanyi and co-workers,[53] who employed VUV sources significantly more intense than the one described in this dissertation and in Ref. (70).

Multiphoton ionization has been used extensively to detect H_2 :[75–83] both (2+1) resonance-enhanced multiphoton ionization (REMPI), via the $E,F\,^1\Sigma_g^+$

state and (1+1) REMPI through the $\tilde{B}$ and $\tilde{C}$ state have been employed to determine quantum state populations of H_2 , HD and D_2 . (1+1) REMPI requires a VUV photon to reach the $\tilde{B}$ or the $\tilde{C}$ state: use of the $\tilde{C}$ state results in much improved detection sensitivity, approximately three orders of magnitude better than LIF or (2+1) REMPI; it does however require wavelengths around 100 nm, below the LiF cutoff. The nonlinear optical conversion process must therefore take place in a rare gas pulsed jet, rather than a static gas cell and LiF windows.

TABLE 1. Assignment of H_2 LIF Spectrum[a]

ASSIGNMENT				LINE POSITION		DEVIATION
v'	v''	J'	J''	ν_{lit}	ν_{obs}	$\Delta\nu = \nu_{obs} - \nu_{lit}$
1	0	1	2	91204.42	91203.8	-0.6
1	0	4	3	91180.70	91180.5	-0.2
1	0	2	3	90926.79	90927.7	+0.9
1	0	5	4	90895.69	90895.9	+0.2
1	0	3	4	90572.97	90573.5	+0.5
1	0	6	5	90534.84	90536.6	+1.8
0	0	1	0	90242.35	90241.3	-1.1
0	0	2	1	90201.17	90200.9	-0.3
0	0	0	1	90085.05	90083.4	-1.7
0	0	3	2	90080.32	90078.5	-1.8
0	0	1	2	89888.01	89886.3	-1.7
0	0	4	3	89880.88	89879.1	+1.8
0	0	2	3	89614.17	89612.9	-1.3

a. In vacuum wavenumbers (cm^{-1}).

REFERENCES

1. W. Kolos and L. Wolniewicz, *J. Chem. Phys.* **41**, 3663 (1964).
2. W. Kolos and L. Wolniewicz, *J. Chem. Phys.* **43**, 2429 (1965).
3. W. Kolos and L. Wolniewicz, *J. Chem. Phys.* **49**, 404 (1968).
4. W. Kolos and L. Wolniewicz, *J. Mol. Spectrosc.* **54**, 303 (1975).
5. L. Wolniewicz, *J. Chem. Phys.* **78**, 6173 (1983).
6. W. Kolos and L. Wolniewicz, *J. Chem. Phys.* **45**, 509 (1966).
7. W. Kolos and L. Wolniewicz, *J. Chem. Phys.* **48**, 3672 (1968).
8. W. Kolos and L. Wolniewicz, *J. Chem. Phys.* **50**, 3228 (1969).
9. W. Kolos and L. Wolniewicz, *Can. J. Phys.* **53**, 2189 (1975).
10. K. Dressler and L. Wolniewicz, *J. Chem. Phys.* **85**, 2821 (1986).
11. P. Senn, P. Quadrelli and K. Dressler, *J. Chem. Phys.* **89**, 7401 (1988).
12. P. Quadrelli, K. Dressler and L. Wolniewicz, *J. Chem. Phys.* **92**, 7461 (1990).
13. B. P. Stoicheff, *Can. J. Phys.* **35**, 730 (1957).
14. G. Herzberg, *Nature* **166**, 563 (1950).
15. U. Fink, T. A. Wiggins and D. H. Rank, *J. Mol. Spectrosc.* **18**, 384 (1965).
16. J. V. Foltz, D. H. Rank and T. A. Wiggins, *J. Mol. Spectrosc.* **21**, 203 (1966).
17. P. J. Brannon, C. H. Church and C. W. Peters, *J. Mol. Spectrosc.* **27**, 44 (1968).
18. H. L. Buijs and H. P. Gush, *Can. J. Phys.* **49**, 2366 (1971).
19. S. L. Bragg, J. W. Brault and W. H. Smith, *Astrophys. J.* **263**, 999 (1982).
20. J. Reid and A. R. W. McKellar, *Phys. Rev.* **A-18**, 224 (1978).
21. D. E. Jennings and J. W. Brault, *Astrophys. J.* **256**, L29 (1982).
22. G. Herzberg and L. L. Howe *Can. J. Phys.* **37**, 636 (1959).
23. S. Takezawa, F. K. Innes and Y. Tanaka, *J. Chem. Phys.* **46**, 4555 (1967).

24. H. Bredohl and G. Herzberg, *Can. J. Phys.* **51**, 867 (1973).

25. I. Dabrovski and G. Herzberg, *Can. J. Phys.* **54**, 525 (1976).

26. I. Dabrovski, *J. Chem. Phys.* **62**, 1639 (1984).

27. G. Herzberg and A. Monfils, *J. Mol. Spectrosc.* **5**, 482 (1960).

28. A. Monfils, *Bull. Acad. R. Belg. Cl. Sci.* **47**, 585 (1961).

29. A. Monfils, *Bull. Acad. R. Belg. Cl. Sci.* **47**, 599 (1961).

30. A. Monfils, *Bull. Acad. R. Belg. Cl. Sci.* **47**, 816 (1961).

31. A. Monfils, *Bull. Acad. R. Belg. Cl. Sci.* **48**, 460 (1962).

32. A. Monfils, *Bull. Acad. R. Belg. Cl. Sci.* **48**, 482 (1962).

33. T. Namioka, *J. Chem. Phys.* **40**, 3154 (1964).

34. A. Monfils, *J. Mol. Spectrosc.* **15**, 265 (1965).

35. A. Monfils, *J. Mol. Spectrosc.* **25**, 513 (1968).

36. P. G. Wilkinson, *Can. J. Phys.* **46**, 1225 (1968).

37. G. Herzberg, *J. Mol. Spectrosc.* **33**, 147 (1970).

38. S. Takezawa and Y. Tanaka, *J. Chem. Phys.* **56**, 6125 (1972).

39. I. Dabrovski and G. Herzberg, *Can. J. Phys.* **52**, 1110 (1974).

40. T. E. Sharp, *Atom. Dat.* **2**, 119 (1971).

41. G. Herzberg, *Phys. Rev. Lett.* **23**, 1081 (1969).

42. G. Herzberg, "Molecular Spectra and Molecular Structure: I. Spectra of Diatomic Molecules," 2nd Ed., (Van Nostrand Reinhold, New York, 1950).

43. G. N. Haddad, K. H. Lokan, A. J. D. Farmer and J. H. Carver, *J. Quant. Spectrosc. Radiat. Transfer* **8**, 1193 (1968).

44. J. E. Hesser, N. H. Brooks and G. M. Lawrence, *J. Chem. Phys.* **49**, 388 (1968).

45. W. Fabian and B. R. Lewis, *J. Quant. Spectrosc. Radiat. Transfer* **14**, 523 (1974).

46. B. R. Lewis, *J. Quant. Spectrosc. Radiat. Transfer* **14**, 537 (1974).

47. J. Geiger, *Z. Physik* **181**, 413 (1964).

48. J. Geiger and M. Topschowsky, *Z. Naturforsch.* **A21**, 626 (1966).

49. J. Geiger and H. Schmoranzer, *J. Mol. Spectrosc.* **32**, 39 (1969).

50. A. C. Allison and A. Dalgarno, *Atom Dat.* **1**, 289 (1970).

51. A. Dalgarno and T. L. Stephens, *Astrophys. J.* **160**, L107 (1970).

52. E. E. Marinero, C. T. Rettner, R. N. Zare and A. H. Kung, *Chem. Phys. Lett.* **95**, 486 (1983).

53. F. J. Northrup, J. C. Polanyi, S. C. Wallace and J. M. Williamson, *Chem. Phys. Lett.* **105**, 34 (1984).

54. W. Meier, H. Rottke, H. Zacharias and K. H. Welge, *J. Chem. Phys.* **83**, 4360 (1985).

55. W. Meier, G. Ahlers and H. Zacharias, *J. Chem. Phys.* **85**, 2599 (1986).

56. I. N. Levine, "Molecular Spectroscopy," (John Wiley, NY, 1975).

57. A. Schadee, *J. Quant. Spectrosc. Radiat. Transfer* **7**, 169 (1967)..

58. H. Hönl and F. London, *Z. Physik* **33**, 803 (1925).

59. A. Schadee, *Bull. Astr. Inst. Neth.* **17**, 311 (1964).

60. E. E. Whiting, A. Schadee, J. B. Tatum, J. T. Hougen and R. W. Nichols, *J. Mol. Spectrosc.* **80**, 249 (1980).

61. A. Yariv, "Quantum Electronics," 3rd Ed., (John Wiley, NY, 1989).

62. R. N. Zare and P. J. Dagdigian, *Science* **185**, 739 (1974).

63. D. R. Crosley, *J. Chem. Ed.* **59**, 446 (1982).

64. M. A. A. Clyne and I. S. McDermid, in "Dynamics of the Excited State," K. P. Lawley, Ed. (John Wiley, NY, 1982), p.1

65. J. L. Kinsey, *Ann. Rev. Phys. Chem.* **28**, 349 (1977).

66. C. H. Greene and R. N. Zare, *Ann. Rev. Phys. Chem.* **33**, 119 (1982).

67. C. H. Greene and R. N. Zare, *J. Chem. Phys.* **78**, 6741 (1983).

68. A. C. Kummel, G. O. Sitz and R. N. Zare, *J. Chem. Phys.* **88**, 7357 (1988).

69. J. R. Waldeck, A. C. Kummel, G. O. Sitz and R. N. Zare, *J. Chem. Phys.* **90**, 4112 (1989).

70. G. R. Parker Jr., Ph.D. Thesis, California Institute of Technology, 1988, Chapter 6.

71. B. P. Bemand and M. A. A. Clyne, *Chem. S. Far. Trans. II* **69**, 1643 (1973).

72. R. N. Zare, *Mol. Photochem.* **4**, 1 (1972).

73. I. Dabrovski, *Can. J. Phys.* **62**, 1639 (1984).

74. D. Debarre, M. Lefebvre, M. Péalat, J.-P. E. Taran, D. J. Bamford and C. B. Moore, *J. Chem. Phys.* **83**, 4476 (1985).

75. E. E. Marinero, C. T. Rettner and R. N. Zare, *Phys. Rev. Lett.* **48**, 1323 (1982).

76. E. E. Marinero, R. Vasudev and R. N. Zare, *J. Chem. Phys.* **78**, 692 (1983).

77. H. Rottke and K. H. Welge, *Chem. Phys. Lett.* **99**, 456 (1983).

78. W. Meier, H. Rottke, H. Zacharias and K. H. Welge, *J. Chem. Phys.* **83**, 4360 (1985).

79. S. L. Anderson, G. D. Kubiak and R. N. Zare, *Chem. Phys. Lett.* **105**, 22 (1984).

80. A. H. Kung, T. Trickl, N. A. Gershenfeld and Y. T. Lee, *Chem. Phys. Lett.* **144**, 427 (1988).

81. W. Meier, H. Zacharias and K. H. Welge, *Chem. Phys. Lett.* **163**, 88 (1989).

82. K.-D. Rinnen, D. A. V. Kliner, R. N. Zare and W. M. Huo, *Israel J. Chem.* **29**, 369 (1989).

83. K.-D. Rinnen, M. A. Buntine, D. A. V. Kliner, R. N. Zare and W. M. Huo, *J. Chem. Phys.* **95**, 214 (1991).

FIGURE CAPTIONS

Figure 1. Potential energy curves of the $\tilde{X}$, $\tilde{B}$ and $\tilde{C}$ electronic states of H_2 and their vibrational levels.[70]

Figure 2. Apparatus used in the laser induced fluorescence experiments.[70]

Figure 3. Scale drawing of the experimental cell.[70]

Figure 4. Electronics for the LIF experiments.[70] See Chapter 4, Figure 3.

Figure 5. Raw LIF spectrum of H_2 at 2.63 $\times 10^{-4}$ torr. The top panel is the output of the acetone ionization cell, and the bottom the PMT output.

Figure 1.

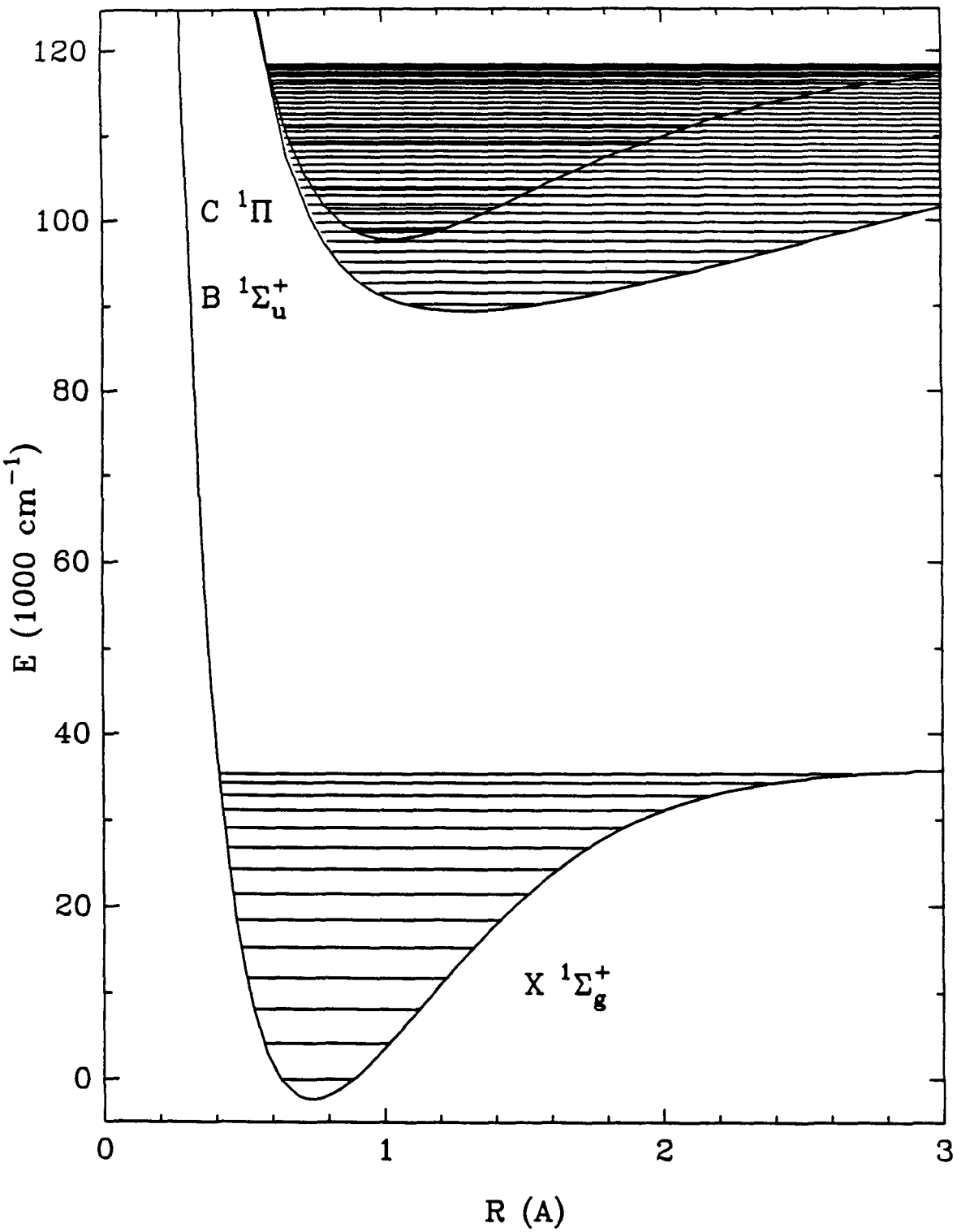

Figure 2.

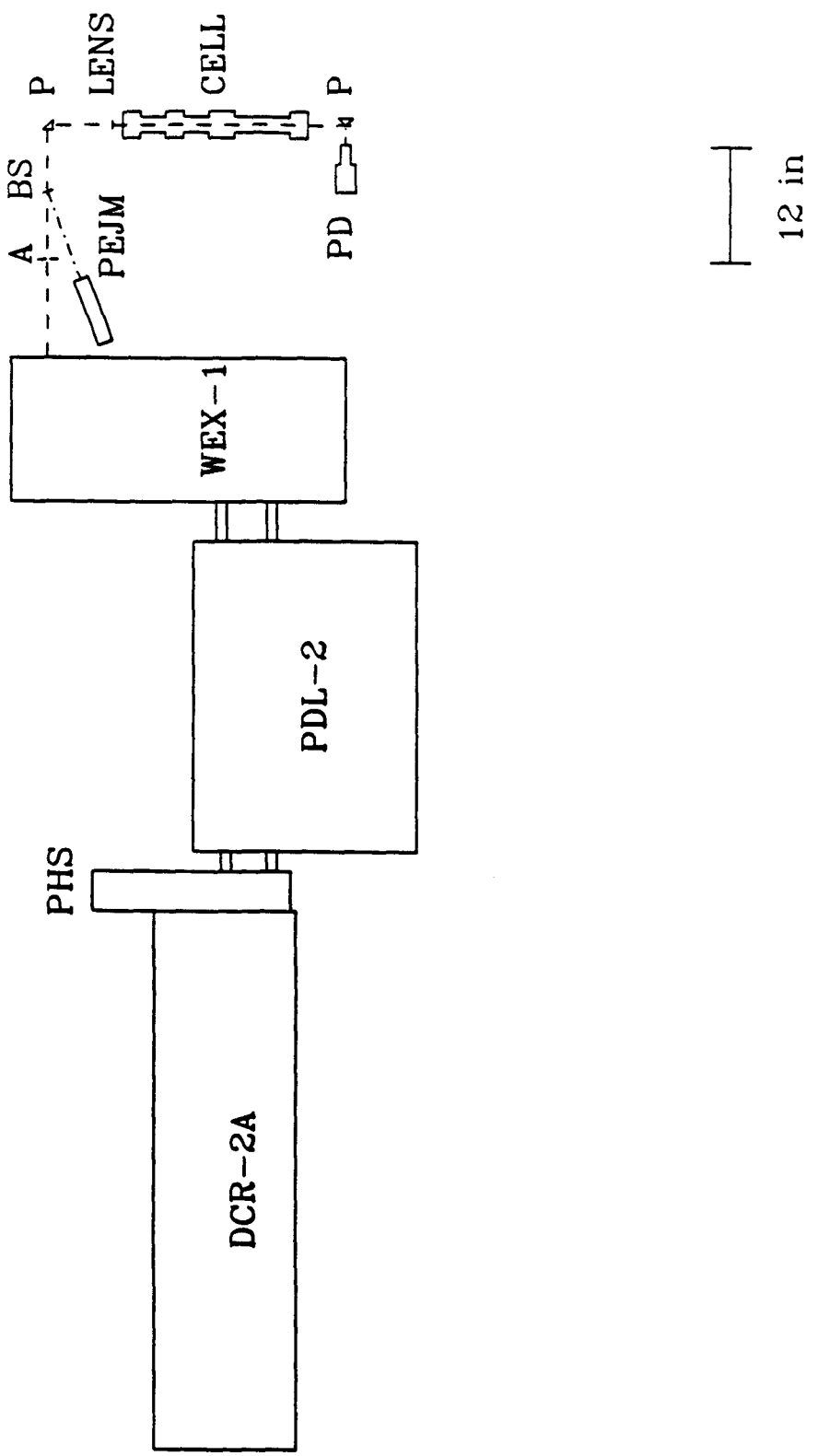

Figure 3.

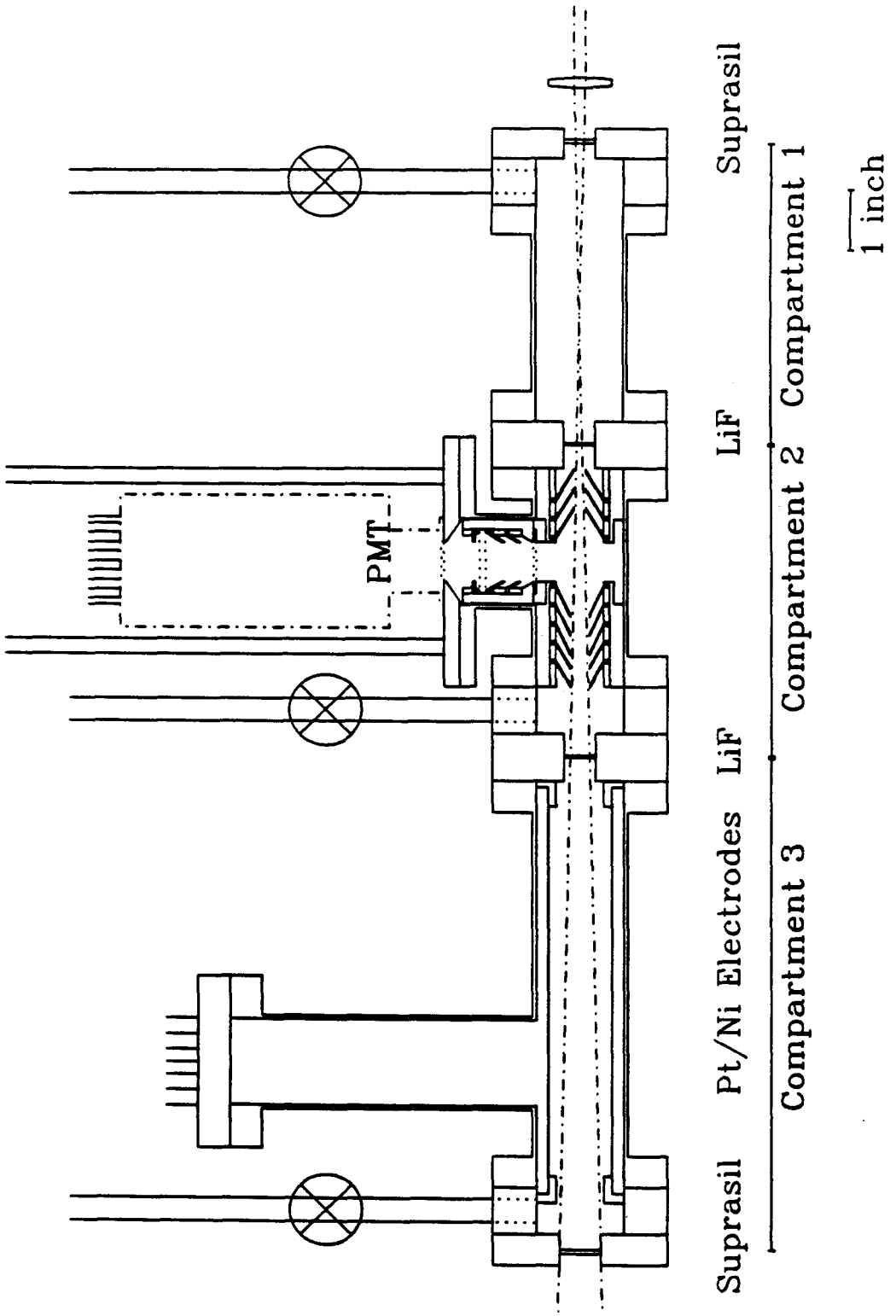
PMT
Suprasil
LiF
Compartment 1
Compartment 2
Pt/Ni Electrodes
LiF
Compartment 3
Suprasil
1 inch

Figure 4.

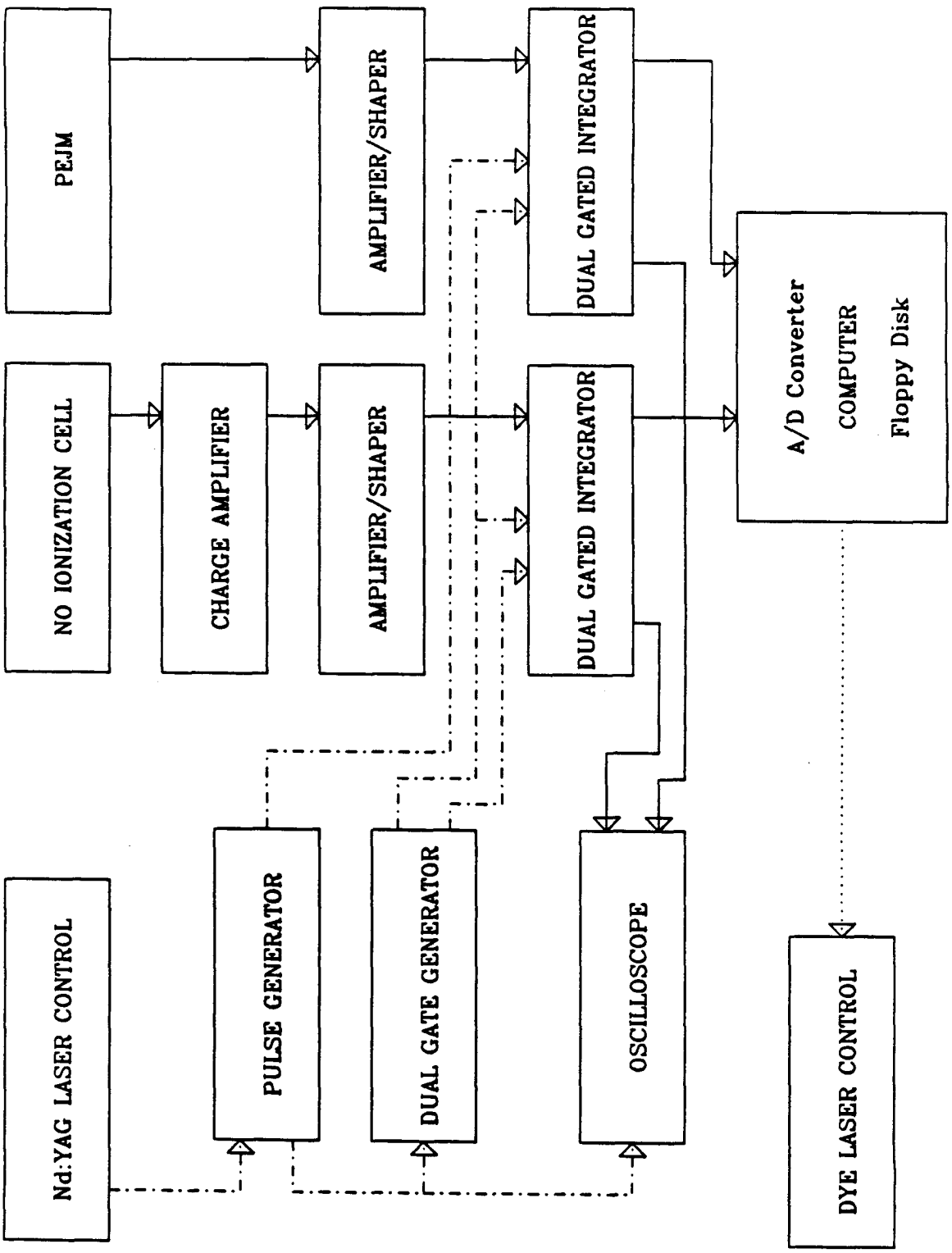
PEJM
AMPLIFIER/SHAPER
DUAL GATED INTEGRATOR
NO IONIZATION CELL
CHARGE AMPLIFIER
AMPLIFIER/SHAPER
DUAL GATED INTEGRATOR
A/D Converter
COMPUTER
Floppy Disk
Nd:YAG LASER CONTROL
PULSE GENERATOR
DUAL GATE GENERATOR
OSCILLOSCOPE
DYE LASER CONTROL

Figure 5.

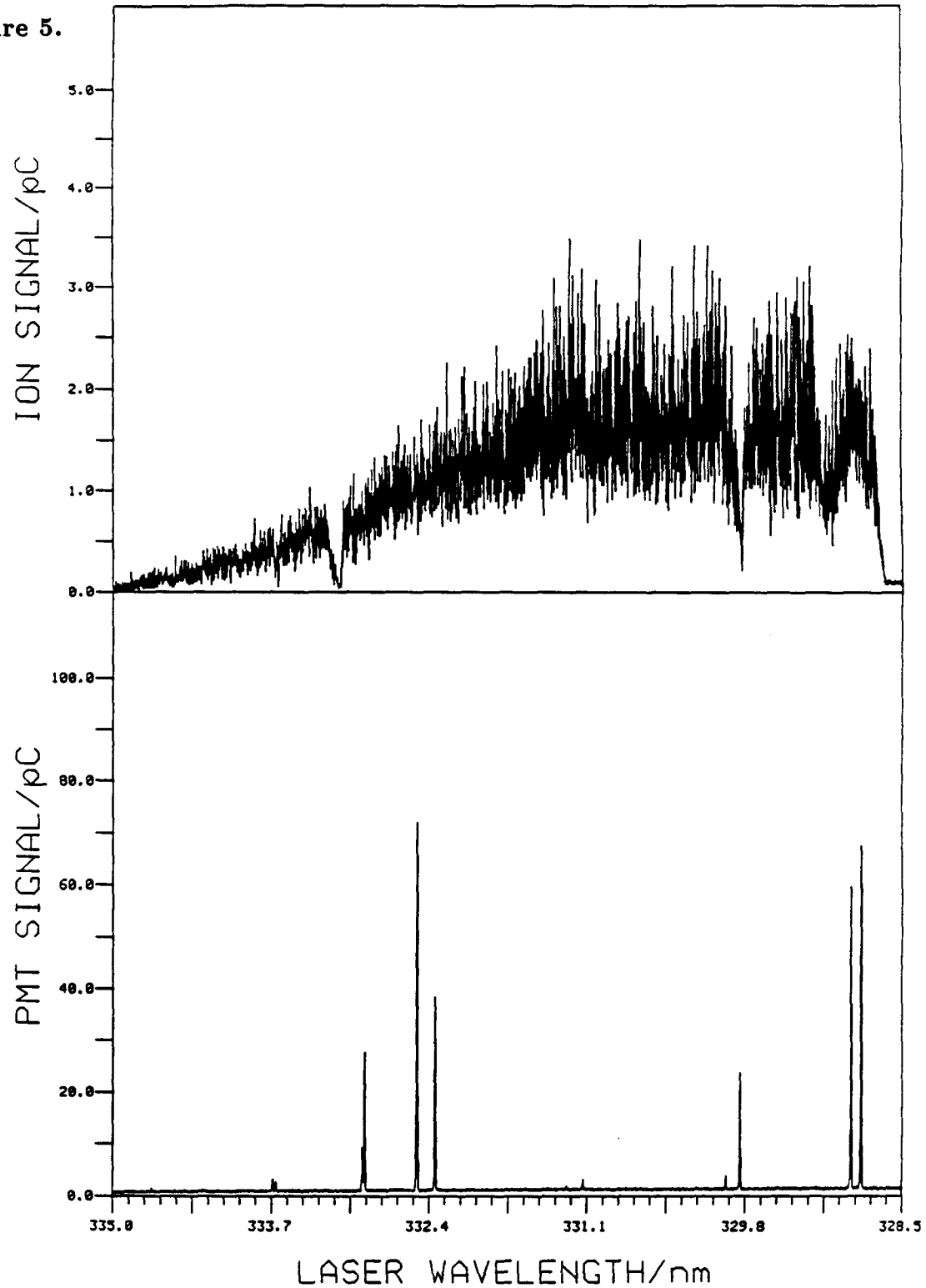
ION SIGNAL/pC
5.0
4.0
3.0
2.0
1.0
0.0
PMT SIGNAL/pC
100.0
80.0
60.0
40.0
20.0
0.0
335.0
333.7
332.4
331.1
329.8
328.5
LASER WAVELENGTH/nm

CHAPTER VI

$H + H_2$ EXPERIMENTS

I. INTRODUCTION

This chapter describes attempts to employ laser induced fluorescence detection of H_2 molecules produced in the H + H_2 hot-atom reaction. This technique combines high sensitivity with linear response, i.e., the LIF signal is directly proportional to the incident laser power. The LIF technique has already been shown to be successful in detecting products of molecular photodissociations.[1-3]

The history of the hydrogen exchange reaction has been summarized in Chapter 2. Although good agreement exists between theoretical[4-9] and experimental[10-13] integral cross sections for the H + p-H_2 , D + H_2 and H + D_2 systems, several questions remain to be addressed. Zare and co-workers[10-13] used resonance-enhanced multiphoton ionization detection of H_2 , while the experiments of Valentini *et al.*[14-16] employed CARS detection. It remains to be explained exactly what feature of the CARS experiments has led to erroneous conclusions about the presence of dynamical resonances. The possibility of resonances in differential cross sections has been pointed out by Manolopoulos and Wyatt,[17] Continetti *et al.*[18,19] and Gentry and co-workers.[20] However the structure observed in the differential cross sections is not as pronounced as that observed in the CARS experiments.

Possible inadequacy of the LSTH potential energy has also been mentioned as one of the possibilities for the disagreement between theory and experiment, since it does not properly account for the conical intersection with the second doublet surface at D_{3h} geometries, has a classical barrier which is believed to be 0.15 kcal/mole too high,[21] and provides a poor description of the van der Waals region.[22] The more recent DMBE surface of Varandas *et al.*[22] remedies these deficiencies, but has a slightly worse root-mean-square error in the analytical fit. Preliminary tests on the DMBE surface[23] show deviations of as much as 10 % between individual S-matrix elements calculated on the LSTH surface versus the DMBE. It is not yet

clear how that can lead to more resonances in the DMBE cross sections than in those calculated on the LSTH surface.

Finally, little consideration has been given to the long range geometrical effects of the conical intersection mentioned above. It has been known for some time[24] that electronic wave functions undergo a sign change when transported adiabatically around any closed loop in nuclear configuration space which circles the conical intersection. As a result, the Born-Oppenheimer wavefunction is no longer single-valued and continuous. Therefore, there must be a compensating sign change in the nuclear part of wavefunction.[25,26] All converged calculations published to date do not include this effect; however there are indications that the geometric phase effect can have a striking effect on the J = 0 results[27]. The main result is that the purely reactive *ortho* → *para* and *para* → *ortho* processes are not affected by the geometric phase, while the *ortho* → *ortho* and *para* → *para* transitions are significantly modified.

In view of these difficulties, it was considered important to provide an independent detection scheme for the products of the hydrogen exchange reaction. It is worrisome that two experiments, differing only in the detection technique, have reached opposite conclusions about the presence or absence of dynamical resonances in the integral cross sections. It was felt that a third detection technique, that of laser induced fluorescence, would be able to resolve the issue of the "participation" of the laser radiation in the reaction, and the question of possible artifacts in the two detection schemes.

II. EXPERIMENTAL DETAILS

A. Apparatus

The experimental set-up is shown in Figure 1. The Quanta-Ray laser is configured as described in Chapter V. The Molectron laser (MY-34 and DL-18) is used with only a longitudinally pumped amplifier, with Rhodamine 590 tetrafluoroborate in methanol as the dye. Typical output powers are 50 mJ/pulse at 560 nm, when pumped with 220 mJ/pulse of the Nd:YAG second harmonic at 532 nm. The UV beam intensity is typically 10 mJ/pulse. The Molectron laser wavelength is fixed at 560 nm, twice the photolysis wavelength. The Quanta-Ray PDL-2 dye laser is scanned between 657 nm and 672 nm typically. The UV beam is separated from the visible by a UG-11 glass filter (84 % transmittance), and focused in the Kr compartment. The cell described in the previous two chapters was used in these experiments, with two important modification: the sample compartment was equipped with flow valves, to allow for constant flow of the reaction mixture through the reaction volume. A VUV bandpass filter is placed in front of the photomultiplier, to prevent stray 280 nm light from reaching the PMT. The quantum efficiency of the solar blind photomultiplier is at least two orders of magnitude higher at 280 nm than at 330 nm, the wavelength used for third-harmonic generation, resulting in excessive background on the PMT signal. The transmission of this filter is 16.8 % at 141.5 nm, with a FWHM of 23.5 nm. The filter is placed between an additional LiF window, and the PMT, and the PMT compartment is pumped separately. In order to keep the residual iodine pressure low in the reaction compartment, a stainless steel cold finger, immersed in a dry ice/acetone slush, was added to the cell. A diagram of the cell is shown in Figure 2.

The pump and probe lasers are collinear and counterpropagating. Burn patterns are taken before positioning of the cell to insure good overlap. The

electronics are shown in Figure 3, and described in Appendix 1. The Laser Timing Controller triggers both flashlamps and Q-switches on the lasers with the appropriate time delay between them. Two channels of data are collected, one for the PMT signal, the other for the ionization cell (VUV laser intensity), as described in the previous chapter.

The photomultiplier data is acquired with the gated integrator in "auto-subtract" mode; as described in Appendix 1, the order of the baseline and signal gates is toggled after every Quanta-Ray pulse, so that the signal present when only one laser fires is subtracted from the signal present when both lasers fires, greatly reducing the background.

B. HI Photodissociation

Several precursor molecules can be used for generating translationally hot H atoms. HI is convenient because there can be no rotational or vibrational excitation of the other fragment, resulting in a well defined translational energy for the hydrogen atom.

The UV and VUV spectrum of HI has been extensively studied.[28-32] The first continuum originates around 27 800 cm^{-1} with a maximum at 45 500 cm^{-1}. The maximum absorption cross section is $\sim 8.4 \times 10^{-19}$. Mulliken[33,34] assigned this continuum to several intersecting repulsive states. Recently, Ginter and co-workers[35-38] performed a complete rotational analysis of each band in the continuum region.

The ground state electronic configuration of HI in molecular orbital symmetry notation[39] is $...(9\sigma)^2(10\sigma)^2(5\pi)^4(2\delta)^4(11\sigma)^2(6\pi)^4$. The four lowest excited states are represented by:[38,39]

$(\sigma^2\pi^3)\,a\sigma^*$	$a\,^3\Pi_i$,	$A\,^1\Pi$
$(\sigma\pi^4)\,a'\sigma^*$	$t\,^3\Sigma^+$,	$V\,^1\Sigma^+$

According to Mulliken, only the V state is bound; the $a\,^3\Pi_1$ and $A\,^1\Pi$ correlate with product atoms H + I ($^2P_{3/2}$), while the $a\,^3\Pi_{0+}$ and the $t\,^3\Sigma^+$ correlate with H + I* ($^2P_{1/2}$). Mulliken's analysis also predicts the orientation of the transition dipole moment for the HI molecule: in the case of diatomics, the transition dipole moment must be either parallel or perpendicular to the molecular axis. From symmetry considerations, $\Sigma^+ \leftrightarrow \Sigma^+$ and $\Sigma^+ \leftrightarrow {}^3\Pi_{0+}$ transitions will be parallel transitions, while $\Sigma^+ \leftrightarrow {}^3\Pi_1$ and $\Sigma^+ \leftrightarrow {}^1\Pi$ will be perpendicular. Therefore, ground state iodine ($^2P_{3/2}$) is formed in a perpendicular transition, while I* ($^2P_{1/2}$) is obtained from a parallel transition.

The branching ratio for the photodissociation process has been measured by Clear *et al.*[40] using time-of-flight mass spectroscopy, and by Schmiedl *et al.*[41] who measured the recoil velocity of the H-atom by Lyman-α laser induced fluorescence Doppler spectroscopy. Both experiments were conducted at 266 nm, and it was determined that $\sim$ 40 % of the I atoms were in the excited state. Wittig and co-workers[42,43] measured the branching ratio at 248 nm and 193 nm, and found 46 % of the I atoms in the excited state at 248 nm, and 10 % at 193 nm.

The photolysis laser first promotes HI to its dissociative continuum. The absorption cross section of HI doubles every 10 nm decrease in the photolysis wavelength. Considering both dissociation channels, the average laboratory energy of the H atom formed in the photodissociation of HI is given by:[31]

$$\langle E_{\mathrm{H}} \rangle = \frac{m_{\mathrm{I}}}{m_{\mathrm{HI}}} \left(\frac{hc}{\lambda} - D_0^0 + kT \right) + \frac{m_{\mathrm{H}}}{m_{\mathrm{HI}}} \frac{3}{2} kT, \qquad (1)$$

which includes the contribution from the translational and rotational energy of the HI molecule. At 280 nm the energy of the H atom will be 1.389 eV.

C. HI Absorption Cross Section

The precursor absorption cross section in the VUV region is an important consideration, since the smallest attenuation of the VUV beam can make the

experiment undoable. It is also important for quantitative measurements that the precursor have a structureless absorption, preferably flat, in the wavelength region of interest.

The total absorption cross section of HI in the region around 110 nm has not been reported in the literature. This spectral region is part of the ionization continuum.[44-49] The ionization cross section has been estimated at $\sim 8 \times 10^{-18}$ cm^2, meaning the total cross section could be expected to be between 10^{-17} and 10^{-16} cm^2. This would cause the VUV beam to be attenuated by 33-98%, a significant amount.

It was decided that a more definitive estimate of the HI absorption cross section was needed. As described in Ref. (50), an experiment with a static cell of HI is extremely difficult: the HI pressure is not constant, but continuously decreasing, due to adsorption onto the cell walls. In addition, material is constantly depositing onto the LiF windows of the cell. In order to minimize the pressure fluctuation effects, a flow system was constructed with two needle valves, and a 4 % mixture of HI in He was flowed at pressures in the range of a few torr.

The absorption cross section was determined by monitoring the output of the ionization cell, alternating blank and HI scans. The absorbance was obtained by dividing the transmitted intensity I by the blank intensity I_0, according to Beer's law:

$$A = log\frac{1}{T} = -log\frac{I}{I_0}. \tag{2}$$

The cross section is given by:

$$2.3A = \sigma nl. \tag{3}$$

The absorption cross section of HI in the range 109.5−110.5 nm is shown in Figure 4. The cross section value of $\sim$ 20 Mb, is in accord with a photoionization cross section of about 8 Mb in this region. The curvature in the spectrum seems to be due

to pressure fluctuations in the beginning of a scan. Since scans were taken in both directions, curvature is observed on both sides. The flow system was observed to operate reliably after the first few minutes of adjusting the needle valves, as determined by several time scans. In the case of the absorption experiments, not enough time was given for the HI to be pumped out before a blank scan, and residual HI is responsible for the cross section dropping at the two sides of the scan. Nonetheless, the estimated value for the cross section is reasonable, and, most important, the cross section appears structureless.

D. Time Delay

The time delay between the pump and the probe laser was determined by an HP 5082-4220 photodiode, used with an -18 V bias, and a risetime of less than 1 ns. The output of the photodiode is monitored on a Tektronix 2465 300 MHz oscilloscope, with a 1.2 ns risetime. The delay is adjusted using the *Q-Switch Timing* potentiometer on the Laser Timing Controller (see Appendix 1). Time delays from 10 to 100 ns were used to try to get this experiment to work.[1]

E. Reaction Mixture

HI from Matheson was purified using a vacuum distillation. After three liquid nitrogen freeze-pump-thaw cycles, the HI was distilled from a glass bulb immersed in a dry ice/acetone bath to a bulb at liquid nitrogen temperatures. This procedure allowed almost complete removal of iodine. The purified HI was stored in dry ice, and later in liquid nitrogen, to prevent subsequent decomposition.

The reaction mixture was prepared the day before the experiment: 2-5 % HI in H_2 (99.9999 % purity form Alpha Products) was prepared, and stored in a blackened bulb in dry ice or liquid nitrogen until needed. The mixture was then flowed at 5-6 torr total pressure, to give HI partial pressures in the 0.1-0.2 torr range.

III. RESULTS AND DISCUSSION

The hydrogen exchange reaction experiment has been attempted many times, with little success. Figure 5 shows a typical experimental run. The main peaks are from the H_2 background, which is not completely subtracted out. There are no lines present that could be assigned to a product molecule in $v = 1$ vibrational state. It was believed that introduction of the flow apparatus would cure most of the problems with the earlier version of this experiment,[1] but apparently that was not sufficient.

The only line in the spectrum that could possibly be assigned to a reaction product is the $^2R_7$ line at 90 824.7 cm^{-1}(660.431 nm in the dye laser fundamental). This is a transition from the ground vibrational level and $J'' = 7$ rotational level to the $v' = 2$, $J' = 8$ level of the $\tilde{B}$ state. The predicted line position is 90 828.19 cm^{-1}. This state has a 1.2168 $\times 10^{-4}$ % of the total population at room temperature. Control experiments were conducted with pure H_2 at the same pressures as during the experiment and no signal could be observed from the $^2R_7$ line under auto-subtract conditions. Calculations of expected signal levels were conducted according to the scheme in Ref. (51), using published state-to-state cross sections,[52] and the expected number of photons at the PMT was found to be of the order of 10^4 photons. The background from H_2 was estimated at at least an order of magnitude less.

It is therefore believed that the signal from the $^2R_7$ line was due to product H_2 molecules; this is one of the stronger transitions,[52] and its presence indicates that several aspects of the experiment still need improving. This is a disappointing result, given the exceptional sensitivity of the LIF technique,[1] far superior to that of CARS, which yet suceeded in obtaining full ro-vibrational distributions for this reaction. As pointed out in this chapter, the main difficulties of the LIF technique lie in the generation of intense VUV laser radiation and the limited choice of

optical materials in this region. The filter used in the H + H_2 experiments reduces the signal by a factor of 6. The precursor absorption imposes limits on reaction mixture concentrations, and the difficulty in handling HI, and preventing it from decomposing or adsorbing onto the cell walls, places additional constraints on the experiment.

Besides the obvious solution of increasing the VUV intensity, another option would be to use a photon counter. Many of the desired transitions are not expected to emit more than a few hundred photons, and spike counting might improve chances of observing the reaction products in a state specific manner.

REFERENCES

1. G. R. Parker, Jr., Ph.D. Thesis, California Institute of Technology, 1988.
2. T. J. Butenhoff, K. L. Carleton and C. B. Moore, *J. Chem. Phys.* **92**, 377 (1990).
3. K. L. Carleton, T. J. Butenhoff and C. B. Moore, *J. Chem. Phys.* **93**, 3907 (1990).
4. J. Z. H. Zhang and W. H. Miller, *Chem. Phys. Lett.* **140**, 329 (1987).
5. J. Z. H. Zhang and W. H. Miller, *J. Chem. Phys.* **88**, 3202 (1988); *Chem. Phys. Lett.* **153**, 465 (1988); *J. Chem. Phys.* **88**, 4549 (1988).
6. J. Z. H. Zhang and W. H. Miller, *J. Chem. Phys.* **90**, 7610 (1989); *J. Chem. Phys.* **91**, 1528 (1989;).*Chem. Phys. Lett.* **159**, 130 (1989).
7. W. H. Miller, *Ann. Rev. Phys. Chem.* **41**, 245 (1990).
8. J. Z. H. Zhang and W. H. Miller, *J. Chem. Phys.* **92**, 1811 (1990).
9. M. D'Mello, D. E. Manolopoulos and R. E. Wyatt, *J. Chem. Phys.* **94**, 5985 (1991).
10. D. A. V. Kliner, D. A. Adelman and R. N. Zare, *J. Chem. Phys.* **94**, 1069 (1991).
11. R. S. Blake, K.-D. Rinnen, D. A. V. Kliner and R. N. Zare, *Chem. Phys. Lett.* **153**, 365 (1988).
12. K.-D. Rinnen, D. A. V. Kliner, R. N. Blake and R. N. Zare, *Chem. Phys. Lett.* **153**, 371 (1988).
13. K.-D. Rinnen, D. A. V. Kliner and R. N. Zare, *J. Chem. Phys.* **91**, 7514 (1989).
14. J. C. Nieh and J. J. Valentini, *Phys. Rev. Lett.* **60**, 519 (1988).
15. J. C. Nieh and J. J. Valentini, *Phys. Rev. Lett.* **92**, 1083 (1990).
16. D. L. Phillips, H. B. Levene and J. J. Valentini, *J. Chem. Phys.* **90**, 1600 (1989).

17. D. E. Manolopoulos and R. E. Wyatt, *Chem. Phys. Lett.* **159**, 123 (1989).

18. R. E. Continetti, B. A. Balko and Y. T. Lee, *J. Chem. Phys.* **93**, 5719 (1990).

19. R. E. Continetti, J. Z. H. Zhang and W. H. Miller, *J. Chem. Phys.* **93**, 5356 (1990).

20. S. A. Buntin, C. F. Giese and W. R. Gentry, *Chem. Phys. Lett.* **168**, 513 (1990).

21. B. Liu, *J. Chem. Phys.* **80**, 581 (1984).

22. A. J. C. Varandas, F. B. Brown, C. A. Mead, D. G. Truhlar and N. C. Blais, *J. Chem. Phys.* **86**, 6258 (1987).

23. M. M. Mladenovic, M. Zao, D. G. Truhlar, D. W. Schwenke, Y. Sun and D. J. Kouri, *J. Phys. Chem.* **92**, 7035 (1988).

24. G. Herzberg and H. C. Longuet-Higgins, *Discussions Far. Soc.* **35**, 77 (1963).

25. C. A. Mead and D. G. Truhlar, *J. Chem. Phys.* **70**, 2284 (1979).

26. C. A. Mead, *Chem. Phys.* **49**, 23 (1980); *J. Chem. Phys.* **72**, 3839 (1980).

27. B. Lepetit and A. Kuppermann, *Chem. Phys. Lett.* **166**, 581 (1990).

28. W. C. Price, *Phys. Rev.* **A-167**, 216 (1938).

29. C. F. Goodeve and W. C. Taylor, *Phys. Rev.* **A-154**, 181 (1936).

30. J. Romand, *Ann. de Phys.* **4**, 529 (1949).

31. J. M. White, Ph.D. Thesis, University of Illinois, Urbana (1966).

32. J. F. Ogilvie, *Trans. Far. Soc.* **67**, 2205 (1971).

33. R. S. Mulliken, *Phys. Rev.* **51**, 310 (1937).

34. R. S. Mulliken, *J. Chem. Phys.* **8**, 382 (1940).

35. S. G. Tilford, M. L. Ginter and A. M. Bass, *J. Mol. Spectrosc.* **34**, 327 (1970).

36. M. L. Ginter, S. G. Tilford and A. M. Bass, *J. Mol. Spectrosc.* **57**, 271 (1975).

37. D. S. Ginter, M. L. Ginter and S. G. Tilford *J. Mol. Spectrosc.* **92**, 40 (1982).

38. D. S. Ginter, M. L. Ginter, S. G. Tilford and A. M. Bass, *J. Mol. Spectrosc.* **92**, 55 (1982).

39. D. S. Ginter, M. L. Ginter and C. M. Brown, *Appl. Opt.* **19**, 4015 (1980).

40. R. D. Clear, S. J. Riley and K. R. Wilson, *J. Chem. Phys.* **63**, 1340 (1975).

41. R. Schmiedl, H. Dugan, W. Meir and K. H. Welge, *Z. Phys. A* **304**, 137 (1982).

42. Z. Xu, B. Koplitz and C. Wittig, *J. Phys. Chem.* **92**, 5523 (1988).

43. Z. Xu, B. Koplitz and C. Wittig, *J. Chem. Phys.* **90**, 2692 (1989).

44. D. T. Terwillinger and A. L. Smith, *J. Chem. Phys.* **63**, 1008 (1975).

45. J. H. D. Eland and J. Berkowitz, *J. Chem. Phys.* **67**, 5034 (1977).

46. T. A. Carlson, P. Gerard, M. O. Krause, G. von Wald, J. W. Taylor and F. Grimm, *J. Chem. Phys.* **84**, 4755 (1986).

47. D. W. Turner, C. Baker, A. D. Baker and C. R. Brundle, "Molecular Photoelectron Spectroscopy" (John Wiley & Sons, New York, 1970).

48. M. G. White, S. H. Southworth, P. Kobrin and D. A. Shirley, *J. Electron. Spectrosc. Rel. Phenom.* **19**, 115 (1980).

49. K. P. Huber and G. Herzberg, "Molecular Spectra and Molecular Structure: IV. Constants of Diatomic Molecules," (Van Nostrand Reinhold, New York, 1979) pp. 324-328.

50. Reference (1), Chapter 5.

51. G. R. Parker, Jr., Candidacy Report, California Institute of Technology, 1983.

52. J. M. Launay and M. Le Dorneuf, *Chem. Phys. Lett.* **163**, 178 (1989).

FIGURE CAPTIONS

Figure 1. Scale drawing of the laser table layout for pump-probe experiments.[1] The Molectron MY-34 Nd:YAG laser and DL-18 dye laser serves as the pump (photolysis) laser, while the Quanta-Ray DCR-2A Nd:YAG laser, PDL-2 dye laser and WEX-1 wavelength extension unit generate the UV laser to be tripled in the THG cell. Abbreviations are as follows: A: Aperture; BS: beamsplitter; P: prism; PD: photodiode; PEJM: pyroelectric joulemeter.

Figure 2. Scale drawing of the experimental cell.[1] See descriptions in Chapters 4 and 5.

Figure 3. Electronics for pump-probe experiments:[1] as shown in the previous chapter, the PMT is the signal channel, while the output of the ionization cell is the laser intensity channel. The Laser Timing Controller sets the delay between the two lasers and toggles the gates on the integrator to allow for "auto-subtract" operation. The solid lines represent analog signal lines, the dash-dot lines represent control lines, and the dotted lines are the digital data bus from the computer to the dye laser.

Figure 4. HI absorption spectrum taken with the Quanta Ray laser system. This spectrum is the average of 4 data collection cycles as described in the text.

Figure 5. Typical LIF spectrum for the H + H_2 experiment: the top panel represents the output of the ionization cell, and the bottom the PMT output.

Figure 1.

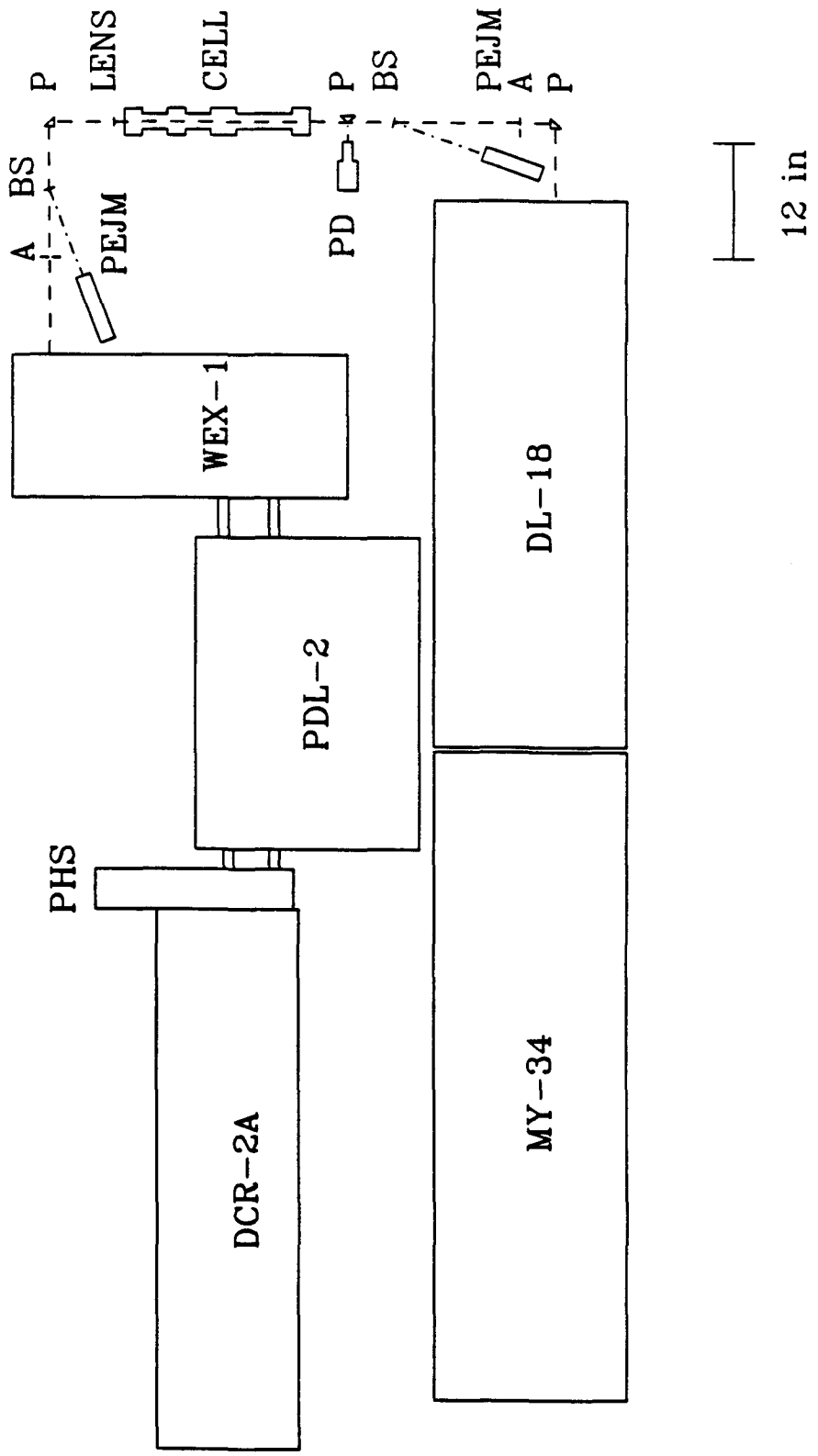
P
LENS
CELL
P
BS
PEJM
A
P
BS
A
PEJM
PD
12 in
WEX-1
DL-18
PDL-2
PHS
DCR-2A
MY-34

Figure 2.

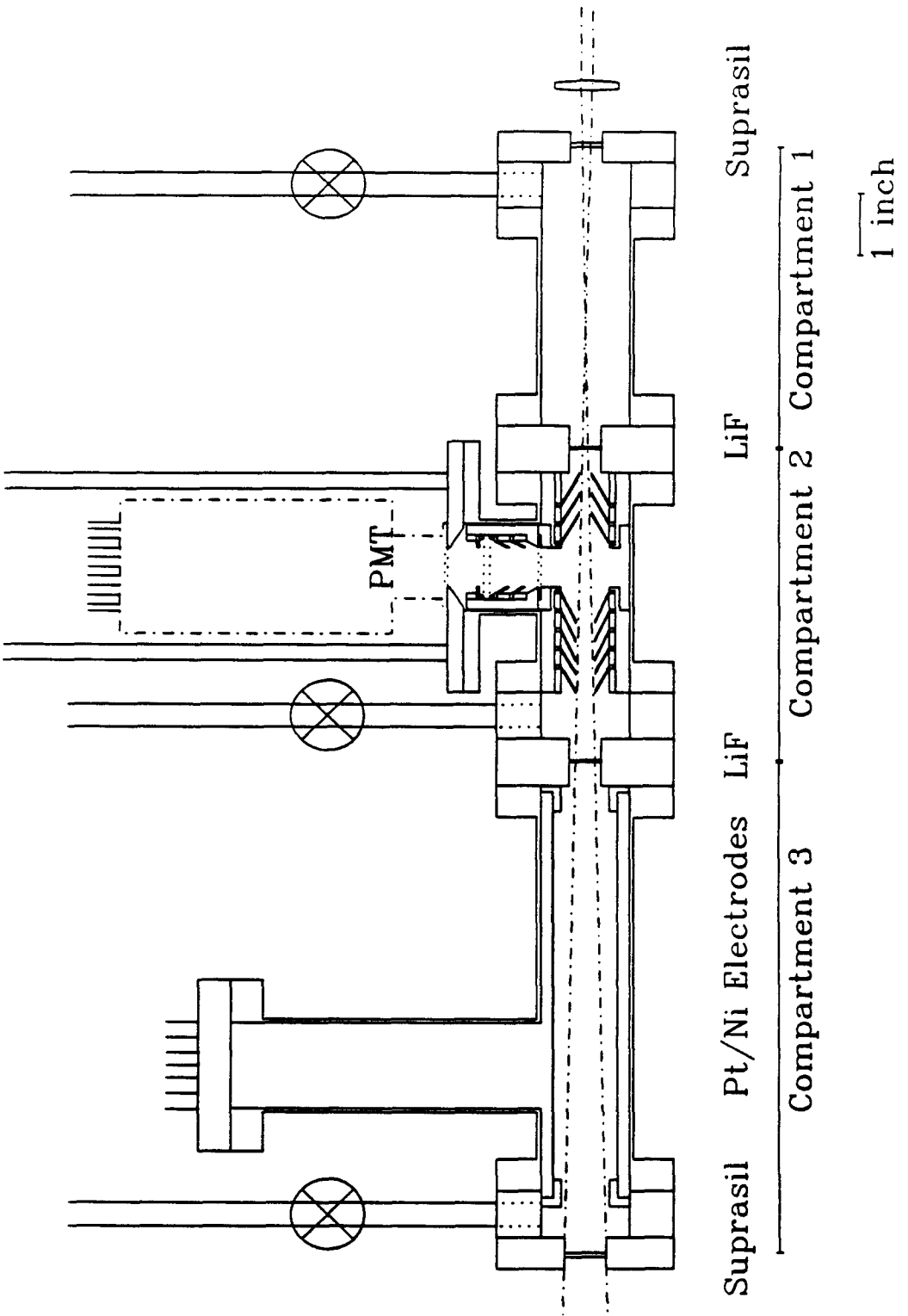
PMT
Suprasil
LiF
Compartment 1
Compartment 2
Pt/Ni Electrodes
LiF
Compartment 3
Suprasil
1 inch

Figure 3.

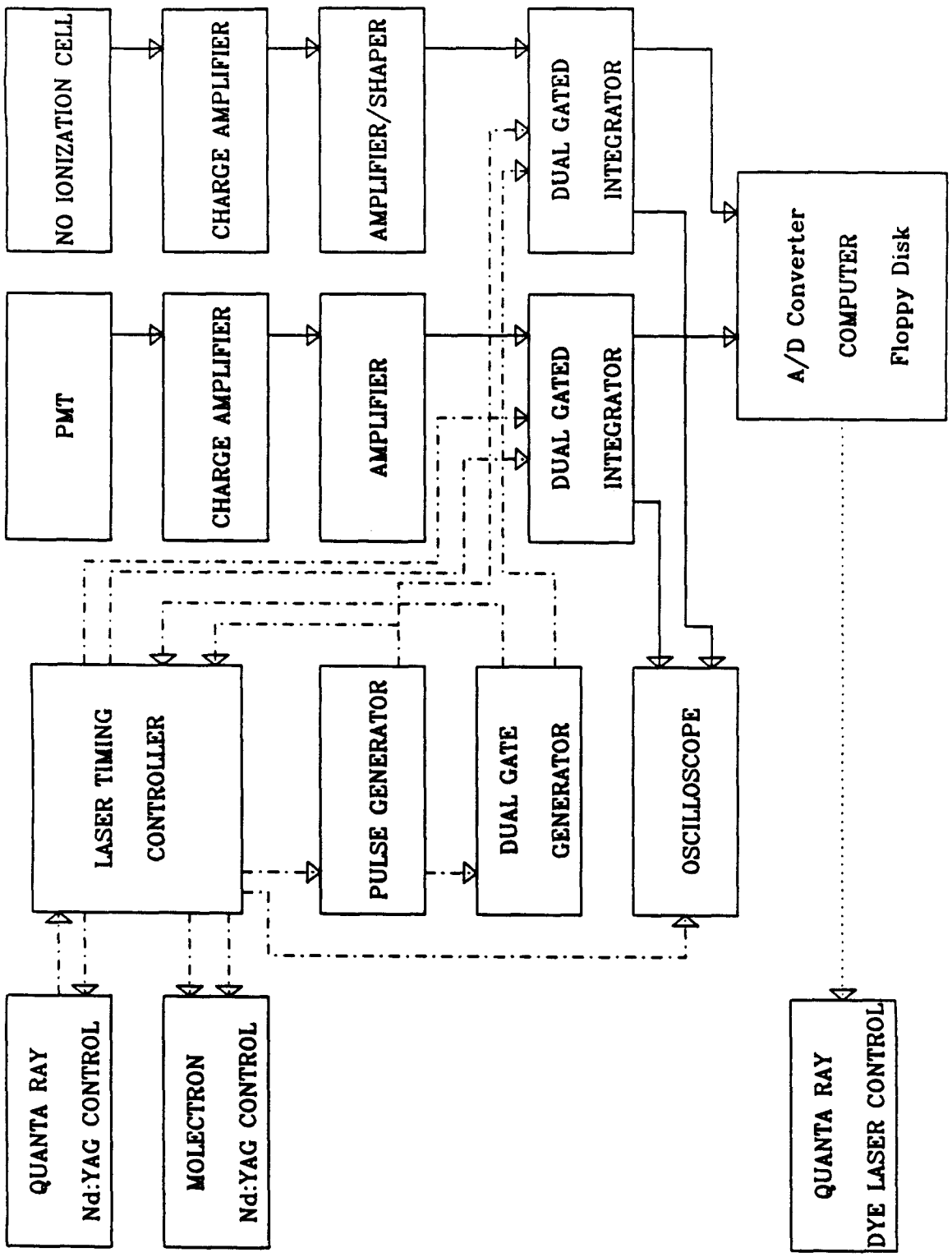
NO IONIZATION CELL
CHARGE AMPLIFIER
AMPLIFIER/SHAPER
DUAL GATED INTEGRATOR
PMT
CHARGE AMPLIFIER
AMPLIFIER
DUAL GATED INTEGRATOR
A/D Converter
COMPUTER
Floppy Disk
LASER TIMING CONTROLLER
PULSE GENERATOR
DUAL GATE GENERATOR
OSCILLOSCOPE
QUANTA RAY Nd:YAG CONTROL
MOLECTRON Nd:YAG CONTROL
QUANTA RAY DYE LASER CONTROL

Figure 4.

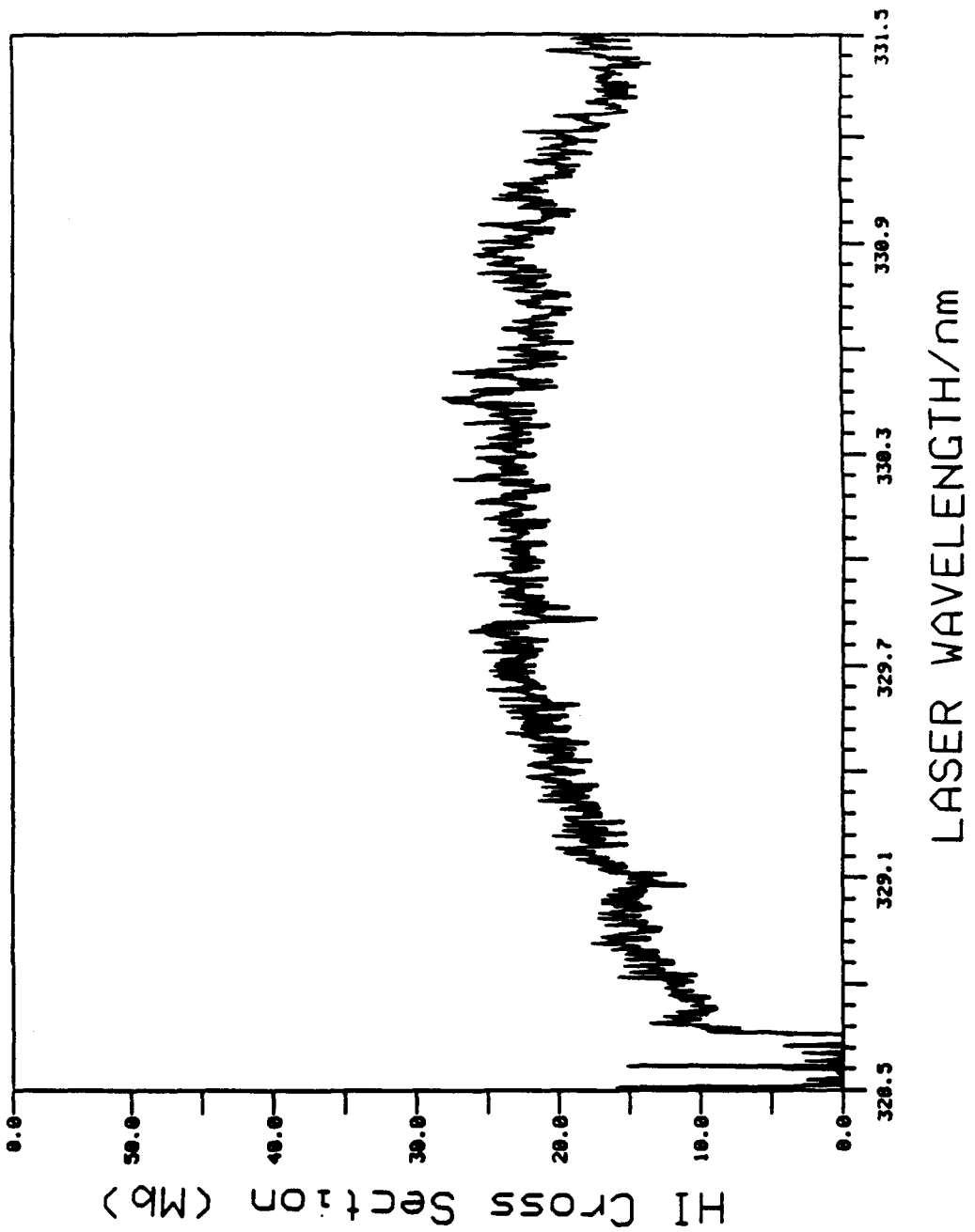
HI Cross Section (Mb)
0.0
10.0
20.0
30.0
40.0
50.0
328.5
329.1
329.7
330.3
330.9
331.5
LASER WAVELENGTH/nm

Figure 5.

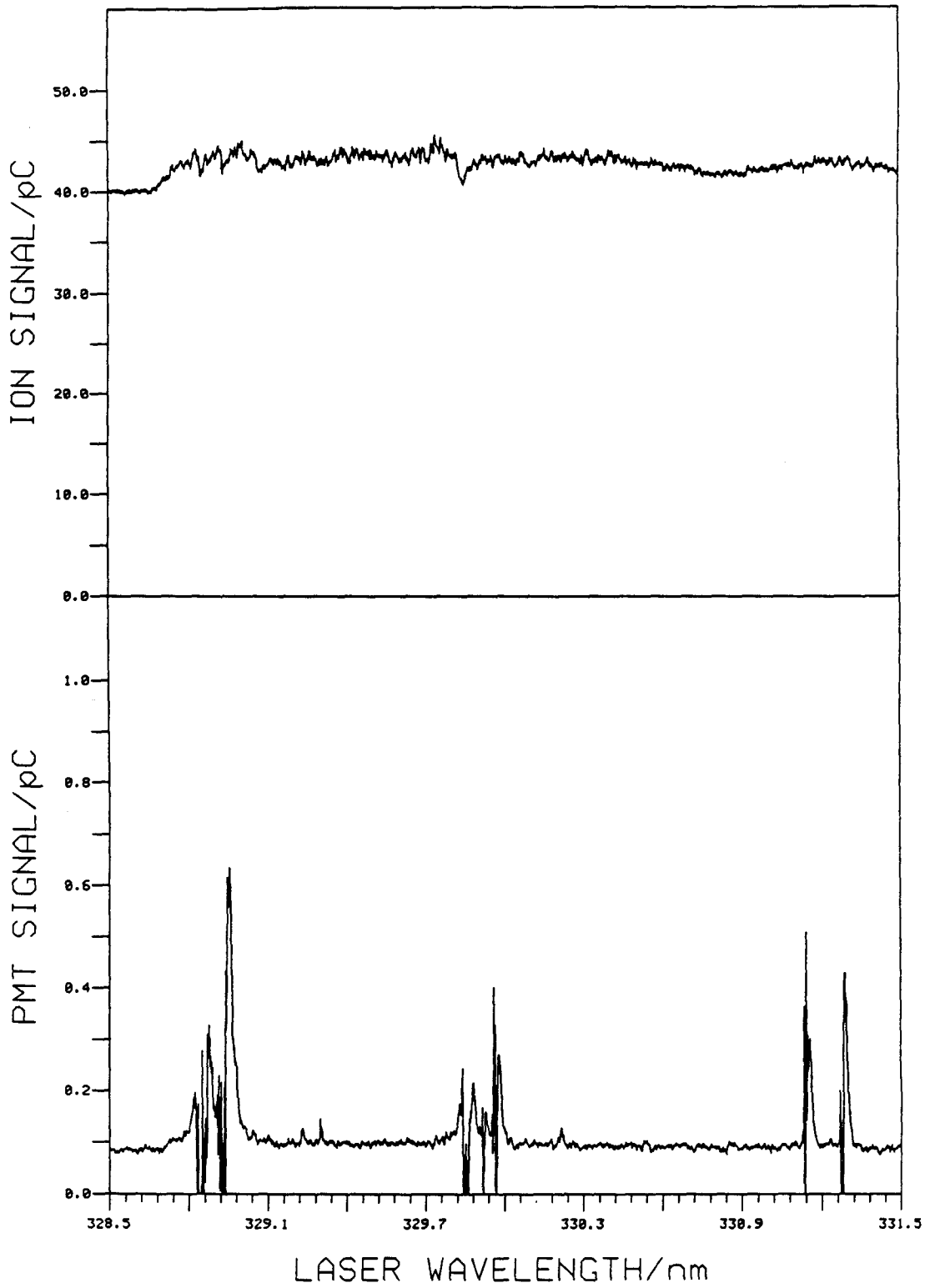
ION SIGNAL/pC
50.0
40.0
30.0
20.0
10.0
0.0
PMT SIGNAL/pC
1.0
0.8
0.6
0.4
0.2
0.0
328.5
329.1
329.7
330.3
330.9
331.5
LASER WAVELENGTH/nm

APPENDIX I

ELECTRONICS

I. INTRODUCTION

This section describes the electronics used in the experiments of Chapters IV-VI, with emphasis on the newly built equipment. The majority of the equipment is described at length in appendix 2 of G. R. Parker's thesis,[1] and only a brief description will be given here; Detailed descriptions and circuit diagrams are provided for the recently built electronics. The rest of this appendix is divided in four sections. Section II describes the photomultiplier, and the electronics associated with it; section III the two types of differential gated integrators used for data acquisition; the fourth section illustrates the electronics controlling the relative timing between the two lasers, and the last the computer system used for data acquisition.

II. PHOTOMULTIPLIER ELECTRONICS

The H_2 fluorescence is collected by a Thorn EMI Gencom[2] solar-blind photomultiplier, with a MgF_2 window and a CsI photocathode. This PMT has a range between 110-220 nm; this linear-focused 14-dynode (BeCu) design, has a 2.2 ns risetime. The interdynode voltages are provided by a divider network, with a total resistance of 2.168 MΩ.[1] The cathode is held at ground potential, while the anode is at positive high voltage. The photomultiplier housing also contains a model A2 preamplifier, which terminates the PMT current output into 51 Ω and amplifies the voltage output by 10. Its gain is 0.510 V/mA. A charge-to-voltage preamplifier is used after the A2 preamp, so that the overall gain is 10 mV/pC. This preamplifier is based on a LeCroy TRA1000 model[3] and it is similar to the one used for the ionization cell: both models are described in more detail in Ref. (1).

The output of the preamp is further amplified by a X10 amplifier, based on a Comlinear CLC400 high-gain operational amplifier, as described in the manufacturer's application note:[4] a gain of 10.6 was measured.

Since it was first acquired, the PMT 3000V power supply suffered from excessive ripple at its switching frequency of 26 kHz. The ripple was amplified by the two preamplifiers. In the past,[1] a passive 7 pole Butterworth filter was placed at the input to the charge-to-voltage preamplifier, in an attempt to remove the ripple from the signal. This approach resulted in excessive ringing of the output signal, with significant loss of signal for the integrators. It was decided to filter the high voltage output of the power supply directly, by building a low-pass filter, which is shown in Figure 1. The filter response curve is shown in Figure 2. An attenuation of 40 dB was obtained at the frequency of 26 kHz, and no visible ripple was observed at the output. The output of the PMT charge preamplifier was then a fast rise, followed by a slow 10 μs decay, with no ringing.

III. DIFFERENTIAL GATED INTEGRATORS

The PMT and ionization cell pulses as they emerge from the respective preamps, are of the order of microseconds; these signals need to be slowed down to milliseconds for the computer to handle. A Molectron Laser Spectroscopy Detection System (LSDS) was originally purchased for the experiment: it consists of a model 122 dual gate generator, two model 131 amplifier-shapers, and two model 112 differential gated integrators, all housed within the same NIM-bin power supply module. This system is described in detail in Ref. (1). The gated integrators contain two RC integrators, one for the signal and the other for the baseline. The output is the difference between the ouputs of the gate 1 integrator and the gate 2 integrator, or the signal minus the baseline.

In the experiments described in this thesis, the integrator time constant RC is approximately equal to the signal pulse width, τ_s, so that the integration capacitor does not have sufficient time to discharge. In this mode of operation, the output of the integrator is a weighted average of the input, with the integrator "forgetting" previous pulses. If δ is the duty cycle t_{gate}/T, where t_{gate} is the gate width and T is the gate repetition period, the effective time constant of the integrator is RC/δ. The model 122 gate generator is used to generate both signal gates for the two channel of data acquisition, while a model 139B E-H pulse generator[5] is used to provide the baseline gates. Typical gate widths used in the LIF experiments were of the order of 100 ns.

The Molectron integrators were used for the experiments until a 200 mV high-frequency ($\approx$ 300 MHz) ripple was found to originate from one of the components of both integrators; this ripple was found to be passed to all other components of the NIM-bin power supply through the integrator power connections. This noise was causing the differential output of both integrators to fluctuate, and it became impossible to zero the integrators before an experiment was conducted. Several

attempts were made to track down the source of the noise, all hampered by the lack of circuit diagrams for the DGI's: capacitors were introduced across the diode bridges on the input to the two single-ended integrators (Analog Devices 42). While this dampened the noise, gate operation was distorted. The final differential output amplifier (TP 1321) was substituted with a CA3100S operational amplifier, with no effect on the noise.

It was decided to build a new differential gated integrator, to handle the PMT signal. The new unit is centered around two single-ended gated integrator boards (model 4130 A) from Evans Electronics.[6] Several of the convenient features of the Molectron integrators were retained: a monitor board was built, which permits viewing of the input pulse and the two gates on the oscilloscope screen, in order to facilitate positioning of the two gates. The diagram for this board is shown in Figure 3. Three LM 310 voltage followers are used to input the signal and the two gates into a Comlinear CLC 400 operational amplifier.[4] This amplifier has a gain of 1.

The two outputs of the Evans integrators (signal and baseline) are inputs of the differential amplifier stage shown in Figure 4. It consists of a pair of Precision Monolithic OP-27[7] op-amps with an output time constant of 50 ms. The new integrator also has the capability of choosing among 5 values for the capacitance and 9 for the resistance for an RC in the range between 30 ns and 3 seconds. Typically an RC of 0.1-1 ns was used. In order to vary the time constant, two RC boards (one for each Evans integrator) were designed. Each of these boards uses four National Semiconductor[8] JFET analog switches (LF 11331), to independently choose R and C. A block diagram of the Evans integrator and a diagram of the external RC board are shown in Figures 5 and 6 respectively. In order to keep the integrator at a gain of 1, regardless of the choice of R and C, a feedback resistor had to be connected to the Evans integrator equal to the variable input resistor.

A board similar to the one in Figure 6, except only containing nine resistors was constructed, so as to switch both the input and feedback R at the same time.

This differential gated integrator has performed very well during the experiments, with a noise of less than 2 mV. It was possible to keep one of the Molectron integrators working, despite of the 300 MHz. noise; it was normally used for the ionization cell signal.

IV. LASER TIMING CONTROLLER

The time sequence between the two lasers is determined by a laser timing controller built by the Chemistry Electronics Shop, and described thoroughly in Ref. (1). Minor modifications were recently introduced, and are discussed here . The pump (Molectron) Nd:YAG laser is a 10 Hz laser, while the probe (Quanta-Ray) laser has an optimum repetition rate of 20 Hz. this poses a unique challenge in trying to set their time delays. With this design, the Quanta-Ray OSC SYNC pulse (3.3 V into 1 kΩ, 3 ms duration) initiates the timing sequence. The flashlamps are fired at the end of this pulse, while the Q-switch is fired 210 μs later. The Molectron laser is externally controlled by supplying a lamp trigger pulse, M-LAMP, (5-12 V, 50 Ω, pulse width between 100 μs and 50 ms), which also brings the Q-switch to its high-voltage state; the Q-switch is fired approximately 600 μs later.

The Laser Timing Controller is shown schematically in Figure 7; this design centers around 4 pairs of monostable multivibrators. The first pair (U1) is triggered by the Quanta-Ray OSC SYNC pulse and generates a 100 μs pulse, with a 2.4 ms delay: this delay can be adjusted by a front panel potentiometer, *LAMP DELAY*, and serves to trigger the Molectron flashlamps. The second pair of multivibrators (U2) is triggered by the output of the first pair, and generates a 780 μs pulse, adjustable by a second front-panel potentiometer, *Q-SWITCH DELAY*, which sets the time delay between the Molectron lamp trigger and the Q-switches. This output also triggers the third and fourth set of multivibrators (U4 and U5). The output of the U4 pair, M-QS, triggers the Molectron Q-switch: this a 1.2 μs pulse, with a delay adjustable by a third front panel potentiometer *Q-SWITCH TIMING*. The output of the U5 pair, QR-QS, is used to trigger the Quanta-Ray Q-switch: this is a fixed 100 ns delay pulse, 1.2 μs wide. The *Q-SWITCH TIMING* adjustment allows the Molectron laser pulse to be 50 ns after to 150 ns before the Quanta-Ray pulse.

The problem of the different repetition rates was overcome by connecting the OSC SYNC output to a J-K flip-flop, "anded" with the Molectron trigger pulses, to prevent it from firing on alternate Quanta-Ray pulses.

The potentiometers have to be adjusted for optimum operation of both lasers. Normally, *Q-SWITCH DELAY* is used to maximize the output of the Molectron laser, while *LAMP DELAY* is used for the Quanta-Ray laser. The time delay between the pump and the probe laser is then set with the *Q-SWITCH TIMING* potentiometer.

It is also desirable to subtract the signal produced when only the probe laser is on, from the signal obtained when they are both on. This can be accomplished by toggling the gates to the integrator. The J-K flip-flop is used to toggle four 2-to-1 multiplexers, whose input is connected to the gate generator, and output to the gate inputs of the integrator. The order of the gates is then toggled on each Quanta-Ray (probe) pulse. If, when both lasers are on, gate A adjusted for the baseline (negative input to the integrator), and gate B for the signal (positive input to the integrator), then the integrator output will be the two-laser signal minus the baseline. If on the next Quanta-Ray pulse the two gates are toggled, A will be on the positive input to the integrator and B on the negative, and the output will be the baseline minus the one-laser signal. After several laser pulses, the output of the integrator will be the average of the two-laser signal minus the one-laser signal, as desired.

The components of the laser timing controller can be found in Table 1. This controller has worked reliably, with jitter in the laser pulses not exceeding 1 ns.

V. COMPUTER SYSTEMS

The Intel SBC 80/20 computer system[9] is described at length in Ref.s (1), (10) and (11). The data acquisition system includes the single board computer which uses an Intel 8080A microprocessor, an Intel SBC 116 combination memory and I/O expansion board, an Intel SBC 310 high-speed mathematics board, an Analog Devices TRI-1200 analog-to-digital and digital-to-analog conversion board, and an iCOM FD3712 dual 8-inch floppy disk drive and controller board. A memory expansion and interface board was designed by R.Q. Rianda and described in his thesis.[10] This board contains a pair of Intel 8253 programmable interval timers, which are the hardware responsible for controlling the dye lasers. The interface board provides the connection between the computer and the crystal controller for the Molectron laser.[11] A description of the laser scanning routines can be found in Ref. (1).

After completion of a scan, the data is stored on 8-inch floppy disks, and analyzed on the divisional VAZ computer. The data conversion and manipulation is done in several steps: first, the unformatted binary file is transferred using the public program FLOPPY. The program CONVERT is used to turn the data into formatted FORTRAN integers. This and other data analysis programs were originally written by G. R. Parker, Jr.: programs to add, subtract, or divide one spectrum by another, as well as baseline correction and smoothing routines are available.

TABLE 1. Laser Timing Controller Components

Component	Value	Description
U1-U5	74LS221	Dual Monostable Multivibrator
U6	74LS107	Dual J-K Flip-Flop
U7	74128	Quad 50Ω Line Driver
U8	74128	Quad 50Ω Line Driver
U9	74128	Quad 50Ω Line Driver
U10	74LS158	Quad 2 to 1 Data Multiplexer
U11	7404	Hex Inverter
U12	7437	Quad NAND
U13	74OL6001	Optocouplers
C1	0.22 μF	
C2	0.01 μF	
C3	0.10 μF	
C4	0.10 μF	
C5	1000 pF	
C6	10 pF	
C7	1000 pF	
C8	10 pF	
C9	91 pF	
R1	10 kΩ	
R2	18 kΩ	
R3	1 kΩ	
R4	8.2 kΩ	
R5	10 kΩ	
R6	20 kΩ	
R7	18 kΩ	
R8	4 kΩ	
R9	5 kΩ	
R10	18 kΩ	
R11	20 kΩ	
R12	18 kΩ	
R13	91 Ω	

REFERENCES

1. G. R. Parker, Ph.D. Thesis, California Insitute of Technology, 1988.
2. THORN EMI Gencom, Inc., 23 Madison Rd., Fairfield, NJ 07006, Model No. G26E314LF.
3. LeCroy Research Systems, Inc., 700 S. Main Street, Spring Valley, NY 10977.
4. Comlinear Corporation, Inc., 4800 Wheaton Drive, Fort Collins, CO 80525.
5. E-H International, Inc., 7303 Edgewater Drive, Oakland, CA 94621.
6. Evans Electronics, P.O. Box 5055, Berkeley, CA 94705.
7. Precision Monolithic Inc., 1500 Space Park Drive, P.O. Box 58020, Santa Clara, CA 95052.
8. National Semiconductor Corporation, 2900 Semiconductor Drive, P.O. Box 58090, Santa Clara, CA 95052.
9. Intel, Inc., 3065 Bowers Ave., Santa Clara, CA 95051
10. R. Q. Rianda, Ph.D. Thesis, California Institute of Technology, 1982.
11. D. J. Moll, Ph.D. Thesis, California Insitute of Technology, 1983.

FIGURE CAPTIONS

Figure 1. PMT power supply filter circuit diagram; L_1 is a 5-turn ferrite toroid with inductances of about 1 nH.

Figure 2. PMT power supply filter response: $dB = 20 \log_{10}(\frac{V_{out}}{V_{in}})$

Figure 3. Monitor circuit board for the differential gated integrator.

Figure 4. Differential amplifier circuit board for the gated integrator.

Figure 5. Block diagram for the Evans Electronics Model 4130 A gated integrator.

Figure 6. RC board for the DGI.

Figure 7. Laser Timing Controller circuit diagram.

Figure 1.

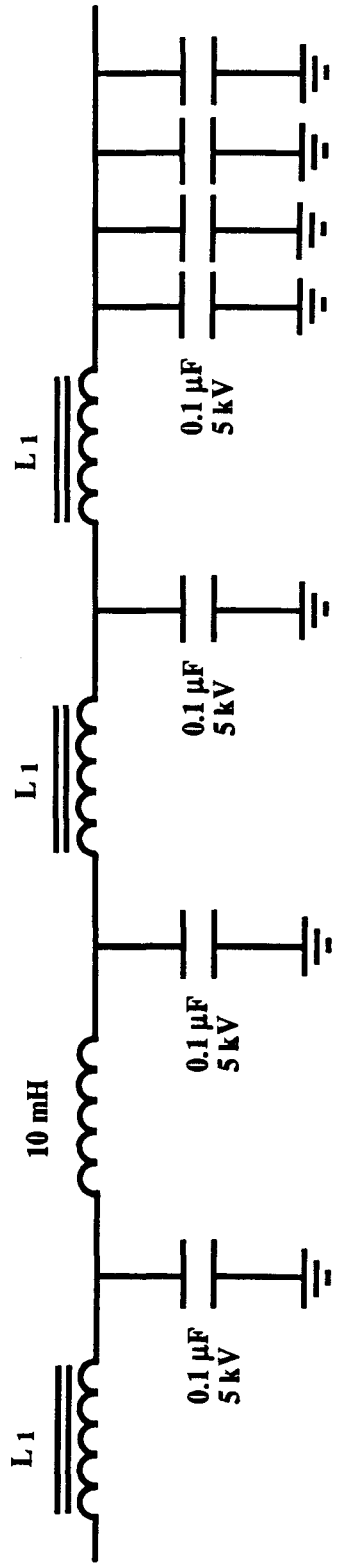

Figure 2.

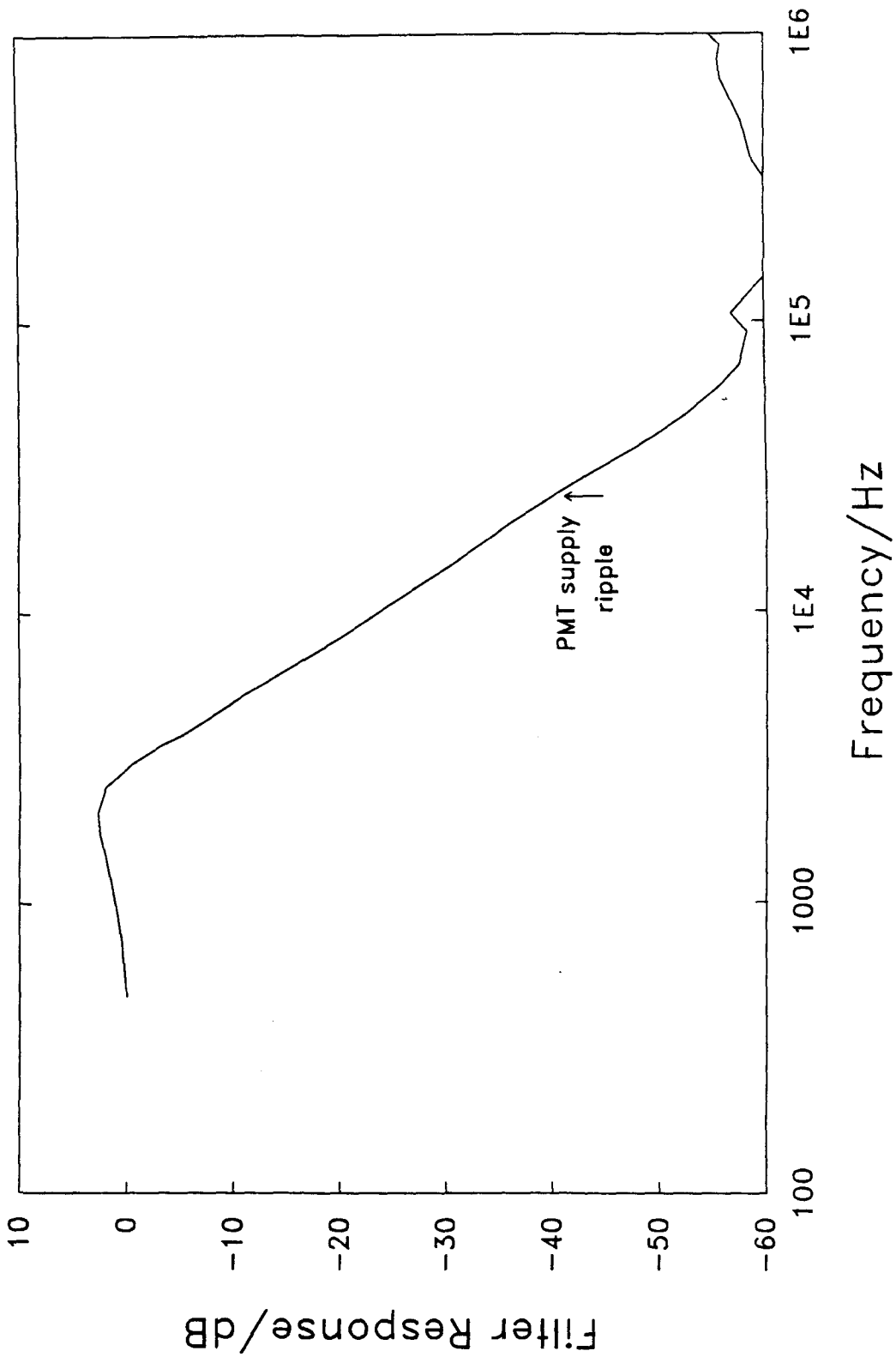
Filter Response/dB
10
0
-10
-20
-30
-40
-50
-60
100
1000
1E4
1E5
1E6
Frequency/Hz
PMT supply
ripple

Figure 3.

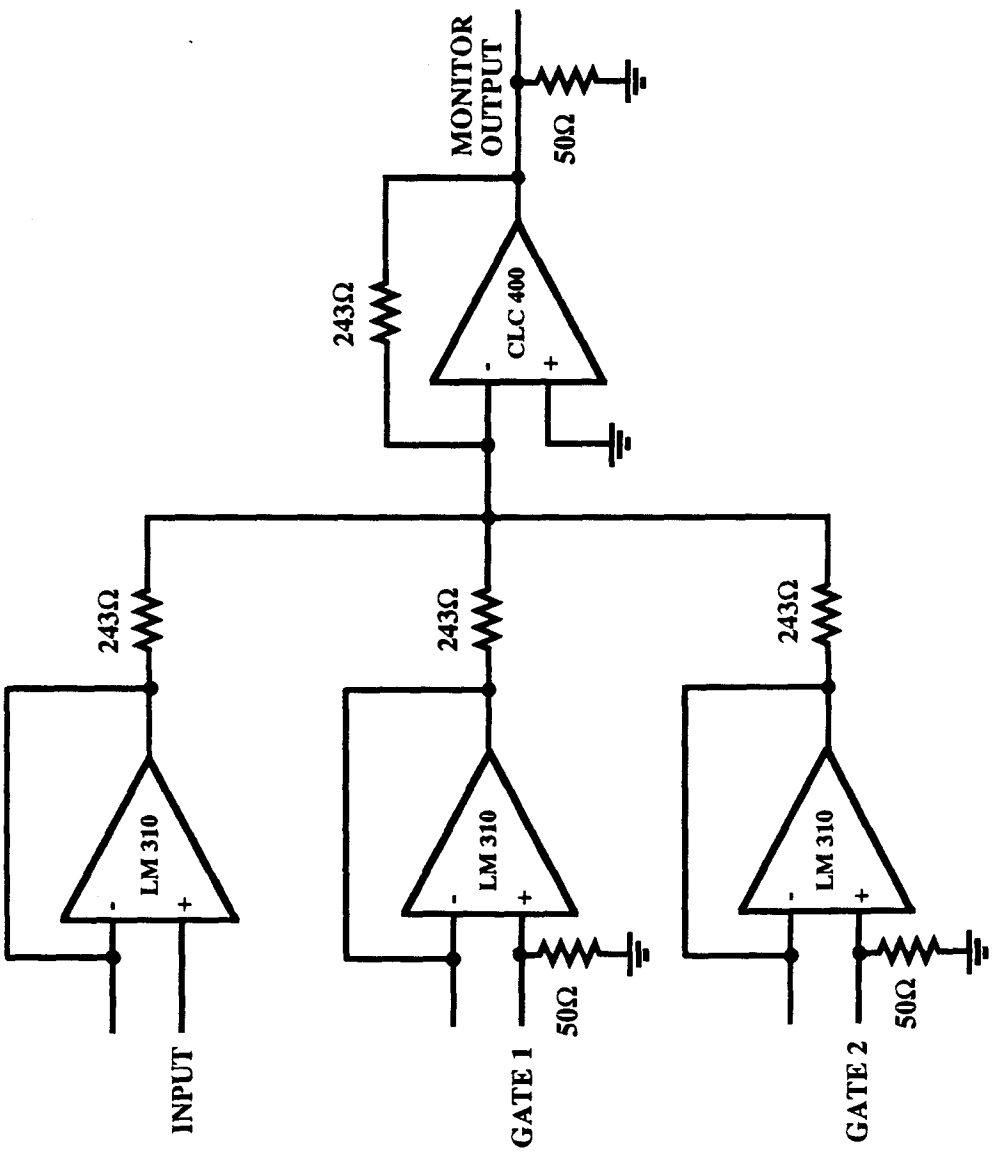
MONITOR OUTPUT
50Ω
243Ω
CLC 400
243Ω
243Ω
243Ω
LM 310
LM 310
LM 310
50Ω
50Ω
INPUT
GATE 1
GATE 2

Figure 4.

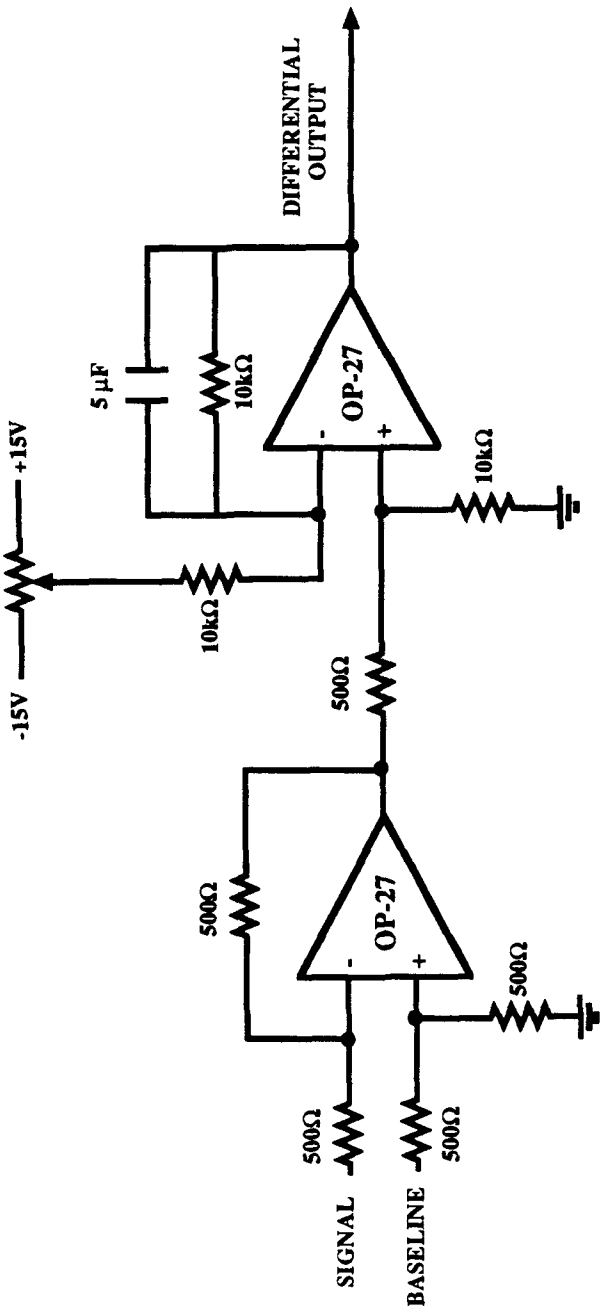
DIFFERENTIAL OUTPUT
OP-27
5 µF
10kΩ
+15V
-15V
10kΩ
10kΩ
500Ω
500Ω
OP-27
500Ω
500Ω
500Ω
SIGNAL
BASELINE

Figure 5.

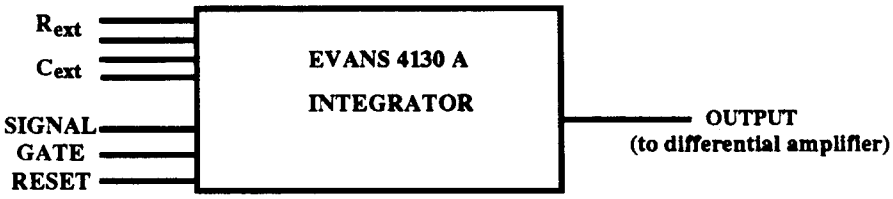
R_{ext}
C_{ext}
SIGNAL
GATE
RESET
EVANS 4130 A
INTEGRATOR
OUTPUT
(to differential amplifier)

Figure 6.

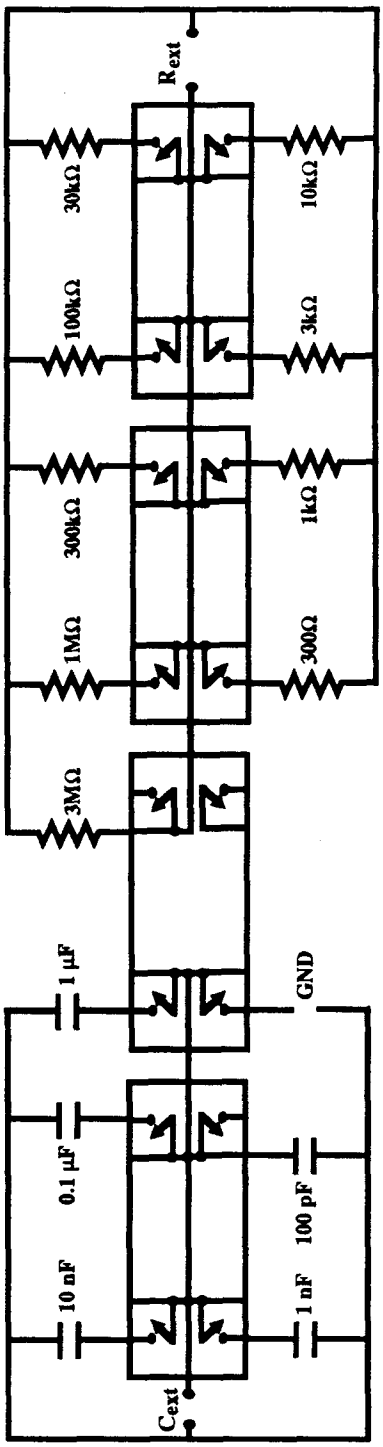
Rext
30kΩ
10kΩ
100kΩ
3kΩ
300kΩ
1kΩ
1MΩ
300Ω
3MΩ
1 µF
GND
0.1 µF
100 pF
10 nF
1 nF
Cext

Figure 7.

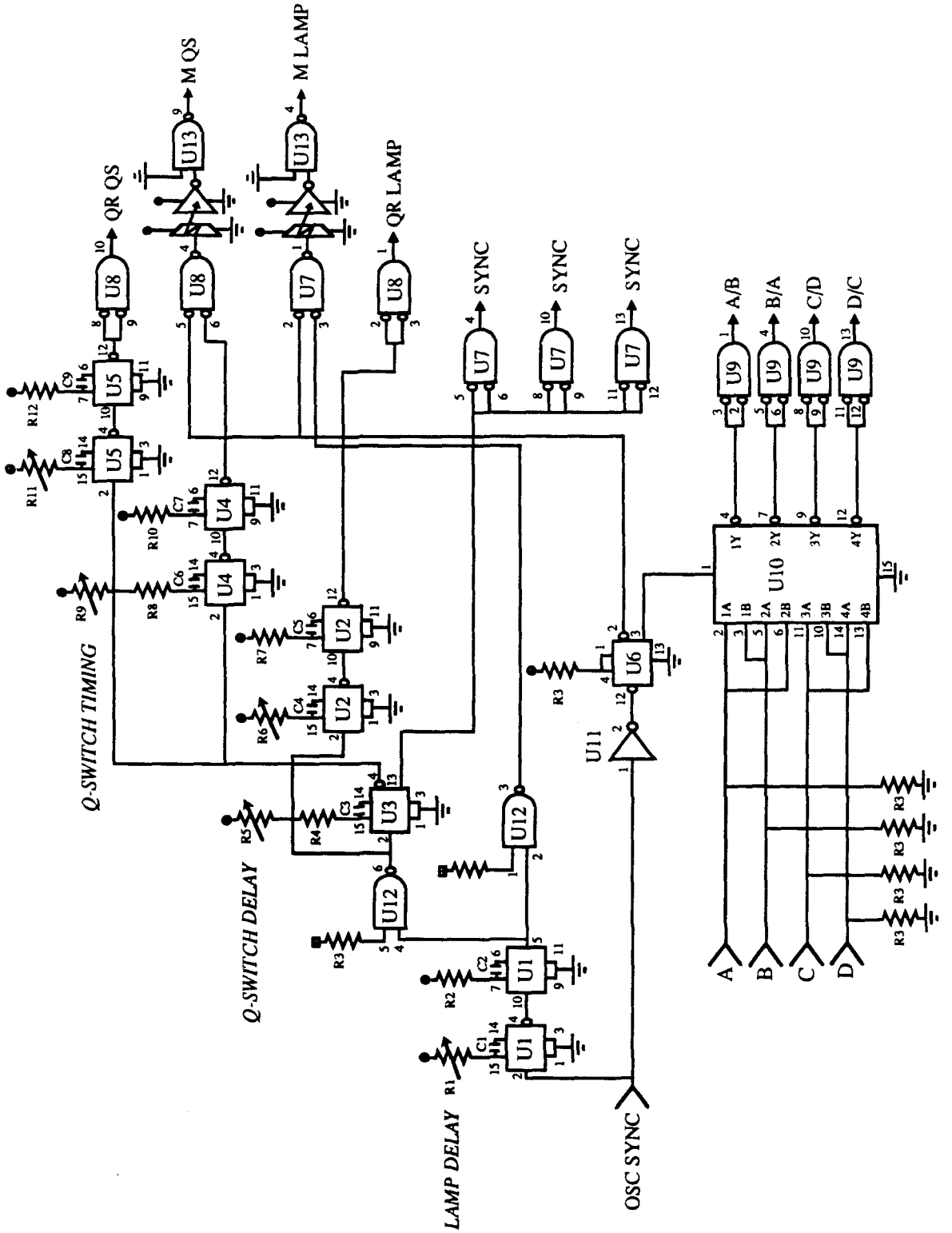
M QS
M LAMP
QR QS
QR LAMP
SYNC
SYNC
SYNC
A/B
B/A
C/D
D/C
U10
U11
Q-SWITCH TIMING
Q-SWITCH DELAY
LAMP DELAY
OSC SYNC
A
B
C
D

APPENDIX II

STUDY OF GAS PHASE PRODUCTS FORMED BY FLASH-VACUUM PYROLYSIS OF HALOMETHANES USING ELECTRON ENERGY-LOSS SPECTROSCOPY

(This paper will appear in *"Collision Processes of Ion, Positron, Electron and Photon Beams with Matter"* A. C. A. Souza, E. F. Silveira, J. C. Nogueira, M. A. C. Nascimento and D. P. Almeida Ed.s (World Scientific Publishing, Singapore 1992)).

STUDY OF GAS PHASE PRODUCTS FORMED BY FLASH-VACUUM PYROLYSIS OF HALOMETHANES USING ELECTRON ENERGY-LOSS SPECTROSCOPY[1]

I. M. Xavier Jr.[2], K. N. Walzl[3], M. R. Giorgi and A. Kuppermann

Arthur Amos Noyes Laboratory of Chemical Physics[4],

California Institute of Technology, Pasadena, CA 91125

Abstract

Thermal decomposition of chlorodifluoromethane, chloroform, dichloromethane and chloromethane under flash-vacuum pyrolysis conditions (900-1100°C) was investigated by the technique of electron energy-loss spectroscopy, using an impact energy of 50 eV and a scattering angle of 10°. The pyrolytic reaction follows a hydrogen chloride α-elimination reaction pathway. The difluoromethylene radical was produced from the chlorodifluoromethane pyrolysis at 900°C and identified by its $\tilde{X}^1A_1 \rightarrow \tilde{A}^1B_1$ band at 5.04 eV.

---

[1] This work was supported in part by the U. S. Department of Energy, Contract No. DE-AM03-76F00767, Project Agreement No. DE-AT03-76ER72004.

[2] Work performed in partial fulfillment of the requirements for the Ph.D. degree in Chemistry at the California Institute of Technology.

Present address: Departamento de Quimica Fundamental, Universidade Federal de Pernambuco, 50739 Recife, PE, Brazil.

[3] Present address: Institute for Defense Analyses, 1801 N. Beauregard Street, Alexandria, VA 22311-1772.

[4] Contribution No.8509

I. INTRODUCTION

The thermal decomposition of four halomethane molecules that follow similar pyrolysis pathways provides clues for generation of gas phase halocarbenes. By comparison between the electronic spectra of the pyrolytic precursor molecule at room temperature and at high temperature, one can determine the efficiency of decomposition and identify the possible pyrolytic products.

This report presents an electron energy-loss study of the hydrogen chloride (HCl) α-elimination from halomethanes under flash-vacuum pyrolysis (FVP) conditions.[1,2] The FVP conditions employed in this study were 1-10 mTorr of the gas sample over a quartz pyrolyzer surface at 900-1100°C. Under these conditions, thermal activation takes place primarily by contact with the hot pyrolyzer walls, so that processes observed in this study result mainly from very fast heterogeneous reactions.[1]

Electron-impact spectroscopy has been previously used in our laboratory for investigation of the methyl (CH_3) radical and some of its pyrolytic precursors.[3] In that work, the number density of CH_3 radicals in the jet at the pyrolysis temperature was estimated to be 10^{13} molecules/cm^3 on the basis of the intensity of the 5.73 eV band.

II. EXPERIMENTAL

The spectrometer used in the present experiment has been described previously.[4] Briefly, electrons are emitted from a tungsten filament and focused into a hemispherical monochromator. The monoenergetic electrons are then focused into the scattering region and, after interaction with the target molecules, enter a hemispherical energy-loss analyzer prior to detection.

The spectrometer resolution (as measured by the full width at half-maximum of the elastically scattered feature) varied between 70 and 100 meV. For all reported spectra, the incident electron energy was 50 eV and the scattering angle was 10°.

In order to produce thermal decomposition of the halomethanes, an *in situ* pyrolysis technique was employed.[3] The pyrolysis takes place within a graphite-coated quartz tube with an inner diameter of 0.060 *in.* The pyrolyzer is heated by tantalum sheathed double stranded tungsten-rhenium alloy wires wound over a 0.35 in length of the quartz tube, and temperatures up to 1100°C (as measured by an optical pyrometer) can be reached. Since the pyrolysis is done at low pressures, the residence time in the pyrolyzer is kept in the few milliseconds' range, and thermal activation results mainly from collisions with the wall. Because the distance from the end of the pyrolyzer to the scattering center region is short, most of the reactive intermediates should be detected. The background pressures in the scattering chamber are quite low ($< 5 \times 10^{-5}$ Torr), so recombination rates are slow.

The investigation of four halomethanes are reported: chlorodifluoromethane (Aldrich, 99.9%); chloroform (J.T.Baker, 99.5%); dichloromethane (J. T. Baker, 99.7%) and chloromethane (Aldrich, 99.5%). The chloroform and dichloromethane samples were subjected to three liquid-nitrogen, freeze-pump-thaw cycles. Hydrogen chloride (Matheson, 99.0%) was used as reference in the study of the high-temperature spectra.

III. RESULTS AND DISCUSSION

Figure 1 shows the electron energy-loss spectrum of the HCl jet. The spectrum is featureless in the region 2.0-6.5 eV, which is followed by a broadband continuum with a maximum around 8 eV. The four peaks in the region above 9 eV consist mainly of the $C^1\Pi$ and $b^3\Pi$ states, which are Rydberg states corresponding to the $\pi \rightarrow 4s$ transition.[5] The strongest peak at 9.62 eV is assigned as $C^1\Pi(v' = 0)$, while the two peaks at 9.93 and 10.28 eV are the $C(v' = 1, 2)$ bands, respectively. The small peak at 9.31 eV corresponds to $b^3\Pi(v' = 0)$.[6]

In Figures 2 and 3, we show the energy-loss spectra of chlorodifluoromethane at room temperature and at 900°C. The room temperature spectrum shows a broadband continuum with the maximum around 8.2 eV, followed by two peaks at 9.24 and 10.00 eV, which can be assigned as the Rydberg transitions $Cl \rightarrow 4s$ and $Cl \rightarrow 4p$, respectively. The high-temperature spectrum suggests an extensive decomposition of the precursor molecule and we can observe the familiar $b(v' = 0)$ and $C(v' = 0, 1, 2)$ bands of HCl at the high-energy-loss side. However, there is a new broadband feature starting at 4.2 eV and peaking at 5.04 eV. We attribute this band to the $\tilde{X}^1A_1 \rightarrow \tilde{A}^1B_1$ transition of the difluoromethylene (CF_2) radical. The spectrum of this radical was first observed and identified in the region 3300-2300 Å by Venkateswarlu.[8] This transition was assigned later by Mathews[9] as $\tilde{X}^1A_1 \rightarrow \tilde{A}^1B_1$. In our case, the possibility of the combination of two CF_2 can be eliminated by comparison with the electron energy-loss spectrum of tetrafluoroethylene.[10] The CF_2 radical appears to be unreactive with itself and is thermochemically stable ($\Delta H_f^o = -49 \pm 3\ kcal/mol$).[11]

Figure 4 shows the chloroform spectrum at room temperature. The first band with the maximum at 7.10 eV can be assigned as an $n \rightarrow \sigma^*$ Rydberg transition.[12] The shoulder at 8.31 eV and the peak at 8.72 eV are both believed to stem from the $n \rightarrow 4s$ Rydberg manifold.[12] The higher energy transition at 9.26 eV can be

attributed as an $n \rightarrow 4p$ Rydberg. The one dominant feature at still higher energy is a peak at 10.62 eV.

Figure 5 presents the chloroform spectrum at 1000°C, which at high energy loss very much resembles the HCl one, as a result of the efficient thermal decomposition. Beginning at about 4 eV, we have two broadband continua with peaks roughly at 6.3 and 8.0 eV. The last one probably corresponds to the HCl continuum, while the first one occurs in the same region (5.0-7.0 eV) where tetrachloroethylene shows an intense broad transition.[16] Tetrachloroethylene can be formed by bimolecular processes that usually do not occur under FVP conditions except in the case of radical-radical reactions.[2] These facts suggest that the first broadband is probably due mainly to the combination of two dichloromethylenes (CCl_2) to give tetrachloroethylene. It is known that the radical CCl_2 has a weak visible absorption band in the region 2.21-2.81 eV[13] and an ultraviolet absorption band centered at 3.76 eV.[14] The shoulderlike band in the region 4.0-5.0 eV could tentatively be attributed as the $^1A_1 \rightarrow {}^1A_2$ band of CCl_2, which *ab initio* and CI calculations predict to be at 4.5 eV.[15] However, there is no conclusive evidence for the presence of thermochemically unstable CCl_2 ($\Delta H_f^\circ = 39 \pm 3$ *kcal/mol*).[11]

In Figures 6 and 7, the dichloromethane spectra are displayed at room temperature and at 1100°C, respectively. The room temperature spectrum has a shoulder at 7.16 eV that can be assigned as an $n \rightarrow \sigma^*$ Rydberg transition.[12] The first peak with the maximum at 8.26 eV can be attributed to degenerate $n \rightarrow 4s$ Rydberg transitions, while the broadband at 9.12 eV is due to $n \rightarrow 4p$ Rydberg transitions.[12] At still higher energy is a sharp peak at 10.30 eV. The high-temperature spectrum suggests that the dichloromethane is only partially decomposed at 1100°C. The strong and sharp peak at 9.6 eV is the $C^1\Pi(v' = 0)$ transition of the HCl. Except for a shoulderlike feature in the region 5.0-6.0 eV that could not be assigned, the rest of the spectrum resembles a broad and noisy version

of the room temperature one. No evidence for the presence of the thermochemically unstable CClH ($\triangle H_f^o = 71 \pm 5\ kcal/mol$)[11] was found at this temperature.

Figure 8 shows the room temperature spectrum of chloromethane. The shoulder from 6.50 to 7.65 eV can be assigned as an $n \rightarrow \sigma^*$ Rydberg transition.[12] The next band centered at 7.91 eV is attributed to an $n \rightarrow 4s$ Rydberg transition.[12] Then, we have an intense feature at 8.91 eV assigned as an $n \rightarrow 4p$ Rydberg transition, followed by a sharp and intense peak at 9.22 eV, which has been tentatively assigned to the $n \rightarrow 3d$ Rydberg transition.[12] Another intense peak is at 10.20 eV and can be considered as the $n \rightarrow 5p$ Rydberg transition.[12]

Finally, Figure 9 presents the spectrum of chroromethane at 1100°C, which is noisy and lacks the fine structure of the one at room temperature. There is no HCl feature about 9.6 eV, and we can assume that there was no measurable thermal decomposition at this temperature.

IV. SUMMARY

In conclusion, we have used the method of electron energy-loss spectroscopy to investigate the pyrolysis of four halomethanes via HCl α-elimination reaction. At sufficiently high temperature we observed a complete and clean thermal unimolecular decomposition of halomethanes that contain at least one hydrogen and one chlorine atom. The difluoromethylene radical can be easily generated by the chlorodifluoromethane pyrolysis at 900°C. We also assigned the far-ultraviolet bands of the pyrolytic precursor molecules based only on the optical spectra. To our knowledge, no low-energy-loss study of these compounds has been published.[17,18]

REFERENCES

1. D. M. Golden, G. N. Spokes, and S. W. Benson, *Angew. Chem. Int. Ed. Engl.*, **12**, 534 (1973).
2. E. Hedaya, *Acc. Chem. Res.*, **2**, 367 (1969).
3. K. N. Walzl, C. F. Koerting, I. M. Xavier Jr., and A. Kuppermann, *J. Chem. Phys.*, **86**, 89 (1987).
4. C. F. Koerting, K. N. Walzl, and A. Kuppermann, *Chem. Phys. Lett.*, **109**, 140 (1984).
5. M. Bettendorff, S. D. Pluerimhoff, and R. Buenker, *Chem. Phys.*, **66**, 261 (1982).
6. J. B. Nee, M. Suto, and L.C. Lee, *J. Chem. Phys.*, **85**, 719 (1986).
7. R. Gilbert, P. Sauvageau, and C. Sandorfy, *J. Chem. Phys.*, **60**, 4820 (1974).
8. P. Venkateswarlu, *Phys. Rev.*, **77**, 676 (1959).
9. C. W. Mathews, *Can. J. Phys.*, **45**, 2355 (1967).
10. M. J. Coggiola, W. M. Flicker, O. A. Mosher, and A. Kuppermann, *J. Chem. Phys.*, **65**, 2655 (1976).
11. S. G. Lias, Z. Karpas, and J. F. Liebman, *J. Am. Chem. Soc.*, **107**, 6089 (1985).
12. B. R. Russell, L. O. Edwards, and J. W. Raymonda, *J. Am. Chem. Soc.*, **95**, 2129 (1973).
13. D.E.Milligan and M. E. Jacox, *J. Chem. Phys.*, **47**, 703 (1967).
14. T. Ha, H. U. Gremlich, and R. E. Bühler, *Chem. Phys. Lett.*, **65**, 16 (1979).
15. M. T. Nguyen, M. C. Kerins, A. F. Hegarty, and N. J. Fitzpatrick, *Chem. Phys. Lett.*, **117**, 295 (1985).
16. C. F. Koerting, K. N. Walzl, and A. Kuppermann, *J. Chem. Phys.*, in press.
17. A. Kuppermann, W. M. Flicker, and O. A. Mosher, *Chem. Rev.*, **79**, 77 (1979).

18. S. Trajmar, D. F. Register, and A. Chutjian, *Phys. Rep.*, **97**, 219 (1983).

FIGURE CAPTIONS

Figure 1. Electron energy-loss spectrum of hydrogen chloride with $E_o = 50$ eV and $\theta = 10°$. All spectra were measured at the same impact energy and scattering angle, using an effusive jet as the target source.

Figure 2. Electron energy-loss spectrum at room temperature of chlorodifluoromethane.

Figure 3. Electron energy-loss spectrum at 900° C of chlorodifluoromethane.

Figure 4. Electron energy-loss spectrum at room temperature of chloroform.

Figure 5. Electron energy-loss spectrum at 1000° C of chloroform.

Figure 6. Electron energy-loss spectrum at room temperature of dichloromethane.

Figure 7. Electron energy-loss spectrum at 1100° C of dichloromethane.

Figure 8. Electron energy-loss spectrum at room temperature of chloromethane.

Figure 9. Electron energy-loss spectrum at 1100° C of chloromethane.

Figure 1.

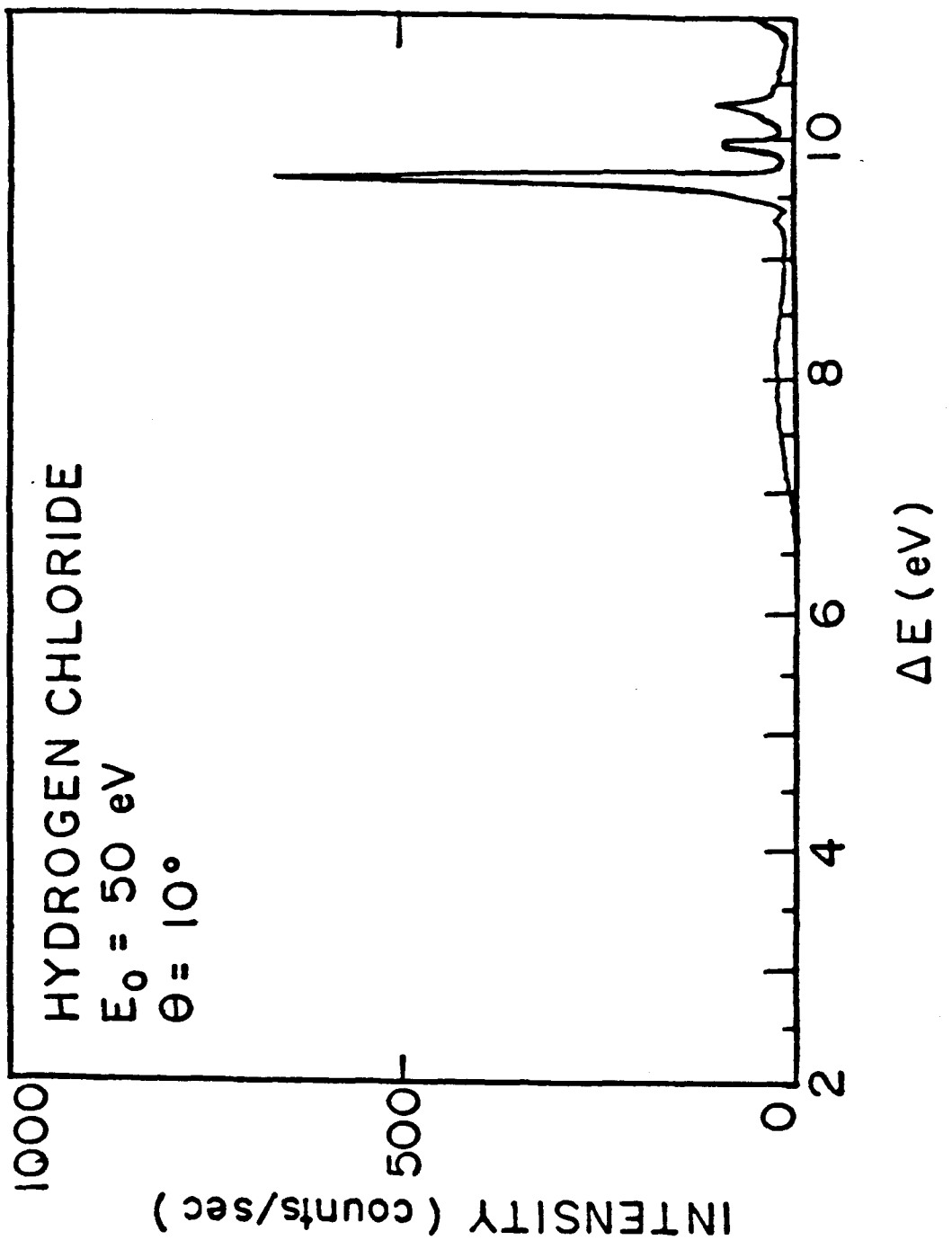
HYDROGEN CHLORIDE
E_o = 50 eV
θ = 10°
INTENSITY (counts/sec)
1000
500
0
2
4
6
8
10
ΔE (eV)

Figure 2.

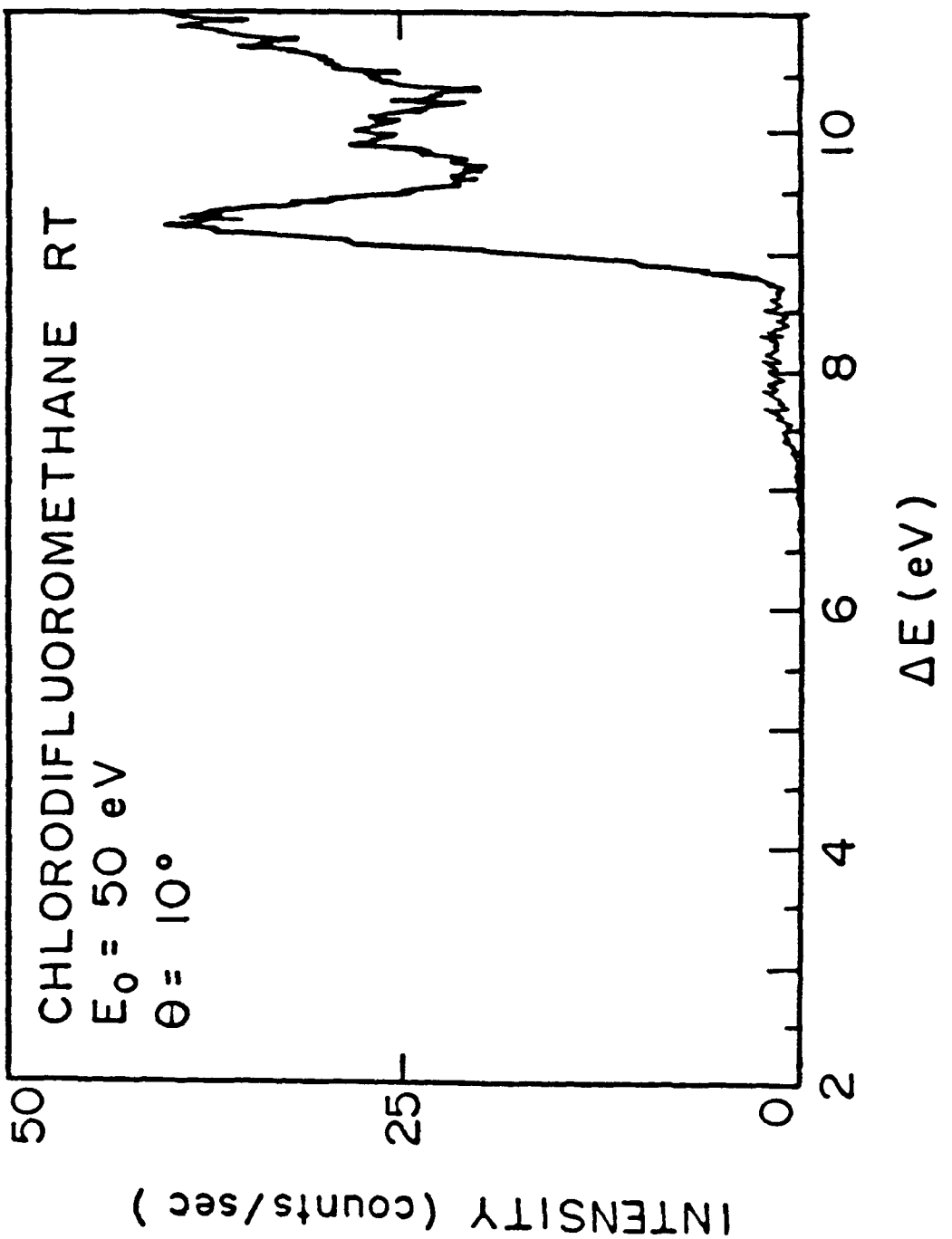
CHLORODIFLUOROMETHANE RT
E_o = 50 eV
θ = 10°
INTENSITY (counts/sec)
50
25
0
2
4
6
8
10
ΔE (eV)

Figure 3.

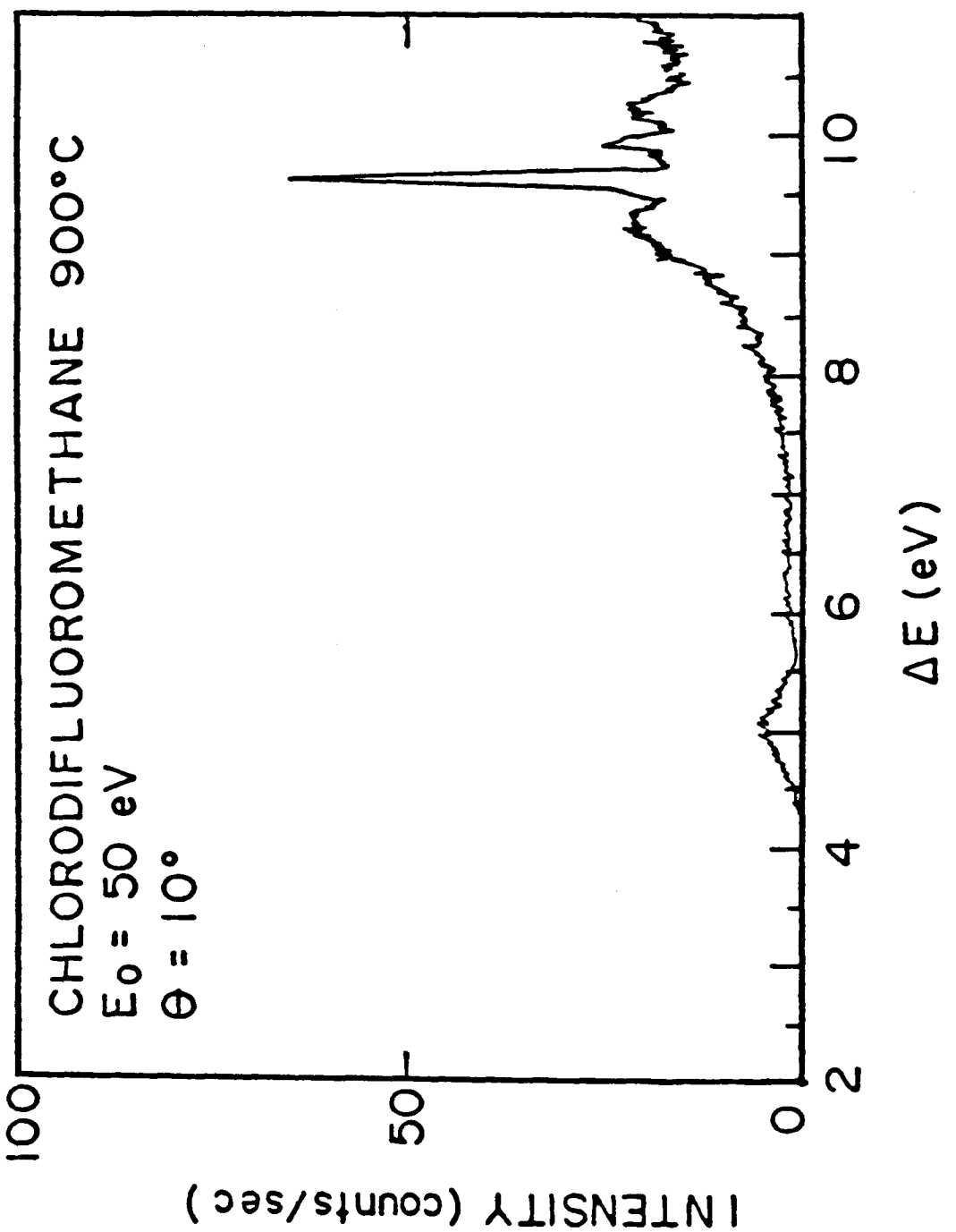
CHLORODIFLUOROMETHANE 900°C
E₀ = 50 eV
θ = 10°
INTENSITY (counts/sec)
100
50
0
2
4
6
8
10
ΔE (eV)

Figure 4.

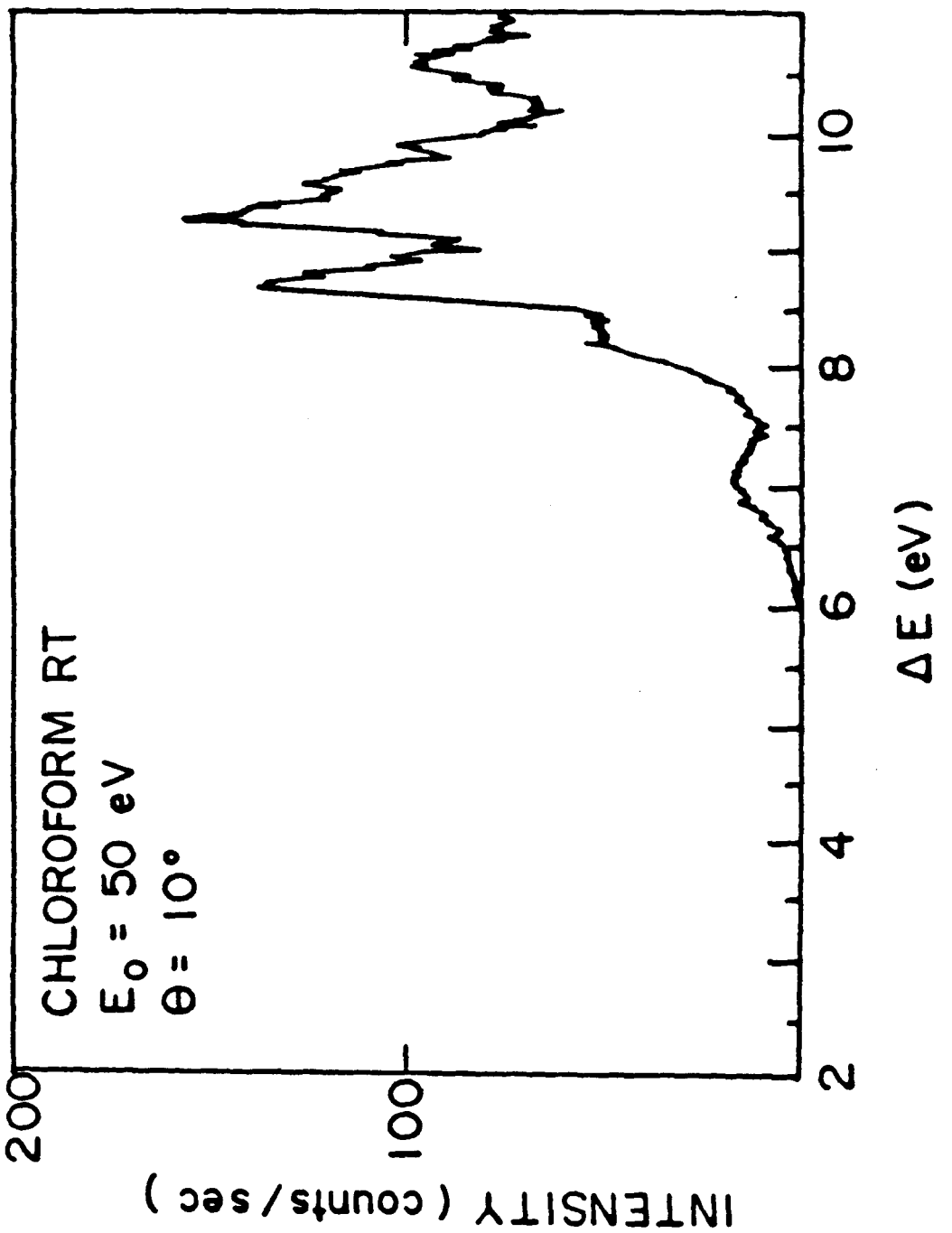
CHLOROFORM RT
E_o = 50 eV
θ = 10°
200
100
INTENSITY (counts / sec)
2
4
6
8
10
ΔE (eV)

Figure 5.

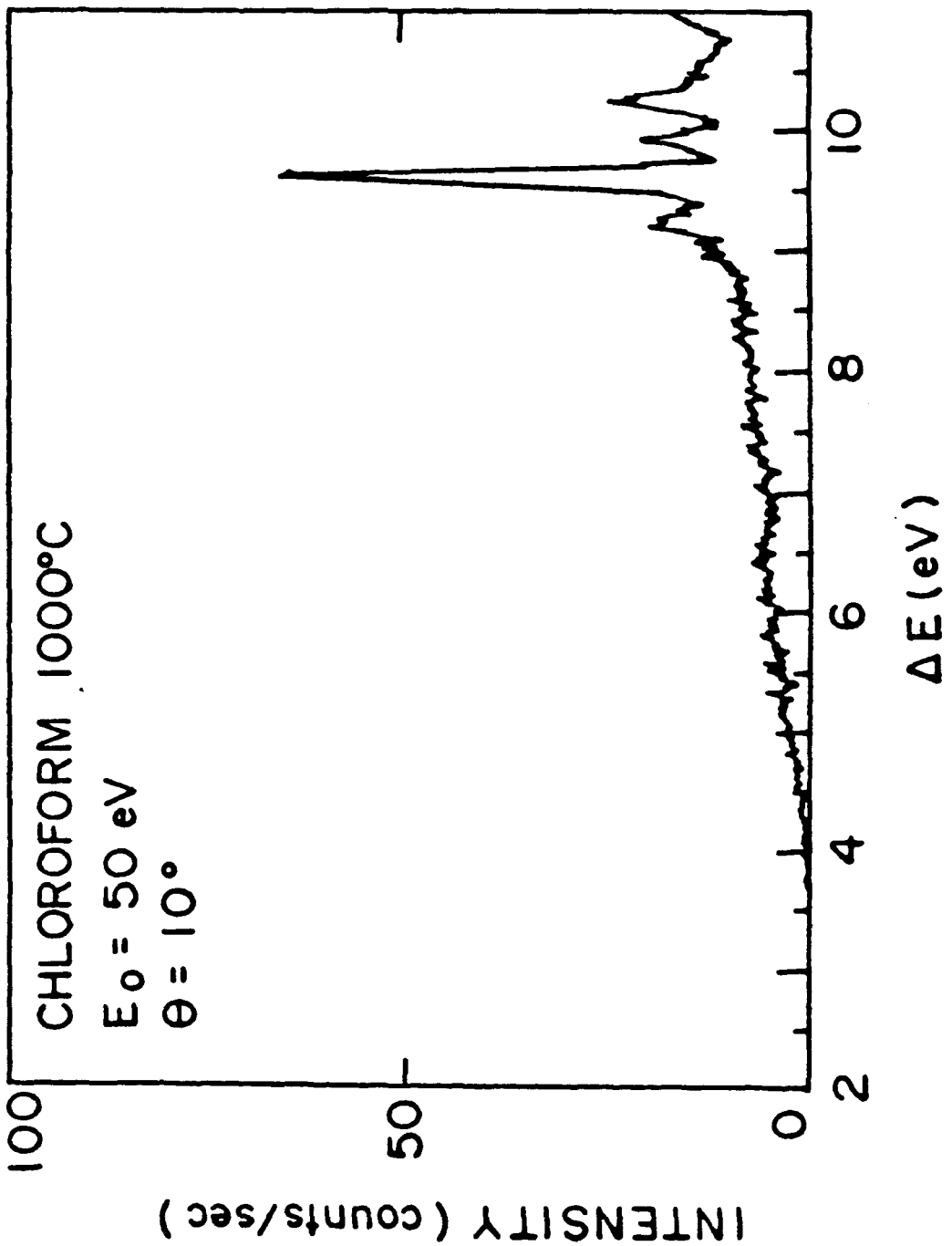
CHLOROFORM 1000°C
E_o = 50 eV
θ = 10°
INTENSITY (counts/sec)
100
50
0
2
4
6
8
10
ΔE (eV)

Figure 6.

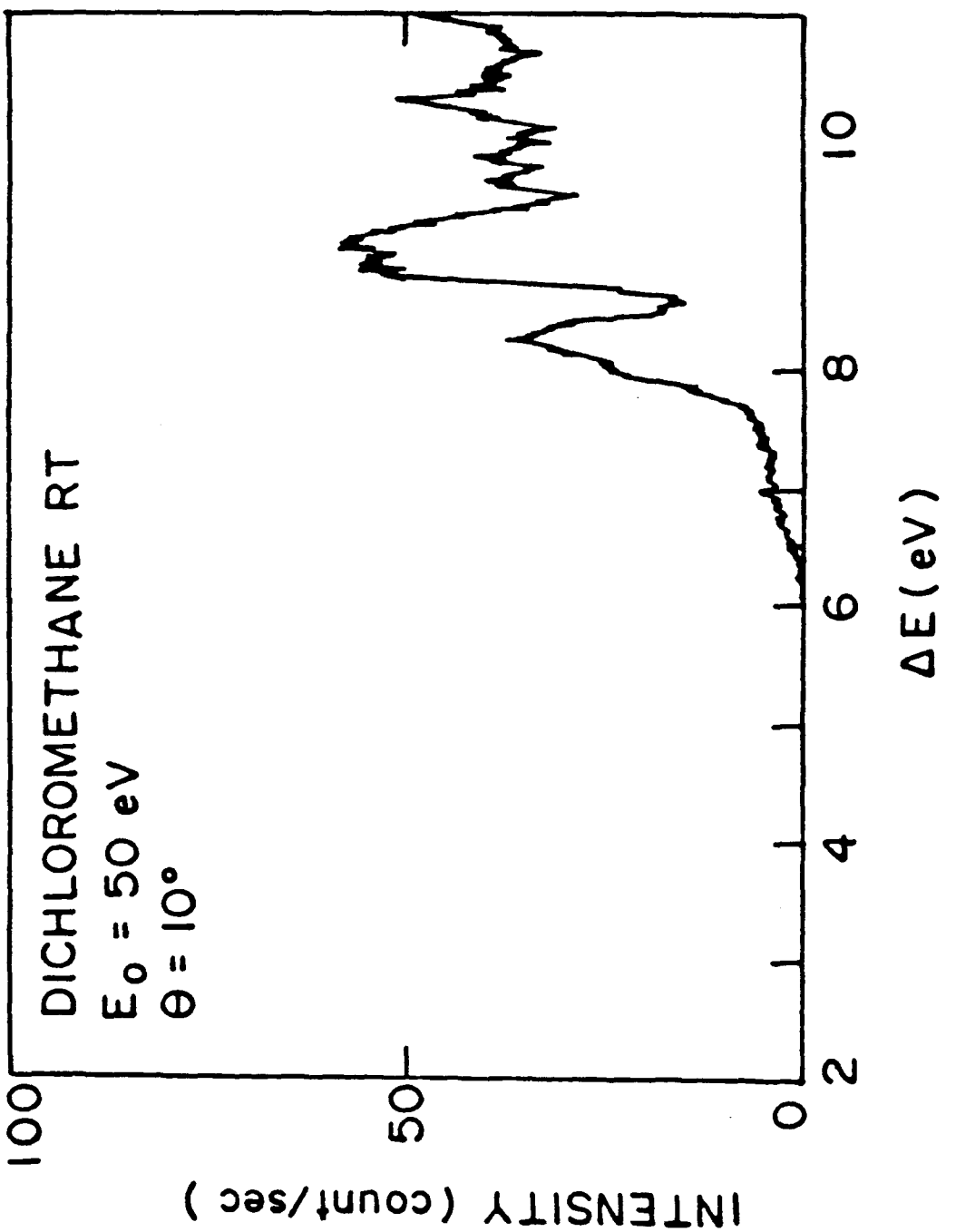
DICHLOROMETHANE RT
E_o = 50 eV
θ = 10°
INTENSITY (count/sec)
100
50
0
2
4
6
8
10
ΔE(eV)

Figure 7.

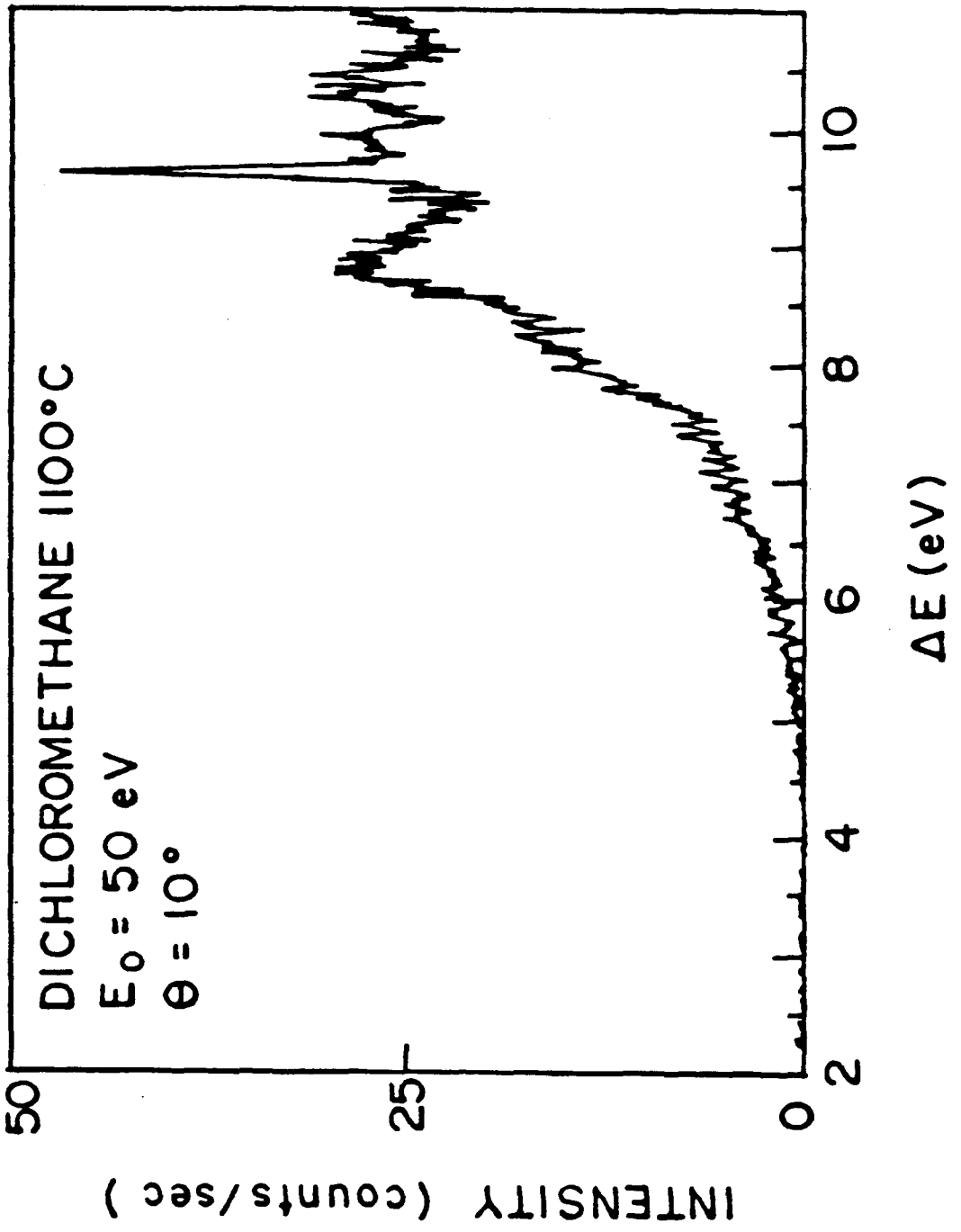
DICHLOROMETHANE 1100°C
E_o = 50 eV
θ = 10°
INTENSITY (counts/sec)
50
25
0
2
4
6
8
10
ΔE (eV)

Figure 8.

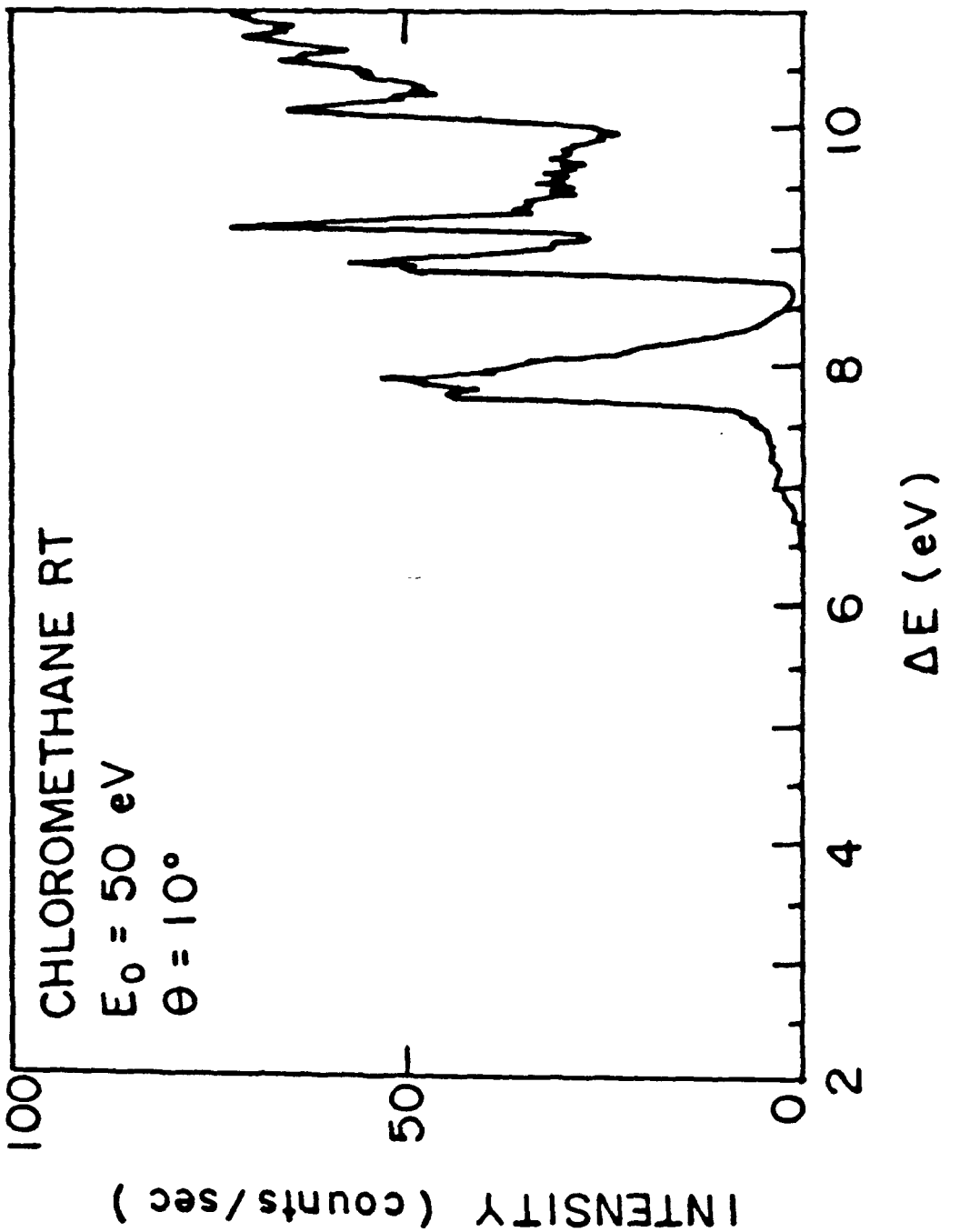
CHLOROMETHANE RT
E_o = 50 eV
θ = 10°
INTENSITY (counts/sec)
100
50
0
2
4
6
8
10
ΔE (eV)

Figure 9.

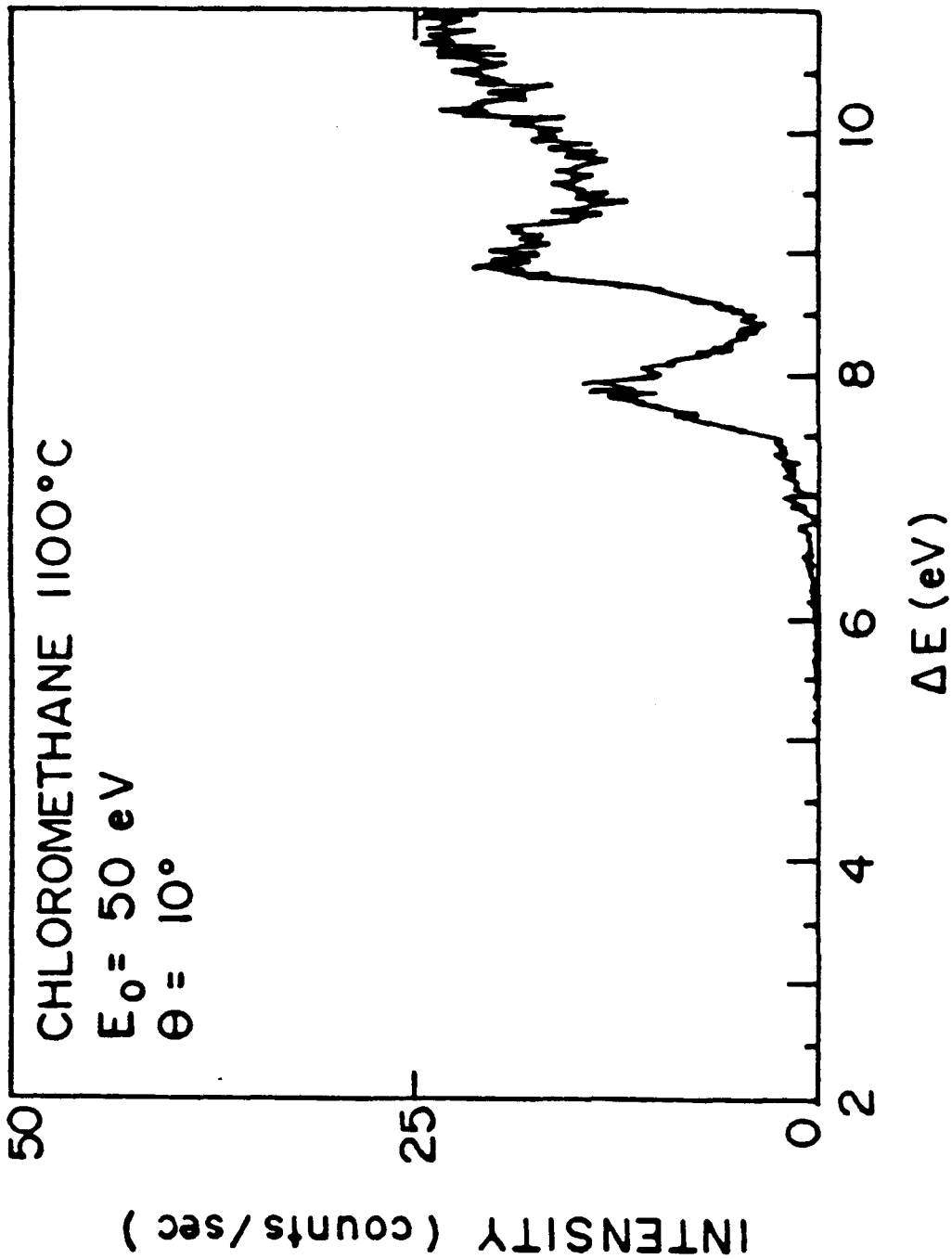
CHLOROMETHANE 1100°C
E_o= 50 eV
θ = 10°
INTENSITY (counts/sec)
50
25
0
2
4
6
8
10
ΔE (eV)

APPENDIX III

AN ELECTRON-IMPACT SPECTROSCOPY INVESTIGATION OF DIKETENE

AN ELECTRON-IMPACT SPECTROSCOPY INVESTIGATION OF DIKETENE[1]

I. M. Xavier Jr.[2], K. N. Walzl[3], M. R. Giorgi and A. Kuppermann

Arthur Amos Noyes Laboratory of Chemical Physics,[4]

California Institute of Technology, Pasadena, CA 91125

(Received)

Abstract

The electronic spectrum of diketene was investigated by the technique of variable-angle, electron energy-loss spectroscopy, using the impact energies of 25 eV and 50 eV, and varying the scattering angle from 10° to 90°. Transitions have been observed at 4.36 eV, 5.89 eV, 6.88 eV and 7.84 eV. Based on the intensity variation of these transitions with impact energy and scattering angle, and through analogy with simpler molecules, the first three are tentatively assigned to an $n \rightarrow \pi^*$ transition, a $\pi \rightarrow \sigma^*(3s)$ Rydberg transition and a $\pi \rightarrow \pi^*$ transition.

---

[1] This work was supported in part by the U. S. Department of Energy, Contract No. DE-AM03-76F00767, Project Agreement No. DE-AT03-76ER72004.

[2] Work performed in partial fulfillment of the requirements for the Ph.D. degree in Chemistry at the California Institute of Technology.

Present address: Departamento de Quimica Fundamental, Universidade Federal de Pernambuco, Ciudade Universitaria, 50.739 Recife, PE, Brazil.

[3] Present address: Institute for Defense Analyses, 1801 N. Beauregard Street, Alexandria, VA 22311-1772.

[4] Contribution No.

I. INTRODUCTION

Low-energy, variable-angle, electron-impact spectroscopy, a useful method for studying both optically forbidden and optically allowed electronic transitions,[1,2] has been used to investigate the electronic spectrum of diketene. Previous optical studies[3,4] of diketene extended to 250 nm (about 5 eV), and showed only a weak, ultraviolet, absorption band at 313 nm (3.96 eV). The present work shows four new, higher energy-loss, electronic transitions including a spin-forbidden one. The diketene (4-methyleneoxetan-2-one, **1**) structure[5,6] was elucidated by x-ray diffraction in 1952, forty-five years after its first preparation.

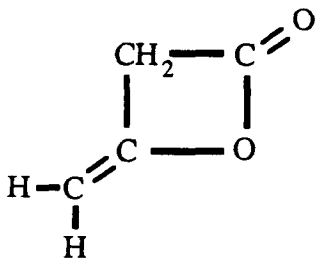

The planarity of the four-membered ring has been established by Raman spectroscopy.[7]

Information about the nature of the excited electronic states observed in an electron-impact spectrum can be obtained by studying the dependence of the intensity of each transition on impact energy and scattering angle.[1,2] Transitions which, in optical spectroscopy, are both electric dipole-allowed and spin-allowed have differential cross sections (DCS) in electron-impact spectroscopy, which are forward-peaked.[1,2] In contrast, spin-forbidden transitions involving changes in the molecular spin quantum number by ± 1, such as singlet $\rightarrow$ triplet excitation, have more nearly isotropic DCS in the angular range 10° to 90°.[1,2] Such transitions occur by the mechanism of electron exchange.[8] Spin-allowed but electric-dipole-forbidden processes are forward-peaked, but often not as much as fully allowed transitions.[9,10] As reflected in the different DCS shapes, optically forbidden processes, and in

particular the spin-forbidden ones, become more intense with respect to the optically allowed processes at large scattering angles.[1,2] Another advantage of the electron-impact method is that spectral features in the far ultraviolet are as easily examined as those in the visible and near ultraviolet.

II. EXPERIMENTAL

The electron spectrometer used in this study was similar to one described previously.[11] Briefly, an electron beam is energy-selected by a hemispherical electrostatic energy analyzer (and the associated focusing lenses) and scattered from the target vapor in a scattering box. In this work, the incident-beam current was between 1-10 nA and was typically 4 nA. Sample pressures were estimated to be between 5-10 mTorr. Electron-energy losses were determined at angles between 10°-90° by means of a second electrostatic energy analyzer and detector. The energy-loss spectrum thus obtained is analogous to an optical absorption spectrum, except that optically forbidden processes are much more readily detected.[1,2]

The spectrometer resolution (as measured by the full width at half-maximum of the elastically scattered feature) varied between 50 and 100 meV for all reported spectra and was typically 80 meV. Diketene was obtained from Aldrich, and had a stated purity of 98%. All samples were subjected to three liquid nitrogen freeze-pump-thaw cycles and used without further purification.

III. RESULTS AND DISCUSSION

Figure 1 shows the low-energy-loss portion of the diketene electron-impact spectrum at: a) $E_0 = 50$ eV, $\theta = 10°$; b) $E_0 = 50$ eV, $\theta = 90°$; c) $E_0 = 25$ eV, $\theta = 10°$; and d) $E_0 = 25$ eV, $\theta = 90°$. These figures indicate the presence of four transitions having maximum intensities at 4.36 eV, 5.89 eV, 6.88 eV and 7.84 eV energy loss. In Fig. 2 we display the corresponding differential cross-section curves at the impact energies of 25 eV and 50 eV, obtained by a method previously described.[9]

The most intense feature has a peak intensity at 6.88 eV. From Fig. 2 the elastic peak and the peak at 6.88 eV exhibit an intensity variation of about two orders of magnitude over the angular range, as should fully allowed bands. The transitions at 7.84 eV and 5.89 eV have DCS curves less forward-peaked, but they can still be considered as allowed bands. The DCS of the 4.36 eV transition is nearly isotropic and has the characteristic behavior of a spin-forbidden transition.[1,12]

Up to now, no far ultraviolet spectra of diketene have been reported. In the absence of any calculations directly relevant to the electronic spectroscopy of this molecule, we are tentatively assigning these observed transitions of diketene under the qualitative assumptions described below.

Diketene contains two important chromophores: the carbonyl and the ethylene groups. The carbonyl in small monoketones exhibits the well-known (n, π^*) band in the ultraviolet followed by three Rydberg bands $(n, (3s, 3p, 3d))$ in the far-ultraviolet.[13] The (π, π^*) band is expected to be at relatively high-energy loss (possibly as high as 9.0 eV) superimposed by Rydberg bands.[13,14] The carbon double bond in monoalkenes exhibits an intense (π, π^*) absorption band, which coincides with, or is preceded by, a $(\pi, 3s)$ Rydberg band.[13] In ethylene itself, the Rydberg band is superimposed on the low-frequency wing of the (π, π^*) band,[15]

while in highly methylated or fluorinated olefins, the Rydberg $(\pi, 3s)$ becomes the first spectral band and is well separated from the (π, π^*) band.[13]

The observed spectral bands of diketene can be tentatively assigned by analogy to the properties of the isolated carbonyl and ethylene chromophores. In the energy-loss range of this work (3.5-8.5 eV), the spin-forbidden transition at 4.36 eV is the only spectral feature that can be attributed to the carbonyl chromophore. By analogy with previous electron-impact assignments in monoketones,[14,16] this transition is assigned as $n \rightarrow \pi^*(S - T)$. The other three spin-allowed transitions can be attributed as due to mainly the carbon-carbon, double-bond chromophore. The strongest transition at 6.88 eV is assigned as $\pi \rightarrow \pi^*(S - S)$, based on the electron energy-loss spectroscopy of methyl-substituted ethylenes[17] and fluoroethylenes.[18] The shoulder at 5.89 eV resembles the shoulder on the strongest feature in the energy-loss spectrum of the fluoroethylenes[18] and is assigned as $\pi \rightarrow \sigma^*(3s)$ Rydberg $(S - S)$. Finally, the spin-allowed band at 7.84 eV is probably another Rydberg band, similar to those observed in ethylenes.[15]

IV. SUMMARY

In conclusion, we have used the method of low-energy, variable-angle, electron-impact spectroscopy to study the far-ultraviolet spectrum of diketene. Four new transitions have been observed, including one that is spin-forbidden. Tentative assignments of these transitions was made under qualitative assumptions. We hope that calculations will be available in the near future in order to confirm these assignments.

REFERENCES

1. A. Kuppermann, J. K. Rice, and S. Trajmar, *J. Phys. Chem.*, **72**, 3094 (1968).
2. S. Trajmar, J. K. Rice, and A. Kuppermann, *Advan. Chem. Phys.*, **18**, 15 (1970).
3. J. D. Roberts, R. Armstrong, R. F. Trimble, and M. Burg, *J. Am Chem. Soc.*, **71**, 843 (1949).
4. M. Calvin, T. T. Magel, and C. D. Hurd, *J. Am. Chem. Soc.*, **63**, 2174 (1941).
5. R. J. Clemens, *Chem. Rev.*, **86**, 241 (1986).
6. E. T. Seidl and H. F. Schaefer III, *J. Am. Chem. Soc.*, **112** , (1990) 1493.
7. J. R. Durig and J. N. Willis Jr., *Spectrochim. Acta*, **22**, 1299 (1966).
8. J. R. Oppenheimer, *Phys. Rev.*, **29**, 433 (1927).
9. O. A. Mosher, W. M. Flicker, and A. Kuppermann, *J. Chem. Phys.*, **62**, 2600 (1975).
10. D. C. Cartwright, W. J. Hunt, W. Williams, S. Trajmar, and W. A. Goddard III, *Phys. Rev.*, **A8**, 2436 (1973).
11. (a) C. F. Koerting, K. N. Walzl, and A. Kuppermann, *Chem. Phys. Lett.*, **109**, 140 (1984); (b) C. F. Koerting, *Ph.D. Thesis* (California Institute of Technology, Pasadena, CA, 1985).
12. A. Kuppermann, W. M. Flicker, and O. A. Mosher, *Chem. Rev.*, **79**, 77 (1979).
13. C. Sandorfy and L. S. Lussier in *Photophysics and Photochemistry in the Vacuum Ultraviolet*, S. P. McGlynn, G. L. Findley and R. H. Huebner, Eds., Reidel, Dordrecht (1985), p. 819.
14. K. N. Walzl, C. F. Koerting, and A. Kuppermann, *J. Chem. Phys.*, **87**, 3796 (1987).
15. A. J. Merer, and R. S. Mulliken, *Chem. Rev.*, **69**, 639 (1969).

16. R. P. Frueholtz, W. M. Flicker, and A. Kuppermann, *Chem. Phys. Lett.*, **38**, 57 (1976).

17. W. M. Flicker, O. A. Mosher, and A. Kuppermann, *Chem. Phys. Lett.*, **36**, 56 (1975).

18. M. J. Coggiola, O. A. Mosher, W. M. Flicker, and A. Kuppermann, *Chem. Phys. Lett.*, **27**, 14 (1974).

FIGURE CAPTIONS

Figure 1. Diketene electron energy-loss spectra at: a) E_0 = 50 eV, θ = 10°; b) E_0 = 50 eV, θ = 90°; c) E_0 =25 eV, θ = 10°; d) E_0 = 25 eV, θ = 90°.

Figure 2. Differential cross sections of diketene at: a) E_0 = 50 eV and b) E_0 = 25 eV. Elastic scattering (□) and transitions to the excited states lying at 4.36 eV (○), 5.89 eV (△), 6.88 eV (+), and 7.84 eV (×) above the ground state.

Figure 1.

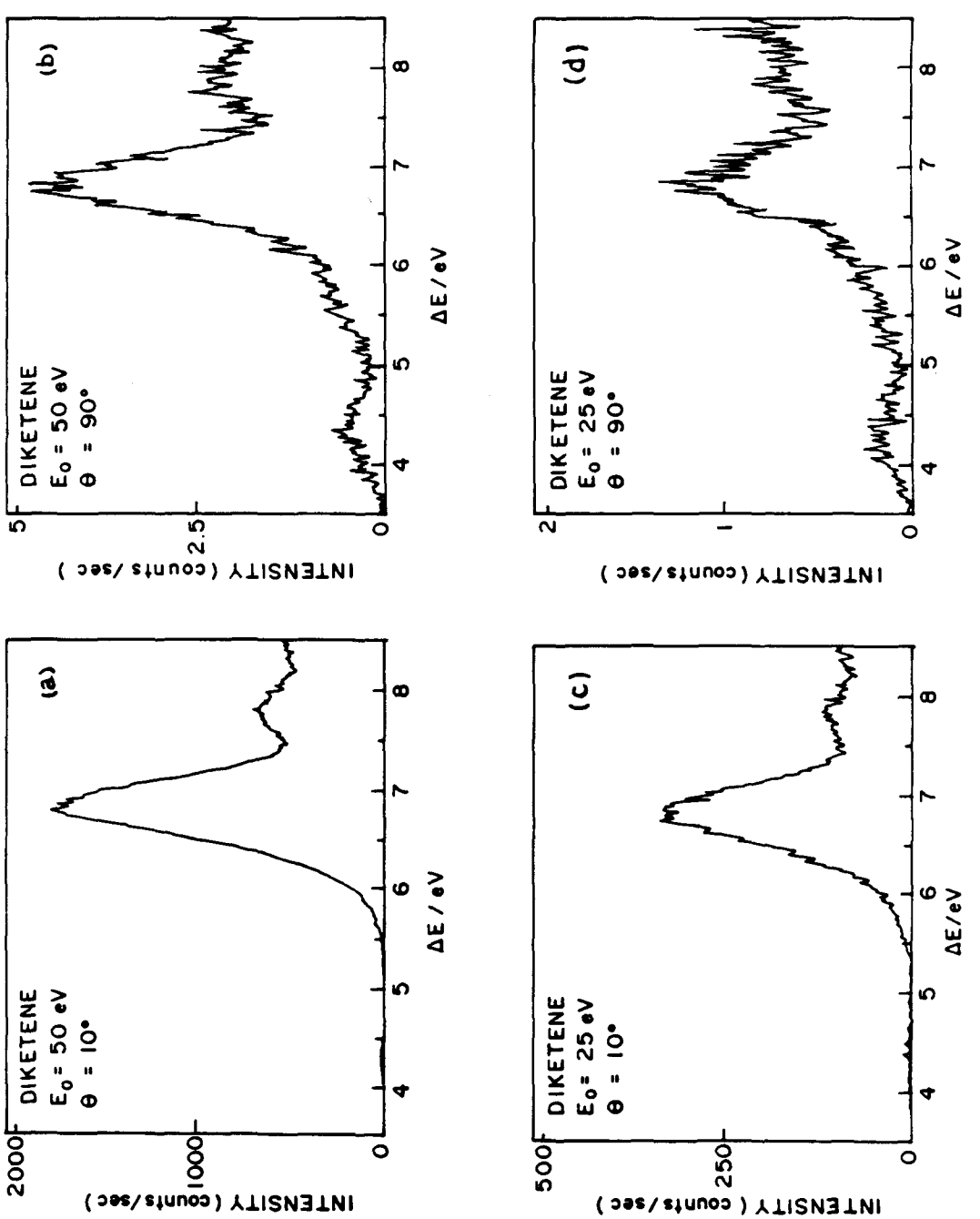
(a)
DIKETENE
E_0 = 50 eV
θ = 10°
INTENSITY (counts/sec)
ΔE / eV
(b)
DIKETENE
E_0 = 50 eV
θ = 90°
INTENSITY (counts/sec)
ΔE / eV
(c)
DIKETENE
E_0 = 25 eV
θ = 10°
INTENSITY (counts/sec)
ΔE/eV
(d)
DIKETENE
E_0 = 25 eV
θ = 90°
INTENSITY (counts/sec)
ΔE / eV

Figure 2.

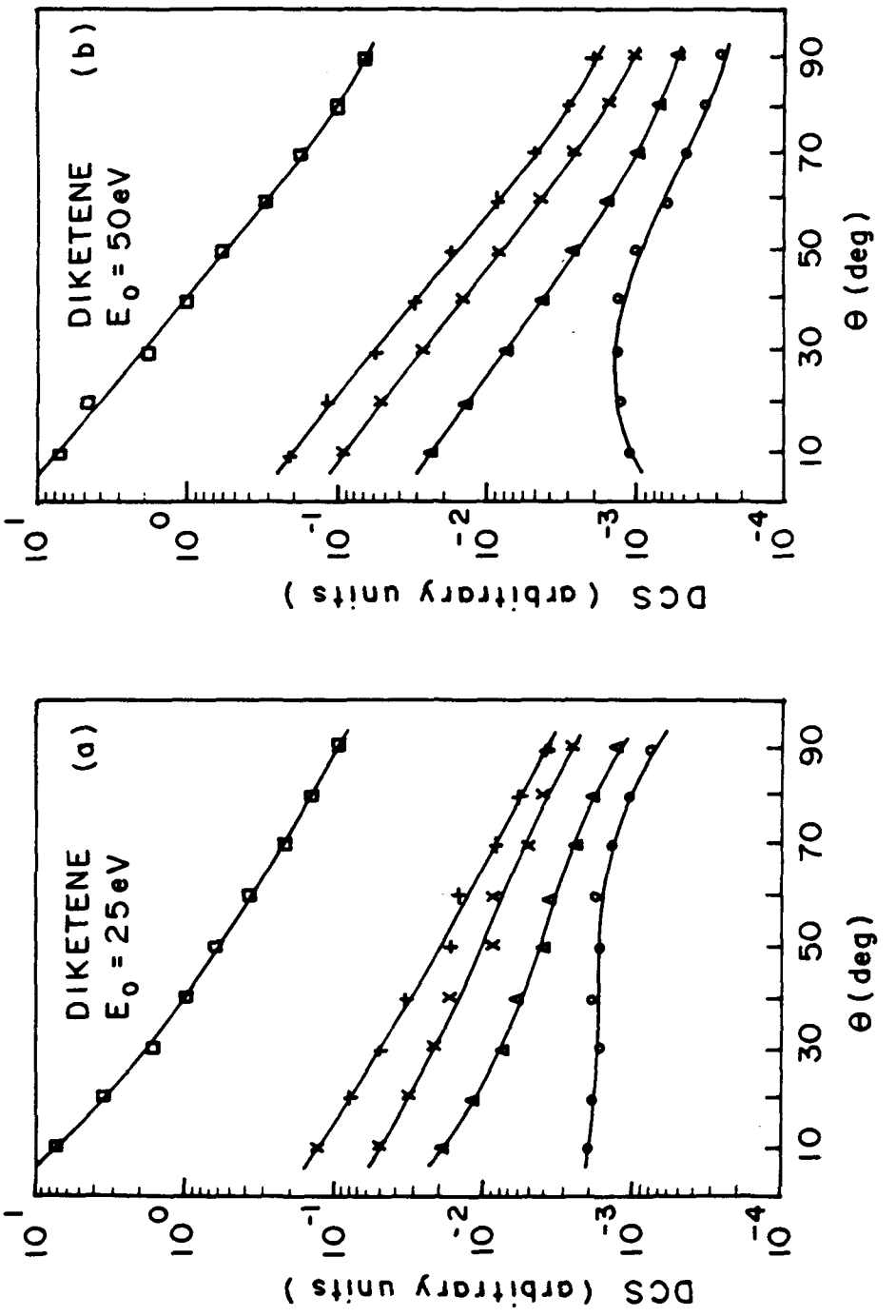
(b)
DIKETENE
E_o = 50eV
(a)
DIKETENE
E_o = 25eV
DCS (arbitrary units)
θ (deg)
10
30
50
70
90
10^{1}
10^{0}
10^{-1}
10^{-2}
10^{-3}
10^{-4}